Title
Multichroic Bolometric Detector Architecture for Cosmic Microwave Background Polarimetry Experiments

Author
Suzuki, Aritoki

Publication Date
2013

Peer reviewed|Thesis/dissertation

Multichroic Bolometric Detector Architecture for Cosmic Microwave Background Polarimetry Experiments

by

Aritoki Suzuki

A dissertation submitted in partial satisfaction of the
requirements for the degree of
Doctor of Philosophy

in

Physics

in the

Graduate Division

of the

University of California, Berkeley

Committee in charge:

Professor Adrian T. Lee, Chair
Professor William Holzapfel
Professor Aaron Parsons

Fall 2013

Multichroic Bolometric Detector Architecture for Cosmic Microwave Background Polarimetry Experiments

Abstract

Multichroic Bolometric Detector Architecture for Cosmic Microwave Background Polarimetry Experiments

by

Aritoki Suzuki

Doctor of Philosophy in Physics

University of California, Berkeley

Professor Adrian T. Lee, Chair

Characterization of the Cosmic Microwave Background (CMB) B-mode polarization signal will test models of inflationary cosmology, as well as constrain the sum of the neutrino masses and other cosmological parameters. The low intensity of the B-mode signal combined with the need to remove polarized galactic foregrounds requires a sensitive millimeter receiver and effective methods of foreground removal. Current bolometric detector technology is reaching the sensitivity limit set by the CMB photon noise. Thus, we need to increase the optical throughput to increase an experiment's sensitivity. To increase the throughput without increasing the focal plane size, we can increase the frequency coverage of each pixel. Increased frequency coverage per pixel has additional advantage that we can split the signal into frequency bands to obtain spectral information. The detection of multiple frequency bands allows for removal of the polarized foreground emission from synchrotron radiation and thermal dust emission, by utilizing its spectral dependence. Traditionally, spectral information has been captured with a multi-chroic *focal plane* consisting of a heterogeneous mix of single-color pixels. To maximize the efficiency of the focal plane area, we developed a multi-chroic *pixel*. This increases the number of pixels per frequency with same focal plane area.

We developed multi-chroic antenna-coupled transition edge sensor (TES) detector array for the CMB polarimetry. In each pixel, a silicon lens-coupled dual polarized sinuous antenna collects light over a two-octave frequency band. The antenna couples the broadband millimeter wave signal into microstrip transmission lines, and on-chip filter banks split the broadband signal into several frequency bands. Separate TES bolometers detect the power in each frequency band and linear polarization. We will describe the design and performance of these devices and present optical data taken with prototype pixels and detector arrays. Our measurements show beams with percent level ellipticity, percent level cross-polarization leakage, and partitioned bands using banks of two and three filters. We will also describe the development of broadband anti-reflection coatings for the high dielectric constant lens. The broadband anti-reflection coating has approximately 100% bandwidth and no detectable loss at cryogenic temperature.

We will describe a next generation CMB polarimetry experiment, the POLARBEAR-2, in detail. The POLARBEAR-2 would have focal planes with kilo-pixel of these detectors to achieve high sensitivity. We'll also introduce proposed experiments that would use multi-chroic detector array we developed in this work. We'll conclude by listing out suggestions for future multichroic detector development.

To Yukoku Suzuki, Mariko Suzuki, Mio Suzuki, Monchan and Friends

Contents

List of Figures

List of Tables

Acknowledgments

This is the most difficult section in the thesis. I met so many people that had positive influence on me. I cannot possibly mention everybody here. I apologize in advance for people I was not able to include here.

I would like to thank my advisor Adrian Lee. His support and freedom he gave me made it possible for me to be creative. He is unique in the field that he trains students to learn detector fabrication techniques. Such skill is highly desired in our field, and also beyond our field. I would like to thank Paul Richards for many advices he gave me. His advice was helped me to succeed in research, but it also helped me to become better scientist overall. Bill Holzapfel always had useful suggestions. His advice turned troubling dewar into the cold dewar. When Billy and I were stuck on sealing method for 3He adsorption fridge, Bill gave us an advice that allow us to seal it on the first try.

I was surrounded by great graduate students. Roger O'Brient dedicated so much of his busy schedule at the end of his graduate career to train me. He was a great mentor that in half year he trained me in so many things that I needed to survive. He kept giving me advices and ideas even after his graduation. I inherited his work and pushed on, so much of this thesis stems from his ideas and his work. Mike Myers gave suggestions that steered research into right direction at critical points. Kam Arnold taught me art of making detector array. Many of detector array design stems from POLARBEAR-1 detector array that he designed and fabricated. In private life. his advice on where to propose in Hawaii island definitely helped. Ziggy Kermish always had answer when we asked him how we should go about designing the POLARBEAR-2 receiver. Erin Quealy and I worked together on broadband anti-reflection coating problem. I learned importance of paying attention to details from working with her. Bryan Steinbach's sharp questions pushed me to become more quantitative scientist. Ben Westbrook was great lab-buddy and fab-buddy. We shared many dewar runs together. Adnan Ghribi gave me many useful suggestion when superconductor did not behave the way I wanted. Recently new talents joined out group. Ari Cukierman and Parker Fegrelius will play big role in making the POLARBEAR-2 happen. I was lucky to have talented undergraduate to work with. Darin Rosen and I worked together on broadband anti-reflection coating. It was his idea of mixing different types of epoxy that made the broadband antireflection to work. It was fun to work with William Walker on 3He adsorption fridge project. We are about to fill the fridge with 3He. I cannot wait to see how it would work.

Microwave engineering work was done with collaborative effort with UCB physics department, UCB astronomy department and UCSD electrical and computer enginering department. Greg Engargiola gave me an idea to remove via at center of antenna. Gabriel Rebeiz provided helpful rule of thumbs that helped to come up with initial design. Jen Edwards did careful study of sinuous antenna with silicon lens. I borrowed a lot of antenna behavior from her work. Her successful work on sinuous antenna gave me confidence to push on to make sinuous antenna work at millimeter wavelength.

Many people from UCSD contributed to the work. It was helpful to have Brian Keating's comments on papers and proceedings. Although I almost drowned, surfing with him at UCSD was fun. I would like to thank Praween Siritanasak for his work on the POLARBEAR-2 lenslet. His

work was crucial since detector is only complete with the lenslet. He also helped me with detector simulation work. Stephanie Moyerman helped to fabricate lenslet seating wafer. Darcy Barrons helped us put together POLARBEAR-2 optical test dewar. It was fun deploying to Chile with Nate Stebor and Dave Boettger. Without Dave, I could not meet quinoa.

I would like to thank Masashi Hazumi to let me visit KEK often and participate many professional events in Japan. It was very helpful to be able to exchange information face to face. I enjoyed exchanging ideas freely with Takayuki Tomaru. I learned many hands on techniques from him. I also enjoyed working with Takahiro Okamura until late at night at KEK. Suguru Takada taught me tricks in cryogenics. Tomotake Matsumura and I worked together on the material development. Tomo figured out how to improve the Fourier transform spectrometer setup for material development. Masaya Hasegawa took me out every night when I visited KEK. Yuji Chinone taught me most of cosmology I know. Without him I could not pass the qualification exam. Whenever I had question about polarization, Haruki Nishino was always there to give me an advice. Working until late at night with Hideki Morii was always enjoyable. I miss going to gym with him. Kaori's measurement on interdigitated capacitor was crucial for its R&D. Yuki Inoue's accurate measurement on material and anti-reflection coating gave confidence in our design. It was fun to work with Yuta Kaneko to create DC SQUID readout from scratch to test bolometers. I learned so much about SQUID through that process.

I borrowed so much of mapping speed calculation from Nils Halverson's memo. His comments during mapping speed discussion helped me to develop the code that I used extensively to optimize the focal plane. Readout parameter would not converged without input from Matt Dobbs. Colin made stay at Chile enjoyable. I cannot wait to see the dewar at Dalhousie taking data with the POLARBEAR-2 wafer. It was critical to have talented machinists in our building to make rapid progress that we made. Machinists at physics machine shop did not just machined beautiful parts for us. They were great advisors that taught us how design should be done. Pete Thussen especially taught me many machining related topics that were critical to designs I made. Xiaofan Meng helped us greatly during fabrication. Xiaofan kept the machine in working condition. He helped me diagnose odd things I see during fabrication. Exchanging ideas on absorption loss in alumina, anti-reflection coating and simulation method with Tom Nitta was helpful.

I would like to thank YuryKolomensky to give me advices and much needed help at early stage of my graduate student career. Without him I would not be where I am today.

We acknowledge support from the NASA, NASA grant NNG06GJ08G. Detectors were fabricated at Berkeley nanofabrication laboratory.

Chapter 1

Cosmic Microwave Background

1.1 Introduction

Observations of distant luminous objects showed that the Universe is expanding [52]. Thus, at the early Universe, we expect the scale of the Universe to be smaller. In the 1940s, Gamow, Alpher and Herman [39, 9] formulated the Big-Band model. In the hot Big-Bang model, the Universe was once extremely hot and dense. Hot plasma filled the universe. Photons were tightly coupled to ionized electrons and protons through scattering in the early Universe. As the Universe expanded, the average temperature of the Universe dropped. When the Universe was 380,000 years old, the scattering rate between photons, electrons and protons fell below the expansion rate of the Universe and the photon decoupled from the ionized electrons and protons. At this moment, the Cosmic Microwave Background (CMB) was created. Since then, photons have streamed freely through the Universe - except for the brief period of time around $z = 10 \sim 6$ when the first stars formed - to reionize neutral hydrogen atoms. Reionized hydrogen atoms and photons interacted for the last time. Studying CMB is a great way to understand the evolution of the Universe because it was generated at the very early Universe where perturbations were still linear. It also acts as well-understood back light source with known black body spectrum. This allowed the detection of high z galaxy through the SunyaevZel'dovich effect. The CMB red-shifted with the expansion of the Universe. Today, the CMB has a wavelength of a few millimeters; putting the CMB experiment in a unique field of its own - between radio and infrared astronomy.

Since its discovery in 1965, CMB observations have given us a wealth of information about the Universe [30, 97]. The Far-Infrared Absolute Spectrophotometer (FIRAS) measured the CMB spectrum and found that the CMB has a 2.73 Kelvin black body spectrum [80]. The black body spectrum of the CMB is one of the pillars of the hot Big Bang model. Relative temperature measurements of the CMB between different parts of the sky showed that the CMB has an anisotropy of the order 10^{-5} Kelvin. It was first detected by the Differential Microwave Radiometer (DMR) aboarded on the Cosmic Background Explorer satellite (COBE) [114]. Many ground experiments, balloon experiments and satellite experiments have mapped the temperature anisotropy with increasing sensitivity and angular resolution. Recently, a full-sky map was published by the Planck

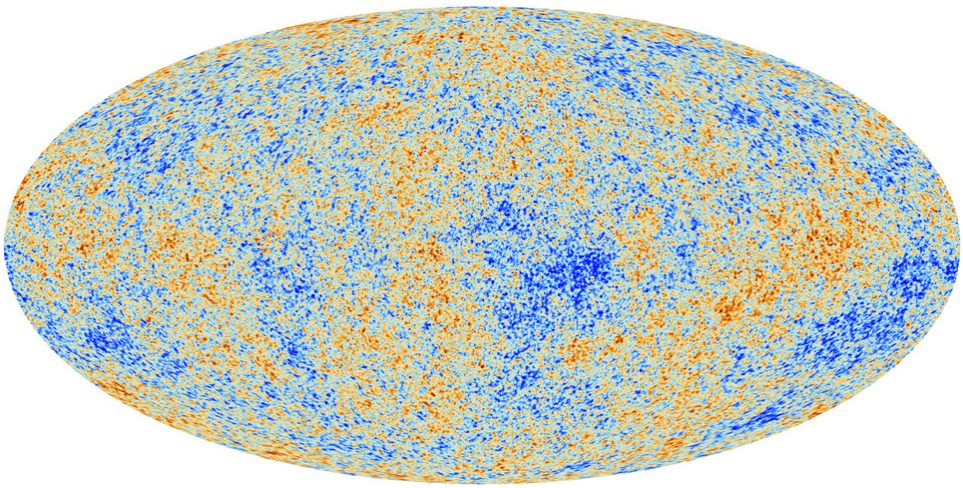

Figure 1.1: Full sky temperature anisotropy map of the CMB after removing the dipole component of the anisotropy and the contribution from the Milky Way galaxy [34].

satellite experiment as shown in Figure 1.1. The results agree with the Λ Cold Dark Matter (ΛCDM) model of the Universe: the Universe is geometrically flat at the cosmological scale and its expansion is being accelerated by Dark Energy.

In 2002, the Degree Angular Scale Interferometer (DASI) first detected the CMB polarization [64]. Since then, various experiments have continued to map the CMB polarization. Results from these experiments show that the measurements of the parity-conserving polarization pattern of the CMB (called E-mode polarization) agree with the expectation from the temperature anisotropy measurements [100, 24, 17]. We also expect some fraction of the CMB to have a parity-violating polarization pattern, called B-mode polarization. There are two sources of B-mode polarization. The first source is weak gravitational lensing from large scale structures that mix the E-mode and the B-mode polarization patterns [51]. This lensing B-mode was recently detected [46]. The second source of B-mode polarization is the primordial gravitational wave [111]. Detecting the primordial B-mode will put constraints on the inflation models and energy level of the inflation potential.

1.2 Anisotropies

Temperature Anisotropy

We are interested in gathering statistical data on CMB temperature. CMB temperature can be expressed using a spherical harmonic expansion:

$$T(\theta,\phi) = \sum_{lm} a_{lm} Y_{lm}(\theta,\phi) \tag{1.1}$$

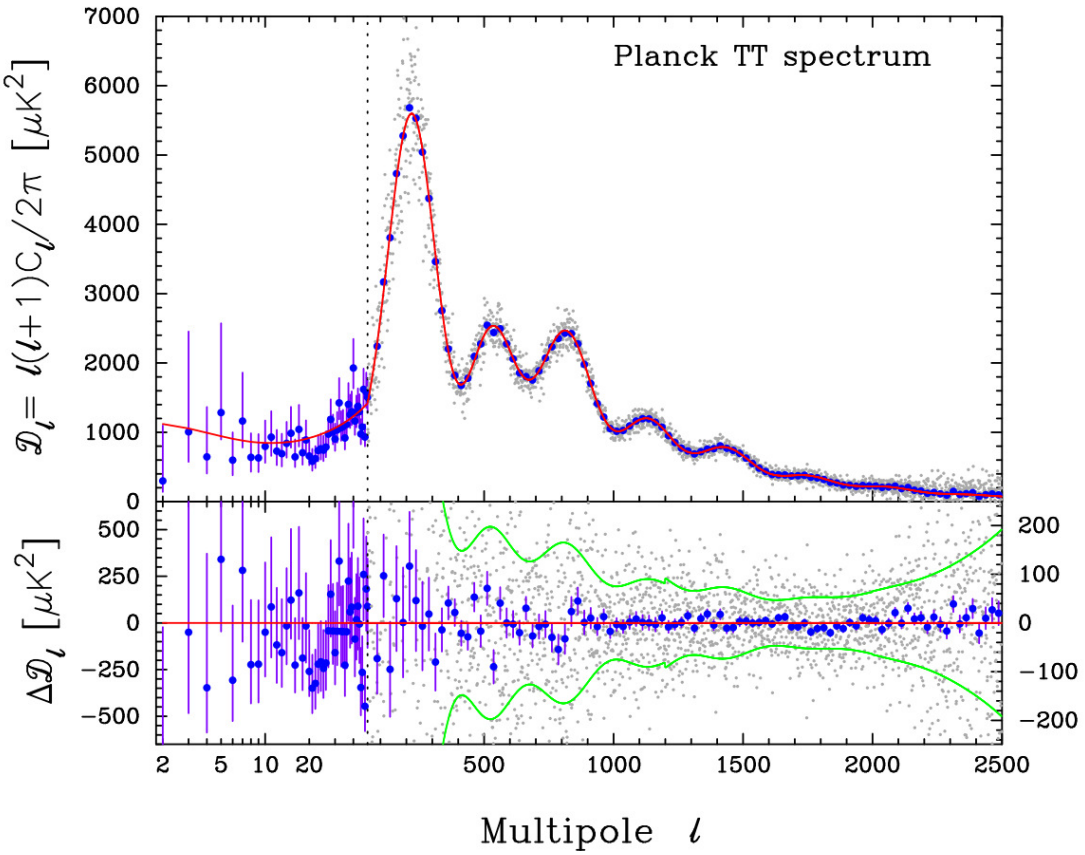

Figure 1.2: Temperature anisotropy power spectrum plot from the Planck 2013 result [1]

The monopole ($l = 0$) component of the CMB is constrained to 2.72548 ± 0.00057 Kelvin [36]. The dipole ($l = 1$) component arises from the doppler shift motion of the solar system in the isotropic CMB at velocity of $v/c = 1.23 \times 10^{-3}$ [5]. Quadrupole and higher terms are plotted on Figure 1.1. Currently, no evidence for non-gaussianity a_{lm} has been found, although, recently, there has been some evidence for deviation from isotropy at a small level [4, 3]. If we assume that the primordial CMB anisotropies corresponded to an isotropic Gaussian random field, then we can describe the CMB anisotropy with a variance of the a_{lm}.

$$\langle a_{lm} a^*_{l'm'} \rangle = \delta_{ll'} \delta_{aa'} C_l \tag{1.2}$$

Plot of $l(l+1)C_l/2\pi$ as function of multiple moments of the spherical hormonics is shown in Figure 1.2. The plot as shown in Figure 1.2 is one where theory and experimental data meet. The theory determines a set of cosmological parameters that defines the shape of the CMB anisotropy power spectrum. The experiments measure the shape of the power spectrum. Ripples in the temperature anisotropy power spectrum plot at $l > 200$ is where the acoustic peaks exist. Before recombination, photons and baryons were tightly coupled through electron-photon scattering. Photons and

baryons were acting as a single fluid. The photon-baryon fluid underwent a series of compression and expansion under the influence of gravitational potential wells that were setup by dark matter. Since the anisotropy plot shows variance, the peaks represent the size of potential wells that the photon-baryon fluid is either fully compressed or fully expanded. The troughs represent the size of potential wells that the photon-baryon fluids rebounded to the neutral position. These peaks and troughs are dampened at the smaller angular scale. A finite coupling strength between the photons and baryons allowed the photons to perform a random walk through the fluid to homogenize the temperature anisotropy at the smaller scale. On the larger angular scale, we do not see acoustic oscillations since these modes were too large to enter the horizon prior to recombination. The Sach-Wolfe plateaus on a large angular scale, see effect of evolving potential well through integrated Sach-Wolfe effect.

Inflation

The monopole component of the CMB temperature suggests that points that appears to be not causally connected share the same temperature. Temperature anisotropy measurements suggest that the universe is geometrically flat and the perturbation is gaussian. Inflation theory unites these two findings by proposing that the Universe underwent an accelerated expansion period when the Universe was a fraction of a second old. Superluminal expansion grows the causally connected part of the sky beyond the observable universe. Inflation reduces the geometrical curvature small enough to prevent the Universe from collapsing. Inflation also provides a natural mechanism for the initial gaussian perturbations for potential wells to form.

We can derive the *acceleration equation* from time-time and space-space components of the zeroth-order Einstein equation,

$$\frac{\ddot{a}}{a} = -\frac{4}{3}\pi G(\rho + 3p) \tag{1.3}$$

where a is a scale factor of the Universe. ρ and p represent the energy density and pressure of the fields, respectively. The dot represents the derivative against conformal time. Accelerating the universe satifies $p < -\rho/3$. A field that is dominating the Universe during inflation must have negative pressure. The simple inflation model proposes a single scalar field ϕ. We can derive the energy density and pressure of this field from the energy-memtum tensor:

$$\begin{aligned} \rho &= \frac{1}{2}\left(\frac{d\phi}{dt}\right)^2 + V(\phi) \\ p &= \frac{1}{2}\left(\frac{d\phi}{dt}\right)^2 - V(\phi) \end{aligned} \tag{1.4}$$

where $V(\phi)$ is the potential for the field. A field configuration with negative pressure is one with more potential energy than kinetic energy. Potential energy is described by two parameters $\varepsilon(\phi)$

and $\eta(\phi)$ which describes the slope and curvature of the potential energy, respectively.

$$\begin{aligned} \varepsilon(\phi) &= \frac{m_{PL}^2}{16\pi}\left(\frac{V'}{V}\right) \\ \eta(\phi) &= \frac{m_{PL}^2}{8\pi}\left(\frac{V''}{V}\right) \end{aligned} \tag{1.5}$$

where m_{PL} is Planck mass, and prime is the derivative with respect to ϕ. The amount of expansion, N e-foldings, and potential parameter ε are related by

$$N \approx \frac{2\sqrt{\pi}}{m_{PL}} \int_{\phi_i}^{\phi_f} \frac{1}{\sqrt{\varepsilon(\phi)}} d\phi \tag{1.6}$$

The $N = 64$ expansion is required to meet CMB's observed conditions - homogeneous temperature and flatness. This requires a small ε, a potential with small slope.

Gravitational Wave

Inflation-generated perturbations in the scalar part of the metric acts as seeds for potential wells. Inflation also generated *gravity waves*, tensor fluctuations in the metric. The decomposition theorem states that the scalar, vector and tensor parts of the metric perturbations did not couple. Scalar perturbations of the metric coupled with energy density fluctuations. The combined evolution was complicated with many degenerate parameters. Since tensor perturbations did not couple to the scalar mode, induced fluctuations in the CMB from tensor mode gives clean detection of signature of inflation. During inflation, the Universe was filled with an inflationary scalar field and the metric. This field fluctuates quantum mechanically, and non-zero variance in this fluctuation evolves as inflation progresses. Tensor perturbations in the metric can be written with $h_\times$ and h_+ defined as:

$$g_{ij} = a^2 \begin{pmatrix} -1 & 0 & 0 & 0 \\ 0 & 1+h_+ & h_\times & 0 \\ 0 & h_\times & 1-h_+ & 0 \\ 0 & 0 & 0 & 1 \end{pmatrix} \tag{1.7}$$

Tensor perturbations evolves as

$$\ddot{h} + 2\frac{\dot{a}}{a}\dot{h} + k^2 h = 0 \tag{1.8}$$

where k is a wavevector for perturbation. Defining $\tilde{h}$ transforms this equation. The equation becomes identical to that of a simple harmonics oscillator (SHO)

$$\ddot{\tilde{h}} + \left(k^2 - \frac{\ddot{a}}{a}\right)\tilde{h} = 0 \tag{1.9}$$

Since the average quantum fluctuation is 0, we are interested in the variance of the fluctuation.The variance of a quantized SHO can be calculated as

$$\langle \hat{\tilde{h}}(\vec{k})^\dagger \hat{\tilde{h}}(\vec{k}) \rangle = (2\pi)^3 P_h \delta^3(\vec{k} - \vec{k}') \tag{1.10}$$

where $\hat{\hat{h}}(\vec{k})$ is the quantum operator for the oscillator and P_h is the power spectrum of the primordial perturbation to the metric. P_h can be solved by solving for $\ddot{a}/a$ during inflation. The power spectrum is calculated to be

$$P_h = \frac{8\pi}{k^3}\frac{H^2}{M_{PL}^2} \propto k^{n_T-3} \tag{1.11}$$

Where H is a Hubble rate at the time when the mode of interest leaves the horizon due to inflation expansion. The Hubble rate is close to constant during inflation because of the small slope of scalar potential. Since potential energy is bulk energy during the inflationary era, measuring H would be equivalent to determining the potential during inflation. Tensor spectral index is zero for scale invariant (Harrison-Zeldovich) power spectrum, but slow-roll inflationary model predicts some slope in potential define by ε, $n_T = -2\varepsilon$.

Scalar perturbations of the metric evolved during the inflationary period. However, as scalar perturbations evolved, it coupled to energy density fluctuations. This coupled field complicates mathematics, but a similar result can be attained through the power spectrum. The power spectrum for scalar perturbations is

$$P_\Phi = \frac{8\pi}{9k^3}\frac{H^2}{m_{PL}^2} \propto \frac{1}{k}^3 \left(\frac{k}{H_0}\right)^{n_S-1} \tag{1.12}$$

where n_S is scalar spectrum index. Again, the change in H due to the slope of V during inflation defines n_S as $n_S = 1-4\varepsilon-2\eta$.

Our goal is to relate the power spectrum to anisotropies we see in the CMB. One important parameter is the ratio between CMB fluctuations from scalar perturbations C_l^S and the tensor perturbations C_l^T

$$r = \frac{C_l^T}{C_l^S} \approx 16\varepsilon \tag{1.13}$$

Therefore, by measuring C_l^T, and hopefully n_T, we can perform a consistency check of the predicted inflation model. We can also relate r to the energy scale during inflation by:

$$r = 0.008\left(\frac{\mathrm{E_{inf}}}{10^{16}\mathrm{GeV}}\right)^4 \tag{1.14}$$

The single scalar model predicts r greater than approximately 0.001. Therefore, if we detect r we would be proving physics at 10^{15}GeV scale, much higher energy level than can be achieved via particle accelerators.

Polarization

The decomposition theorem between scalar and tensor perturbation allows clean measurements. It also gives us an opportunity to perform a consistency check between two independent sources of perturbations. Since tensor perturbations did not couple with energy density, detecting the signal from tensor perturbations provides a cleaner look into inflation. Tensor perturbations produced

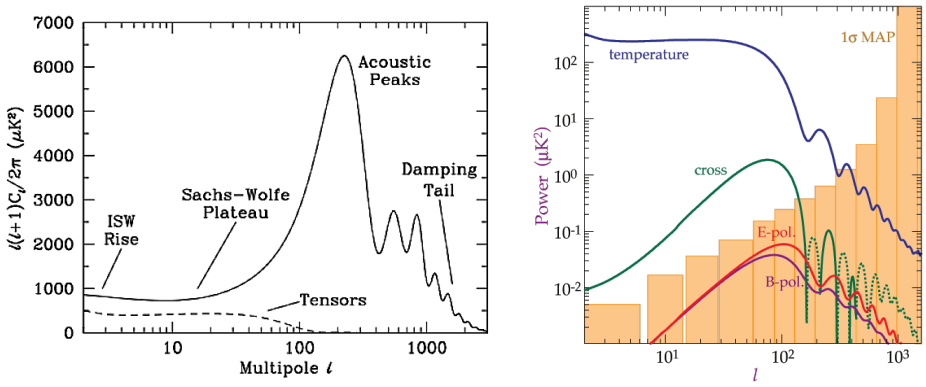

Figure 1.3: (Left) The solid line is the temperature anisotropy power spectrum from scalar perturbations. The dash line represents the temperature anisotropy power spectrum from tensor perturbations. (Right) Predicted temperature and polarization power spectrum from tensor perturbation [50].

a temperature anisotropy and polarization in the CMB as shown in Figure 1.3. However, scalar perturbations also produced a temperature anisotropy and polarization in the CMB. As shown in Figure 1.3, temperature anisotropy from tensor perturbations peaks at low l. Cosmic variance is defined as

$$\frac{\Delta C}{C} = \sqrt{\frac{2}{2l+1}} \tag{1.15}$$

Cosmic variance increases at low l. It becomes impossible to decouple temperature anisotropy from scalar and tensor modes. Measuring polarization provides an opportunity to detect the tensor mode. The polarization field can be decomposed into two orthogonal modes. Then we can perform similar decompositions between scalar and tensor perturbations. Scalar perturbations produce even-parity polarization patterns (E-mode polarization) but not an odd-parity polarization pattern (B-mode polarization). Tensor perturbations produce both E-mode and B-mode polarization patterns. Thus, we can detect CMB B-mode polarization to measure tensor perturbations.

CMB polarization is produced through Thomson scattering. Suppose an electron experiences radiation from four directions. Photons scattered by electrons has an electric field that is perpendicular to both the incident and exiting photons. Thus, if the temperature of the incident photons from two orthogonal directions are different, the scattered light would have polarization as shown in Figure 1.4. For a scalar perturbation, the induced quadrupole is symmetric around the perturbations wavevector as shown in Figure 1.4. The symmetry makes polarization either aligned with or perpendicular to projected wavevector onto the sky. This polarization pattern is parity-conserving, thus scalar modes produce E-mode polarizations. Tensor perturbations create temperature anisotropy that varies around wavevector as shown in Figure 1.4. A lack of symmetry allows the tensor mode to excite the polarizations in all direction around the wavevector. Thus, the tensor modes produce both E-mode and B-mode polarizations, as shown in Figure 1.3.

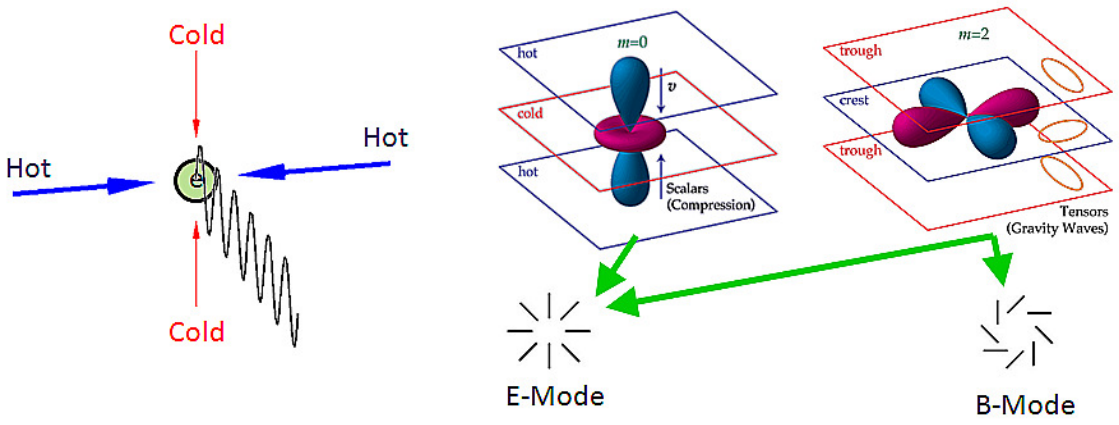

Figure 1.4: (Left) Schematic drawing of Thomson scattering of light by an electron. The incoming light has quadrupole anisotropy such that the scattered light is polarized. (Right) Temperature anisotropy with respect to wavevector in $\hat{z}$ direction. Scalar perturbations (left) produces E-mode polarization, and tensor perturbation (right) produces E-mode and B-mode perturbation. Visual representation of curl-free E-mode and divergence-free B-mode pattern is shown [50].

B-mode Polarization

The B-mode polarization has two sources. The first source is from E-mode polarization sheared into B-mode polarization by the gradient in the gravitational field. This gravitational field gradient is from large scale structures between us and the surface of the last scattering [51]. Weak lensing effect is sensitive to the matter density of all intervening objects. We can measure things like the sum of all neutrino masses and understand the evolution dark energy's equation of state. The B-mode signal from weak gravitational lensing is expected to peak around ten arcminutes. The second source of B-mode polarization is from the primordial gravitational waves [111]. Inflation models predict the existence of a B-mode signal at approximately two-degree angular scales. The two contributions to the B-mode are shown in Figure 1.5. We can use the angular scale difference between the B-mode from two different sources to decouple the two sources. The predicted level of primordial B-mode is four orders of magnitude below the temperature anisotropy. Thus, we need an experiment with a large number of detectors to achieve high sensitivity, while maintaining small systematic errors.

1.3 Foregrounds

There are non-primordial polarized millimeter source in the sky that can confuse the B-mode detection. Polarized galactic sources from synchrotron radiation and thermal dust emissions are two major foregrounds. As shown in Figure 1.6, synchrotron radiation and thermal dust emission have different spectral dependances from the CMB. We can subtract *foreground* contribution and detect

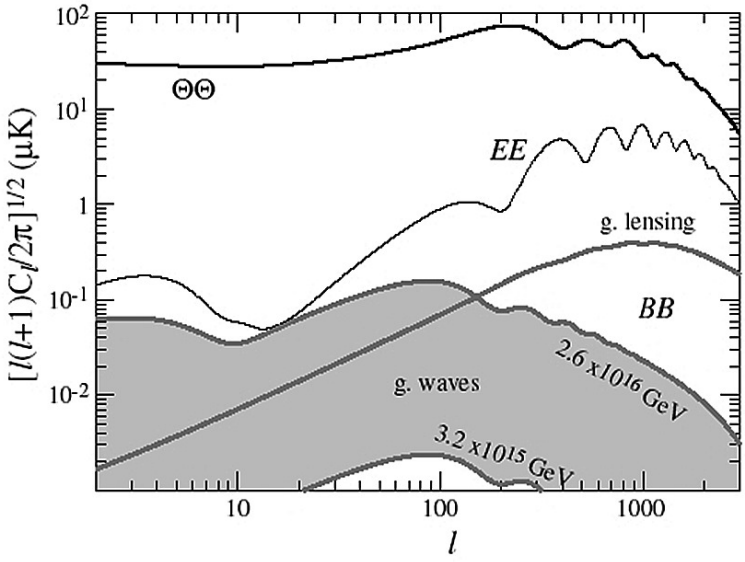

Figure 1.5: TT, EE, BB power spectrum is shown. Two contributions to B-mode are shown. B-mode from weak gravitational lensing of E-mode peaks at $l \approx 1000$. B-mode from primordial graviational wave peaks at $l \approx 100$. The gray band of primordial gravitational wave contribution to B-mode represents the theoretically predicted amplitudes [50].

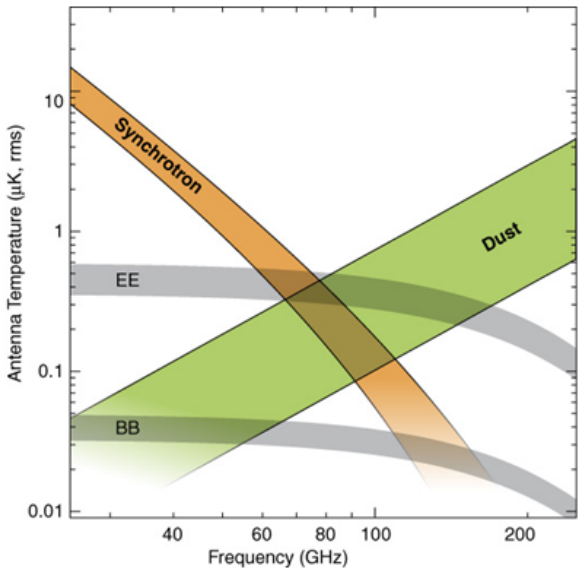

Figure 1.6: Antenna temperature of the predicted synchrotron radiation and thermal dust emissions along with EE and BB. Assuming $r = 0.01$ and $2 < l < 20$ [19].

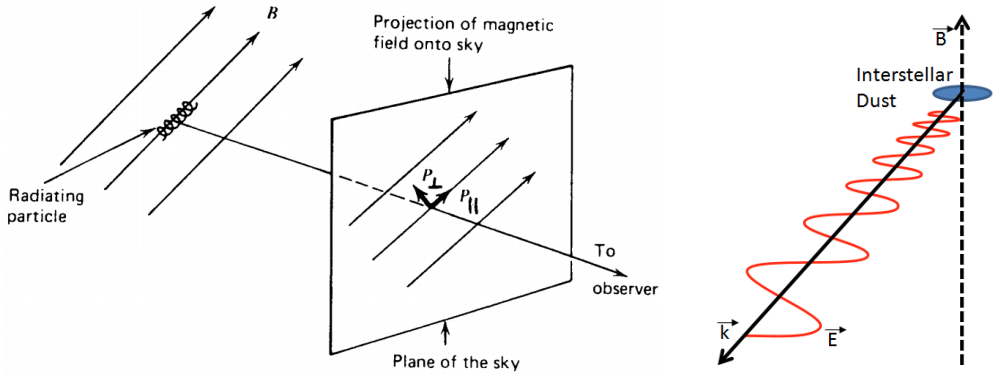

Figure 1.7: Schematic drawing for synchrotron radiation (left) and thermal dust emission (right). For synchrotron radiation, the emitted light is highly polarized. Light is mostly polarized perpendicular to the magnetic field. For spinning thermal dust, the dust grains are perpendicular to the magnetic field and its spin axis is parallel to the magnetic field. The emitted radiation is polarized perpendicular to the magnetic field. [107]

the primordial B-mode by observing at multiple frequency bands.

Synchrotron radiation is emitted by accelerating charged particles through galactic magnetic fields. The synchrotron radiation spectral index is $\beta \approx -3$ from WMAP data. Its degree of polarization is defined as

$$\frac{P_\perp - P_\parallel}{P_\perp + P_\parallel} = \frac{p+1}{p+7/3} \tag{1.16}$$

Where p is defined as $\beta = -(p+3)/2$; thus, the synchrotron radiation polarization fraction could be as high as 0.75 and perpendicular to the magnetic field.

The polarized thermal dust emission arises from the alignment of the spin axis of the interstellar dust grains along the magnetic field. Thus, it radiates light with polarization also perpendicular to the magnetic field. It has a rising spectrum as a function of frequency $I(\nu) \propto \nu^\beta B(T)$ where B is brightness for a given temperature T. We typically model dust emissions with two components: $T = 9.5$ Kelvin and 16 Kelvin with $\beta = 1.7$ and 2.7, respectively. We will get more information on dust emissions from Planck HFI in the future.

1.4 Current State of Field

The current upper limit on the tensor-to-scalar ratio is $r < 0.11$ [115, 2]. This upper limit is set by measurements from temperature anisotropy. The current limits on selected parameters are summaried in Table 1.1. Currently, each experiment that is taking CMB polarization data contains approximately one thousand detectors. A list of recently deployed experiments that aim to detect CMB B-mode are in Table 1.2. Recently, lensing B-mode were detected through cross-correlation

Parameter	Current Limit	
r	$r < 0.11$	SPT+WMAP7+H0+BAO
	$r < 0.11$	Planck + WMAPpol + HighL
n_S	$n_S = 0.954 \pm 0.008$	SPT+WMAP7+H0+BAO
	$n_S = 0.958 \pm 0.007$	Planck + WMAPpol + HighL
$\sum m_\nu$	$\sum m_\nu < 0.23$eV	Planck + WMAPpol + HighL + BAO
w_{DE}	$w = -1.09 \pm 0.17$	Planck + WMAPpol + SNIa

Table 1.1: Current limit on selected parameters [115, 2, 1].

Experiment	Year	Location
Planck	2009 - 2012	Satellite, L2
EBEX	2012	Balloon, South Pole
BICEP2 / Keck Array	2010 -	Ground, South Pole
SPTpol	2012 -	Ground, South Pole
POLARBEAR-1	2012 -	Ground, Atacama
ABS	2012 -	Ground, Atacama
ACTpol	2013 -	Ground, Atacama

Table 1.2: Lists of recent CMB polarization experiments [90]

with lensing potential and B-mode data [46]. Detection of B-mode from auto-correlation would be interesting, and its data analysis is underway. The next generation CMB experiments will observe at multiple frequencies with approximately ten thousand bolometers. This will push r detection limit down to approximately 0.01. Many single-scalar field inflation models predict $r = 0.01$. Satellite projects, aiming to make a definitive measurement of B-mode polarization, are also being proposed. This is an active field with important physics waiting to be discovered.

1.5 Conclusion

Characterization of the Cosmic Microwave Background (CMB) B-mode polarization signal will test models of inflationary cosmology, as well as constrain the sum of the neutrino masses and other cosmological parameters. The low intensity of the B-mode signal combined with the need to remove polarized galactic foregrounds requires a sensitive millimeter receiver and effective methods of foreground removal. CMB polarimetry experiments are aiming to improve tensor-to-scalar ratio measurement by an order of magnitude. Current bolometric detector technology is reaching the sensitivity limit set by the CMB photon noise. Thus, we need to increase the optical throughput to increase an experiment's sensitivity. To increase the throughput without increasing the focal plane size, we can increase the frequency coverage of each pixel. Increased frequency coverage

per pixel has additional advantage that we can split the signal into frequency bands to obtain spectral information. The detection of multiple frequency bands allows for removal of the polarized foreground emission from synchrotron radiation and thermal dust emission, by utilizing its spectral dependence. Traditionally, spectral information has been captured with a multi-chroic *focal plane* consisting of a heterogeneous mix of single-color pixels. To maximize the efficiency of the focal plane area, we developed a multi-chroic *pixel*. Many next generation CMB experiments will use the multichroic pixel archtechture to map the CMB with high sensitivity.

Chapter 2

POLARBEAR-2

2.1 Project Overview

The POLARBEAR-2 is a next-generation CMB polarimetry experiment with 13 collaborating international institutions [125, 122]. Its main goal is to make a sensitive B-mode polarization map of the CMB. The POLARBEAR-2 experiment will observe from the James Ax Observatory at an altitude of 5,200 meters on the Cerro Toco site in the Atacama Desert. The Desert has a median precipitable water vapor (PWV) of 1.5mm [121] and is one of the best places to do the millimeter wave observation from the ground. Experiments in the Atacama Desert enjoy a dry atmosphere, wide-sky coverage and year-around access. There are currently many millimeter and sub-millimeter observations occurring in the Atacama Desert. Some of our neighbors are the Atacama Cosmology Telescope, ALMA and APEX. The POLARBEAR-1 experiment has been mapping the CMB

Figure 2.1: Histogram of precipitable water vapor at APEX weather station for 2012 (left) [121]. Median for 2012 was 1.5 mm. Location of POLARBEAR project site (right) [8].

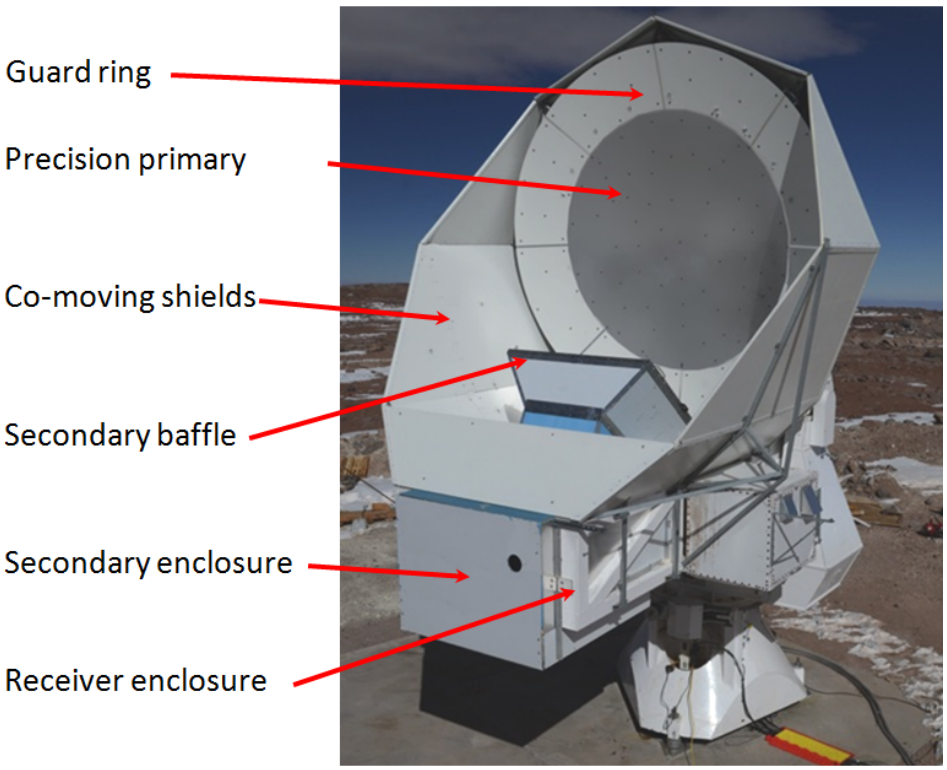

Figure 2.2: Overview of the Huan Tran Telescope. 3.5 m primary mirror with panel extension that would reflect the side lobes to the sky. Co-moving shields and secondary baffle further suppresses the side-lobes. The secondary and receiver enclosures provide weather protection. The cryogenic receiver fits inside the receiver enclosure.

polarization since January 2012 [61, 123]. The POLARBEAR-2 will depoly at the same site in 2014.

The POLARBEAR-2 receiver will be mounted on a telescope with the same design as the Huan Tran Telescope (HTT); HTT is currently observing with the POLARBEAR-1. Picture of the HTT is shown in Figure 2.2. The HTT features an offset Gregorian design meeting the Mizuguchi-Dragone condition and co-moving baffles that minimize instrumental polarization and sidelobes. The 3.5 meter primary mirror produces a 3.5-arcmin (5.2-arcmin) full width half max (FWHM) beam at 150 GHz (95 GHz). We plan to cover 20% of the sky over three years with an instantaneous array sensitivity of 5.7 μK$\sqrt{s}$. Assuming 10% observation efficiency, we will achieve 10 μK-arcmin sensitivity. As shown in Figure 2.3, the POLARBEAR-2 will be able to put a constraint on the signal from the inflationary primordial gravitational waves corresponding to a tensor-to-scalar ratio of $r = 0.01$ (2σ C.L.). Using the weak gravitational lensing signal, the experiment will also be able to put a constraint on the sum of neutrino masses to 90 meV (1σ C.L.) and 65 meV (1σ C.L.) when its data is combined with Planck data.

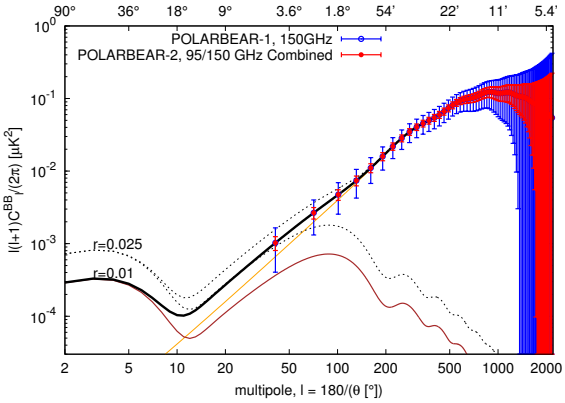

Figure 2.3: Projected sensitivity of the POLARBEAR-1 (blue) and the POLARBEAR-2 (red) with 95 GHz and 150 GHz bands combined. Orange line is expected B-mode contribution from weak lensing. Dotted line is expected B-mode level with $r = 0.025$. Solid line is expected B-mode level with $r = 0.01$. Courtesy of Yuji Chinone.

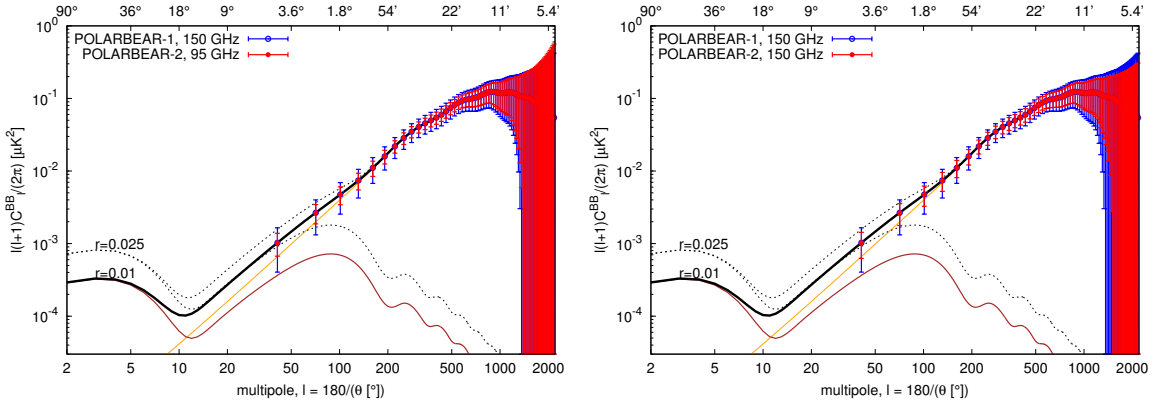

Figure 2.4: Projected sensitivity of the POLARBEAR-1 (blue) and the POLARBEAR-2 (red) with 95 GHz only (left) and 150 GHz only (right). Orange line is expected B-mode contribution from weak lensing. Dotted line is expected B-mode level with $r = 0.025$. Solid line is expected B-mode level with $r = 0.01$. Courtesy of Yuji Chinone.

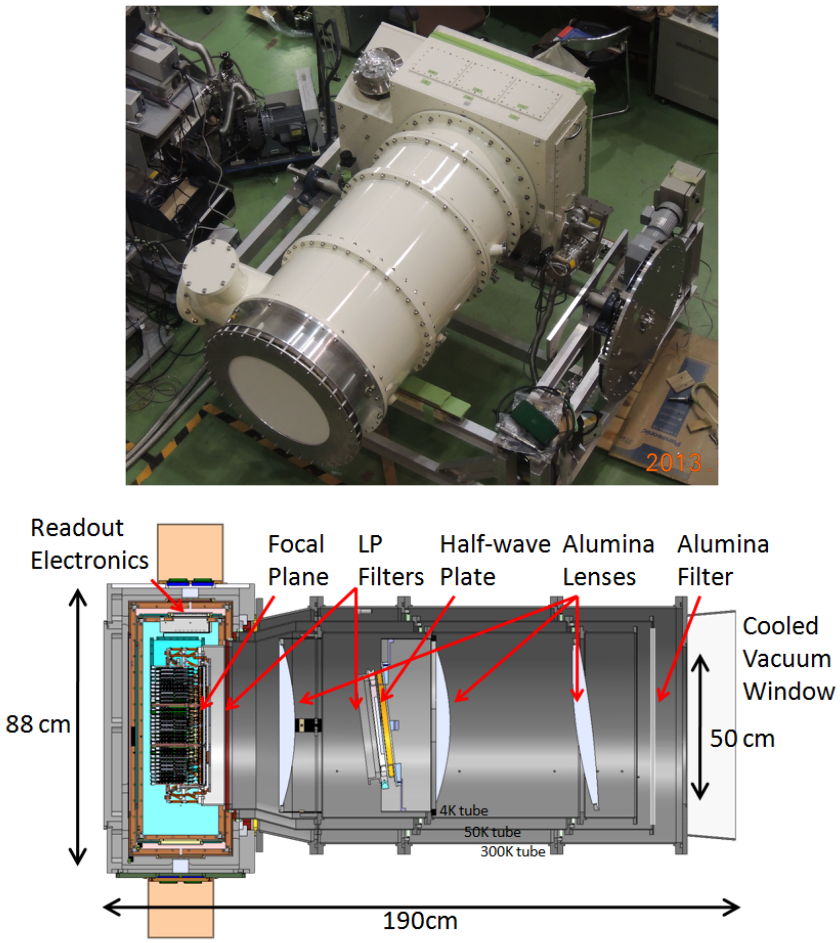

Figure 2.5: Photograph of the POLARBEAR-2 receiver (top), and cross section of the POLARBEAR-2 receiver (bottom)

2.2 Instrument

A cross-sectional view of the POLARBEAR-2 receiver is shown in Figure 2.5. The receiver is 1.9 meters long, 1.2 meters wide and 0.88 meters high. Its design resembles a single-lens reflex (SLR) camera. The rectangular portion of the receiver houses a focal plane tower and cryogenic readout components. The optics tube houses cryogenically cooled lenses. The optics tube is attached to the front of the receiver. Two Cryomech PT415 pulse-tube coolers cool the receiver [53]. Each cooler provides 50 Kelvin and 4 Kelvin stages. Both coolers are tilted by 21 degrees with respect to the optics tube to perform optimally when the telescope is scanning at an elevation of 45 degrees. One pulse-tube cooler is placed near the window of the optics tube to efficiently reduce thermal emissions. Another pulse-tube cooler is placed near the focal plane to cool the focal plane and the

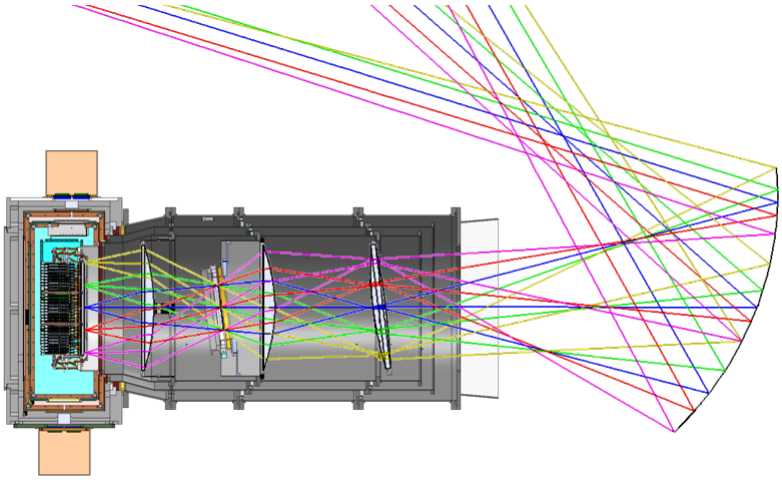

Figure 2.6: The POLARBEAR-2 receiver with ray tracing. Secondary mirror is shown on right.

readout electronics. Annealed 6-N aluminum strips were epoxied to the receiver shells to increase the thermal conductivity of the receiver. A three-stage helium sorption refrigerator cools the focal plane tower with 2 Kelvin, 350 milli-Kelvin and 250 milli-Kelvin stages [75].

The ray tracing for the POLARBEAR-2 is shown in Figure 2.6. The optics has a field-of-view of 4.8° [85]. High purity (99.5%) alumina was used as an infrared filter to reduce the thermal loading from the 500 mm diameter window in the optics tube. Alumina absorbs infrared photons effectively, yet it is transparent at the millimeter wave. Alumina has three orders of magnitude better thermal conductivity at 100 Kelvin than plastics, which are commonly used as dielectric filters [55].

Three lenses were fabricated from high purity (99.9%) alumina. The high dielectric constant of alumina ($\varepsilon_r \approx 10$) allows an optics design with a large field of view with high strehl ratio. High purity alumina also has low loss ($\tan\delta \approx 1 \times 10^{-4}$). Alumina has high thermal conductivity that helps with the overall cryogenic performance. However, the high dielectric constant of alumina requires anti-reflection (AR) coating to minimize the reflection at the dielectric boundary. Since the POLARBEAR-2 observes at 95 GHz and 150 GHz simultaneously, the AR coating on the lens must cover a wide frequency range. We developed a two-layer epoxy-based AR coating [117, 28]. Details on lenses material and AR coating development will be discussed in Chapter 3.

We place 4 Kelvin cold stop and an achromatic half-wave plate at the aperture. The cold stop is designed for $\mathrm{F}/\# = 1.9$ optics. The achromatic half-wave plate is made from stacks of sapphire crystals. The half-wave plate rotates on a superconducting bearing to modulate polarized signal to reduce systematic error from the optics [83, 84].

The focal plane is shown on Figure 2.7. The focal plane design was based on the POLARBEAR-1 design. A 365 mm diameter focal plane tower has 2 Kelvin, 350 milli-Kelvin and 250 milli-Kelvin stages. Each stage was isolated by hollowed vespel legs. The focal plane tower houses seven detector array modules. Each module has a hexagonal detector array wafer and readout elec-

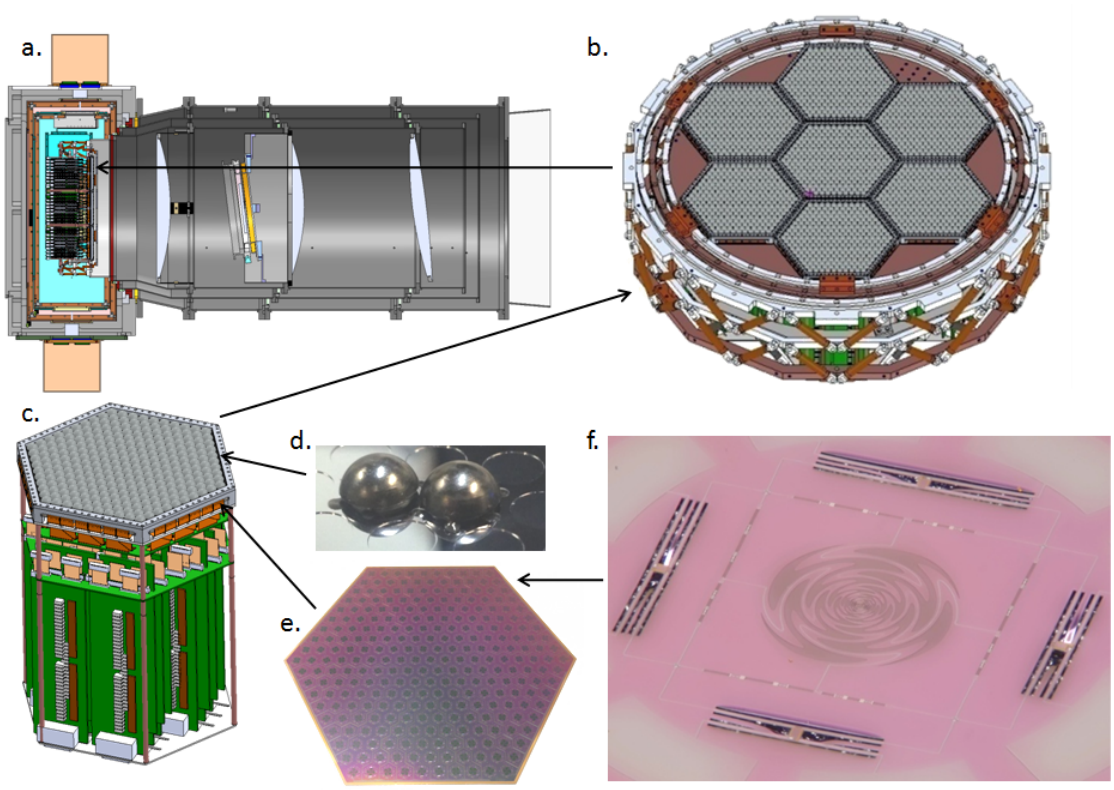

Figure 2.7: Components of the POLARBEAR-2 focalplane. a. Shows the location of the focal plane in the receiver. b. CAD drawing of the focal plane tower with seven detector modules. c. CAD drawing of the detector module. d. Photograph of the two-layer AR coated lenslet. e. Photograph of device wafer. f. Microscope photograph of detector.

tronics. The detector array was fabricated on a 150 mm wafer at the Berkeley nano-fabrication laboratory [68]. Each wafer has 271 dual linear polarized pixels that simultaneously detect both the 95 GHz and 150 GHz bands. Each pixel has a lens-coupled broadband antenna that couples the optical signal onto RF circuits on a wafer. The bandpass filters on the wafer split the signals into two separate bands, then the transition edge sensor (TES) bolometers detect the signal [94, 117, 116]. 7,588 bolometers fill the focal plane.

Readout electronics sits behind the detector array inside the detector module to use the focal plane area efficiently as shown in Figure 2.7. We use frequency multiplexed Superconducting Quantum Interference Device (SQUID) amplifiers to read-out the TES bolometers. A schematic drawing of a read-out chain is shown in Figure 2.8. A high multiplexing factor allows the read-out of many detectors without thermally loading the focal plane. Each SQUID uses a few MHz of bandwidth to read-out 36 TES bolometers. High frequency read-out increases phase delays in the feedback loop and the parasitic impedance of the read-out circuit. We use a digital active nulling technology that actively corrects for the phase delay and reduces parasitic inductance from circuit

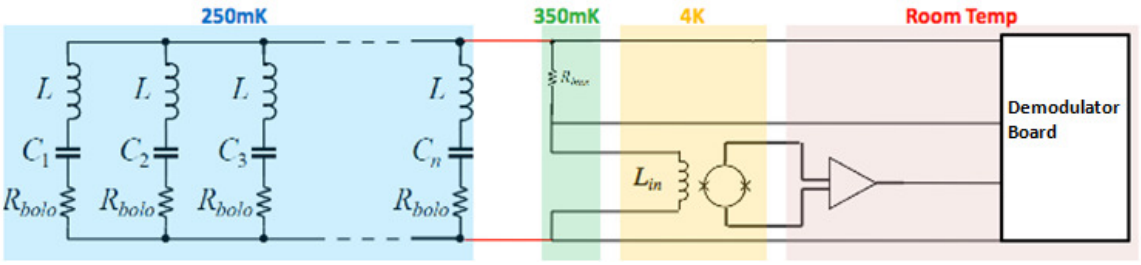

Figure 2.8: Schematic of the read-out chain. Lithographed inductors and capacitors are in series with bolometers to select frequency channels. Niobium-titanium transmission lines thermally isolate the 250 milli-Kelvin stage (red line). Bias resistors are placed at 350 milli-Kelvin to minimize the physical distance between the bias resistors and the focal plane.

elements between the bias resistor and the SQUID [42, 47]. We fabricated interdigitated capacitors with niobium traces on high-resistivity (> 10 KΩ/cm) silicon wafers to reduce parasitic resistance from capacitors. The interdigitated capacitors have less than 100 mΩ parasitic resistance at 3 MHz. The capacitors achieve sub-percent capacitance accuracy that allows consistent frequency spacing. More details on the fabrication of the read-out components will be discussed in Section 5.13. We also fabricated niobium-titanium parallel plate transmission line for 250 milli-Kelvin to 350 milli-Kelvin connection. Niobium-titanium provides thermal isolation, while the high width-to-height ratio of the parallel plate transmission line provides low inductance per length ($\approx$ 1nH/cm).

2.3 Conclusions

The POLARBEAR-2 experiment is designed to measure the CMB's B-mode polarization with sensitivity of 10 μK – arcmin. The stringent control of systematic errors, large optical throughput, and high detector count bring new challenges to the experiment. We have addressed these challenges with the innovative use of materials, a multichroic detector design, and a new digital electronics design. Currently we are testing many of the components described here. The POLARBEAR-2 is scheduled to deploy in 2014 to Atacama, Chile for 3 years of observations.

Chapter 3

Lens Material and Anti-Reflection Coating

3.1 Introduction

The POLARBEAR-2 has an aggressive receiver optics design that achieves four degrees field-of-view. The POLARBEAR-2 uses a telescope with the same design as the HTT, thus, the optics design effort was focused on the lenses in the cryogenic receiver. We first tried to design lenses with ultra-high molecular weight polyethylene (UHMWPE) since that was used for the POLARBEAR-1 receiver [61]. However, we discovered that achieving the required strehl ratio (> 0.8) over the 36.5 mm diameter focal plane required the optics tube to be too long to fit into the HTT. We then considered using single-crystal high-resistivity silicon as lens material as it has successfully been used for the Atacama Cosmology Telescope [37]. High-resistivity silicon has many desirable properties when used as millimeter wave lens. High-resistivity silicon has a typical loss tangent of 10^{-5} to low 10^{-4}, and high thermal conductivity to facilitate cooing [78]. Also, its high index of refraction allows lens to have high lensing power with a large curvature radius. The largest diameter high-resistivity silicon ingot we were able to find was a 450 mm diameter ingot from Silfex [112]. We then began designing around the silicon ingot. We found that the length limit of the optics tube from the existing telescope design forced lenses to be larger than 450 mm in diameter. Attempting to design optics around silicon showed us that the high index of refraction was really beneficial. We looked for materials with similar properties to silicon but that can be larger than 450 mm in diameter. 99.9% pure alumina from Nihon Ceratec met the criteria [76]. It has a refraction index of 3.20 ± 0.01 at room temperature and loss-tangent of $(9 \pm 2) \times 10^{-5}$ at 140 Kelvin. It is available up to 1000 mm in diameter, with a maximum thickness of 50 mm. Alumina has high thermal conductivity [55] and is also mechanically very strong - unlike silicon, which is brittle. Receiver optics were successfully designed with three alumina lenses, each having a diameter of 500 mm and maximum thickness of 50 mm. The receiver cross-section with a ray tracing overlay is shown in Figure 2.6. The POLARBEAR-2 uses lenslet-coupled multichroic detector. For the lenslet, we decided to use single crystal high-resistivity silicon since the detector wafer was already made out of silicon.

Alumina and silicon are ideal lens materials for cryogenic millimeter-wave optics. However,

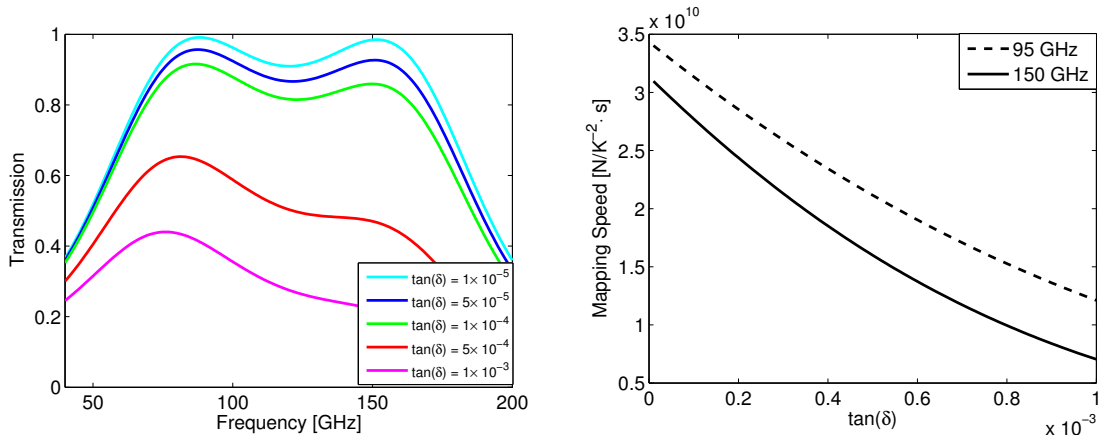

Figure 3.1: (left) Transmission through three 50 mm thick alumina with refraction index of $n = 3.2$. Fabry-Perot fringes were removed. We assumed that each slab has a two-layer anti-reflection coating with a dielectric constant of 2 and 5 on each surface. Each layer of anti-reflection coating has thickness of $\lambda/4$ at 120 GHz. Loss in anti-reflection coatings were ignored. (right) Mapping speed as function of loss-tangent of alumina lens. Nominal loading from Table 4.1 and Table 4.2 were assumed for 95 GHz and 150 GHz except for efficiency through alumina. Pixel diameter is nominal 6.789 mm.

one downside of the high dielectric constant is the reflection at the vacuum-dielectric interface, which can be as high as 30%. There are many effective AR coatings using a thin dielectric coating, metal-mesh layers or sub-wavelength structures [71, 102, 133, 87]. However, these coatings will not work for the next generation CMB experiments with multichroic detectors. Most reported millimeter-wave, dielectric-based AR coatings are single layer and, thus, limited to narrow bandwidths. A single-layer coating for our application would have a 41% fractional bandwidth with less than 10% reflection. We have developed a multilayer epoxy-based dielectric AR coating with more than 90% fractional bandwidth. While multilayer dielectric coatings have been developed in the past [102, 105, 108], our innovative, moldable adhesive coatings are applicable for high dielectric constant curved lenses. We have demonstrated these coatings on small lenslets and 50 mm diameter flat surfaces and believe that this approach may be extended for 500 mm lenses. Additionally, we can tune the dielectric constant of our layers, which allows for the broad application of our coatings. AR coating development was previously published by Suzuki and Rosen [117, 28]. We provide more details about developing the AR coating in this chapter.

$\tan(\delta)$	**95 GHz band**	**150 GHz band**
1×10^{-5}	97.3%	95.5%
5×10^{-5}	93.8%	90.4%
1×10^{-4}	89.5%	84.1%
5×10^{-4}	61.9%	47.2%
1×10^{-3}	39.1%	22.9%

Table 3.1: Transmission through three 50 mm alumina lenses for 95 GHz band and 150 GHz band. We assume each slab has two-layer anti-reflection coating with dielectric constant of 2 and 5 on both surface. Each layer of anti-reflection coating has thickness of $\lambda/4$ at 120 GHz. Loss in anti-reflection coatings were ignored.

3.2 Material Development

Material Development

To study absorption loss, we looked at the loss-tangent ($\tan(\delta)$) of the material. The loss-tangent is defined as the tangent of an angle between the real and imaginary dielectric constant of the material $\tan(\delta) = \mathrm{Im}(\varepsilon)/\mathrm{Re}(\varepsilon)$. We can calculate the propagation constant (γ) of plane wave traveling through a medium with dielectric constant of ε.

$$E_0 e^{-i\gamma z} \tag{3.1}$$

Where E_0 is an amplitude of an electric field at $z = 0$. z is a distance that wave traveled in medium. Attenuation factor is $\mathrm{Im}(\gamma)$. We can write γ with explicitly using $\tan(\delta)$ as

$$\gamma = \omega\sqrt{\mu\mathrm{Re}(\varepsilon)(1 - i\tan(\delta))} \tag{3.2}$$

We plotted the expected loss as function of $\tan(\delta)$ of alumina in Figure 3.1. Plot assumes plane wave traveling through three 50 mm alumina lens with dielectric constant of 10.2. We also assumed two-layer anti-reflection coating on both sides of all lenses. Calculated in-band transmission were tabulated on Table 3.1. Figure 5.32 shows expected mapping speed as a function of $\tan(\delta)$. Since loss in mapping speed was steep function of $\tan(\delta)$, we set a criteria that lens material needs to have $\tan(\delta) < 1\times10^{-4}$.

We varied the refraction index of the lens of each design to determine how accurate we need to know the refraction index. We then looked at how the strehl ratio degraded as a function of how the refraction index deviated from its designed value. From this test, we determined that the refraction index needs to be measured to within 1% accuracy.

Measurement

We obtained three types of aluminas from Nihon Ceratec. We studied 99.5% LD purity alumina, 99.9% purity alumina and APJF alumina, which has a different sintering process and produces

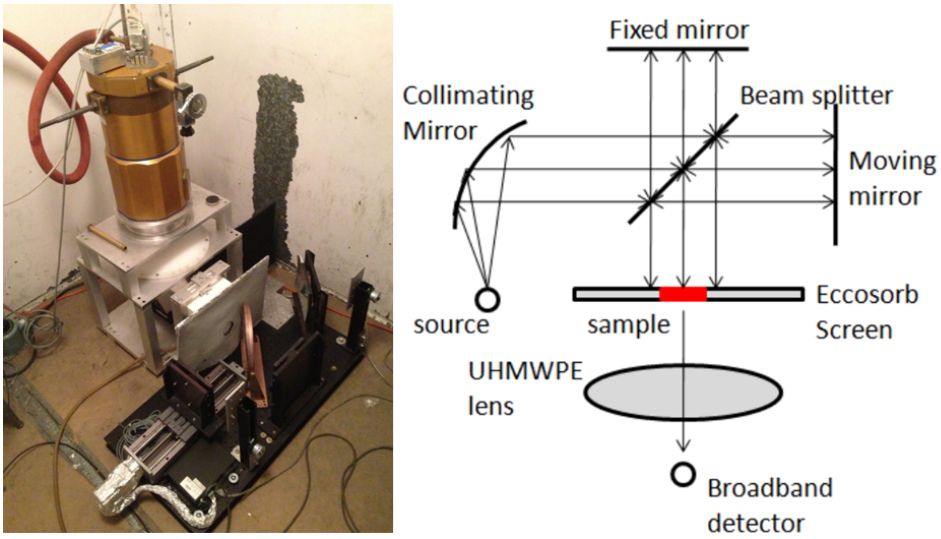

Figure 3.2: A schematic of the Michelson FTS measurement. We placed the sample at the collimated output of the FTS. An absorber (eccosorb ANW-72) was placed around the aperture. The signal was collimated by an UHMWPE lens to a broadband (70-250 GHz) bolometric detector.

low loss alumnina at lower cost. We got two samples of each type of alumina: the first sample is 4 mm thick and the second sample is 40 mm thick. Both samples were 50 mm diameter cylinders. Since alumina is sintered ceramic, its absorptive loss depends on many factors such as the kinds of contamination, the sintering temperature and the sintering method [7, 92]. Thus, the samples from Nihon Ceratec must be measured to get the accurate expected absorptive loss.

To measure the refraction index and absorptive loss in the sample, we used the Fourier Transform Spectrometer (FTS). A photograph and schematic drawing of the setup is shown in Figure 3.2. The FTS uses the contrast as a signal between the 800 Kelvin ceramic heater and the 300 Kelvin Eccosorb ANW-72 absorber. Mirrors are 152 x 152 mm in cross-section. The beam splitter is made out of 0.25 mm thick Mylar, which has peak efficiency at 180 GHz. The sample holder, which is placed at the output of the FTS, has a 50 mm diameter aperture. An absorbing screen terminates rays that do not go through the aperture. The rays that go through the aperture are focused onto a broadband detector using an ultra high molecular weight polyethylene (UHMWPE) lens. For the detector, we used a broadband antenna-coupled TES bolometer, as explained in this thesis. We used a detector that has no band defining filter between the antenna and the bolometer as shown in Figure 3.3. The detector's bandwidth was only limited by the antenna. The detector had sensitivity from 70 GHz continuously up to 250 GHz. We scanned the FTS such that we measured up to 300 GHz with a resolution of 1.6 GHz. Details regarding the dewar and readout are given in Chapter 6.

We did not apodize the interferrogram prior to the Fourier transformation to get the spectrum. To obtain transmission data regarding the sample, we divided the spectrum with the sample in the aperture and out of the aperature. Sample-in data was taken right after sample-out data. Typically

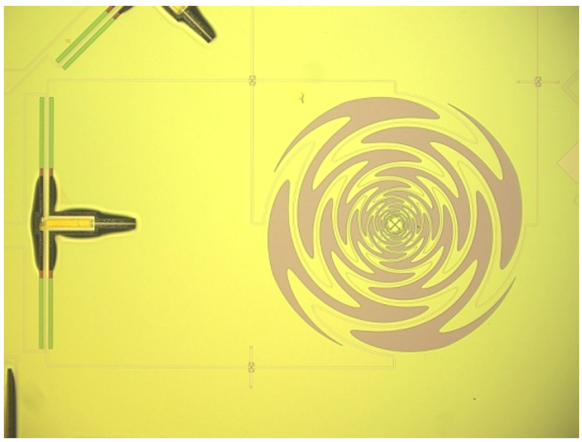

Figure 3.3: Photograph of detector used for the sample measurements. Sinuous antenna is shown on right. There is no filter between antenna and bolometer. Bolometer is the T-shaped object on left.

we took more than three sets of sample-in and sample-out data, then we averaged the results for each set.

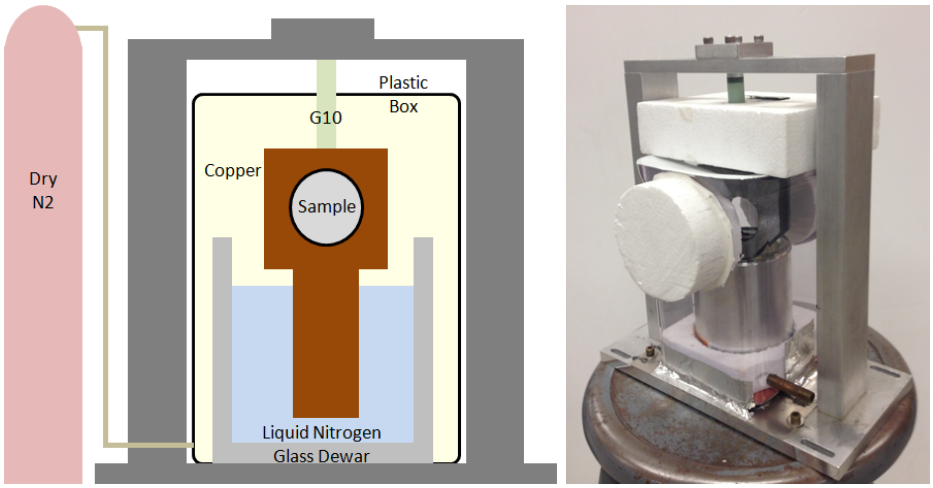

Figure 3.4: Schematic of cold sample holder is shown on left. Sample is inserted into the copper sample holder and cooled by conduction. The sample is kept dry by filling the plastic chamber with dry nitrogen gas. A photograph of the cold sample holder is shown on right.

To perform a test with the cooled sample, we made a sample holder that would hold the cooled sample as shown in Figure 3.4. The sample is cooled by conduction through copper leg that get immersed into liquid nitrogen in a small glass dewar. A plastic box surrounds the cooled sample, and we fill the plastic box with dry nitrogen gas to prevent ice from forming on the surface of the sample. We cut a hole in the plastic box and fill it with 100 mm thick styrofoam to let the

Sample	**Index**	$\tan(\delta)$ **at 300 K**	$\tan(\delta)$ **at 100 K**
Alumina APJF	3.19 ± 0.01	$(7.2 \pm 0.3) \times 10^{-4}$	$(6.3 \pm 0.5) \times 10^{-4}$
Alumina 99.5% LD	3.13 ± 0.01	$(6.3 \pm 0.3) \times 10^{-4}$	-
Alumina 99.9%	3.20 ± 0.01	$(3.7 \pm 0.2) \times 10^{-4}$	$(0.9 \pm 0.2) \times 10^{-4}$

Table 3.2: Summary of results from alumina measurements.

millimeter-wave through with less attenuation. Also, thick styrofoam provides thermal isolation from cold nitrogen vapor inside the plastic box. This prevents water condensation on the surface of the styrofoam. The copper sample holder is thermally isolated by a hollow G10 rod. An aluminum holder was built around the box such that the sample holder can be taken out to insert/remove the sample to do sample-in/sample-out measurements. It is important that the sample holder returns to the same place after each sample has been replaced - the aluminum jig ensures this. With this setup, we were able to cool the sample to approximately 100 Kelvin. It was important to keep sample above liquid nitrogen because liquid nitrogen was so absorptive that we would not be able to get an accurate *sample out* measurement if we simply immersed the sample holder into liquid nitrogen.

Result

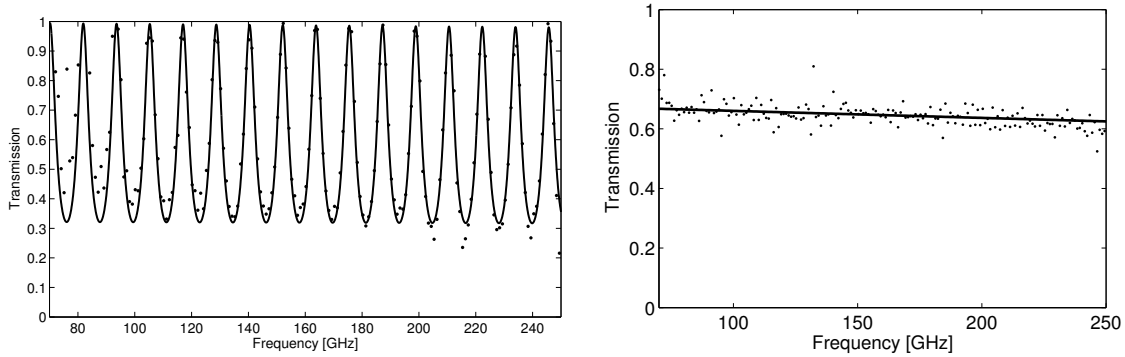

Figure 3.5: (left) Transmission through 4 mm thick 99.9% purity alumina measuered at room temperature. Refraction index was $n = 3.20 \pm 0.01$. (right) Transmission through 40 mm thick 99.9% purity alumina measured at 100 Kelvin. Loss-tangent was $\tan(\delta) = (0.9 \pm 0.2) \times 10^{-4}$.

To get an accurate measurement of the refraction index, we used data from the 4 mm sample. The Fabry-Perot fringes in sample transmittance data occurs with a frequency space of $\Delta f = c/(2dn)$ where d is the thickness of the sample. Thus, to get a large number of fringes while being able to resolve the fringes within the FTS's resolution, the 4 mm sample had a good thickness. Example data from 99.9% alumina is shown in Figure 3.5. To get an accurate measure-

ment for $\tan(\delta)$, we used 40 mm sample. Since $\tan(\delta)$ we are after is small, we needed a thicker sample to measure the loss.

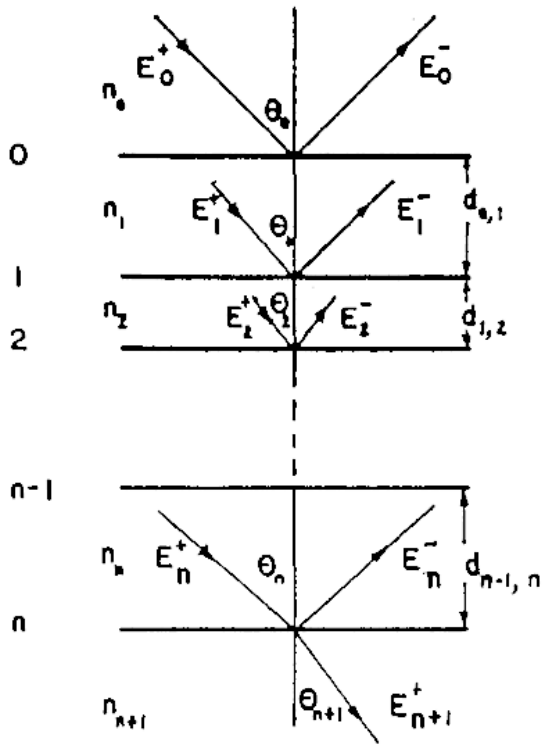

Figure 3.6: Schematic for characteristic method calculation. E_n^+ and E_n^- are incoming and reflected electric field at layer n respectively. [49]

For refraction index calculations, we fitted the data with an analytical model obtained with the characteristic matrix method [95, 49]. As shown in Figure 3.6, the electric field incident on a multilayer stack is related to the outgoing electric field by

$$\begin{pmatrix} E_0^+ \\ E_0^- \end{pmatrix} = \prod_{j=0}^{N} \frac{D_j}{t_j} \begin{pmatrix} E_{N+1}^+ \\ E_{N+1}^- \end{pmatrix} \tag{3.3}$$

Where

$$D_j = \begin{pmatrix} X_{ij} & 0 \\ 0 & X_{ij}^{-1} \end{pmatrix} \begin{pmatrix} 1 & r_j \\ r_j & 1 \end{pmatrix}, i = j-1 \tag{3.4}$$

where $X_{ij} = exp[i\gamma d_{ij}]$ describes the propagation of the field between boundary i and j through dielectric with thickness d_{ij}. t_i and r_i are the Fresnel transmission and reflection coefficient at boundary i, respectively. The material we used was so thick that the fringe spacing was too narrow to resolve with the FTS. Each data point in the spectrum data provides an average of multiple fringes - so only its slope provides useful information. To calculate $\tan(\delta)$ for the material, we used

a linear approximation fit since argument of exponential was small. The results are summarized in Table 3.2. From the results, we concluded that 99.9% purity alumina from Nihon Ceratec meets our absorptive loss requirement. The POLARBEAR-2 decided to using 99.9% purity alumina for a lens material. For the refraction index, we measured the refraction index to the required accuracy for a 4 mm sample. There is still some concern that the refraction index might change, depending on the lens thickness. Our collaborators at KEK are working to measure index uniformity across lens.

3.3 Anti-Reflection Coating

Design

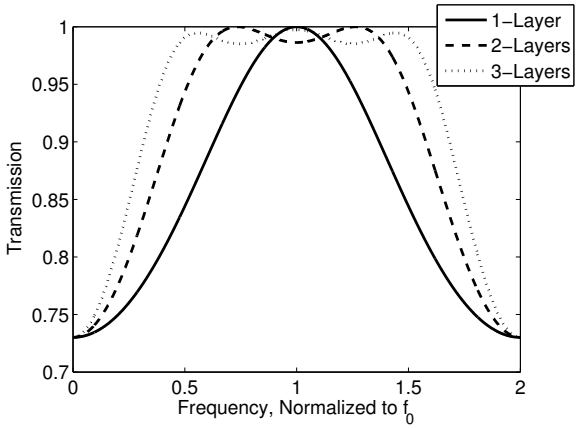

Figure 3.7: Frequency normalized transmission for AR coating on alumina ($\varepsilon_r = 10$). Each layer is $\lambda/4$ at center frequency f_0. For single layer coating $\varepsilon_r = 3.2$. For two layer coatings, $\varepsilon_r = 2,5$. For three layer coatings, $\varepsilon_r = 2,4,7$ were used.

The POLARBEAR-2 will simultaneously observe at 95 GHz and 150 GHz with one receiver and multichroic pixel. The AR coating applied on the optical element must have enough bandwidth to cover both bands. Generally, the coating bandwidth increases with the number of correctly tuned layers as shown in Figure 3.7, but the absorptive loss also increases due to the increased thickness. We tried to achieve the required bandwidth with the minimum number of layers.

We used characteristic matrix method to calculate the transmission through multiple thin films. We optimized using layer thicknesses that correspond to one-quarter wavelength at the center frequency f_0 for both layers. We chose the geometric mean of the center frequency of two bands for f_0. We then optimized the dielectric constants of each layer to maximize the transmission over the observation band. We found that a two-layer coating with relative dielectric constants of $\varepsilon_r =$ 2 and 5 and $f_0 = 120$ GHz would give sufficient bandwidth to cover both 95 GHz and 150 GHz bands. We also studied wider AR coating for future experiments that would cover 95, 150 and

220 GHz bands simultaneously. We found that a three-layer coating, centered around 150 GHz with dielectric constants of $\varepsilon_r = 2$, 4, and 7, would have acceptable bandwidth.

Coating Material

For the coating material, we wanted a material that would conform to a highly curved surface, adhere without any additional layer, withstand thermal cycling and have a tunable dielectric constant to achieve the optimal dielectric constant. We chose epoxy as the base material for its adhesion properties and malleability. We referred to Lamb for the approximate dielectric constants of epoxies [69]. To measure dielectric constants and absorption losses, we used the same method that was used to measure alumina's dielectric constant and loss.

We mixed Emerson and Cuming's Stycast 1090, Stycast 1266A and Stycast 2850FT with their corresponding catalysts - Catalyst 9, Stycast 1266B and Catalyst 23LV respectively. For the mixing ratio, we followed each product's data sheets and avoided mixing more than 100 mL of sample at a time as heat from the exothermic reaction hardens the mixture too quickly for our application. Cylindrical aluminum molds 25 mm deep and 50 mm in diameter were coated with Mann Ease Release 200 mold release. We poured the mixture into the mold, then placed the mold in a 90°C oven for a few hours.

We cut the cured samples to 6 mm thick and machined both sides to be parallel within 0.1 mm. We finished the surface of the sample with 400 grit sand paper. We then measured its dielectric constants using the FTS. We found that Stycast 1090, Stycast 1266A and Stycast 2850FT have dielectric constants of 2.06, 2.60 and 4.95, respectively. We successfully obtained mixtures with intermediate dielectric constants by mixing two types of epoxy. To obtain a dielectric constant higher than 4.95, we mixed Stycast 2850FT with $SrTiO_3$ powder from Fisher Scientific which has been shown to have a high dielectric constant at lower frequencies up to 10 GHz [72]. We tried other high dielectric constant powder such as TiO_2 and $BaTiO_3$. These dielectric powders have high dielectric constant at lower frequency, but we suspect that its dielectric constant relaxed at 100 GHz. Also mixing dielectric powder made epoxy very thick with small amount of powder. Thus powder needed to have very high dielectric constant to be effective. For these high dielectric mixtures, we vacuum-pumped the mixture for 5 minutes to remove air bubbles. With a Stycast 2850FT and $SrTiO_3$ mixture, we obtained dielectric constants as high as 7.44. We summarize the results in Figure 3.8.

Anti-Reflection Coating

To test AR-coating performance, we AR-coated cylindrical 99.5%-RF pure alumina samples from Coorstek as shown in Figure 3.9. The alumina sample have a dielectric constant of 9.6 and were 51 mm in diameter and 6.35 mm thick. For better adhesion, we lightly sanded the surface of the alumina sample with 400 grit sand paper prior to applying the coatings. We prepared epoxy mixtures as described in Section 3.2 and then applied a thin layer of the mixture on the alumina sample by pouring this mixture onto the alumina. After the mixture cured, we sanded down each layer to 25 μm thickness accuracy before applying next layer. The thickness of each coating layer

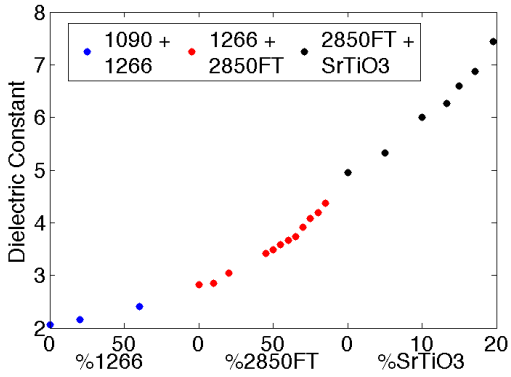

Figure 3.8: Dielectric constants of various epoxy and $SrTiO_3$ mixtures at room temperature as a function of the percent by weight of the total mixture.

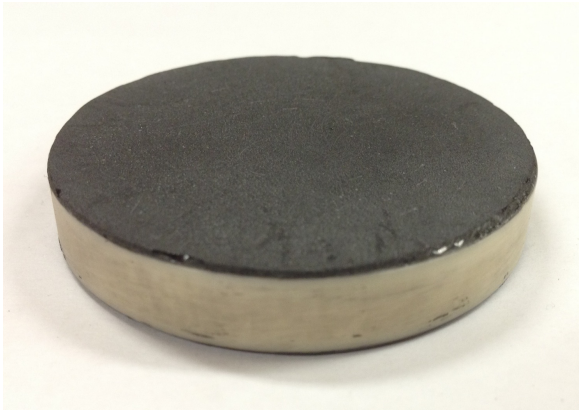

Figure 3.9: Photograph of two-layer AR coated alumina sample. AR coating is applied on both side. Sample is 6 mm thick and 50 mm in diameter. Coatings were 354 μm, and 224 μm for Stycast 1090 layer and Stycast 2850FT layer respectively

corresponds to 354 μm, 250 μm, 224 μm, and 189 μm for dielectric constants of 2, 4, 5, and 7 respectively. For an expedited curing process, we placed the samples in a 90°C oven for a few hours. However, the highest dielectric layer with Stycast 2850FT and $SrTiO_3$ was difficult to sand when fully cured. For a coating with this mixture, we removed the sample from the oven after 45 minutes to sand the surface before it had completely cured.

We measured transmission as a function of frequency using the FTS. Transmittance plots for two-layer and three-layer coatings are shown in Figure 3.10. The measurement shows uncoated alumina which has high Fabry-Perot fringes due to high reflection, whereas the coated sample has high transmittance over a wide band. The modeled curve assumed a constant loss tangent at 150 GHz. The agreement between theory and measurement is good with a difference consistent with an increase in the loss tangent with frequency, a typical loss trend for epoxies in the millimeter

range [69].

Cooling the samples reduced the band-integrated absorption loss from 15% to less than 1% for the two-layer coating and from 21% to 10% for the three-layer coating. The larger loss for the three-layer coating can be attributed to the thicker epoxy layers and high absorption in strontium titanate. However, in typical CMB experiments, lenses operate around 4 Kelvin. Because the loss tangent decreases with temperature for many materials [69], we expect better performance at operating temperatures.

As shown in Figure 3.10, the reflection was suppressed to below 10% over 92% and 104% fractional bandwidth for the two-layer and three-layer coatings, respectively. To calculate the bandwidth of low reflection for the three-layer coating, we corrected for this loss and measured the fractional bandwidth above 90% transmittance. This bandwidth can be visualized by observing the frequency range over which the transmittance appears relatively flat. This is only 12% greater than the two-layer coating bandwidth although theory predicts a difference of 25%. However, the theoretical band for the three-layer coating extends lower than our setup accurately detects. Thus, the coating itself may have a wider bandwidth than we were able to detect.

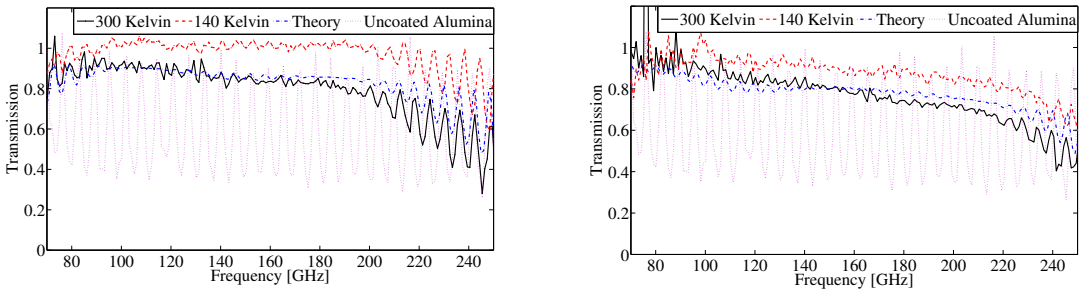

Figure 3.10: Transmittance spectra of two-layer (top) and three-layer (bottom) AR coated alumina at 300 Kelvin (solid black) and 140 Kelvin (dashed red), the modeled curve at 300 Kelvin (dash-dotted blue), and uncoated alumina (dotted magenta). A widened transmittance band can be inferred from the lack of Fabry-Perot fringes.

3.4 Lenslet Coating

To make a sufficiently precise AR coating on a lens, we designed a mold with a cavity that leaves a thin gap between the lens and mold as shown in Figure 3.11. The cavity was made using a precision machined, ball-ended mill. We machined a small indentation in a piston to hold the lenslette in place. We made a piston and cavity with two dissimilar metals to prevent galling between pieces. We were able to create coatings with a thickness variation within 25 μm, which is approximately 10% of the thickness of each layer. The performance degredation from the 10% error in thickness was negligible. We sprayed the cavity with mold release, and then filled the cavity with the appropriate amount of mixed epoxy to fill down to 20 degrees from the flat surface

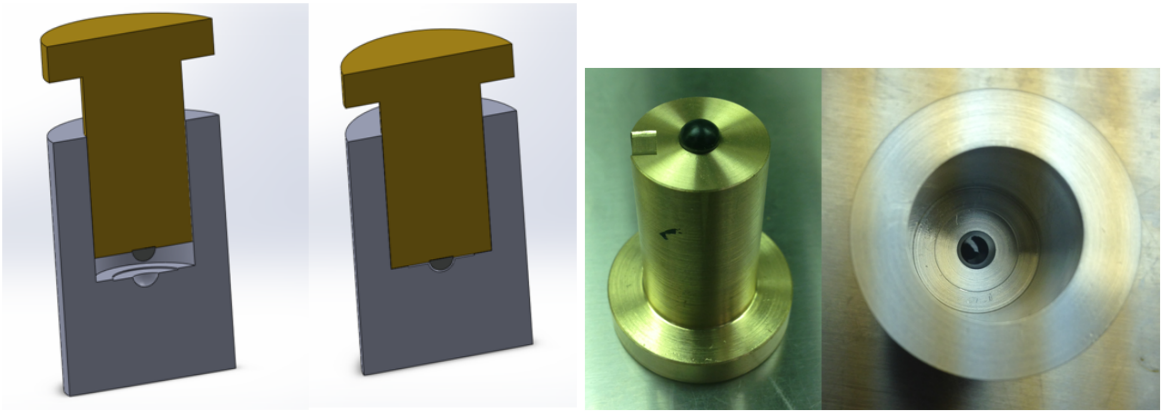

Figure 3.11: (left) CAD drawing of cross section of a piston and a mold. (right) Photograph of piston with a coated lenslet. Photograph of cavity with small drop of epoxy inside. Courtesy of Praween Siritanasak

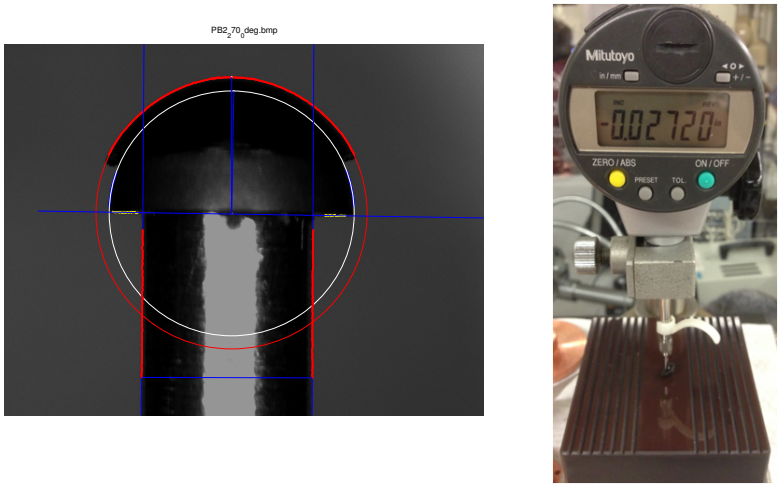

Figure 3.12: (left)Photograph of lenslet coating for inspection. Curve fitting finds contrast in image and fits circle with center position and radius as free parameter. (right) Photograph of micrometer setup to check thickness of stripped coating directly. Courtesy of Praween Siritanasak

of the lenslet as shown in Figure 3.11. For additional layers, we repeated the process using molds with different spacing.

We assessed the quality of the coatings by taking photographs of the side profile and fitting the surface to the expected circular shape as shown in Figure 3.12. From the fit, we verified that the diameter of the coatings was within 25 μm and translation errors were within 25 μm in all directions. We also confirmed the accuracy by removing the AR coating from mold-release coated lenslets and measuring directly with micrometers. Our tolerance corresponds to approximately 10% of a single layer's thickness, which would result in less than a 1% decrease in transmittance.

To test cryogenic adhesion, we made twelve two-layer coated 6.35 mm diameter lenses. We kept one sample as a control and slowly cooled nine samples in a vacuum to liquid nitrogen temperature. These nine samples all survived ten slow thermal cycles in the dewar and 18 dunks in liquid nitrogen, returning to room temperature between dunks. Two additional samples were rapidly thermal cycled between room temperature and liquid nitrogen temperature until failure. Failure for one sample occurred after 18 dunks and the other after 50 dunks. There was no change to the control sample that was kept at room temperature. Since this test, we made many 2-layer coated lenslet-arrays as shown in Figure 5.40, and successfully thermal cycled them. Additionally, the optical properties of the two-layer coating have been cold tested multiple times without a detectable change in performance. We concluded that the coatings have sufficient optical and mechanical stability for our applications.

Anti-Reflection Coating on Large Surface

We tried to extend this AR coating technique to a larger surface to coat alumina lenses. However, we noticed that coating on a large surface delaminated at cryogenic temperatures. We solved the problem by making a 40 μm wide slit in the AR coating. The slit was made in a 2 inch by 2 inch pattern. Even though this solved the delaminating issue, we have not evaluated how this would affect the polarization of transmitted light. Alternative ideas for AR coating over large surfaces are discussed in Section 7.2 as potential future projects.

3.5 Conclusion

By devising methods to tune the dielectric constant of a mixture between 2.06 and 7.44, we have created an effective epoxy-based, broadband anti-reflection coating for millimeter-wave optics. We reduced the reflection from an alumina slab to less than 10% over 92% and 104% fractional bandwidths with the respective two-layer and three-layer anti-reflection coatings. When samples were cooled to 100 Kelvin, the absorptive loss was suppressed to less than 1% in the two-layer coating and 10% in the three-layer coating. Using a precise molding technique, we achieved high-precision coating application to a curved surface. We also demonstrated that the coatings can survive numerous thermal cycles. Coating over a large, flat surface has proven to be difficult. There is a proposed solution to segment the AR coating into smaller sections, but its effect on polarization at the millimeter wave needs to be studied in detail.

Chapter 4

Multichroic Focal Plane Design

4.1 Introduction

Focal plane parameters drive many decisions of an experiment. Focal plane needs to be carefully designed to maximize the sensitivity of the experiment. Important decision for the focal plane optimization is a chosing correct pixel size. The basic concept of pixel size optimization is simple. Since the focal plane size is limited by optics design, greater number of pixels fill the focal plane if pixels are smaller in size. Signal to noise ratio increases as square-root of number of pixels. However, a beam from a diffraction-limited pixel widens for a smaller pixel. As the beam widens, a larger fraction of the beam terminates on the aperture and a smaller fraction of the beam receives a signal from the sky. Thus, the smaller pixel has a lower signal-to-noise ratio per pixel. The optimization process calculates the signal-to-noise ratio of a single pixel as a function of pixel size and multiplies it with the square-root of the number of pixels to find the best pixel size [41, 44].

The multi-chroic detector brings an additional challenge to the pixel size optimization process. Different frequency bands share same pixel size. Pixel size might not be optimized for any frequency, but the goal is to find the optimal size for the entire experiment. As we optize pixel size, we will optimize various detector parameters. Pixel size optimization is multi-dimensional optimization problem. To present the material with concrete example, we will demonstrate how the POLARBEAR-2 experiment optimized its pixel size.

4.2 Focal Plane Size and Pixel Count

The POLARBEAR-2 experiment will use a telescope with the same design as the HTT. The refractive optics inside the cryogenic receiver were designed to maximize the focal plane area. During the optics design, F/# of the optics were decided to be 1.9. Smaller F/# minimizes spill-over efficiency loss, where the spill-over efficiency is defined as fraction of the beam that goes through an aperture. Thus, smaller pixel still achieves high signal to noise ratio. This allows the physical size of the focal plane to be small. Cryogenically cooling large focal plane is difficult, so minimizing the focal plane size is crucial. However, small F/# makes hard to design large telecentric focal plane

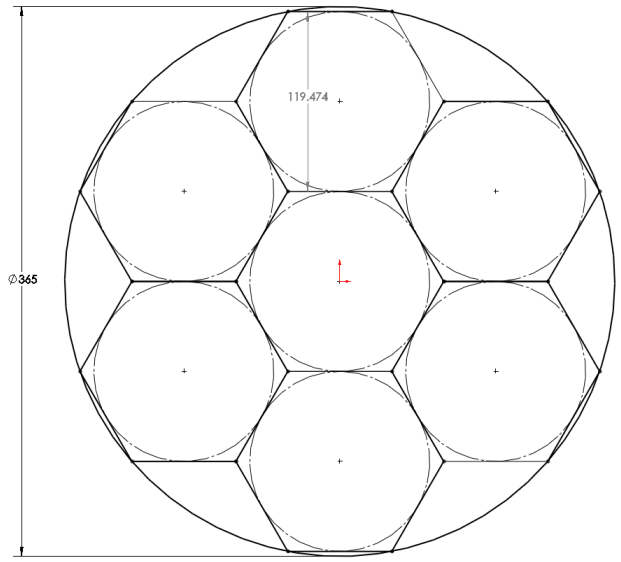

Figure 4.1: CAD drawing of focal plane planning. Circle represent 365 mm available focal plane area. Hexagon is 120 mm side to side.

with diffraction-limited rays. High F/# optics makes optics tube longer. For the POLARBEAR-2, we were running into size constraint from the HTT. Thus, for the POLARBEAR-2 experiment, we decided that F/# $= 1.9$ as a compromise. That gave an acceptable strehl ratio (< 0.8) for a focal plane diameter of 365 mm.

We chose a close-packed hexagonal pattern to maximally fill the 365 millimeter diameter focal plane with least number of wafers. We used seven hexagonal-shaped wafers with side-to-side size length of 120 mm as shown in Figure 4.1. We reserve approximately 10 mm for hardware. Available side-to-side hexagonal size is $S = 110$ mm. The total area available ($A_{available}$) for pixels are:

$$A_{available} = N_{wafer} \frac{\sqrt{3}}{2} S^2 \left(\frac{1}{6}\right) \pi\sqrt{3} \tag{4.1}$$

Where we first calculated the area of N_{wafer} hexagon with a side-to-side length of S. Then we multiplied by a factor to extract an area that will be available for close packed circular pixel. Suppose each pixel has a diameter of D mm, then the area per pixel would be $A_{pixel} = \frac{\pi D^2}{4}$. Number of pixel is then

$$N_{pixel} = \frac{A_{available}}{A_{pixel}} = N_{wafer} \frac{\sqrt{3}}{2} S^2 \left(\frac{1}{6}\right) \pi\sqrt{3} \frac{4}{\pi D^2} = N_{wafer} \frac{S^2}{D^2} \tag{4.2}$$

Number of pixels as a function of pixel size is shown in Figure 4.2.

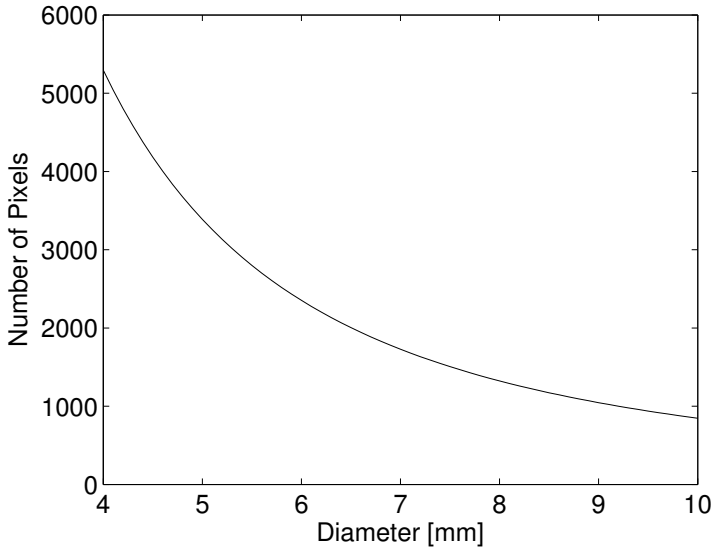

Figure 4.2: Number of close packed circular pixels as function of pixel size for 365 mm diameter focal plane with seven hexagonal wafers. Each hexagonal wafer is 110 mm wide.

4.3 Optical Loading and Photon Noise

We calculated optical loading on a single detector by adding up emissions and absorptions from every optical elements between the CMB and the detector. Each optical element absorbs part of incident light, and the element emits black body radiation characterized by its temperature and emissivity. We made direct measurements of emissivity and thermal conductivity for few elements such as the alumina used for the lenses. For other elements, we estimated the value using values used for past experiments [45, 12, 60].

Optical Elements

Table 4.1 and Table 4.2 list optical elements for the POLARBEAR-2 experiment for 95 GHz channel and 150 GHz channel respectively.

We use simple model shown in Figure 4.3 to demonstrate how we calculated power received by a detector. The brightness of an object with emissivity ε and temperature T is

$$B(\varepsilon, T, \nu) = \frac{2\varepsilon h\nu^3}{c^2\left[e^{\left(\frac{h\nu}{Tk_B}\right)} - 1\right]} \tag{4.3}$$

Where h is the Planck's constant, k_B is the Boltzmann constant, c is the speed of light and ν is a frequency. The total power emitted by the object that can be received by a single linear polarized

Element	Efficiency	Emissivity	Temperatre [K]
CMB	1.000	1.000	2.725
ATM(1mm PWV 60deg EL)	0.9696	0.031	277
Primary Mirror	0.990	0.010	277
Secondary Mirror	0.990	0.010	277
ZoteFoam	0.990	0.010	150
Cold Window Support	0.950	0.050	150
50 K Filter	0.950	0.050	50
Field Lens	0.970	0.030	4
Aperture Lens	0.970	0.030	4
HWP	0.900	0.100	4
Lyot	0.537	1.000	4
Aperture Filters	0.950	0.050	4
Collimating Lens	0.970	0.030	4
0.35 K Filter	0.950	0.050	0.75
Silicon Lens	0.950	0.050	0.25
Antenna Backlobe	0.950	1.000	0.25
Antenna Feed Mismatch	0.990	0.000	0.25
Microstrip Filter	0.900	0.000	0.25
Microstrip Loss	0.870	0.000	0.25
Load Resistor	1.000	0.000	0.50

Table 4.1: List of optical elements for $f_{center} = 94.3$ GHz and $Frac_{BW} = 30.6\%$. Loss through the field lens, aperture lens and collimating lens assume $\tan\delta = 1 \times 10^{-4}$ dielectric loss. Microstrip loss assumes $\tan\delta = 2 \times 10^{-3}$ dielectric loss

detector is

$$P = \frac{1}{2}\int A\Omega B(\varepsilon, T, \nu) d\nu \tag{4.4}$$

The factor $\frac{1}{2}$ is there because we are looking at single linear polarization. $A\Omega$ is an optical throughput of the detector. For a single moded detector, $A\Omega = \lambda^2$. Where λ is wavelength of a signal. Simplified model only has detector, microstrip filter, Lyot stop, lens and the CMB, but a realistic model is simply the repetition of elements that we consider in the simplified model. We will look at the optical elements in time reversal order, from the detector to the CMB.

Microstrip Filter

There is no element between a filter and a detector. Therefore every power that was emitted by the filter goes into the detector, $P_{1emit} = P_{1detect}$. Where $P_{n\ emit}$ is emitted power from n^{th} element, and

Element	Efficiency	Emissivity	Temperatre [K]
CMB	1.000	1.000	2.725
ATM(1mm PWV 60deg EL)	0.9682	0.034	277
Primary Mirror	0.990	0.010	277
Secondary Mirror	0.990	0.010	277
ZoteFoam	0.990	0.010	150
Cold Window Support	0.950	0.050	150
50 K Filter	0.950	0.050	50
Field Lens	0.950	0.050	4
Aperture Lens	0.950	0.050	4
HWP	0.900	0.100	4
Lyot	0.849	1.000	4
Aperture Filters	0.950	0.050	4
Collimating Lens	0.950	0.050	4
0.35 K Filter	0.950	0.050	0.75
Silicon Lens	0.950	0.050	0.25
Antenna Backlobe	0.950	1.000	0.25
Antenna Feed Mismatch	0.990	0.000	0.25
Microstrip Filter	0.900	0.000	0.25
Microstrip Loss	0.810	0.000	0.25
Load Resistor	1.000	0.000	0.50

Table 4.2: List of optical elements for $f_{center} = 147.8$ GHz and $Frac_{BW} = 26.0\%$. Loss through field lens, aperture lens and collimating lens assume $\tan\delta = 1 \times 10^{-4}$ dielectric loss. Microstrip loss assumes $\tan\delta = 2 \times 10^{-3}$ dielectric loss

$P_{n\ detect}$ is power received by the detector that was emitted by n^{th} element.

$$\begin{aligned} P_{1emit} &= \int \frac{\varepsilon_1 h\nu}{e^{\left(\frac{h\nu}{T_1 k_B}\right)} - 1} d\nu \\ P_{1detect} &= \int \frac{\varepsilon_1 h\nu}{e^{\left(\frac{h\nu}{T_1 k_B}\right)} - 1} d\nu \end{aligned} \tag{4.5}$$

Lyot Stop

Lyot stop, a cold aperture stop, is a *negative* element where fraction of beam that hits the Lyot is $(1-\eta_2)$ where η_n is a frequency dependant efficiency of n^{th} element. Emitted power from the Lyot must go through a bandpass filter, thus emitted power is reduced by the efficiency of the microstrip

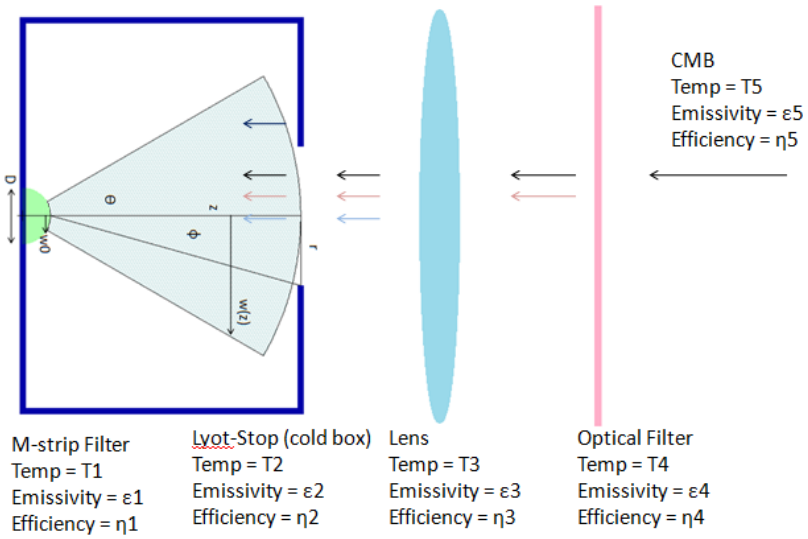

Figure 4.3: Simple model of a cryogenic receiver. Dark blue box represents a cold box with an aperture (Lyot stop). Green hemisphere represents a lenslet of a detector. Circular fan coming out from a lens represents detector beam. Arrows represent optical loading contributions from optical elements.

filter η_1.

$$\begin{aligned} P_{2emit} &= \int \frac{\varepsilon_2(1-\eta 2)h\nu}{e^{\left(\frac{h\nu}{T_2 k_B}\right)}-1} d\nu \\ P_{2detect} &= \int \frac{\eta_1\varepsilon_2(1-\eta 2)h\nu}{e^{\left(\frac{h\nu}{T_2 k_B}\right)}-1} d\nu \end{aligned} \tag{4.6}$$

Lens

Example of lens can be repeated for other optical elements such as thermal filters and half-wave plate. Its emitted power is reduced by efficiencies of optical elements between the source and the detector. For the simple case, efficiency is reduced at Lyot stop and microstrip filter.

$$\begin{aligned} P_{3emit} &= \int \frac{\varepsilon_3 h\nu}{e^{\left(\frac{h\nu}{T_3 k_B}\right)}-1} d\nu \\ P_{3detect} &= \int \frac{\eta_1\eta_2\varepsilon_3 h\nu}{e^{\left(\frac{h\nu}{T_3 k_B}\right)}-1} d\nu \end{aligned} \tag{4.7}$$

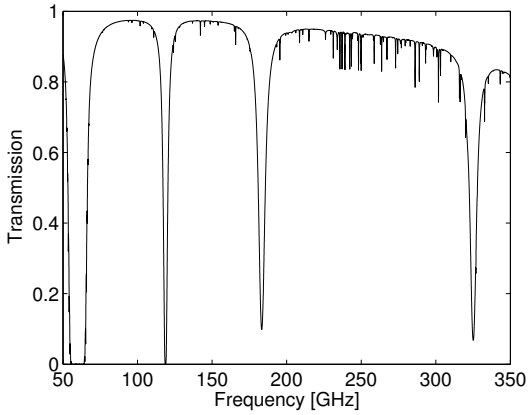

Figure 4.4: Transmission of atmosphere for 1 mm PWV 60 degrees elevation between 50 GHz and 350 GHz.

CMB

Finally the CMB is the farthest radiation source, thus it goes through every optical element.

$$\begin{aligned} P_{4emit} &= \int \frac{\varepsilon_4 h\nu}{e^{\left(\frac{h\nu}{T_4 k_B}\right)} - 1} d\nu \\ P_{4detect} &= \int \frac{\eta_1 \eta_2 \eta_3 \varepsilon_4 h\nu}{e^{\left(\frac{h\nu}{T_4 k_B}\right)} - 1} d\nu \end{aligned} \tag{4.8}$$

Generalization

Except for the Lyot stop, an optical element will load the detector with optical power of

$$P_{i\ detect} = \int \frac{\eta_i^{cum} \varepsilon_i h\nu}{e^{\left(\frac{h\nu}{T_i k_B}\right)} - 1} d\nu \tag{4.9}$$

Where

$$\eta_i^{cum} = \prod_{n=1}^{i-1} \eta_n \tag{4.10}$$

Atmosphere

am atmospheric model was used to calculate the atmospheric model as shown in Figure 4.4 [96]. *am* atmospheric model splits the atmosphere into stacks of layers. Then the code calculates temperature, pressure and density of gas for each layer such that they are consistent to adjacent layer. It is possible to modify variables such as PWV and the angle of propagation. *am* then calculates the

opacity of a given stack and its effective temperature. *am* code also comes with *cookbooks* that are already setup for common millimeter wave observation sites. I used the cookbook for Chajnantor site with 1 mm PWV at 60 degrees elevation to calculate atmospheric loading.

am code outputs effective temperature and opacity as a function of frequency. Since formalism we presented before assumes brightness of blackbody with a single temperature and an emissivity for given element, integrated loading from *am* code was converted to effective temperature and emissivity. We calculated total amount of power emitted from given temperature and opacity as a function of frequency and integrated across frequency after multiplying power with frequency dependant efficiency of the receiver. Then we fixed atmospheric temperature to 277 Kelvin, and calculated effective emissivity that gives same amount of loading onto a detector.

Extension Length and Waist Size

When we are optimizing the pixel size, we looked at the beam's divergence angle as function of pixel size. Lyot truncates beam at half-angle defined by $\theta_{Lyot} = \tan^{-1}(2\mathrm{F}/\#)^{-1}$, thus the beam divergence is directly related to efficiency of each pixel.

For the pixel optimization calculation, we assumed detector has a Gaussian beam profile. As shown in Figure 4.6 it is a good approximation. It is well known that point source maps to collimated ray if a point source is placed on a far foci of an dielectric elliptical lens with an eccentricity equal to inverse of refractive index of the lens ($\varepsilon = 1/n$) [48]. A truly elliptical lens is costly to manufacture in large volumes, thus we approximate elliptical lens with a combination of a hemisphere and extension. We would like to pick extension length at an elliptical point that gives maximum directivity. Pixel with same diameter achieves the highest spill over efficiency at the elliptical point. In addition, beam from a lens with extension length at elliptic point is less sensitive to feed imperfections [35, 33]. We coat our lenslet with two layer AR coatings to broaden its operational band, therefore optimal extension length would be different from what was calculated by Edwards [33]. We studied how directivity changes as a function of extension length using a 3-D electro-magnetic high frequency structural simulator (HFSS). The HFSS uses the finite element method (FEM) [10]. FEM splits model into many tetrahedras. An EM solution is calculated for each tetrahedra, and they are inter-related such that Maxwell's equations are satisfied between boundaries. Advantage of using such 3-D EM simulator is that it can account for effects that is difficult to get analytical solution, such as interaction of antenna with reflected field inside the lens. Disadvantage is that simulation requires large (approximately 100 Gb) of RAM and many CPU hours to solve large structure. The results are shown in Figure 4.6. From the study, directivity peaks when the extension length (L) is 0.46 times radius of a *silicon lens* (R). For the simulated model, the Gaussian beam waist size was 2.3 mm. We also need space for two-layer AR coating and some finite space to assemble lenses with close-hexagonal pattern. For the simulated lens size, we would need to have diameter of $D = 6.789$ mm per pixel. This makes the waist to pixel diameter ratio:

$$w_0 = \frac{D}{2.95} \tag{4.11}$$

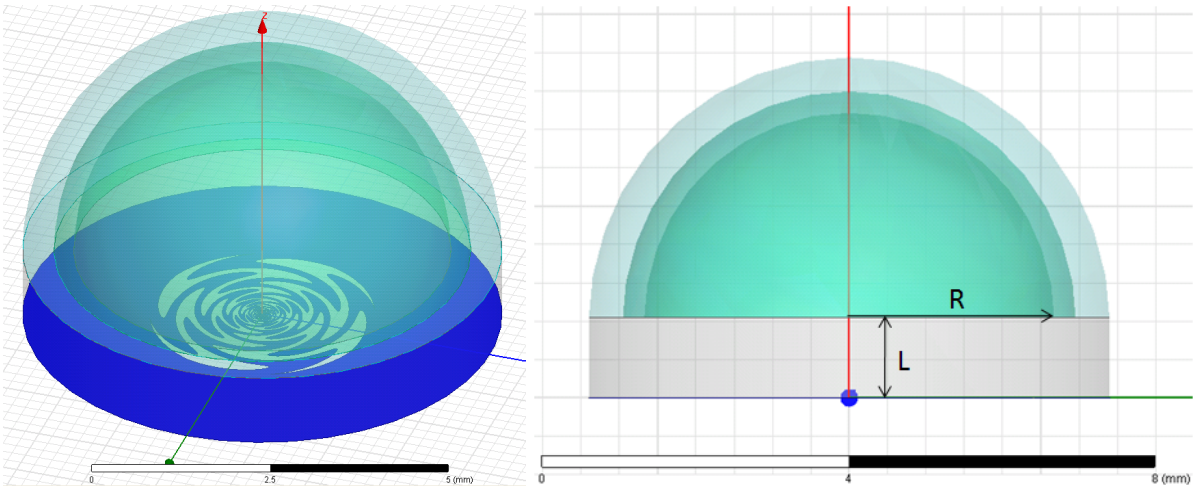

Figure 4.5: CAD of the simulated 3-D model. 16-cell sinuous antenna was placed under lenslet with differential excitation. Radius of silicon ($\varepsilon_r = 11.7$) lenslet is $R = 2.673$ mm. Two layer AR coating was represented by two shells with $\varepsilon_r = 2,5$, with thickness of $\lambda/4$ at 120 GHz. Silicon cylinder extension has radius of sum of radius of lenslette and thickness of AR coatings.

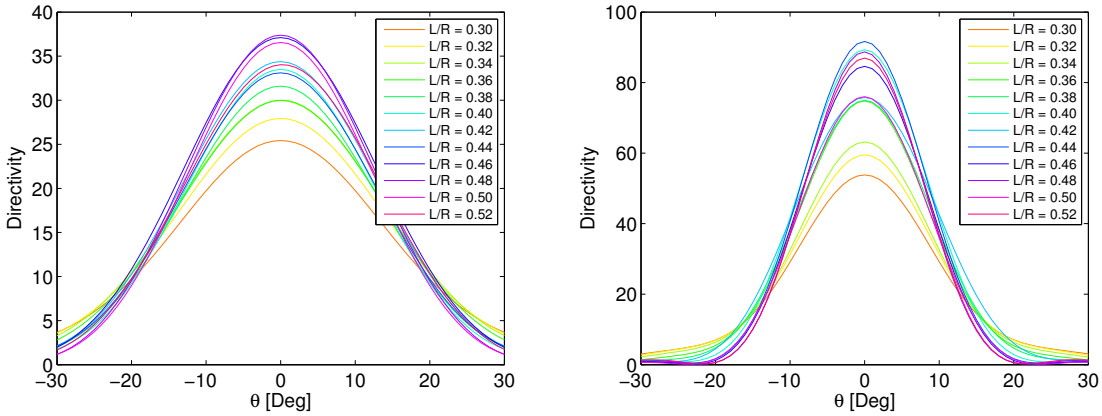

Figure 4.6: Directivity of the beam on E-plane for various L/R ratio for 95 GHz (left) and 150 GHz (right).

Gaussian beam profile has angular dependency of

$$\theta = \frac{\lambda}{\pi w_0} \approx \frac{w(z)}{z} \tag{4.12}$$

Where θ is a half-angle where intensity falls by e^{-2}.

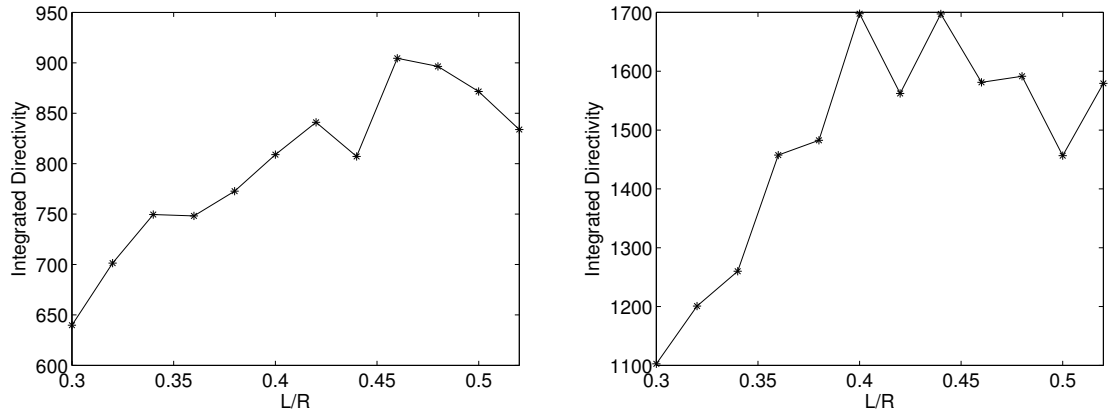

Figure 4.7: Integrated directivity for 95 GHz (left) and 150 GHz (right). Directivity was integrated down to the angle defined by F/#.

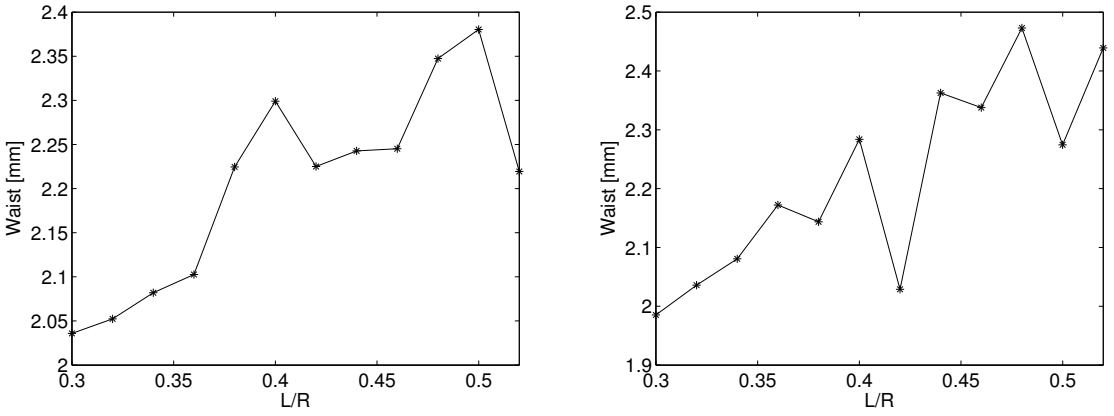

Figure 4.8: Gaussian beam waist size for simulated beam for 95 GHz (left) 150 GHz (right)

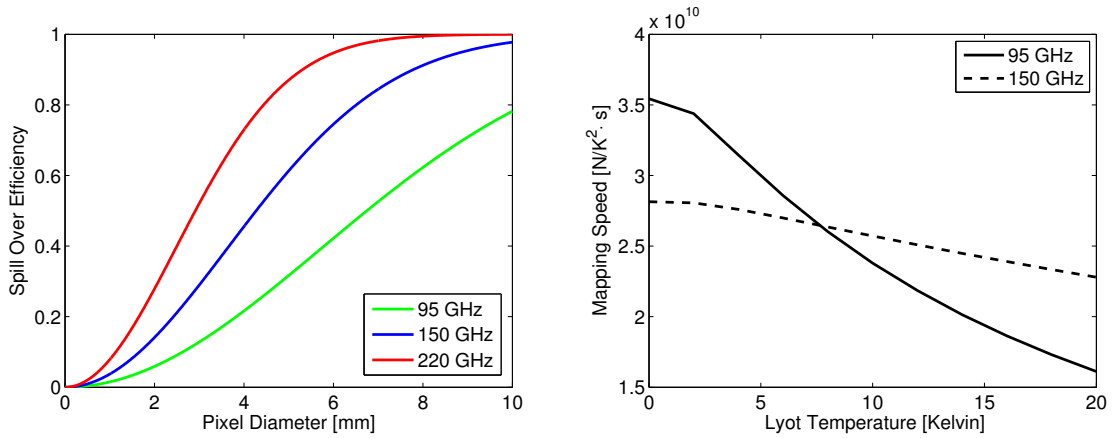

Figure 4.9: (left) Spill over efficiency for F/# = 1.9 and waist to pixel diameter ratio of $D/w_0 = 2.95$. (right) Effect of Lyot temperature to mapping speed.

Lyot Stop

Lyot stop is a optical aperture stop that is cryogenically cooled to truncate the beam of a detector at θ_{Lyot}. Using a time reversal symmetry of electro-magnetism, we can calculate efficiency of the detector through Lyot stop by thinking as if beam is diverging out from a detector. The fraction of beam that would make through a Lyot stop with a opening radius r is

$$\eta_{\rm SE} = 1 - e^{-\frac{2r^2}{w(z)^2}} = 1 - e^{-\frac{\pi^2}{2}\left(\frac{w_0}{F\lambda}\right)^2} = 1 - e^{-0.548\left(\frac{D}{F\lambda}\right)^2} \tag{4.13}$$

This is referred to as *spill-over efficiency*. $w(z)$ is a size of waist at distant z away from a detector, and $F = \frac{z}{2r}$ is the F/# of optics. Traditionally, the pixel size for mapping speed calculation was quoted in $F\lambda$. This makes the mapping speed equation generic for all frequencies. However, since multichroic pixel will share same pixel size for different frequency bands, we will quote the mapping speed as function of physical pixel size D. Plot of Equation 4.13 is shown on Figure 4.9. The POLARBEAR-2 is considering $D = 6.789$ mm pixel. As seen from the figure, large fraction of beam terminates on the Lyot stop. Therefore as shown in Figure 4.9 it is important to keep the Lyot stop cold to keep sensitivity high.

Total Optical Load and Optical Noise

Total optical load onto the detector is simply a sum of power from each optical element

$$P_{opt} = \sum_i P_{i\ detect} \tag{4.14}$$

Photon noise from blackbody radiation can be calculated from fluctuation in occupation number [63, 106]. For a given blackbody, equilibrium number of photon per standing wave mode per Hz

of bandwidth per second is given by

$$n = \frac{1}{e^{\frac{h\nu}{Tk_B}} - 1} \tag{4.15}$$

Then fluctuation in photon arrival for such blackbody is

$$\langle (\Delta n)^2 \rangle = n + n^2 \tag{4.16}$$

We refer to such fluctuations in occupation number as *photon noise*. Noise equivalent power (NEP) is a signal power that will give signal-to-noise ratio of 1 for 1 Hz of bandwidth. It is defined as

$$\mathrm{NEP}_\gamma = \sqrt{2\int p_{opt} h\nu d\nu + \int p_{opt}^2 d\nu} \tag{4.17}$$

Where p_{opt} is the power spectal density associated with P_{opt}. γ refers to the fact this is a noise due to photon contribution. Because of $\int p_{opt}^2 d\nu$ term, NEP must be calculated using spectral density from P_{optl} instead of calculating NEP from individual P_i and add them in quadrature.

4.4 Bolometer Design and Thermal Carrier Noise

Introduction

The bolometer was invented by Langley [70]. The bolometer is a type of detector that detects incident electromagnetic radiation by converting radiation to heat and read change in electrical resistance of temperature dependant material. In its simplest form, a bolometer has a thermally isolated island that is connected to a thermal bath with temperature T_b via a weak link with thermal conductance G. Isolated island contains an absorber that receives optical signal and a thermister, temperature dependant resistor. A thermistor is either voltage biased or current biased. The isolated island thus receives optical power and electrical power. At steady state, temperature of isolated island T would be

$$P = P_{opt} + P_{elec} = G(T - T_b) \tag{4.18}$$

Where P is a total power on an island. Dynamic heat conductance g is defined as

$$g = \frac{\partial P}{\partial T} \tag{4.19}$$

Suppose P changes to a new value P' instantaneously, then bolometer island reaches to different temperature $T' = T_b + \frac{P'}{G}$ with a time constant

$$\tau_0 = \frac{C}{g} \tag{4.20}$$

Previous generation bolometers were made with carbon resistor and doped semiconductors as thermisters [22, 43]. These thermisters have steep increases in resistance as a function of decreasing

temperature, and their high impedance and negative $\frac{dR}{dT}$ preferred current biasing for stable operation. The bolometer behaves as an ideal linear detector with high sensitivity as the steepness of a transition increases. The superconducting transition of a superconductor metal has very sharp $\frac{dR}{dT}$ curve. Superconducting thermister's low impedance and positive $\frac{dR}{dT}$ prefers thermister to be voltage biased for stable operation [56]. Voltage biased detector has an advantage that current can be amplified by superconducting quantum interference device (SQUID) at cryogenic temperature for to achieve low noise performance. Multiplexing is also easier with voltage biased detectors. Review for superconducting TES bolometer was done by Irwin and Hilton [57]. Detailed calculation of bolometer's response including parasitics in readout were also given in the review. While the complete calculation is useful, we'll first introduce simple calculation to get more intuitive understanding [106, 73, 40]. We'll introduce results from complete derivation when discussing stability criteria.

Basic Operation

Electrical bias power applied to a bolometer with voltage bias is

$$P_{elec} = \frac{V_{elec}^2}{R} \tag{4.21}$$

When temperature of a bolometer island tries to change as optical power changes, temperature of the bolometer island is stabilized by negative feed back.

$$\frac{dP_{elec}}{dT} = -\frac{V_{elec}^2}{R^2}\frac{dR}{dT} = -\frac{P_{elec}\alpha}{T_c} \tag{4.22}$$

Where α is logarithmic slope of superconducting transition $\alpha = \frac{\partial \log R}{\partial \log T} = \frac{T}{R}\frac{\partial R}{\partial T}$. Negative feed back allows operation point of bolometer to be locked onto a sharp transition of a superconductor at transition temperature T_c. Suppose small change in optical power $\delta P_{opt} e^{i\omega t}$ changed temperature of an bolometer island by $\delta T e^{i\omega t}$. We can write down energy conservation of bolometer system as

$$P + \delta P_{opt} e^{i\omega t} - \frac{P_{elec}\alpha}{T_c}\delta T e^{i\omega t} = G(T_c - T_b) + (g + i\omega C)\delta T e^{i\omega t} \tag{4.23}$$

Time varying part of is

$$\delta P_{opt} = \left(\frac{P_{elec}\alpha}{T_c} + g + i\omega C\right)\delta T \tag{4.24}$$

We can view this as amplifier with output $\delta P = \delta P_{opt} + \delta P_{elec} = (g + i\omega C)\,\delta T$ and feedback $\delta P_{elec} = -\left(\frac{P_{elec}\alpha}{T_c}\right)\delta T$. We can define loop gain of such amplifying circuit as

$$\mathscr{L}(\omega) = -\frac{\delta P_{elec}}{\delta P} = \frac{P_{elec}\alpha}{gT_c(1 + i\omega\tau_0)} = \frac{\mathscr{L}}{1 + i\omega\tau_0} \tag{4.25}$$

Where $\mathscr{L} = \frac{P_b \alpha}{g T_c}$ is DC the loop gain. Responsivity $S_I = \frac{dI_{elec}}{dP_{opt}}$ is

$$\begin{aligned} S_I &= \frac{dI_{elec}}{dP_{opt}} && (4.26)\\ &= \frac{1}{V_{elec}} \frac{dP_{elec}}{dP_{opt}} && (4.27)\\ &= \frac{1}{V_{elec}} \frac{-\left(\frac{P_{elec}\alpha}{T_c}\right)\delta T}{\left(\frac{P_{elec}\alpha}{T_c} + g + i\omega C\right)\delta T} && (4.28)\\ &= -\frac{1}{V_{elec}} \frac{\mathscr{L}}{\mathscr{L}+1} \frac{1}{1+i\omega\tau} && (4.29) \end{aligned}$$

Where time constant τ is

$$\tau = \frac{\tau_0}{\mathscr{L}+1} \tag{4.30}$$

Thus bolometer's effective time constant is decreased as loop gain goes up. For a high loop gain amplifier $\mathscr{L} \gg 1$, responsivity reduces to

$$S_I = -\frac{1}{V_{elec}} \tag{4.31}$$

Just like electrical amplifier circuit, high loop gain of negative feedback allows responsivity of bolometer to be independent of bolometer's intrinsic characteristics. This helps array of bolometers to have uniform performance [57].

Thermal Carrier Noise

Noise equivalent power that arises from fluctuation in thermal flow through weak link between two different temperature is given by Mather [81].

$$\mathrm{NEP}_g = \sqrt{4\gamma k_B T_c^2 g} \tag{4.32}$$

Where γ is a numerical factor $\gamma = \frac{n+1}{2n+3} \frac{1-(T_b/T_c)^{2n+3}}{1-(T_b/T_c)^{n+1}}$. n is an index for thermal conductivity where $n = 1$ for electron based conduction and $n = 3$ for phonon heat transfer.

To start the optimization process, we first decide the geometry of the weak link by choosing the best saturated power, P_{sat}. We define P_{sat} as a power that flows through weak link between bolometer island at T_c and thermal bath at T_b. We want to pick P_{sat} to be factor of few times greater than expected P_{opt} we calculated from optical load calculation. This allows P_{elec} to be able to provide enough feedback for stable operation, and it gives extra buffer for increased P_{opt} during non-optimal weather. However, we do not want to increase P_{sat} unnecessarily since increasing P_{sat} will increase NEP_g. The POLARBEAR-2 bolometers were designed with $P_{sat} = 2.5 P_{opt}$. Power flowing though bolometer legs can be calculated from a model $P_{sat} = NAk(T)\frac{dT}{dx}$. Where A is

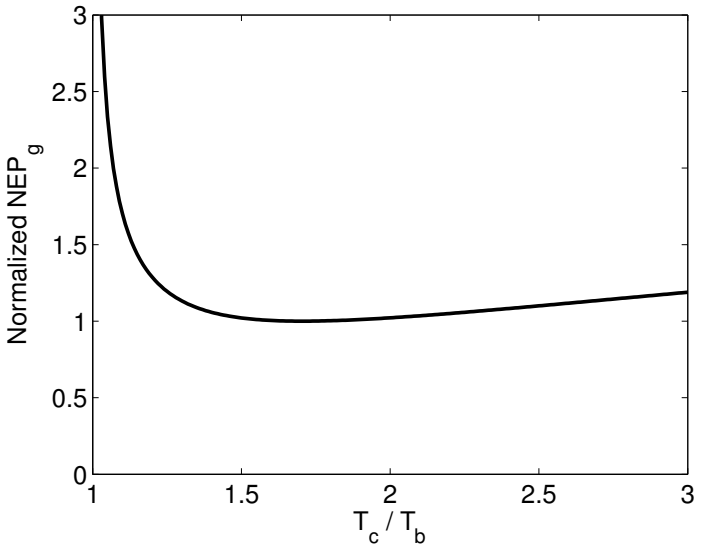

Figure 4.10: Plot of normalized NEP$_g$ as function of $\frac{T_c}{T_b}$. Phonon conduction ($n = 3$) is assumed. Plot is normalized to minima of the the curve.

the cross-sectional area of a bolometer leg, $k(T)$ is thermal conductance and N is a number of bolometer weak links. Suppose we take simple power dependence for conductance $k(T) = k_0 T^n$, and integrating across a leg of bolometer with length l, we can calculate how much power flow through bolometer leg $\int_0^l P_{sat} dx = N \int_{T_c}^{T_b} A k_0 T^n dT$

$$P_{sat} = N \frac{A}{l} \frac{k_0}{(n+1)} \left(T_c^{n+1} - T_b^{n+1} \right) \tag{4.33}$$

Once we decide what P_{sat} is going to be, we need to decide T_c to minimize NEP$_g$. We can rewrite NEP$_g$ as function of $\frac{T_c}{T_b}$

$$\mathrm{NEP}_g = \sqrt{4 k_B P_{sat} T_b} \sqrt{\frac{(n+1)^2}{2n+3} \frac{(T_c/T_b)^{2n+3} - 1}{[(T_c/T_b)^{n+1} - 1]^2}} \tag{4.34}$$

We find minimum of NEP by taking $\frac{d\mathrm{NEP}_g}{d(T_c/T_b)}$. As shown in Figure 4.10 NEP$_\mathrm{g}$ is a slow function around the minimum. Explicit value for minima when $n = 1$ and $n = 3$ is $\frac{T_c}{T_b} = 2.14$ and 1.71 respectively. We fabricate our weaklink with low stress silicon nitride leg, thus thermal carrier is phonon ($n = 3$). The POLARBEAR-2 uses two-stage 3He adsorption cooler to cool the focal plane to 250 milli Kelvin, thus T_c should be 428 milli Kelvin. When designing bolometer we tuned P_{sat} by changing length of bolometer legs. For thermal conductivity, we measured silicon nitride leg with cross sectional area $A = 33$ um^2 has $A \frac{k_0}{n+1} = 40 \frac{\mathrm{mm \cdot pW}}{\mathrm{K}^4}$. From these, we can calculate leg

length to be

$$l = N\frac{A}{P_{sat}}\frac{k_0}{(n+1)}\left(T_c^{n+1} - T_b^{n+1}\right) \tag{4.35}$$

Once P_{sat} is set, we can calculate G and g by

$$G = \frac{P_{sat}}{T_c - T_b} = N\frac{A}{l}\frac{k_0}{(n+1)}\frac{T_c^{n+1} - T_b^{n+1}}{T_c - T_b} \tag{4.36}$$

and

$$g = \frac{\partial P_{sat}}{\partial T_c} = N\frac{A}{l}k_0 T_c^n \tag{4.37}$$

Once g get calculated, NEP_g can be calculated with Equation 4.32.

4.5 Readout Noise

Before we decide on the resistance of the TES at the operation point (R_{TES}) and inductance for readout (L), read-out noise needs to be considered. For the POLARBEAR-2, we followed noise contribution calculated for the POLARBEAR-1 [15, 60]. There were contributions from bolometer noise and demodulator noise. Bolometer noise includs contributions from SQUID noise, noise on SQUID controller board and Johnson noise from various resistors used in the readout chain. Demodulator noise included amplifier noise and digitation noise. Expected readout noise referred to input coil of a SQUID was $7\frac{\mathrm{pA}}{\sqrt{\mathrm{Hz}}}$. The POLARBEAR-1 measured $9\frac{\mathrm{pA}}{\sqrt{\mathrm{Hz}}}$. For the POLARBEAR-2 calculations, we used $\mathrm{NEI}_{\mathrm{read}} = 7\frac{\mathrm{pA}}{\sqrt{\mathrm{Hz}}}$.

4.6 Readout Parameters

Since we decided $P_{sat} = 2.5P_{opt}$, $P_{elec} = 1.5P_{opt}$. We can convert $\mathrm{NEI}_{\mathrm{read}}$ to $\mathrm{NEP}_{\mathrm{read}}$ with responsivity at high loop gain $\frac{1}{V_{elec}}$, such that $\mathrm{NEP}_{\mathrm{read}} = V_{elec}\mathrm{NEI}_{\mathrm{read}}$. Suppose we want to keep total noise increase due to readout noise contribution to be less than 10%

$$\mathrm{NEP}_{\mathrm{read}}^{\mathrm{max}} = \sqrt{((1.1)^2 - 1)(\mathrm{NEP}_\gamma^2 + \mathrm{NEP}_g^2)} \tag{4.38}$$

This constraints maximum V_{elec}^{max}.

$$V_{elec}^{\mathrm{max}} = \mathrm{NEP}_{\mathrm{read}}^{\mathrm{max}}/\mathrm{NEI}_{\mathrm{read}} \tag{4.39}$$

Since $P_{elec} = \frac{V_{elec}^2}{R_{TES}}$ we can calculate R_{TES}^{max}

$$R_{TES}^{\mathrm{max}} = \frac{V_{elec}^2}{P_{elec}} \tag{4.40}$$

From the point view of minimizing the non-ideal effect from parasitic resistance, we want to maximize $R_{TES}^{\max}$. Typical fluctuation in R_{TES} across wafer is $\pm 15\%$ that predominantly arises from different etch rate of aluminium during wet-etch process. We can then set $R_{TES} = R_{TES}^{\max}/1.15$ and $R_{TES}^{\min} = R_{TES} \times 0.85$. One component of such a stray resistance is the dielectric loss in a capacitor used to make LCR circuit. We developed super conducting interdigitated capacitor on high resistivity silicon to minimize ohmic loss and dielectric loss at capacitor. Discussion of interdigitated capacitor is given in Section 5.13. We can describe such loss as an equivalent series resistance (ESR). The ESR is related to $\tan(\delta)$ of material and inductance of LCR circuit by

$$R_{ESR} = 2\pi f L \tan(\delta) \tag{4.41}$$

We used single crystal float-zone silicon with 10 K $\Omega-$cm resistivity. $\tan(\delta)$ for similar silicon was $\tan(\delta) = 2\times 10^{-4}$ at 10 Kelvin (6.8 GHz) [65]. To keep a stable read-out, we want to minimize R_{ESR}. We set a requirement that R_{ESR} should be less than 20% of R_{TES}^{min}. Next we decided on the frequency range of the read-out. We do not want to use very high frequency as this will make the stray inductance requirement more stringent. The benefit of having high frequency is that read-out would use smaller fractional bandwidth and we can use smaller interdigitated capacitors and inductors. Smaller capacitor and inductor would facilitate fabricating effort. We first calculate the largest capacitor that we can fabricate. Then we decided on f_{min}. We can then calculate f_{max} from mux factor and Δf that would satisfy cross-talk requirement. Once we decide on f^{max} we can chose to calculate the maximum allowable L^{max} by

$$L^{max} = \frac{0.2 R_{TES}^{min}}{2\pi f^{max} \tan(\delta)} \tag{4.42}$$

L^{max} will be different for two different frequency bands. For an experiment, it is advantageous to use same inductor value to facilitate fabrication effort. Smaller L value between two frequency bands should be used to clear ESR requirement. Frequency spacing Δf should be set to meet cross-talk requirement. Cross-talk (CT) between channels is

$$\mathrm{CT} = \left(\frac{R_{TES}^{max} + R_{ESR}}{4\pi \Delta f L^{max}} \right)^2 \tag{4.43}$$

We set cross-talk requirement by requiring that only acceptable level of the CMB tempeature anisotropy signal to leak into B-mode polarization spectrum. Such effect get reduced further by sky rotation. We set readout cross-talk requirement to 1%. We find Δf by

$$\Delta f > \frac{R_{TES}^{max} + R_{ESR}}{0.4\pi \Delta f L^{max}} \tag{4.44}$$

chosing The bigger R_{TES} between two frequency bands should be used for the calculation. We then vary frequency spacing with expected accuracy of inductors and capacitor components. Measurement of how accurate we can fabricate inductors and capacitors are on going. We assumed we can fabricate reactive components to 0.5% fractional accuracy. Since many component variables depend on each other, these steps were iterated few times until Δf and L converged.

Time Constants

Time constant τ of bolometer is tuned by changing heat capacity of bolometer island C. There are two bounding requirements for the time constant. If τ is too large, telescope needs to be scanned at a slower speed, thus large angular scale data will be affacted by $\frac{1}{f}$ noise. If τ is too short, the detector bandwidth exceeds the readout bandwidth and the detector becomes unstable. We will discuss two bounding requirements, and we will show our design allow bolometer to operate between two bounding requirements.

Scan Speed

To set an upper limit on τ, we considered telescope scan speed and beam size. The HTT is designed to scan in azimuth direction at 4 degrees per second. The lowest elevation the POLARBEAR-2 is planning to observe is 30 degrees. Thus the fastest scan speed on sky would be 4 [deg/sec] $\times$ $\cos(30^\circ) = 3.47$ [deg/sec]. Beam size for a pixel diameter can be calculated with the Fraunhofer's diffraction relation [21].

$$\psi(\theta) = \int_0^R \int_0^{2\pi} \psi_a(r) e^{-ik\sin(\theta)\cos(\phi)} r dr d\phi \tag{4.45}$$

Where $\psi_a(r)$ is electric field on aperture, and R is outer radius of an aperture. Suppose we calculate this on primary mirror of the HTT. We assumed beam get truncated hard at $R = 1.25$ meters. We assume a truncated Gaussian beam is formed on primary mirror from detector (time reverse sense)

$$\begin{aligned} \psi_a(r) &= e^{-\left(\frac{r}{2F/\#R\tan(\lambda/\pi w)}\right)^2} , r \leq R \\ \psi_a(r) &= 0 , r > R \end{aligned} \tag{4.46}$$

Calculated value for 95 GHz and 150 GHz beam is plotted in Figure 4.11. It is necessary to sample sky faster than Nyquest frequency. Suppose the safety factor is 4, we need to take data at

$$\tau_{beam} = \frac{1}{4[\text{deg/sec}]} \frac{\theta_{FWHM}}{2 \times 4} \tag{4.47}$$

Readout Time Constants Requirement

The lower end of time constant constraint comes from a readout requirement. We first write down the thermal differential equation and electrical differential equation of a voltage biased TES bolometer [57],

$$\begin{aligned} C\frac{dT}{dt} + G(T_c - T_b) &= P_{opt} + P_{elec} \\ V &= L\frac{dI}{dt} + IR_L + IR_{TES} \end{aligned} \tag{4.48}$$

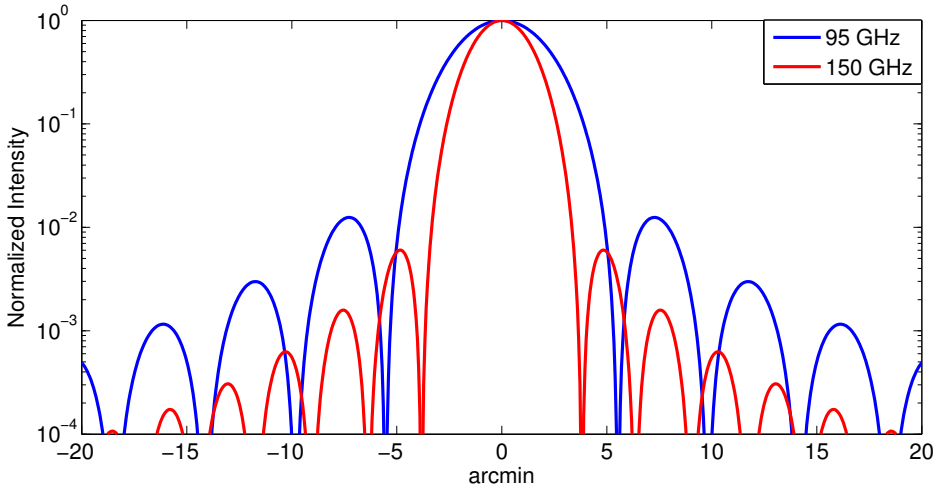

Figure 4.11: Normalized beam calculated from truncated gaussian at radius of 1.25 m. F/# = 1.9, $D = 6.789$ mm and waist to pixel diameter ratio of $D/w_0 = 2.95$ were assumed

Where R_L is a sum of shunt resistor that is providing voltage bias to R_p, L and R_{TES} in series. R_p is a parasitic resistance in series with resistor, and L is an inductance that is also in series with R_{TES}. We analyze what happens when small change in optical power and bolometer island temperature occurs. We obtain two coupled time varying part of differential equations,

$$\frac{d\delta I}{dt} = -\frac{R_L + R_{TES}(1+\beta)}{L}\delta I - \frac{\mathscr{L} g}{I_0 L}\delta T + \frac{\delta V}{L} \tag{4.49}$$

$$\frac{d\delta T}{dt} = \frac{I_0 R_{TES}(2+\beta)}{C}\delta I - \frac{(1-\mathscr{L})}{\tau}\delta T + \frac{\delta P}{C} \tag{4.50}$$

Where I_0 is steady state current through R_{TES}. We included current sensitivity of a TES bolometer $\beta = \frac{I_0}{R_{TES}}\frac{\partial R}{\partial I}$. These two equations can be combined in a matrix form

$$\frac{d}{dt}\begin{pmatrix}\delta I \\ \delta T\end{pmatrix} = -\begin{pmatrix}\frac{1}{\tau_{elec}} & \frac{\mathscr{L} g}{I_0 L} \\ -\frac{I_0 R_{TES}(2+\beta)}{C} & \frac{1}{\tau_I}\end{pmatrix}\begin{pmatrix}\delta I \\ \delta T\end{pmatrix} + \begin{pmatrix}\frac{\delta V}{L} \\ \frac{\delta P}{C}\end{pmatrix} \tag{4.51}$$

The homogeneous part of this equation is a differential equation for an exponential solution. The solution thus has a form

$$\begin{pmatrix}\delta I \\ \delta T\end{pmatrix} = A_+ e^{-\frac{t}{\tau_+}}\vec{v}_+ + A_+ e^{-\frac{t}{\tau_-}}\vec{v}_- \tag{4.52}$$

Where $A_\pm$ is constants, $\tau_\pm$ is a inverse of eigenvalues and $\vec{v}_\pm$ are eigen vectors of 2×2 matrix. We can explicitly write τ_{pm} as

$$\tau_{pm} = \left[\frac{1}{2\tau_{elec}} + \frac{1}{2\tau_I} \pm \frac{1}{2}\sqrt{\left(\frac{1}{\tau_{elec}} - \frac{1}{\tau_I}\right)^2 - 4\frac{R_{TES}}{L}\frac{\mathscr{L}(2+\beta)}{\tau}}\right]^{-1} \tag{4.53}$$

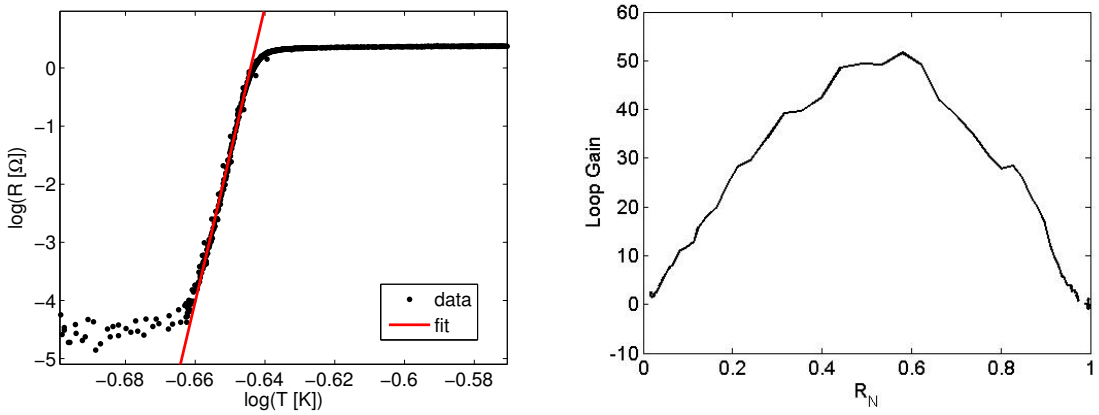

Figure 4.12: (left) T_c measurement of AlTi bilayer sample with linear fit to transition part of the curve. Courtesy of Ben Westbrook. (right) Calculated loop gain for R_{TES}/R_N with α measured from T_c curve.

This system does not exponentially run off if real part of τ_- is greater than zero $\mathrm{Re}[\tau_-] > 0$. We also want to under-damped oscillations in TES responce. In a high loop gain limit with current seisitivity set to zero ($\mathscr{L} \gg 1$ and $\beta = 0$) criteria simplifies to

$$\frac{1}{\tau_{read}} > 5.8\frac{1}{\tau} \tag{4.54}$$

τ_{read} of LCR readout circuit is

$$\tau_{read} = \frac{L^{max}}{R_{min}} \tag{4.55}$$

Loop Gain, Fundamental Time Constant

Fundamental time constant for bolometer and operation bolometer is related by $1+\mathscr{L}\ \tau 0 = (1+\mathscr{L})\tau$. Fundamental time constant τ_0 needs to be designed such that it satisfies two bounding time constant requirements.

$$\tau_{beam} > \frac{\tau_0}{(1+\mathscr{L})} > 5.8\tau_{read} \tag{4.56}$$

Loop gain is given by $\mathscr{L} = \frac{P_{elec}\alpha}{gT_c}$. For aluminum-titanium (AlTi) bilayer TES, we measured α from T_c measurements. We calculated $\mathscr{L}$ using the measured value as shown in Figure 4.12. Suppose we bias between loop gain of 5 and 35, we want to pick C such that τ meets bounding requirements.

$$C = \tau_0 g \tag{4.57}$$

Finally we can read off from Figure 4.12 what fraction of normal state resistance we need to bias TES. Suppose we bias at middle point of loop gain, then I need to multiply R_{TES} by 0.8 to calculate the normal state resistance R_0.

4.7 Total NEP, conversion to NET and Mapping Speed

A noise equivalent temperature (NET) is temperature of signal that will give a signal-to-noise ratio of 1 for 1 second of integration time (0.5 Hz audio bandwidth).

$$\mathrm{NET} = \frac{\mathrm{NEP}}{\sqrt{2}\frac{dP}{dT}} \tag{4.58}$$

Where factor of $\sqrt{2}$ is due to integration time difference (0.5 second and 1 second) between NEP and NET definition. $\frac{dP}{dT}$ is a conversion from power to temperature.

$$\frac{dP}{dT} = \frac{h^2}{k_B}\int \eta n^2 \nu^2 T^2 e^{\frac{h\nu}{k_B T}} d\nu \tag{4.59}$$

So far, we have calculated the NET for a single polarization. Since single pixel has two polarization states per frequency band,

$$\mathrm{NET}_{\mathrm{pixel}} = \frac{1}{\sqrt{2}}\mathrm{NET} \tag{4.60}$$

We then define the mapping speed as

$$\mathrm{MS} = \frac{\mathrm{N}_{\mathrm{pixel}}}{\mathrm{NET}_{\mathrm{pixel}^2}} \tag{4.61}$$

4.8 Bandpass Filter Optimization

After all the machinery for calculating mapping speed is laid down, we can calculate for the optimal bandpass center frequency and fractional bandwidth. A sweep of various center frequency and fractional bandwidth were made. We assumed pixel size $D = 6.789$ mm. Parameters such as optical loading, bolometer parameter and total NET were re-optimized for each condition. Mapping speed for various center frequency and fractional bandwidth were plotted as shown in Figure 4.13. Wider bandwidth gives more signal, but band will be more likely to hit atmospheric lines. From measurements of prototype pixels, we know that we can obtain the fractional bandwidth that is consistent with design as shown in Figure 6.15. It is more difficult to achieve accurate center frequency due to changes in kinetic inductance of Nb. We allowed ourself 10% margin in center frequency error. We picked 94.3 GHz and 147.8 GHz as our center frequency with fractional bandwidth of 30.6% and 26.0% respectively.

4.9 Pixel Size Optimization

Once bandpass locations are set, we can run mapping speed calculation while sweeping pixel size as shown in Figure 4.14. Historically, result is often plotted as function of $\mathrm{F}/\#\lambda$. For a multichroic detector, it is more straightforward to plot mapping speed as a function of physical pixel size as different frequency bands shares same pixel size.

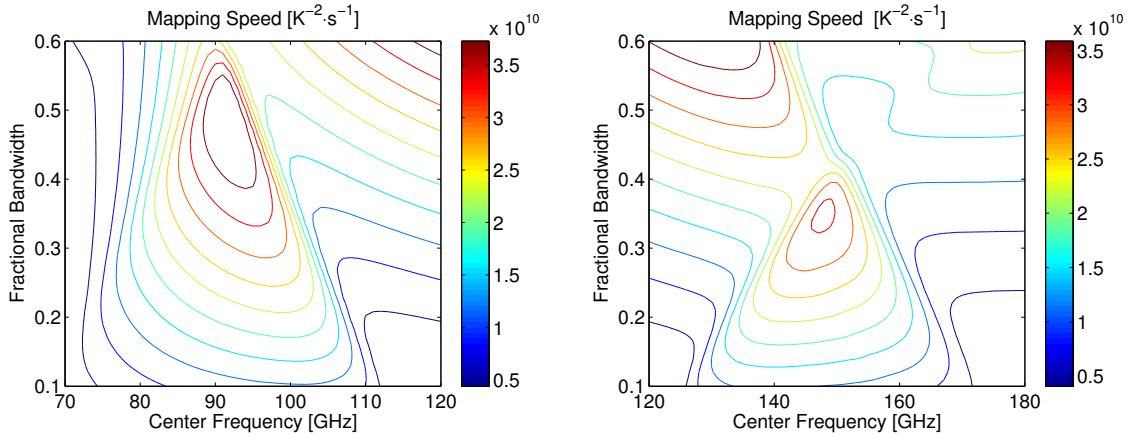

Figure 4.13: Mapping speeds were calculated for various center frequency and fractional bandwidth. For parameters that does not change as function of center frequency and fractional bandwidth (ex. pixel size) nominal values were used.

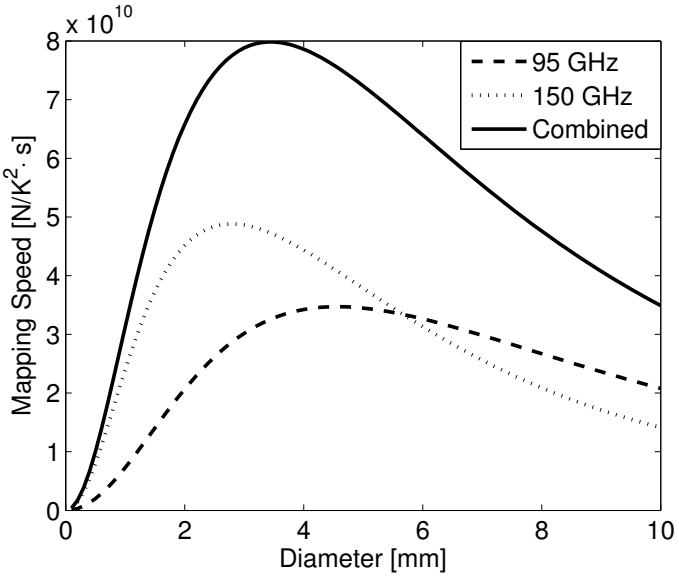

Figure 4.14: Mapping speed as function of pixel diameter.

4.10 Other Constraints

Pixel size optimization calculation only maximized the mapping speed. For the actual experiment, there were various constraints that forces us to pick a non-optimal pixel size. However, even if that was the case, pixel optimization study was important as it became a tool to calculate sensitivity of various contributions to the mapping speed. In this section we listed the constraints that we considered.

Readout Capacity

The POLARBEAR-2 read-out thousands of detectors with SQUIDs. We use frequency multiplexed SQUID read-out method that read-out multiple bolometers with a single SQUID [31, 42]. Multiple bolometer signals are summed at milli-Kelvin temperature. Thus number of wire from milli-Kelvin stage get reduced by multiplexing factor. This helps to reduce thermal loading to a focal plane through readout wires. Also multiplexing reduces number of SQUIDs and electronic parts for the experiment.

For the POLARBEAR-2, we are planning to use three wiring harnesses. Each wiring harness can hold ten SQUID mounting printed circuit boards (PCBs). Each SQUID mounting PCBs hold eight SQUIDs. Thus POLARBEAR-2 will use 240 SQUIDs. At the time of writing, the base line is to use 36 multiplexing factor. Thus the POLARBEAR-2 will have capability to read 8640 bolometers. Each pixel has four optical bolometers, thus it could technically readout 2160 pixels. Figure 4.2 shows pixel size to number of pixel ratio for 365 mm diameter focal plane. It shows pixel cannot be smaller than 6.5 mm. In reality we want to readout some dark bolometers and calibration resistors, thus effective number of channels available for optical bolometers get reduced slightly.

Lens Size to Wavelength Ratio, Sensitivity to Extension Length

Mapping speed calculation favors smaller pixels. However, as pixels gets smaller and smaller we need to start to consider a lens size to wavelength ratio. Silicon lens loses focusing power for lenslet radius smaller than $= 1\lambda_0$ [58]. Where λ_0 is a wavelength of a light in vacuum. Lower bound on 95 GHz frequency band is 80 GHz. This corresponds to a radius of 3.75 mm. The POLARBEAR-2 uses lenslette with radius of 2.673 mm. If we include the AR coating, total radius increases to becomes 3.43 mm. This corresponds to 91.5% of λ_0 at 80 GHz. Kasilingam also calculated radius can be smaller for lower dielectric constant material. Thus size of the lenslet the POLARBEAR-2 uses is close to minimum size that should be used for 95 GHz band. Experimentally we found that as lens size get smaller, the beam shape start to become sensitive to its construction and alignment as discussed in Section 6.4. This could be due to resonances of the spherical modes in the lens [59, 91]. We simulated beam shape as function of lens radius in the HFSS. We only studied the case where lenslette was aligned to an antenna perfectly. For the limited case that we studied, beam shape did not degrade down to lenslette radius of 2 mm.

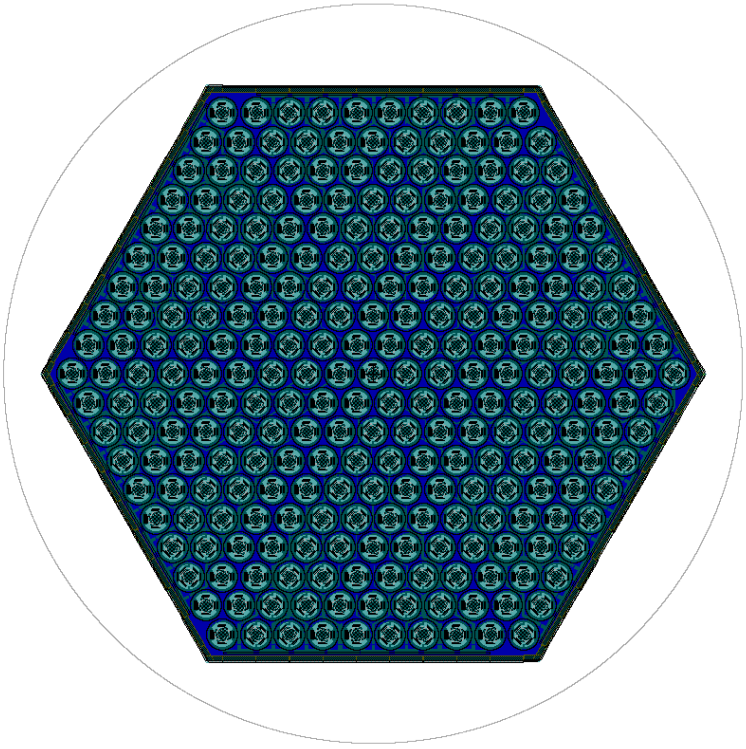

Figure 4.15: CAD drawing of detector array with circle representing 150 mm diameter wafer.

Wafer Size and Compatibility to POLARBEAR-1 hardware

Since we are fabricating on a 150 mm diameter silicon wafer, we need to consider if desired pixel size nicely fills available space on a wafer. To study this, we simply filled 150 mm diameter wafer with various pixel size in close-packed hexagonal geometry. Detector array's size changes discretely for a given pixel size as modifying number of rows in hexagonal detector array requires adding and subtraction of each *ring* of hexagon. We iterated a few times until we make sure that wafer is used maximally as shown in Figure 4.15.

Another thing we considered was compatibility with spare POLARBEAR-1 parts. Since many constraints were pushing our design close to POLARBEAR-1's pixel-to-pixel spacing, we decided to use same pixel spacing as the POLARBEAR-1. We calculated the lens size that would have same pixel spacing with thicker AR coating. This allowed us to use spare parts from POLARBEAR-1 to quickly test prototype wafers as shown in Figure 4.16.

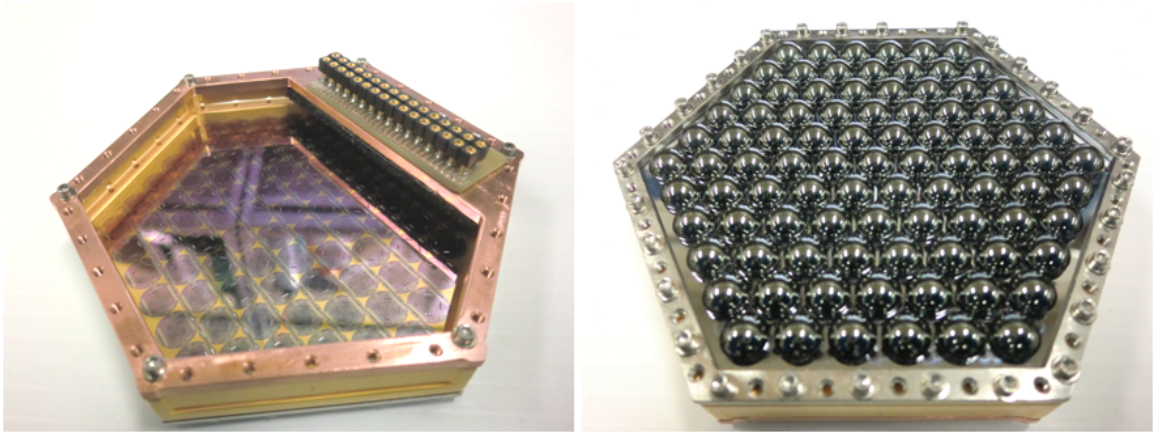

Figure 4.16: (left) Photograph of sinuous array in POLARBEAR-1 spare invar holder. (right) POLARBEAR-1 spare lenslet array was used for testing

4.11 Sensitivity

We decided the POLARBEAR-2 would have a pixel to pixel spacing of 6.789 mm. 271 pixels fills 150mm wafer. This summed up to 7,588 optically active bolometers. Our read-out has capability to read 8640 bolometers, so it also worked well with upper limit of readout capability. Extra channels allowed us to wire up bolometers that are not connected to antenna, dark bolometers, to be readout as a check against direct stimulation on bolometers. Also a pixel spacing that is same as the POLARBEAR-1 allowed some initial tests by using POLARBEAR-1 spare parts.

Sensitivity

We can translate this to a sensitivity to the CMB B-mode

$$\Delta C_l^{BB} = \sqrt{\frac{2}{(2l+1)f_{sky}}}\left[C_l^{BB} + w_P^{-1}W_l^{-1}\right] \tag{4.62}$$

Where f_{sky} is fraction of full-sky the POLARBEAR-2 planning to observe. Weight factor w_P^{-1} is given by

$$w_P^{-1} = \frac{4\pi f_{sky}}{t}\frac{1}{\mathrm{MS}} \tag{4.63}$$

and assuming Gaussian illumination on primary mirror, window function W_l^{-1} is

$$W_l^{-1} = e^{l(l+1)\sigma^2} \tag{4.64}$$

Where σ is spread in Gaussian beam profile $\frac{1}{2\pi\sigma^2}e^{-\theta^2/2\sigma^2}$ [129]. For time t, we multiplied planned observation of 3 years with conservative estimate of efficiencies. Observation efficiency is summarized in Table 4.6

	95 GHz	**150 GHz**
F/#	1.9	
Lenslette size	5.346 mm	
AR coating	0.72 mm	
LR Ratio	0.46	
f_{center}	94.3 GHz	147.8 GHz
f_{BW}	30.6 %	26.0 %
Optical efficiency	22.5 %	31.8 %
P_{opt}	2.9 pW	4.9 pW
P_{sat}	7.2 pW	12.2 pW
$f_{P_{elec}/P_{opt}}$	1.5	
T_c	428 mK	428 mK
T_b	250 mK	250 mK
G	40.7 pW/K	69.1 pW/K
g	76.4 pW/K	129.6 pW/K
C	0.76 pJ/K	1.30 pJ/K
R_{TES}	0.89	1.13
f_{R_N}	0.6	
R_0	1.48	1.89
α	250	
$\mathscr{L}$	40	
τ	0.25 ms	
τ_0	10 ms	

Table 4.3: Detector parameters

4.12 Summary of PB-2 Focal Plane Parameters

Summary of focal plane parameters for the POLARBEAR-2 experiment are listed on Table 4.5. Detector parameters are listed on Table 4.3. Readout parameters are listed on Table 4.4. Noise estimate and sensitivity prediction for the POLARBEAR-2 experiment is summarized on Table 4.7.

	Value
Number of Harnesses	3
Number of SQUID card per Harness	10
Number of SQUID per SQIOD card	8
Mux factor	36
Frequency range	1.6 - 2.3 MHz
Inductance	60 μH
Capacitance	167pF - 77pF
Frequency Spacing (log)	17.7 - 25.8 KHz
ESR	0.12 Ω - 0.17 Ω
$\tau_{readout}$ (95 GHz)	0.05 ms
$\tau_{readout}$ (150 GHz)	0.05 ms

Table 4.4: Readout parameters

	Value
Number of wafers	7 [wafers]
Focal Plane Diameter	365 [mm]
Wafer size (side-to-side)	119.5 [mm]
Pixel to pixel spacing	6.789 [mm]
Pixel Count	1898 [pixels]
Optical Bolometer	7588 [bolometers]
Dark Bolometer	3794 [bolometers]

Table 4.5: Focal plane parameters

	Efficiency
Weather	0.8
Telescope Maintenance	0.9
CMB Patch	0.5
Scan Efficiency	0.8
Receiver Yield	0.7
Data Selection	0.7
Data Filtering	0.7
Total	0.1

Table 4.6: Lists of observation efficiency. Conservative estimates were given to each entry. Courtesy of Yuji Chinone.

	95 GHz	**150 GHz**
$\mathrm{NET}^{\mathrm{bolo}}_{\mathrm{photon}}$	250 $\mu\mathrm{k}\cdot\sqrt{\mathrm{s}}$	284 $\mu\mathrm{k}\cdot\sqrt{\mathrm{s}}$
$\mathrm{NET}^{\mathrm{bolo}}_{\mathrm{bolo}}$	193 $\mu\mathrm{k}\cdot\sqrt{\mathrm{s}}$	182 $\mu\mathrm{k}\cdot\sqrt{\mathrm{s}}$
$\mathrm{NET}^{\mathrm{bolo}}_{\mathrm{readout}}$	145 $\mu\mathrm{k}\cdot\sqrt{\mathrm{s}}$	154 $\mu\mathrm{k}\cdot\sqrt{\mathrm{s}}$
$\mathrm{NET}^{\mathrm{bolo}}_{\mathrm{total}}$	347 $\mu\mathrm{k}\cdot\sqrt{\mathrm{s}}$	371 $\mu\mathrm{k}\cdot\sqrt{\mathrm{s}}$
$\mathrm{NET}^{\mathrm{pixel}}_{\mathrm{total}}$	246 $\mu\mathrm{k}\cdot\sqrt{\mathrm{s}}$	262 $\mu\mathrm{k}\cdot\sqrt{\mathrm{s}}$
MS	$3.14\times10^{10}\ \mathrm{k}^{-2}\cdot\mathrm{s}^{-1}$	$2.76\times10^{10}\ \mathrm{k}^{-2}\cdot\mathrm{s}^{-1}$
$\mathrm{f}_{\mathrm{sky}}$	0.2	
$\mathrm{Year}_{\mathrm{obs}}$	3	
Sensitivity	10.3 $\mu\mathrm{K}\cdot\mathrm{arcmin}$	

Table 4.7: Summary of POLARBEAR-2 Sensitivity

Chapter 5

Multi-chroic Detector Array Design and Fabrication

5.1 Introduction

Overview of the focal plane design is shown in Figure 2.7. Focal plane is composed of seven detector modules with 7,588 optical bolometers. Each module houses lenslet array, detector wafer and readout components. Lenslet array has two-layer anti-reflection coated lenslets arranged in close-packed hex pattern. Lenslet is a 5.356 mm diameter silicon hemisphere. Each lenslet is placed into pockets that was deep reactive ion etched into silicon, then they are epoxied in place by small drops of stycast 2850FT. Detector wafers were fabricated on 150 mm wafers. Each detector wafer holds 271 dual-polarized diplexed pixels. Lenslet array and detector module is aligned under infrared microscope, and they are clamped together by an invar holder. The invar holder has thermal contraction matched to silicon wafer. It would keep alignment between lesnlet wafer and detector wafer during cryogenic thermal cycling. Readout components sit behind detector wafer. This allows lenslets to maximally fill focal plane area to receive light. Detectors are read-out by 36 frequency multiplexing readout. Superconducting interdigitated capacitor and superconducting inductors fabricated on a high resistivity silicon are used to split signal into frequency combs. In this chapter we will discuss how each components were designed and fabricated. The discussion will follow signal path.

5.2 Lenslet

Lenslet coupling scheme is widely used technique to boost gain of an antenna [104]. We couple signal onto a focal plane through a broadband anti-reflection coated lenslet. For the broadband anti-reflection coating, we used a technique described in Section 3.4. Coupling with a lenslet has several benefits [104]. Obvious reason to use a lenslet is to increase antenna's forward gain to have a better match with the receiver optics's $F/\#$. Hemispheric shape of a lenslet suppresses substrate mode that couples neighboring pixels. Also by having dielectric lens on one side of a

planar antenna helps to increase its forward gain by a factor of approximately $\varepsilon_r^{3/2}$ [27]. For a sinuous antenna, this improves the antenna's forward efficiency from 50% to 95% [33]. A planar antenna on a dielectric lenslet can be thought of as the antenna on an infinite dielecric half-space. This lowers an effective impedance of an antenna by $1/\sqrt{\varepsilon_{eff}}$, where effective dielectric constant of a dielectric half-space ε_{eff} is given by

$$\eta_{eff} = \frac{\eta_0}{\sqrt{\frac{\varepsilon_r+1}{2}}} \tag{5.1}$$

Where η_0 is the antenna's impedance in a vacuum. Lower impedance allows microstrip line to couple to the antenna efficiently while meeting a line width requirement from fabrication.

It is well known that elliptical lenslet focuses parallel ray to a focus on far side. Relationship between index of refraction of lenslet n, a major axis of an ellipse and a minor axis is given by [48]

$$\text{Majoraxis} = \frac{\text{Minoraxis}}{\sqrt{1-\frac{1}{n^2}}} \tag{5.2}$$

True elliptical lenslet is expensive to fabricate. We approximated the elliptical lenslet with a hemisphere and an extension to form a synthesized elliptical lenslet as shown in Figure 5.1[35]. We optimized the extension length to maximize integrated directivity by using the HFSS in Section 4.3. Simulated model included sinuous antenna, silicon lenslet, silicon extension and two-layer AR coating.

High dielectric material is advantageous to gain benefits from lenslet outlined at beginning of this section. Single crystal silicon has high dielectric constant $\varepsilon_r = 11.7$ and low loss [102]. We also fabricate the detector array on a silicon wafer. Using silicon lenslet allows antenna beam to propagate without reflection from interfaces with different dielectric constants. Another good candidate for lenslet material was alumina with dielectric constant of $\varepsilon_r = 9.6$. Alumina has an advantage that it is mechanically stronger against mechanical stress induced by thermal contraction of multilayer anti-reflection coating. However, we picked silicon lens to have homogeneous dielectric material.

5.3 Pixel Overview

Detector array is composed of tiles of hexagonal pixels. Layout of each pixel is shown in Figure 5.2. Circular part in middle is reserved for main detector components. Outside of circle is reserved for read-out traces. Circular design has an advantage that when constructing Q and U pixel, structures can be rotated without modifying layout. This would minimize systematic error that could arise from changing wire layout. Connection between inner part of pixel and read-out traces has three-fold rotational symmetry that allows consistent wiring layout for all six side of wafer. We decided to make layout as symmetric as possible. Sinuous antenna is at the center of the pixel. Wire snakes out on its arm. Just outside of sinuous antenna, diplexer filter splits signal into

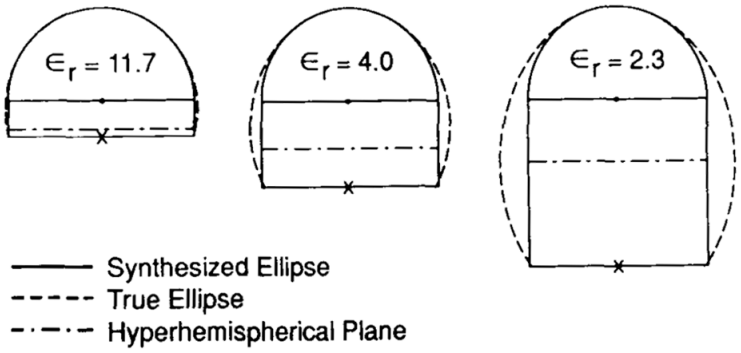

Figure 5.1: Extension length as a function of dielectric constant of lens [35].

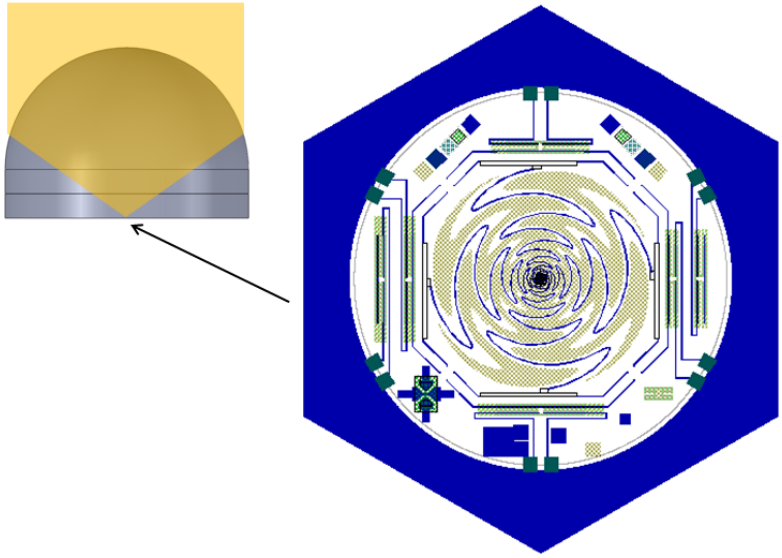

Figure 5.2: CAD of a pixel. Sinuous antenna is at the center of the pixel. Four diplexer filters surround the sinuous antenna. Four optical bolometers surrounds the filters. Dark bolometers and test structures surrounds optical bolometers. Twelve pads at the edge of circle connects wiring inside of pixel to on-wafer wiring.

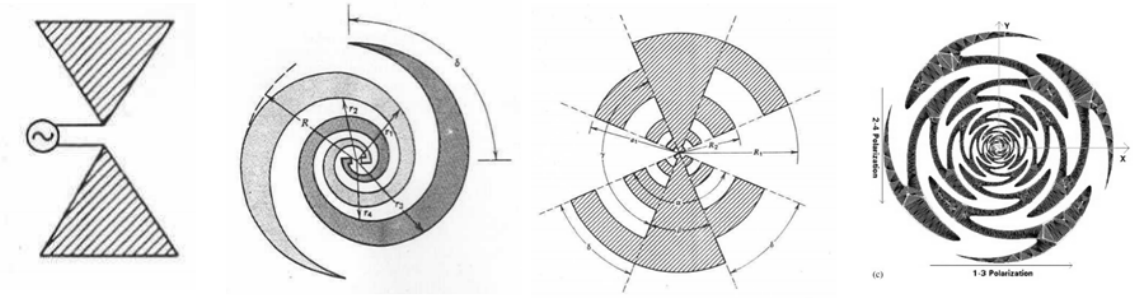

Figure 5.3: Samples of broadband log-periodic planar antennas. From left: bow-tie antenna, log-spiral antenna, log-periodic antenna and sinuous antenna.

two frequency bands. Two transmission lines cross over before optical power is detected at four optical bolometers that surrounds the antenna. Bolometer that is not connected to antenna (dark bolometer) and fabrication test structures surrounds optical bolometers.

5.4 Sinuous Antenna

Sinuous Antenna

Multichroic detector design is a extension of successful single frequency design [88, 13]. Microstrip filter defines the final bandwidth of the detector, but the maximum bandwidth of single frequency detector was limited by bandwidth of a double slot antenna. O'Brient *et al.* experimented with various kinds of broadband antenna. We found that sinuous antenna met many criteria to replace the double slot antenna to increase bandwidth of a pixel. We also changed single frequency band-pass filter to multiplexing bandpass filter. We successfully partitioned broadband signal into two, three and seven bands [93, 94]. In this thesis various improvements to the design were made such that detector can be used for the CMB observation. Also this is the first multichroic array that was fabricated on 150 mm wafer at Berkeley. Changes were made on fabrication steps to make successful detector arrays.

Since we fabricate detector using a planar lithography technique, we looked for a broadband planar antenna. Some common broadband planar antennas are shown in Figure 5.3. Bow-tie antenna did not have beam shape that met our criteria. Spiral antenna is sensitive to circular polarization. Log-periodic tooth antenna had high cross-pol and high polarization wobble amplitude. Sinuous antenna stood out as a broadband antenna with many desireble properties. Sinuous antenna has sensitivities to two linear polarization, stable input impedance, good beam shape and small polarization axis rotation (polarization wobble) amplitude.

Sinuous antenna is a type of broadband log-periodic antenna patented by DuHamel in 1987 [32]. Sinuous antenna can be arranged to have N-fold symmetric structure. For linear and circular

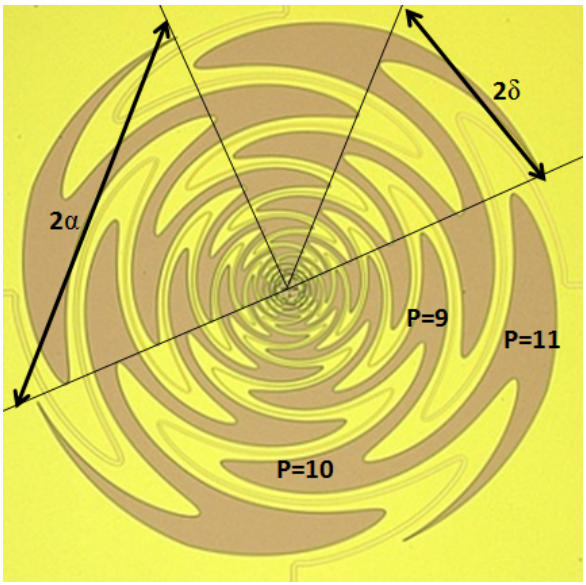

Figure 5.4: Photograph of a sinuous antenna. This sinuous antenna has 11-cell, $\alpha = 45^\circ$, $\delta = 22.5^\circ$, $\tau = 1.3$ and $R_1 = 24$ μm.

polarization application, $N = 4$ terminal is typically used. Equation that describes sinusoidal curve of a sinuous antenna in polar coordinate is [32]

$$\phi(r) = (-1)^p \alpha_p \sin\left[\pi \frac{\ln(r/R_p)}{\ln \tau_p}\right] \pm \delta_p \tag{5.3}$$

Where p is a cell number in integer value $(p = 1, 2, 3 \cdots)$, α_p is angular amplitude of sinusoidal curve, R_p is inner radius of p^{th} cell, $\tau_p \geq 1$ is a logarithmic expansion factor, and δ_p is angular width of each arm. A cell is a half-wavelength switchback of sinusoidal arm. Inner radius of sinuous antenna expands as $R_{p+1} = \tau R_p$. Figure 5.4 shows 11-cell sinuous antenna with $\tau = 1.3$, $\alpha = 45^\circ$ $\delta = 22.5^\circ$ and $R_1 = 24$ μm.

We studied antenna's fundamental property such as input impedance, beam shape and polarization axis orientation with the HFSS. We simulated a model with 16-cell slot sinuous antenna with $\tau = 1.3$, $\alpha = 45^\circ$ $\delta = 22.5^\circ$ and $R_1 = 24$ μm curved into perfect conductor. Lenslet is 5.346 mm diameter silicon ($\varepsilon_r = 11.7$) hemisphere with extension length of 1.069 mm of silicon extension. Two-layer anti-reflection coatings are two layers of quarter-wave (at 120 GHz) thick dielectric with dielectric constant of $\varepsilon_r = 5$ for an inner layer and $\varepsilon_r = 2$ for an outer layer. Figure 4.5 shows the simulated model. The model was simulated in frequency domain from 70 GHz to 170 GHz in steps of 5 GHz.

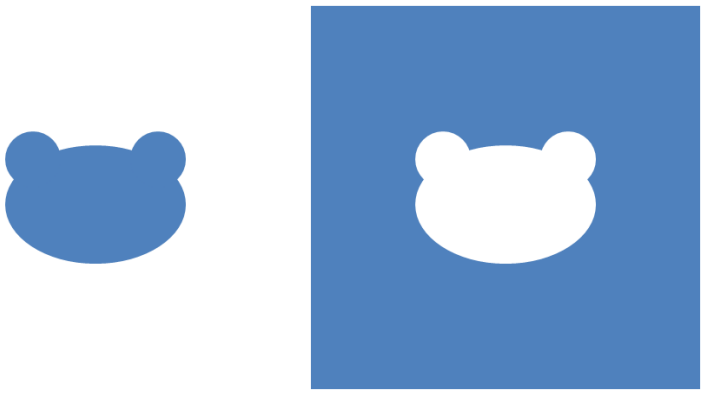

Figure 5.5: Example of complementary structure. Sinuous antenna is *self*-complementary that slot (white) and metal (colored) region has identical shape.

Input Impedance

Sinuous antenna achieves frequency indepent characteristic through self-complementary and log-periodic structure. Babinet principle generalized to electromagnetism gives relationship between two complementary planar structures [16]. Two objects are complementary if one is obtained from the other by removing the object as shown in Figure 5.5. Booker extended this relationship to calculate impedance of two complementary structures with two terminals [20]. He found two impedances Z_1 and Z_2 are related by

$$Z_1 Z_2 = \left(\frac{1}{2}\eta\right)^2 \tag{5.4}$$

Where η is intrinsic impedance of surrounding medium. Suppose two-terminal antenna is *self-complementary*, that is *metal* and *slot* have identical shape, then by symmetry $Z_1 = Z_2 = \frac{\eta}{2}$. Thus self-complementary structure have frequency independent real input impedance. General case for N terminal was studied by Deschamps [29]. Input impedance for free-space impedance for $N = 4$ self-complementary structure is $Z_{0,diff} = 267\Omega$. For our application, antenna is not a perfect self-complementary structure since planar antenna is on silicon-air halfspace. For half-dielectric half-space $Z_{0,diff}$ is corrected by effective dielectric constant of dielectric half-space. For silicon-air half-space, differential input impedance for sinuous antenna is $Z_{diff} = 106\Omega$. Thus it has a driving impedance of $Z_{drive} = 53\Omega$. Input impedance from simulation is shown in Figure 5.6. 3-D EM simulation result agrees with previously published simulated value from 2-D EM simulation result [33]. Deviation from perfectly self-complementary structure causes input impedance to deviate from single value and oscillates with log-period τ. Simulation shows that oscillation is small enough that return loss from input impedance to 106 Ω load is under -10dB in antenna bandwidth.

Often sinuous antenna is excited by a balanced feed that is perpendicular to the antenna [6, 109, 130, 23]. However, because we fabricate detector using planar lithography technique, we needed

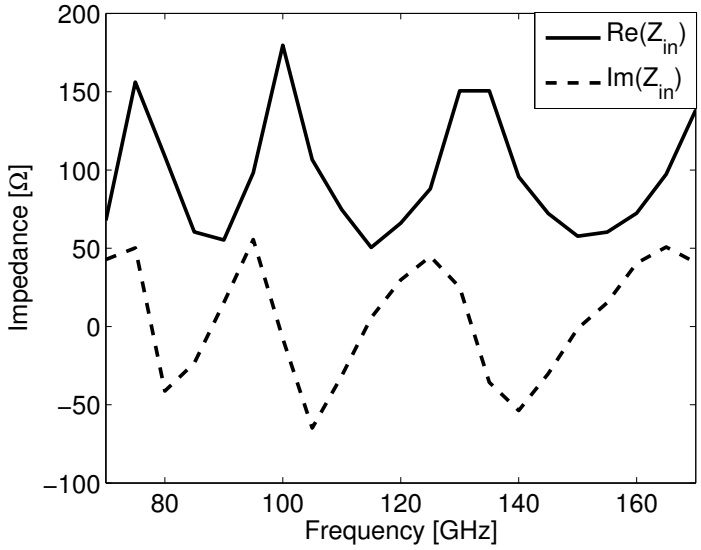

Figure 5.6: Input impedance of antenna from full 3D simulation.

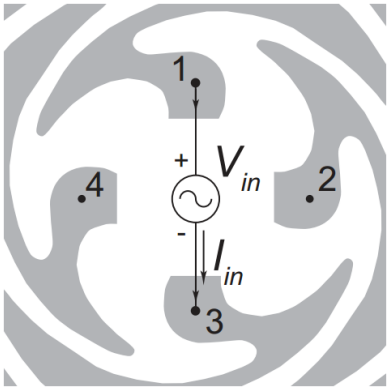

Figure 5.7: Schematic of differential excitation at feed point[33]

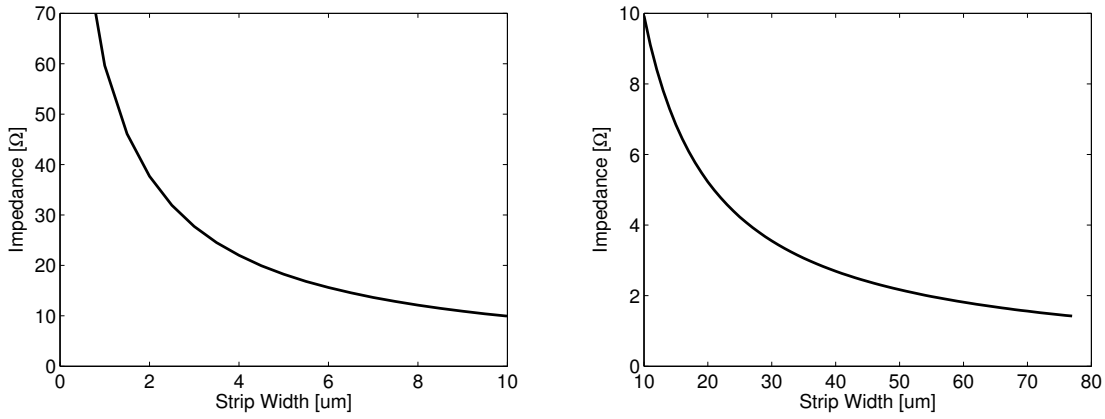

Figure 5.8: Impedance of niobium microstrip line with 0.5 μm thick silicon oxide ($\varepsilon_r = 3.8$) as functoin of strip width.

a way to feed antenna with planar technology. Since we curve out slots in ground plane, there is a continuous ground plane that extends beyond the antenna. Thus we solved the issue by using metallic arms of sinuous antenna as ground planes for microstrip lines. We then covered antenna with a layer of silicon dioxide as insulating layer with a niobium strip on top to form a microstrip line as shown in Figure 5.7.

We designed differentially fed microstripline to have matching impedance to antenna's driving impedance (53Ω). We calculated impedance of microstrip line as a function of strip width with superconducting niobium ground plane, 0.5 um thick silicon dioxide insulator and superconducting niobium strip. We calculated characteristic impedance of microstripline while taking into penetration depth of superconductor into effect following [127, 131]. Characteristic impedance versus strip line width is plotted in Figure 5.8

Mirostrip line needs to be 1.3 μm wide to couple efficiently to antenna. 1.3 μm structure is difficult to make during fabrication as lines become thinner than design during plasma etching. I designed strip at 2.0 μm, and relied on the thinning effect of the plasma etch with small amount of oxygen gas. We can reliably etch line width to be between 1 μm to 2 μm micron. Reflection is small for line width between 1 μm and 2 μm as shown in Figure 5.9.

2.0 μm line is still challenging width for the fabrication. Previously fabricated sinuous detectors [93] used 0.6 μm thick niobium strip to clear step coverage between top niboium layer and 0.5 μm thick silicon oxide layer. Etching 0.6 μm thick metal while maintaining 2.0 μm width was a challenge. To make fabrication more robust, we created a design that removed all vias between strip layer and ground plane layer. Then we reduced the thickness of niobium strip to 0.3 μm. Lower limit on niobium thickness comes from superconducting transmission line's wave speed as a function of metal thickness. Phase velocity is a function of penetration depth [79]. Penetration depth settles to a constant value for a superconducting metal thicker than $\tilde{5}$ times London penetration depth. Niobium's London penetration depth is 39 ± 5 nm [86]. Thus minimum thickness

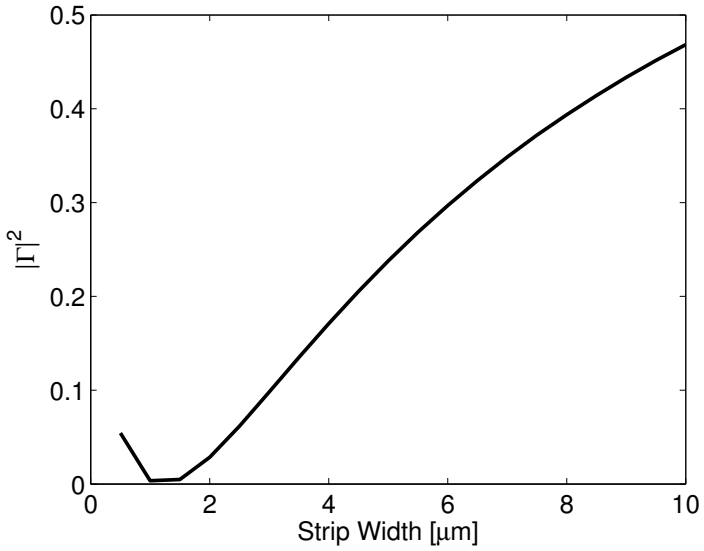

Figure 5.9: Reflection at antenna feed as function of width of strip for niobium microstrip line with 0.5 μm thick silicon oxide ($\varepsilon_r = 3.8$)

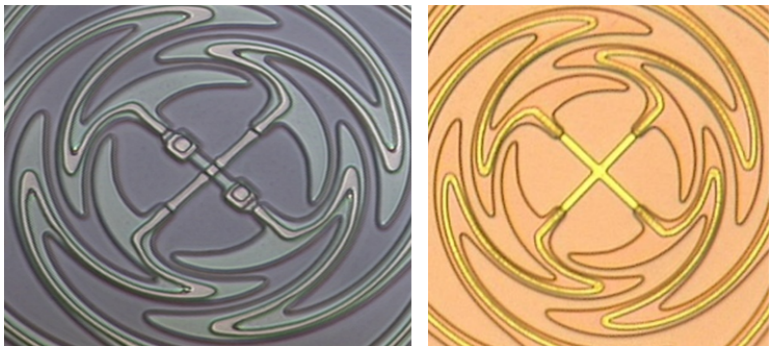

Figure 5.10: Microscope photograph of center of sinuous antenna with cross over (left) and without (right)

would be 0.2 μm, and we kept the strip layer thick enough to give some room for niobium quality variation.

Desired excitation mode of an antenna is an odd-mode excitation where there is a node at center of the antenna as shown in Figure 5.7. We realized that two feeds from orthogonal polarization could be in physical contact while maintaining RF signal isolation. Instead of fabricating complicated crossover structure at center of the antenna we decided to simply cross feed line at the center of antenna as shown in Figure 5.10.

We widen microstrip to 10 μm to route signal with more robust microstrip line. 10 μm line has a characteristic impedance of 10 Ω. Impedance transformation from 53 Ω to 10 Ω must be done correctly to minimize reflection loss. To cover wide range of frequency band, we used tapered line impedance matching method with Chebyshev profile [99]. Transmission line is 9.6 mm long from center of antenna to outside. We performed impedance transformation on antenna arm as shown in Figure 5.7. 95 GHz band and 150 GHz band corresponds to approximately 8λ and 12λ respectively. Expected reflection from impedance transformation over such long transmission line is negligible ($< 1\%$).

Antenna's Free Parameters

Sinuous antenna has six parameters that can be varied: N, α, δ, τ, R_1, and number of cells p_{max}. It is possible to construct sinuous antenna with varying parameter as a function of radius or cell, but we considered constant parameters. We chose $N = 4$ for two linear polarization states, and $\alpha = \frac{360^\circ}{2N} = 45^\circ$ and $\delta = \frac{\alpha}{2} = 22.5^\circ$ for a self-complementary structure.

Expansion Factor τ

One of a feature that makes sinuous antenna frequency independent is its log periodic structure. Log-periodic structure ensures characteristic of antenna repeats every log period defined by τ. Ideally τ should be as close to as 1 as possible. As τ becomes smaller, cross-pol becomes smaller and amplitude polarization wobble becomes smaller as shown in Figure 5.11 [33]. However, as τ get smaller width of antenna arm becomes narrower as well. As shown in Figure 5.7 we form a microstripline using antenna's arm as a ground plane, and ground plane becomes as narrow as strip at the inner most radius with $\tau = 1.3$. We used $\tau = 1.3$ to meet required microstrip line width.

R_1 and number of cells

Sinuous antenna efficienly radiates when length of single cell is odd multiple of half-guided wavelength [32]. Smallest radius that satisfies this condition is

$$R_{rad} = \frac{\lambda_{eff}}{4(\alpha + \delta)} \tag{5.5}$$

Where $\lambda eff = \lambda_0/\sqrt{\varepsilon_{eff}}$. For broadband application it will be important to feed anntena from center such that lowest mode excitation at R_{rad} is picked up. Due to feed line's geometrical constraint, we chose R_1 = 24 μm. We designed R_1 to be as small as possible to be compatible with future 220 GHz band upgrade. 220 GHz band will observe up to approximately 250 GHz, which corresponds to $R_{rad} = 101$ μm. We gave extra room interior of exciting region such that frequency of interest is not sensitive to the termination. At low frequency, we observed that beam shape from the antenna is sensitive to sudden termination of its structure. Initially, we measured beam from a sinuous antenna with $R_1 = 24$ μm and $p_{max} = 11$ which corresponds to $R_{p=11} = 330$ μm. Lowest frequency we will observe with the POLARBEAR-2 is approximately 80 GHz, which corresponds

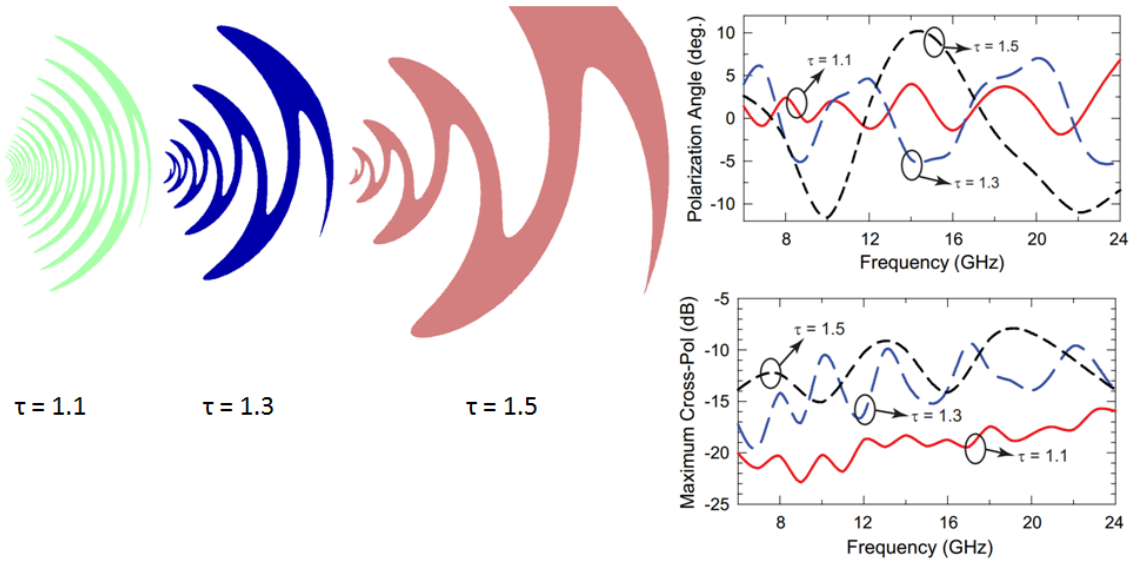

Figure 5.11: (left) Sinuous antenna with three different τ value (right) Simulated polarization wobble angle and maximum cross-pol level for different τ [33].

to $R_{rad} = 316\ \mu$m. As shown in Figure 5.12 we noticed that lower frequency band had elliptic beam while higher frequency band at 150 GHz had circular beam.

We tracked down cause of low frequency beam distortion with HFSS simulation. We simulated structure that we tested except for reducing lenslet diameter in half due to computation time. We noticed that for low frequency beam, antenna's edge had some amount of current density as shown in Figure 5.13. Current at edge of antenna decreased as p_{max} was increased. As p_{max} increased, beam shape and polarization angle behave as expected. We used ellipticity, as a figure of merit. Ellipticity is defined as $\varepsilon = (|\sigma_1 - \sigma_2|)/(\sigma_1 + \sigma_2)$ where $\sigma_{1,2}$ are spread of two dimensional gaussian that was fitted to a beam. Most number of cells we could fit under 6.789 mm pixel with other components such as filters were 17. Thus we studied 11-cell, 17-cell and intermediate 14-cell to see how cell number affacted low frequency performance. Ellipticity and frequency wobble as a function of frequency for three different number of cells are plotted on Figure 5.14. It is important to note that ellipticity rotated more than 45° as function of frequency, and it had no correlation with how polarization axis rotated as a function of frequency. We took this effect into account by averaging beams from 80 GHz to 105 GHz in steps of 2.5 GHz. Averaged beam is plotted in Figure 5.15. When data points were averaged over frequency, 11-cell, 14-cell and 17-cell antenna had 5.05 %, 3.53 % and 1.45 % ellipticity respectively.

To decouple if the problem was due to sinuous antenna alone or antenna-lens coupled system, we simulated just a sinuous antenna in free space. We simulated between 190 GHz and 270 GHz to adjust for the change in effective dielectric constant. As shown in Figure 5.16, slot sinuous antenna in free space had input impedance value that oscillates slightly around 250 Ω, which is

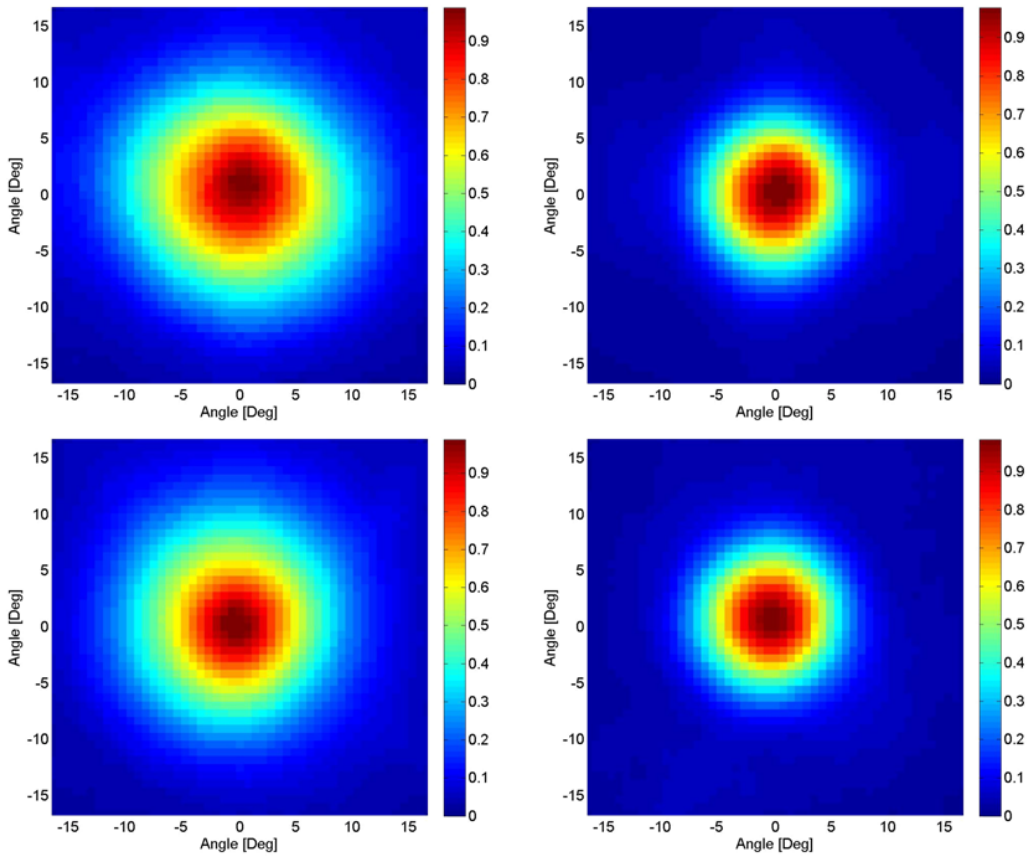

Figure 5.12: Comparison of measured beam shape for 11-cell sinuous antenna (top row) and 16-cell sinuous antenna (bottom row). Left column shows 95 GHz beam and right column shown 150 GHz beam. Ellipticity for 95 GHz and 150 GHz 11-cell beam was 4.0% and 1.0% respectively. Ellipticity for 95 GHz and 150 GHz 17-cell beam was 1.2% and 1.5% respectively.

close to 267 Ω expected from Deschamp's method. As frequency gets lower, impedance for 11-cell antenna start to deviate from the stable value, where as it stays stable for 17-cell antenna. Figure 5.17 compares beam of 11-cell and 17-cell antenna. 17-cell antenna produced expected round main beam in broadside direction. 11-cell antenna produced distorted beam. We concluded that cause of distorted beam is not due to interaction between lens and antenna but due to antenna's size.

We did similar study with simulation where we varied τ. Varying τ did not help dampen left over current. We also terminated extra current at the end of antenna with lossy conductor. Lossy conductor helped to stabilize antenna's input impedance by minimizing reflection of current at the end of antenna. However, it did not improve beam shape. So far, only increasing physical size of antenna had significant effect on antenna's ellipticity at low frequency. We concluded that it

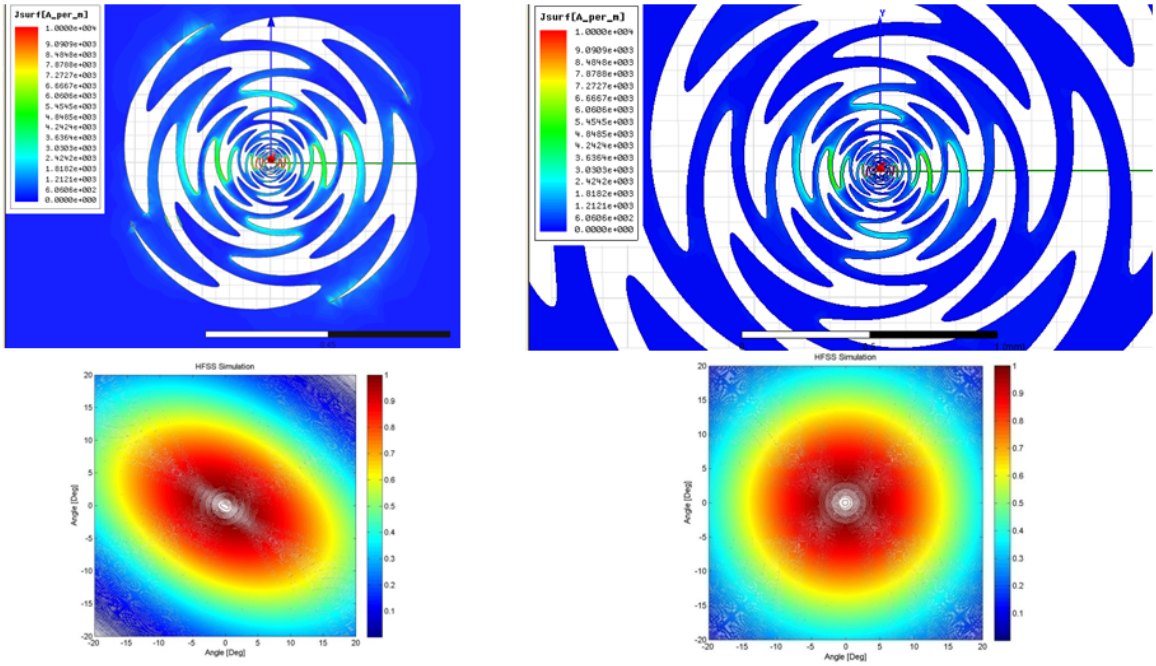

Figure 5.13: 3-D EM simulation result for 80 GHz beam with 11-cell (left) and 17-cell (right) sinuous antenna. Current density is shown on top row. For 11-cell antenna, edge of sinuous antenna shows sign of left over current.

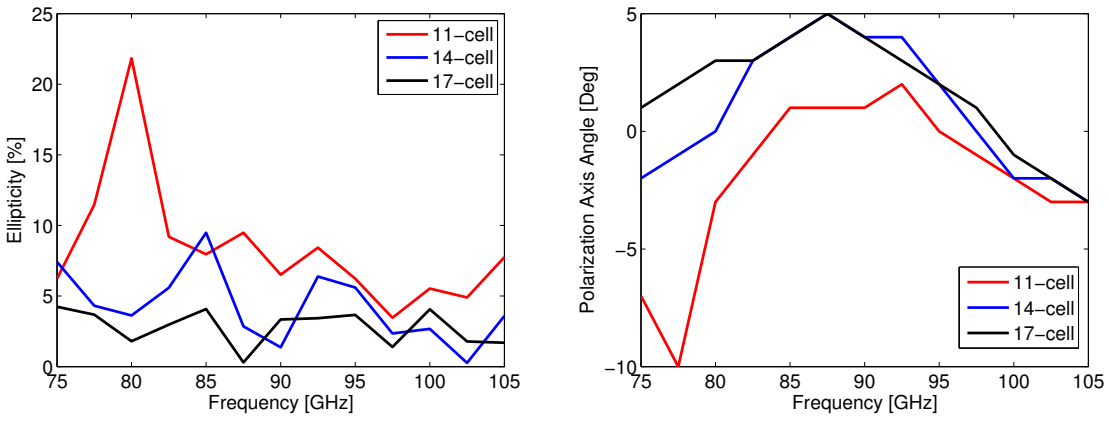

Figure 5.14: (left) Ellipticity as function of frequency and number of cells. (right) Polarization wobble as function of number of cells

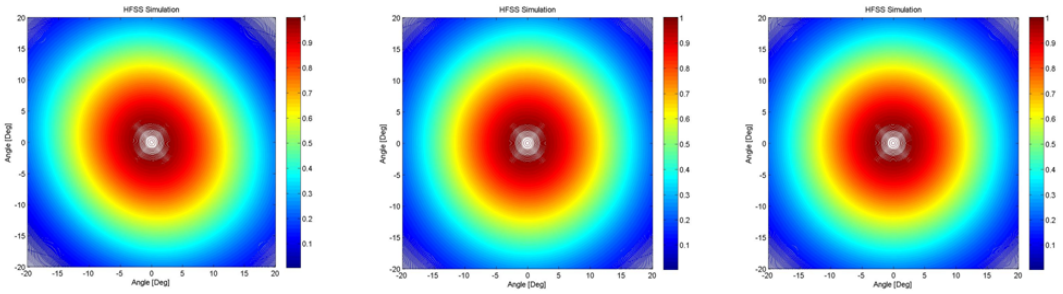

Figure 5.15: Band-averaged beam from 75 GHz to 105 GHz. From left, 11-cell, 14-cell and 17-cell sinuous antenna's beam is shown. Beam had 5.05%, 3.53% and 1.45% ellipticity respectively.

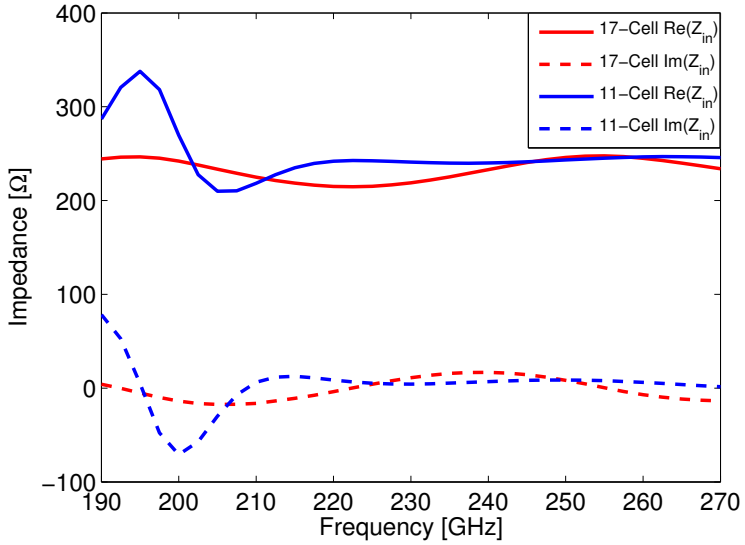

Figure 5.16: Input impedance of sinuous antenna in vacuum as function of frequency. 11-Cell antenna's impedance start to deviate from expected 267 Ω of self-complementary antenna at low frequency.

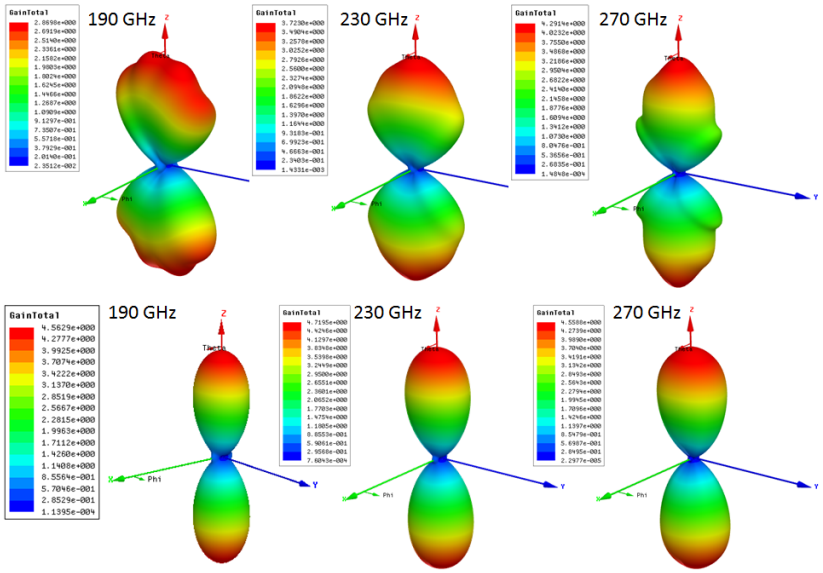

Figure 5.17: 3-D normalized beam of sinuous antenna in vacuum. 11-cell sinuous antenna's beam is shown on top, and 17-cell sinuous antenna's beam is shown on bottom. 11-cell antenna has interesting *fan* like shape at low frequency, where as 17-cell antenna has expected beam shape.

is important to increase antenna's size. In detector array configuration, we decided to use 16-cell design due to pixel size constraint.

Polarization Wobble Cancellation

Log-periodic antenna is known to have a *polarization wobble*, polarization axis that oscillates as function of freqency. Sinuous antenna has a mild wobble amplitude compared to other types of log-periodic antenna. Simulated sinous antenna's wobble is approximately ± 5 degrees for the antenna with $\tau = 1.3$ as shown in Figure 5.18. This agrees with measured value with same $\tau = 1.3$ [33]. Small wobble angle help to reduce cross-polarization leakage. Band-averaged leakage at boresight is 0.4% for 95 GHz band and 0.5% for 150 GHz band. Since there is a wobble as function of frequency, calibration at single frequency will not tell us polarization orientation of the detector. It would be ideal if there was a way to get information about incident light's polarization angle and intensity without knowing anything about how polarization axis wobbles. We propose having two *senses* of sinuous antenna that are inverted respect to one of the axis will solve this issue. Two *senses* of sinuous antennas are shown in Figure5.19. We'll compare detector without polarization wobble and detector with wobble. We will show that having two senses we would be able to cancel polarization wobble, and extract incident light's polarization angle and intensity.

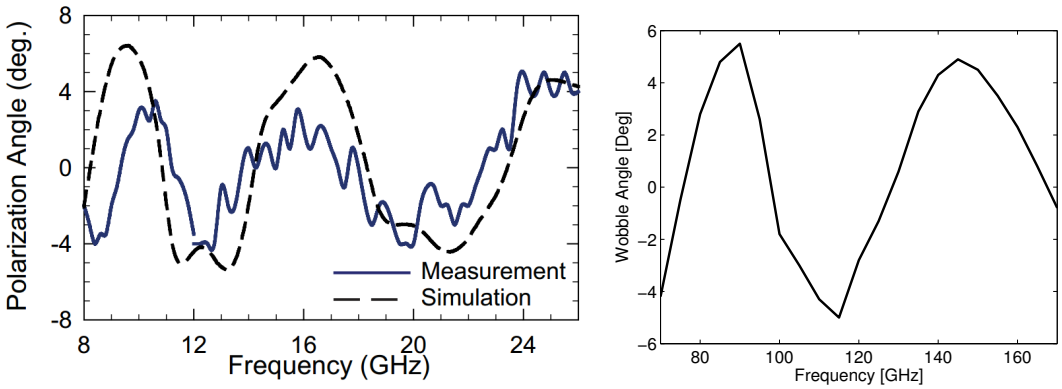

Figure 5.18: (left) Comparison of simulated wobble angle and measurement of the sinuous antenna at 8 GHz to 25 GHz. Discrepancy between simulation and measurement comes from exlusion of 10 mil subtrate layer ($\varepsilon_r = 10.2$) in simulation [33]. (right) 3-D EM simulation result between 70 GHz to 170 GHz.

Figure 5.19: Two different *sense* of the sinuous antenna

Review of Detector without Wobble

We picked double slot dipole antenna as an example of detector without wobble. The antenna's polarization angle is well defined by its gemetry. Two types of pixels are required to obtain two stokes parameter (Q and U) without polarization modulation device such as half-wave plate. As shon in Figure 5.20, Q pixel is defined as a pixel with polarization axes aligned to 0 degree and 90 degree, and U pixel is defined as a pixel with polarization axes aligned to 45 degree and -45 degree. In following discussion, we focused just on polarized portion of the light. Light can have non-polarized component but it would not affect the result so we omitted it in our discussion. Suppose incident light has polarization angle $\theta(\nu)$ respect to the detector with polarized E-field

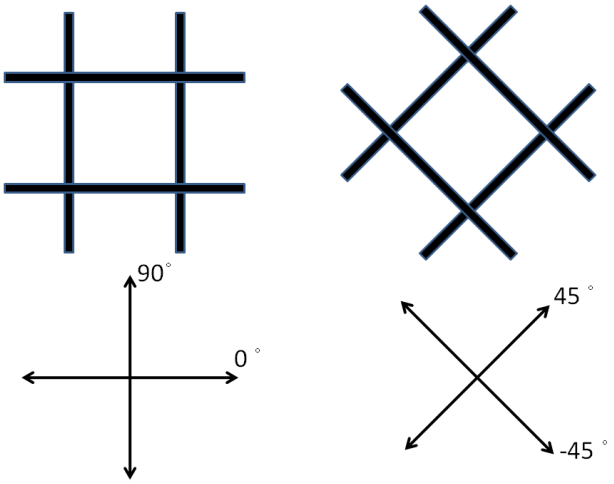

Figure 5.20: (Left) Q pixel of slot dipole antenna (Right) U pixel of slot dipole antenna

amplitude of $E(\nu)$. Ignoring constants, power received by the bolometer is

$$\begin{aligned} P_0 &= \int \eta(\nu)\left[E(\nu)\cos\left(\theta(\nu)\right)\right]^2 d\nu \\ P_{90} &= \int \eta(\nu)\left[E(\nu)\sin\left(\theta(\nu)\right)\right]^2 d\nu \\ P_{45} &= \int \eta(\nu)\left[E(\nu)\cos\left(\frac{\pi}{4}-\theta(\nu)\right)\right]^2 d\nu \\ P_{-45} &= \int \eta(\nu)\left[E(\nu)\sin\left(\frac{\pi}{4}-\theta(\nu)\right)\right]^2 d\nu \end{aligned} \tag{5.6}$$

Where P_x stands for power received by bolometer attached to antenna that is sensitive to polarization at angle x. $\eta(\nu)$ stands for detector's efficiency as a function of frequency. We assumed matching $\eta(\nu)$ between detectors. This is fairly good assumption given results from Figure 6.13 and Figure 6.14. Any deviation from matching $\eta(\nu)$ could be worked out by simply inserting different $\eta(\nu)$ for different detector. We kept every parameter as a function of frequency, but to extract *theta* we assume that polarization angle of the incident light does not change within bandwidth of the detector. Then we can define stokes parameter, Q and U as:

$$\begin{aligned} Q &= P_0 - P_{90} = \cos(2\theta)\int \eta(\nu)E^2(\nu)d\nu \\ U &= P_{45} - P_{-45} = \sin(2\theta)\int \eta(\nu)E^2(\nu)d\nu \end{aligned} \tag{5.7}$$

Then we can extract θ by

$$\theta = \frac{1}{2}\tan^{-1}\frac{U}{Q} \tag{5.8}$$

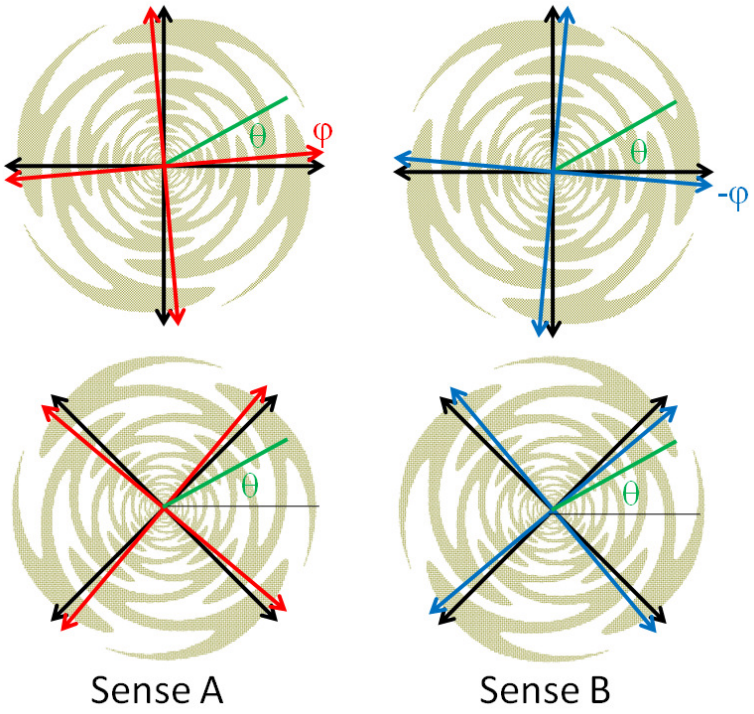

Figure 5.21: Polarized signal (green) coming in at angle θ respect to detector coordinate. Two senses and Q/U pixel combinations are shown.

To extract $E(\nu)$, we have to know the spectral shape of $E(\nu)$. Just as an example, if we assume constant E,

$$E^2 = \frac{(P_0 + P_{90})}{\int \eta(\nu) d\nu} = \frac{(P_{45} + P_{-45})}{\int \eta(\nu) d\nu} \tag{5.9}$$

We can obtain $\eta(\nu)$ from performing spectrum measurement of detector using the FTS. $\int \eta(\nu) d\nu$ can be obtained with total (integrated) efficiency measurement using beam filling modulated temperature source.

Solution for Sinuous Antenna Wobble

Sinuous antenna has polarization axis that wobbles as function of frequency $\phi(\nu)$. However, wobble angle amplitude for sinuous antenna is small (≈ 5 degrees). Cross-pol induced by the wobble is $\approx 0.5\%$ for a detector with $\approx 30\%$ bandwidth. Suppose we define antenna with one orientation *Sense A* and its mirror image orientation *Sense B* as shown in Figure 5.21. Power received by

bolometers for polarized light with polarization angle of θ be:

$$\begin{aligned}
P_{A0} &= \int \eta(\nu)\left[E(\nu)\cos\left(\theta(\nu)-\phi(\nu)\right)\right]^2 d\nu \\
P_{A90} &= \int \eta(\nu)\left[E(\nu)\sin\left(\theta(\nu)-\phi(\nu)\right)\right]^2 d\nu \\
P_{A45} &= \int \eta(\nu)\left[E(\nu)\cos\left(\frac{\pi}{4}-\theta(\nu)+\phi(\nu)\right)\right]^2 d\nu \\
P_{A-45} &= \int \eta(\nu)\left[E(\nu)\sin\left(\frac{\pi}{4}-\theta(\nu)+\phi(\nu)\right)\right]^2 d\nu \\
P_{B0} &= \int \eta(\nu)\left[E(\nu)\cos\left(\theta(\nu)+\phi(\nu)\right)\right]^2 d\nu \\
P_{B90} &= \int \eta(\nu)\left[E(\nu)\sin\left(\theta(\nu)+\phi(\nu)\right)\right]^2 d\nu \\
P_{B45} &= \int \eta(\nu)\left[E(\nu)\cos\left(\frac{\pi}{4}-\theta(\nu)-\phi(\nu)\right)\right]^2 d\nu \\
P_{B-45} &= \int \eta(\nu)\left[E(\nu)\sin\left(\frac{\pi}{4}-\theta(\nu)-\phi(\nu)\right)\right]^2 d\nu
\end{aligned} \tag{5.10}$$

We do same operation as we did with double slot dipole antenna to get Q and U parameter with wobble. We first subtract signal from two orthogonal arms of antenna as we did with double slot dipole example. It is important that this operation happens first to cancel out common mode fluctuation such as change in atmospheric loading. We again assume θ is constant across band,

$$\begin{aligned}
Q_A &= P_{A0}-P_{A90} = \int \eta(\nu)E^2(\nu)\cos\left[2(\theta-\phi(\nu))\right]d\nu \\
Q_B &= P_{B0}-P_{B90} = \int \eta(\nu)E^2(\nu)\cos\left[2(\theta+\phi(\nu))\right]d\nu \\
U_A &= P_{A45}-P_{A-45} = \int \eta(\nu)E^2(\nu)\sin\left[2(\theta-\phi(\nu))\right]d\nu \\
U_B &= P_{B45}-P_{B-45} = \int \eta(\nu)E^2(\nu)\sin\left[2(\theta+\phi(\nu))\right]d\nu
\end{aligned} \tag{5.11}$$

We use trigonometry identity to decouple θ and ϕ

$$\begin{aligned}
Q_A &= \int \eta(\nu)E^2(\nu)\left[\cos(2\theta)\cos(2\phi(\nu))+\sin(2\theta)\sin(2\phi(\nu))\right]d\nu \\
Q_B &= \int \eta(\nu)E^2(\nu)\left[\cos(2\theta)\cos(2\phi(\nu))-\sin(2\theta)\sin(2\phi(\nu))\right]d\nu \\
U_A &= \int \eta(\nu)E^2(\nu)\left[\sin(2\theta)\cos(2\phi(\nu))-\cos(2\theta)\sin(2\phi(\nu))\right]d\nu \\
U_B &= \int \eta(\nu)E^2(\nu)\left[\sin(2\theta)\cos(\phi(\nu))+\cos(2\theta)\sin(2\phi(\nu))\right]d\nu
\end{aligned} \tag{5.12}$$

By subtracting and adding Q_A and Q_B (also U_A and U_B), we get

$$\begin{aligned} Q_1 &= \frac{Q_A+Q_B}{2} = \cos(2\theta)\int \eta(\nu)E^2(\nu)\cos(2\phi(\nu))d\nu \\ Q_2 &= \frac{U_B-U_A}{2} = \cos(2\theta)\int \eta(\nu)E^2(\nu)\sin(2\phi(\nu))d\nu \\ U_1 &= \frac{Q_A-Q_B}{2} = \sin(2\theta)\int \eta(\nu)E^2(\nu)\sin(2\phi(\nu))d\nu \\ U_2 &= \frac{U_B+U_A}{2} = \sin(2\theta)\int \eta(\nu)E^2(\nu)\cos(2\phi(\nu))d\nu \end{aligned} \tag{5.13}$$

Then we can get θ by dividing taking ratio of $U_{1,2}$ and $Q_{2,1}$.

$$\theta = \frac{1}{2}\tan^{-1}\frac{U_{1,2}}{Q_{2,1}} \tag{5.14}$$

We can get to $E(\nu)$ in same way we obtained $E(\nu)$ for double slot dipole,

$$\int \eta(\nu)E^2(\nu)d\nu = P_{A0}+P_{A90} = P_{A45}+P_{A-45} = P_{B0}+P_{B90} = P_{B45}+P_{B-45} \tag{5.15}$$

Just like the case of detector without wobble, we have to know the spectrum shape of $E(\nu)$. Just as an example if we assume constant $E(\nu)$ within band, E is

$$E^2 = \frac{P_{A0}+P_{A90}}{\int \eta(\nu)d\nu} = \frac{P_{A45}+P_{A-45}}{\int \eta(\nu)d\nu} = \frac{P_{B0}+P_{B90}}{\int \eta(\nu)d\nu} = \frac{P_{B45}+P_{B-45}}{\int \eta(\nu)d\nu} \tag{5.16}$$

We can obtain $\eta(\nu)$ from performing spectrum measurement of detector using the FTS. $\int \eta(\nu)d\nu$ can be obtained with total (integrated) efficiency measurement using beam filling modulated temperature source.

How to Calibrate Polarization Angle

Calibration of polarization axis orientation is important for the CMB polarimetry experiment. Detector with a polarization wobble present a challenge as polarization angle changes as a function of frequency. As shown in Figure 5.18, polarization angle is sensitive to accurate knowledge of dielectric constant and extension length. We cannot simply rely on simulation to extrapolate polarization axis from one frequency. Thus we need more rubust way of measuring this. By using the *mirror imaged pair* we can calibrate 0 angle accurately.

Suppose we have calibration source with good polarization property and narrow frequency band such as gunn diode with rectangular horn. As we rotate the calibration source, one pixel will have peak intensity at polarization angle of $\phi(\nu)$ and its pair will have peak intensity of $-\phi(\nu)$ where ν is the frequency of gunn diode. Then angle that is bisecting between ϕ and $-\phi$ is the 0 degree angle of the detector.

Pixel Placement

When populating detector array, it makes sense to populate Q and U pixels side by side for a detector without wobble. Subtraction of two orthogonal polarization happens within pixel to minimize common mode noise contribution, then division between Q and U happens. For detectors with wobble, it still does subtraction of two orthogonal polarization signal within same pixel to again minimize common mode noise. But next step is adding or subtracting Q_A with Q_B and U_A with U_B, we placed pixel in order of Q_A, Q_B, U_A and U_B in scan direction.

5.5 Microstrip Filter

The advantage of coupling photon onto microstrip line is an ability to be able to do signal processing prior to detection at a bolometer. It is this technology that allowed the development of the multichroic detector. We explored two types of filters. Distributed filter is made with resonant structures of transmission line, and lumped filter is made with short high impedance section of line as an inductor and parallel plate capacitors formed between a ground plane and strip of microstrip line.

For a basic filter design, we designed with 3-pole Chebyshev filter since it is a good design when optimizing for sensitivity by balancing at in-band loss and roll-off speed [12]. To calculate component values, we followed the insertion loss method [99]. Then we followed Pozar to transform calculated values to distributed stub filters. For lumped filters, we followed O'Brient and Kumar when transforming calculated components values to planar designs [93, 66, 67]. After calculating geometrical design, we optimized the design with 2.5 dimension EM simulator (Sonnet) to account for parasitics. We simulated effect of superconductor by adding 0.13 pH/□ surface impedance [62].

Basic Filter Design

To calculate components' value, we used the insertion loss method. First we define power loss ratio $P_{LR} = 1/(1-|\Gamma(\omega)|^2)$ that is defined as power available from source divided by power delivered to load. We then specify functional form of P_{LR} for different type of filters. Chebyshev filter is a type of filter that has a sharper cut off but has ripples in passband. Its P_{LR} is defined as

$$P_{LR} = 1 + k^2 T_N^2 \left(\frac{\omega}{\omega_c}\right) \tag{5.17}$$

Where $T_N^2\left(\frac{\omega}{\omega_c}\right)$ is a Chebyshev polynomial of order N. N is number of reactive element pair for a band-pass filter equals the order. Chebyshev filter will have ripples of amplitude $(1+k^2)$. ω_c is an angular frequency where $P_{LR} = (1+k^2)$. For a third order, 0.5 dB Chevyshev filter power loss ratio is explicitly

$$P_{LR} = 1 + (0.35)^2 \left[4\left(\frac{\omega}{\omega_c}\right)^2 - 3\left(\frac{\omega}{\omega_c}\right)^2\right]^2 \tag{5.18}$$

We calculate input impedance of N^{th} order low pass filter with a source impedance of 1 Ω as shown in Figure 5.22. Then we calculate input impedance Z_{in} and reflection coefficient $\Gamma = (Z_{in}-1)/(Z_{out}+1)$. We can then calculate $P_{LR} = 1/(1-|\Gamma(\omega)|^2)$ in terms of L,C,R,ω. Finally we equate the P_{LR} to Equation 5.18 to extract each element's value to achieve desired filter performance. In theory any filter with desired ripple level can be calculated this way. However, in practice we use tabulated value for common filter type [38]. Odd order of Chebyshev filter couples to same source and load impedance. Since we are placing filter between two microstriplines that has equal impedance, we picked a third order. For a third order Chebyshev polynomial, elemental values are

$$\begin{aligned} g_0 &= 1.0000 \\ g_1 &= 1.5963 \\ g_2 &= 1.0967 \\ g_3 &= 1.5963 \\ g_4 &= 1.0000 \end{aligned} \tag{5.19}$$

We then scale these elemental values to input imepdance $R_0 = 10\ \Omega$, and calculate each element in bandpass filter with

$$\begin{aligned} L_n &= \frac{g_n R_0}{\omega_0 \Delta}\ (\text{series}) = \frac{\Delta R_0}{g_n \omega_0}\ (\text{shunt}) \\ C_n &= \frac{\Delta}{g_n R_0 \omega_0}\ (\text{series}) = \frac{g_n}{\Delta R_0 \omega_0}\ (\text{shunt}) \end{aligned} \tag{5.20}$$

L_n and C_n are n^{th} element in bandpass filter. Z_0 is source impedance, $\omega_0 = \sqrt{\omega_{\text{UB}}\omega_{\text{LB}}}$ is geometric mean of upper and lower bound of bandpass. $\Delta = (\omega_{\text{UB}} - \omega_{\text{LB}})/\omega_0$ is a fractional bandwidth.

Distributed Filter

Design steps for distributed filter were shown in Figure 5.22. Loss less shorted quarter wave stub has an equivalent input impedance as parallel *LC* circuit. For a parallel *LC* circuit, input impedance is

$$Z_{in} = \left(\frac{1}{j\omega L} + j\omega C\right)^{-1} \tag{5.21}$$

Resonance frequency is $\omega_0 = 1/\sqrt{LC}$. Near resonance, input impedance can be taylor expanded around ω_0. If we let $\omega = \omega_0 + \delta\omega$, with small $\delta\omega$

$$Z_{in} = \left(\frac{1-\delta\omega/\omega_0}{j\omega_0 L} + j(\omega_0+\delta\omega)C\right)^{-1} = \frac{1}{j2C\delta\omega} \tag{5.22}$$

Shorted stub with characteristic impedance of Z_0 has the input impedance of

$$Z_{in} = jZ_0 \tan(\beta l) \tag{5.23}$$

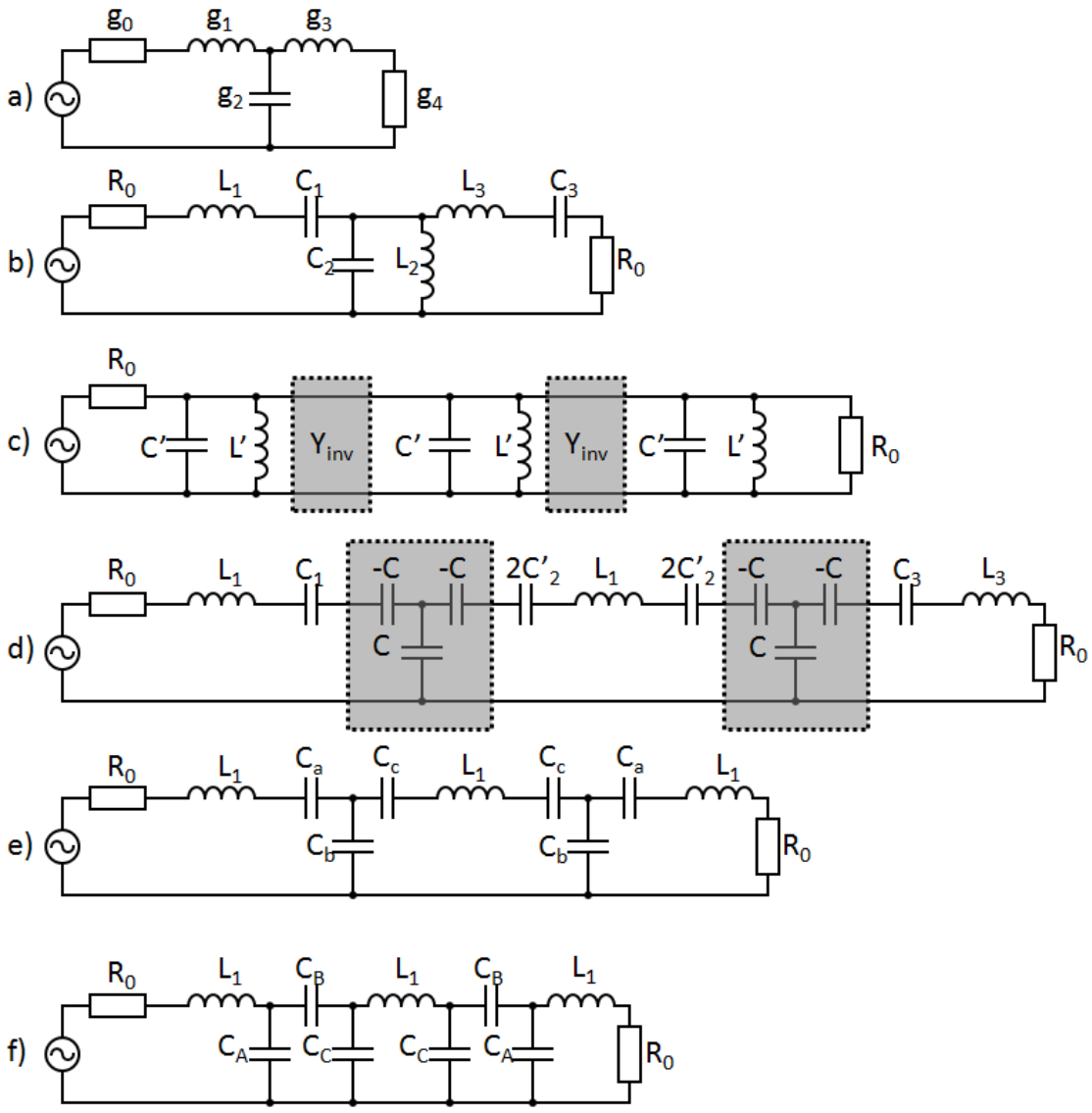

Figure 5.22: Circuit diagram for filter design. a. Low-pass prototype design. b. Band-pass design. c. Circuit diagram for a stub. d. Band-pass design with impedance inverter. e. Lumped filter design with T-capacitor network. f. Lumped filter design with π-capacitor network

Just like we did with parallel *LC* circuit, we Taylor expand around ω_0

$$\beta l = \frac{\pi}{2} + \frac{\pi\delta\omega}{2\omega_0} \tag{5.24}$$

Inserting this back to Z_{in}, we obtain

$$Z_{in} = \frac{Z_0}{j\pi\delta\omega/2\omega_0} \tag{5.25}$$

This is in same form as input impedance for parallel LC circuit. We can calculate equivalent inductance and capacitance for shorted quarter-wave stub as

$$\begin{aligned} L' &= \frac{4Z_0}{\pi\omega_0} \\ C' &= \frac{\pi}{4\omega_0 Z_0} \end{aligned} \tag{5.26}$$

We convert this parallel *LC* circuit to a series *LC* circuit with quarter-wave admittance inverter. Quarter wave long transmission line with characteristic admittance of $J = 1/R_0$ transforms load admittance Y_L to input admittance Y_{in} with $Y_{in} = J^2/Y_L$. Admittance looking toward second stub is

$$\begin{aligned} Y &= j\omega C_2' + \frac{1}{j\omega L_2'} + \frac{1}{R_0^2}\left(\frac{1}{R_0} + \frac{1}{j\omega L_1'} + j\omega C_1'\right)^{-1} \\ &= j\sqrt{\frac{C_2'}{L_2'}}\left(\frac{\omega}{\omega_0} - \frac{\omega_0}{\omega}\right) + \frac{1}{R_0^2}\left(\frac{1}{R_0} + j\sqrt{\frac{C_1'}{L_1'}}\left(\frac{\omega}{\omega_0} - \frac{\omega_0}{\omega}\right) + \right)^{-1} \end{aligned} \tag{5.27}$$

Admittance looking toward second element for last original circuit is

$$\begin{aligned} Y &= j\omega C_2 + \frac{1}{j\omega L_2} + \left(R_0 + \frac{1}{j\omega C_1} + j\omega L_1\right)^{-1} \\ &= j\sqrt{\frac{C_2}{L_2}}\left(\frac{\omega}{\omega_0} - \frac{\omega_0}{\omega}\right) + \left(R_0 + j\sqrt{\frac{L_1}{C_1}}\left(\frac{\omega}{\omega_0} - \frac{\omega_0}{\omega}\right)\right)^{-1} \end{aligned} \tag{5.28}$$

Equating two admittance equations, they are equal if it satisfies

$$\begin{aligned} R_0^2\sqrt{\frac{C_1'}{L_1'}} &= \sqrt{\frac{L_1}{C_1}} \\ \sqrt{\frac{C_2'}{L_2'}} &= \sqrt{\frac{C_2}{L_2}} \end{aligned} \tag{5.29}$$

Solving them forL_1' and L_2' yields $L_1' = \frac{R_0^2}{L_1\omega_0^2}$ and $L_2' = L_2$. Inserting this back to Equation 5.26 and solving for Z_0 yield

$$Z_0 = \frac{\pi R_0 \Delta}{4g_n} \tag{5.30}$$

We can then translate to physical dimension by using stub width to impedance ratio from Figure 5.8. For input impedance and fractional bandwidth we are interested in, stub's impedance can be as low as few Ω. Such stub is so wide that it could carry higher order mode. To suppress such mode, we tapered part of stub that connects stub to a transmission line.

In theory we could considered surface inductance effect of superconductor to adjust stub length to be quarter wavelength at center frequency. But we noticed that measured band had shift of 10 % with time constant of about few month. We believe that material property on the detector, such as kinetic inductance in niobium, is changing as machine condition changes. Thus we adjusted stub's length using most recent measurement.

For a demonstration of filter design, suppose we are desining three-pole Chebyshev band-pass filter for center frequency of $f_0 = 147.8$ GHz and bandwidth of 26.0%. Using Equation 5.30, impedance of each stubs should be

$$\begin{aligned} Z_1 &= 1.2792\Omega \\ Z_2 &= 1.8620\Omega \\ Z_3 &= 1.2792\Omega \end{aligned} \tag{5.31}$$

Stub that has this impedance corresponds to

$$\begin{aligned} W_1 &= 86\mu\text{m} \\ W_2 &= 58\mu\text{m} \\ W_3 &= 86\mu\text{m} \end{aligned} \tag{5.32}$$

From recent band measurements with the FTS, we know 200 μm corresponds to 150 GHz. Suppose that's close enough for initial design, final design is drawn on Figure 5.23. For diplexer and triplexer design, we first tuned each filter individually. Then they were combined to a single junction with some length of microstripline. Length of microstrip line was adjusted in simulator until isolation of approximately -20 dB was achieved. For the diplexer, optimization was fairly easy, however, for triplexer this turned out to be very difficult to achieve. Compromise was made between bandwidth of each band and inband transmission performance.

Lumped Filter

Another approach to make a filter is to create lumped capacitor and inductor. If we can make arbitual value and type of inductors and capacitors, we will simply make a filter designed in basic filter design sub-section. However, shunt inductor is difficult to fabricate and some capacitor values were too large to fabricate. Thus we went through series of identities to convert shunt *LC* pair to series *LC* pair with impedance transformers. Then we converted T-network to π-network to reduce required capacitance. Previous realization of such filter had vias from strip layer to ground plane layer [93, 67]. To achieve thinner strip layer for more reliable fine line realization during etching, vias were removed in the final design. Uniformity tolerance, surface inductance tolerance and adjustability study were also taken into account for the final design.

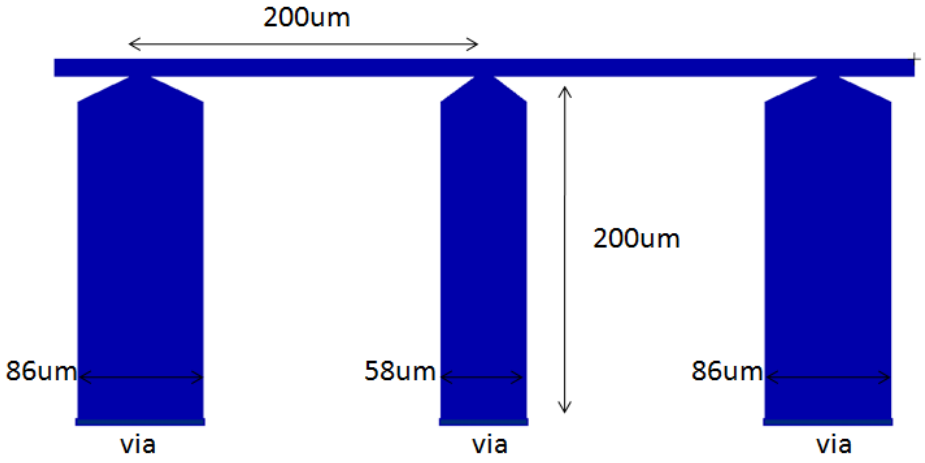

Figure 5.23: Stub filter design for 150 GHz

Design steps were shown in Figure 5.22. To convert shunt LC to series LC, we use impedance inverter. Parallel shunt admittance Y_p can be converted to series impedance Z_s with an identity $Z_s = K^2 Y_p$. Impedance inverter is implemented with two T-network with two negative series capacitance and one shunt capacitance with $C = 1/\omega_0 K$. Admittance is $Y_p = j\omega C_2 + \frac{1}{j\omega L_2}$, and if we pick inductance for converted inductor to have same value with rest of filter ($L_1 = L_3$) , series impedance is $Z_s = j\omega L_1 + \frac{1}{j\omega C_2'}$. Then $K^2 = L_1/C_2$ and $C_2' = L_2 C_2/L_1$. For ease of optimization, symmetric structure was obtained by first splitting C_2' into equivalent two series capacitor ($2C_2'$ each), and combine with $-C$ to form new capacitor $C_c = (1/2C_2' - 1/C)^{-1}$. Similarly we can combine C_1 and $-C$ to form $C_a = (1/C_1 - 1/C)^{-1}$. Finally shunt capacitance is simply $C_b = C$. These capacitors values were too large to fabricate with dielectric (SiO_2) and its thickness 0.5 μm. Therefore we decrease requried capacitance by converting C_a, C_b and C_c T-network to C_A, C_B and C_C π-network. There's simple conversion rule

$$C_{A,B,C} = \frac{1}{C_{c,b,a}} \frac{1}{\mathscr{C}} \tag{5.33}$$

Where $\mathscr{C} = \frac{1}{C_a}\frac{1}{C_b} + \frac{1}{C_a}\frac{1}{C_c} + \frac{1}{C_b}\frac{1}{C_c}$.

For a capacitor, we used a simple parallel plate design. For pre-simulation design, we assumed $C = \varepsilon \frac{A}{d}$. Since we used same dielectric as microstrip line to form a capacitor, we used $d = 0.5$ μm and $\varepsilon = \varepsilon_r \varepsilon_0 = 3.8\varepsilon_0$. For an inductor, we used approximate equivalent circuit for short transmission line section method [99]. Equivalent inductance for short transmission line with impedance Z_0 is approximately $L = l\beta Z_c/\omega$ where l is a length of line, β is a propagation constant and Z_c is characteristic impedance of transmission line. As l start to get longer than $\lambda/8$, filter start to have leakage at three times ω_0. Thus to acquire enough inductance with short section of line, it is important to use tranmission line with high characteristic impedance. We improved our lumped filter design over many tries. Three generations of lumped filter designs are shown in Figure 5.24. Since

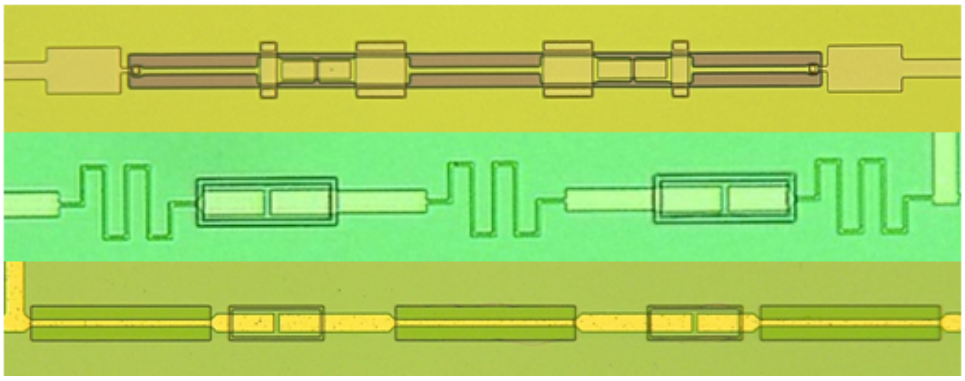

Figure 5.24: Three lumped filter design in chronogical order. (top) Lumped filter design with co-planar inductor design with via. (middle) Lumped filter design with microstrip inductor design without via. (bottom) Lumped filter design with co-planar inductor design without via

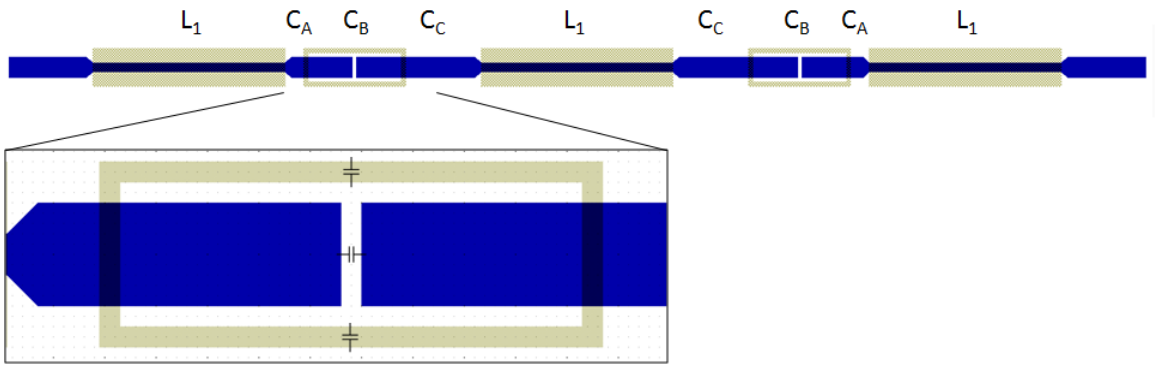

Figure 5.25: Lumped filter design for 150 GHz. Zoomed in CAD for capacitor part shows possible parasitic capacitance

we already form transmission line with microstrip line, it would be simple if we could form high impedance microstrip line. We designed lumped inductor with short section of microstrip line as shown in Figure 5.24 (center). However, high impedance is hard to achieve with a microstrip line, and longer line that we used caused higher frequency leakage as shown in Figure 6.15. We used 1 μm strip for microstrip lines to form inductors. This caused inductance to be highly dependant on over-etching. To achieve high impedance line, we designed inductor with co-planar waveguide (CPW) as shown in Figure 5.25. CPW is easier to achieve higher imepdance since distance from a strip to a ground plane can be made far. To make a conversion from microstrip line to true co-planar waveguide, vias are necessary. As we discussed in antenna feed section, we would like to avoid having via to keep thickness of strip layer down. Thus we formed quasi-CPW by keeping strip on the upper layer. Thickness of dielectric is much smaller compared to strip to ground plane width,

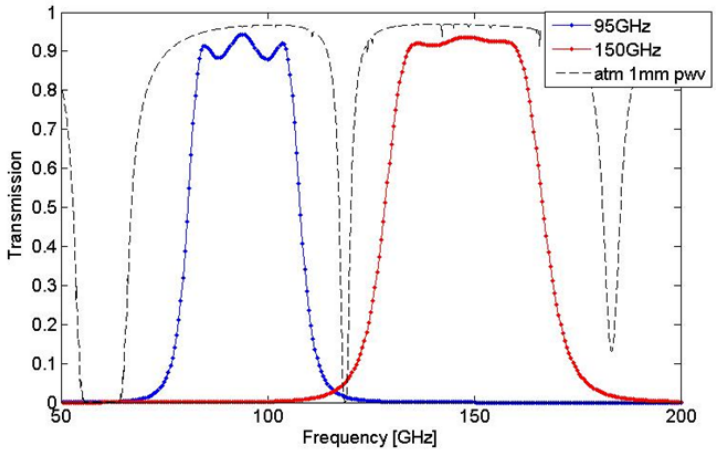

Figure 5.26: Response of lumped diplexer. Atmospheric transmission line is added to show atmospheric window.

thus even if strip layer is not truely co-planar, it approximately behaves as a CPW. Such non-ideal effect was simulated with the Sonnet 2.5 dimension EM simulator [54]. Parallel plate capacitor for C_A and C_C were formed between strip layer and ground plane. To make a series capacitor for C_B, we isolated part of ground plane from rest of ground plane, and formed parallel plate capacitor between strip layer and ground layer. Such structure cause parasitic capacitance between isolated part of ground plane and ground plane, effectively increasing shunt capacitance as shown in Figure 5.25. This parasitic effect were accounted by reducing C_A and C_C. Filter was designed such that ω_0 can be adjusted by modifying just a strip layer. This was necessary to account for long time constant drift we observed in wave speed. Inductance could be adjusted by changing width of the strip. Capacitors can be adjusted by adjusting width of the strip. Another design criteria was robustness against etch non-uniformity. When making array on 150 mm wafer, it is important to minimize variability within wafer. This was especially problematic for high impedance line since it usually required thinner line, and its fractional error was large compared to etch uniformity. We increased width of slot for quasi-CPW to achieve high impedance line even with wide strip line. However, when wide slot is curved into ground plane, we need to worry about radiation from the CPW. Such radiation can be suppressed if we bridge two opposing side of slot with a short. Lumped filter is designed such that ground plane under C_A and C_C serves as the shorting bridge.

For a multiplex filter design, filter for each band were optimized using Sonnet simulator while taking into superconducting effect by adding surface inductance to metal layers [54, 62]. Once filter for each band was optimized, filters were simply joined to a junction. Multiplexer was simulated to see if additional parasitics needs to be removed. Unlike stub filter, multiplexed lumped filter's performance was as good as stand alone filter. Result from such optimization diplexer is shown in Figure 5.26.

For lumped filters, alignment between ground plane and strip layer will become important.

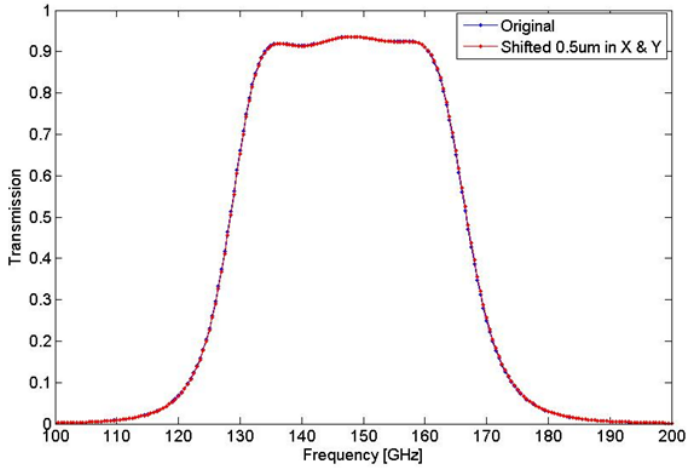

Figure 5.27: Comparison of original design and design with top layer shifted by 0.5 μm in X-Y direction.

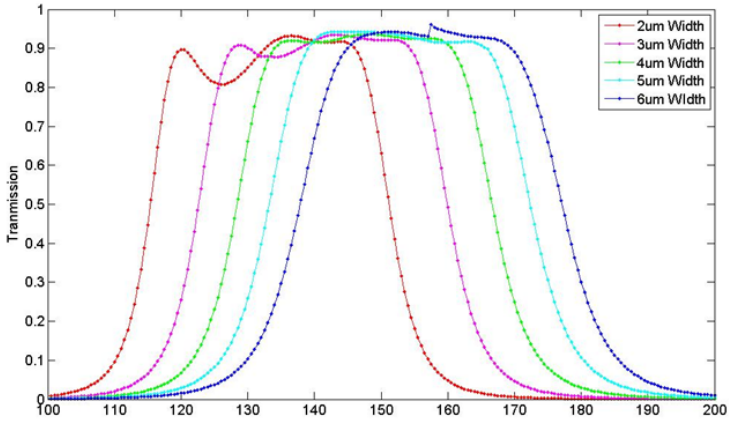

Figure 5.28: Simulation of filter design with varying coplanar strip width. Band shape could be improved by modifying capacitance values at same time. Simulation shows band location can be modified far enough with just modifying top layer.

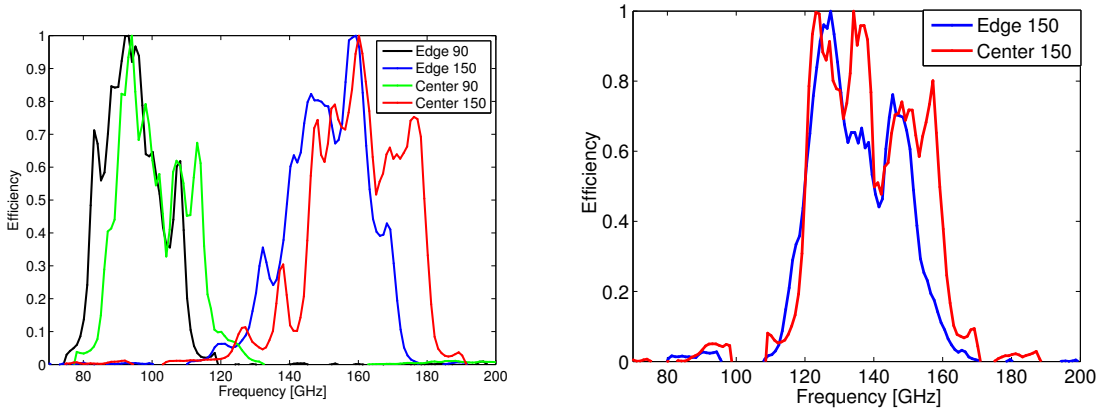

Figure 5.29: Comparison of shift in band location due to pixel location on wafer for stub filter (left) and lumped filter (right)

We can achieve layer to layer alignment tolerance of ± 0.5 μm with GCA stepper. We simulated misalignment of top layer by shifting top in both direction by 0.5 μm. As shown in Figure 5.27 effect is negligible. We simulated filter's ability to adjust frequency by modifying just the strip layer. Knowing that we have much more freedom to change capacitance, we studied the effect by changing inductance by changing strip's width. As shown in Figure 5.28 center frequency can be adjusted $\pm 10\%$. Suppose co-palanr waveguide's strip line width changes by 0.5 μm across wafer, band shift across wafer is 1.7%. This is acceptable from mapping speed study.

Filter Comparison

We desiged stub diplexer and lumped dilexer and compared performance of two filters. As shown in Figure 5.30, stub filter required larger area since it relies on resonant structure. When we compared pass band locations from a pixel at center of wafer versus pixel at edge of wafer, stub design had significantly more shift than lumped filter design as shown in Figure 5.29. We also studied how band shifts respect to surface inductance. We increased kinetic inductance by factor of two in simulation, and we saw distributed filter had fractional bandwidth change of 8.9%, and lumped filter had 3.4%. Also when designing triplexer, lumped filter was very easy to achieve high performance since its performance did not degrade when connected to other channels. For future multichroic pixel development effort, we recommend to use lumped filter over stub filter.

5.6 Crossover

Crossover is necessary to readout differentially-fed dual-polarization antenna. There are two possible arrangements. Two lines could crossover prior to partitioning signal into frequency bands, or two lines could crossover after partitioning into frequency bands. First option requires just one

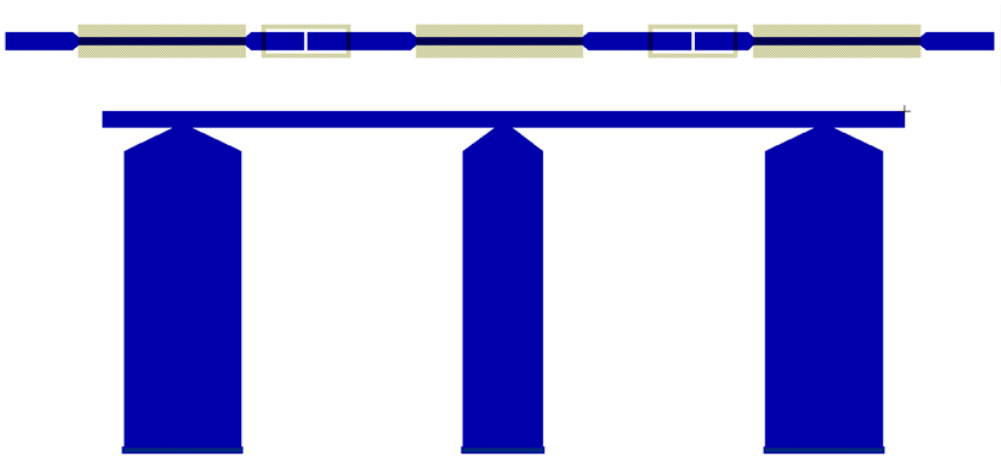

Figure 5.30: Comparison of size difference for 150 GHz filter. Lumped filter is shown on top and stub filter is shown on bottom.

crossover and two dummy crossover to keep feeds balanced. This design makes pixel layout to be asymmetric. For a diplexer, we can keep symmetric design if crossover happens after frequency partitioning even though this requires four crossovers.

Two lines that crosses were narrowed to 4 μm to reduce capacitive coupling between two orthogonal polarization. Narrowed line actus as series inductor. Extra inductance was tuned out by adding extra capacitance by widening microstrip line just after crossover as shown in Figure 5.31. Dimension were optimized using Sonnet simulation [54]. Result from the simulation is shown in Figure 5.31. Reflection were below -20 dB across band. More importantly cross-talk between orthogonal channels were below -40 dB across band. Since we wanted to avoid via between strip layer and ground plane, we added additional dielectric layer and niobium layer just beneath strip layer to form cross-over. Thicknesses were chosen carefully to make sure step coverage requirements were met, while keeping thickness of strip layer as thin as possible.

5.7 Bolometer

Signal from antenna travels on microstrip transmission line. Then signal go through crossover, and finally signal is terminated at load resistor on bolometer. Since incoming lines are 10 Ω microstrip lines that are differentially feeding load resistor, load resistor should have DC resistance of 20 Ω to minimize reflection. We form load resistor with same AlTi bilayer that forms the TES, but we remove most of aluminum from the bilayer to increase its resistace per square. With aluminum removed, we achieve approximately 5 Ω/□. Thus we have 4 squares of AlTi bilayer. The bilayer would act as simple resistive metal for incoming high frequency signal. $E_{gap} = hf_c = 2\Delta \approx 3.5k_BT_c$ with $f_c = 36$ GHz for $T_c = 0.5$ Kelvin thus any signal higher in frequency than f_c would break

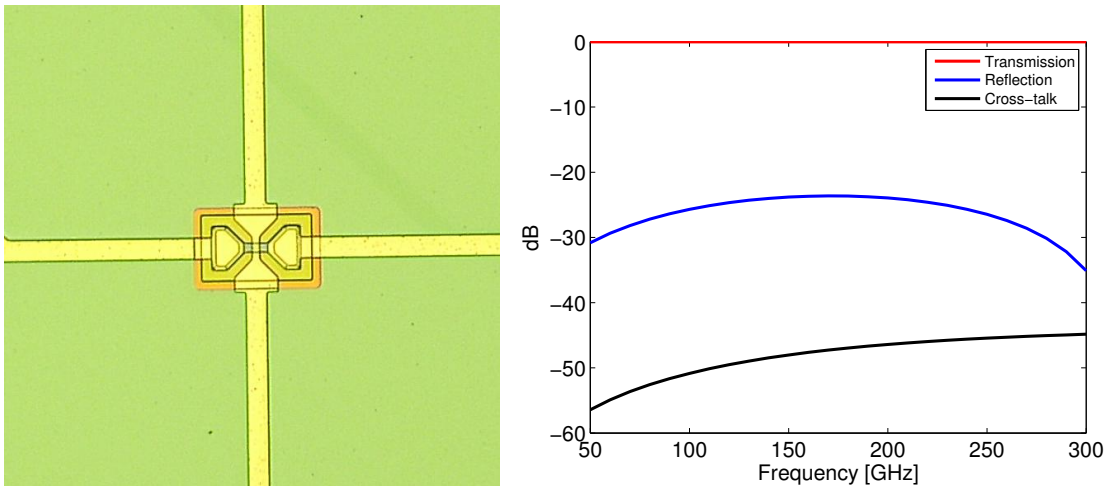

Figure 5.31: Microscope photograph of crossover (left). Simulated responce is shown on right. Reflection was suppressed under -20 dB across required bandwidth.

Cooper pairs. Reflection coefficient $\Gamma = (R-20\Omega)^2/(R+\Omega)^2$ is a forgiving function as a function of error in load resistor value R.

We calculate heat capacity of bolometer island by adding up contribution from everything on bolometer island using published value for heat capacity of material in Table 5.1 [77, 124, 98, 103, 14, 57]. For AlTi bilayer, effect of bilayer was taking into account [132]. Normal metal was added on bolometer island to increase heat capacity until required heat capacity C for desired intrinsic time constant was met. Since we use gold and other prescious metal for this purpose, we call this normal metal a *bling*. We want to put down thickest bling as possible because thermalzation time constant of bolometer island is inversely proportional to the metal's thickess. Thermalization time is proportional to longest length of the bling, thus we made the shape as close to square as possible. Width limit for the bling comes from limit on bolometer island width. Bolometer island's width needs to be small enough such that bolometer release process gets completed in reasonable time during fabrication. We put down 1.5 μm of gold due to practical limit in fabrication that comes from available photo-resist thickness. In future bolometer fabrication, we are planning to increase time constant of bolometer. This would require metal with more heat capacity. We are exploring palladium as a replacement. Palladium has about order of magnitude higher heat capacity at cryogenic temperature [57, 103]. Therefore we can keep size of the bolometer island small, and reduce cost of fabrication by minimizing amount of prescious metal being used. It is important for the bling to be well thermally coupled to a TES. Thus we underlaid bling with AlTi that is connected to TES directly. Titanium also act as adhesion promoting metal to help gold adhesion. We also overlayed 2 μm of gold onto TES to further increase thermal coupling. 3-D microscope photograph in Figure 5.37 shows how bling couples to the TES.

For the TES material, we use AlTi bilayer. Aluminum has nominal transition temperature of 1.20 Kelvin, and titanium has transition temperature of 0.39 Kelvin. By depositing two met-

Material	**Specific Heat at 0.5 K** [pJ/μm$^3 \cdot$k]
Low Stress Nitride	1.05×10^{-7}
Silicon Dioxide	2.63×10^{-7}
Aluminum	7.44×10^{-5}
Titanium	1.74×10^{-4}
Gold	3.57×10^{-5}
Palladium	5.67×10^{-4}
Niobium	1.69×10^{-7}

Table 5.1: Specific Heat at 0.5 Kelvin for materials used on bolometer island [77, 124, 98, 103, 14, 57, 132]

als without breaking vacuum we can form bilayer without oxide layer in between. AlTi bilayer achieves intermediate transition temperature through a proximity effect. It is possible to tune transition temperature by changing thickness of metals. We chose thickness of titanium to be 0.08 μm. We modified thickness of aluminum to control bilayer's T_c. T_c drops approximately 10% during fabrication due to wafer heating and other causes during processing. Therefore we usually target deposition T_c to be slightly higher T_c than what we want in the end. AlTi bilayer has about 1.7 $\Omega/\square$, therefore we adjust size of TES to achieve desired R_{TES}. For laboratory tests it is advantageous to be able to look at 300 Kelvin load without exceeding P_{sat}. Since $P_{sat} \propto \left(T_c^{n+1} - T_b^{n+1}\right)$, we placed aluminum TES in series with AlTi bilayer TES as shown in Figure 5.32. Aluminum has about 2.0 $\Omega/\square$, and we calculated number of square to be such that its normal resistance is about factor of three higher than AlTi bilayer's resistance to reduce effect of parasitic resistance during lab test. Width of aluminum TES was maximized to reduce effect of under cut etching during wet-etch process yet meeting constraint from bolometer island's size.

Size of bolometer was decided such that maximum undercut necessary to release bolometer was 40 μm. Bolometer is relreased by undercutting silicon with XeF_2 gas. XeF_2 is very reactive gas that most component needs to be kept away from the gas during the process by photo-resist. Niobium is especially vulnerable against the gas. Niobium melts instantly when it comes in contact with XeF_2 gas. We protected components with photo-resist during release, but heated environment of chamber and chemical reaction between between photo-resist and XeF_2 gas hardens photo-resist and it lead to occasional photo-resist cracking. To protect niboium ground plane from the gas we retracted niobium from a hole and overlayed it with silicon oxide layer. Silicon oxide has 100:1 selectivity between silicon and silicon oxide, thus even if it gets in contact with the gas, only negligible amount will be removed.

Leg length was determined from Equation 4.35. Extra slot was curved in niobium ground plane and silicon oxide plane. Adjustment to P_{sat} can be done by modifying single mask. H-shaped bolometer was chosen to minimize space that is taken up by bolometer. Also its gemetry allowed to make wider bolometer island that facilitated thermalization of bolometer island. Bolometer geometry is summarized in Table 5.2. Photograph of unlereased bolometer and zoom in of bolometer

	95 GHz	150 GHz
Load Resistor (AlTi)	4□	4□
TES (AlTi)	0.88□	1.12□
TES (Al)	2.25□	2.85□
Bling 1 μm thick palladium	38 μm^2	48 μm^2
l	605 μm	357 μm

Table 5.2: Bolometer parameters

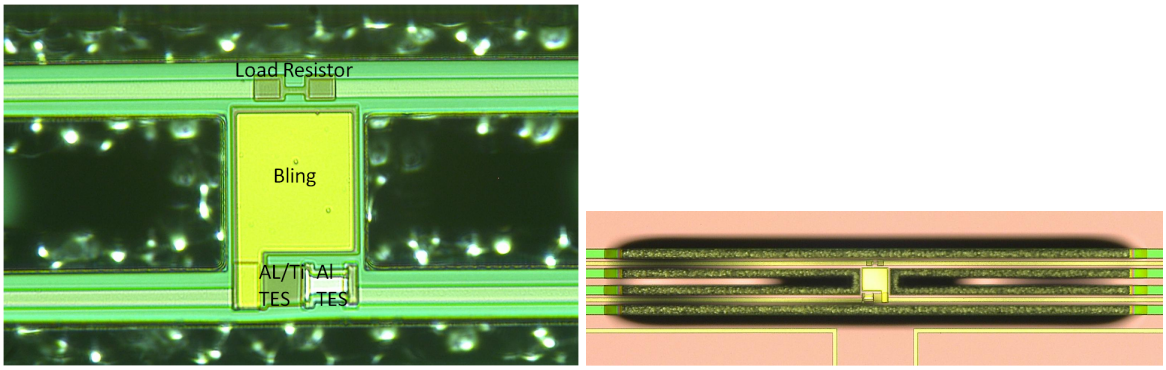

Figure 5.32: Microscope photograph of bolometer island (left) and bolometer (right). Dark background around bolometer is due to cavity formed by XeF_2 silicon etching.

island is shown in Figure 5.32.

5.8 Efficiency

To estimate detector efficiency, we considered the AR coating efficiency, antenna forward gain loss, antenna impedance mismatch, impedance transformation, microstrip line dielectric loss, bandpass filter efficiency, cross-over reflection and load resistor mismatch.

Instead of making optimized shaped anti-reflection coating, we form uniform thickness layer on lenslet. Loss from thickness mismatch after integrating over lenslet is 5%. Because antenna is fabricated on silicon-air dielectric half space, antenna preferentially accept power with efficiency of 95%. Antenna mismatch is negligible, so we assume efficiency of 99%. Impedance transformation happens smoothly over many wavelength, thus its reflection loss can be ignored. Microstrip line dielectric loss was also quoted as function of frequency assuming total length $L_{total} = 14$ mm. Since we do not know exact value of loss-tangent for our dielectric, we graphed range of efficiency with $\tan(\delta)$ from 1×10^{-3} to 7×10^{-3}. $\tan(\delta)$ in silicon dioxide could vary between 1×10^{-3} to 7×10^{-3} depending on deposition conditions [74]. Bandpass filter efficiency was also simulated by entering dielectric loss into simulation. In-band efficiency range for various loss tangent values are

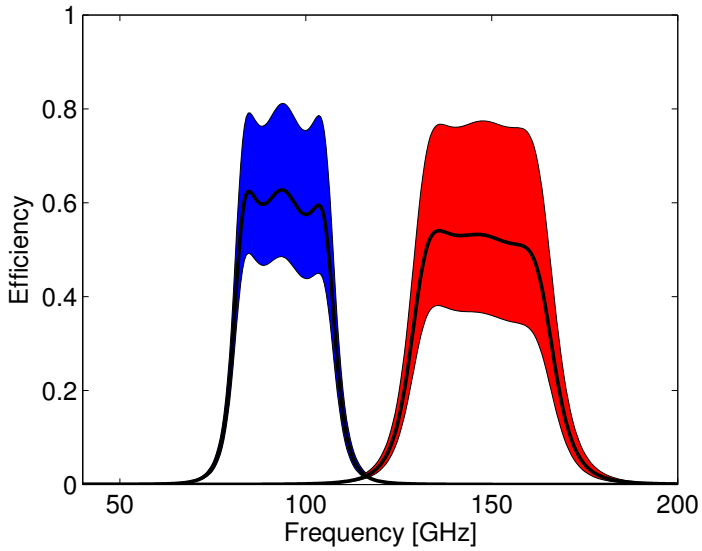

Figure 5.33: Expected detector efficiency assuming loss-tangent between 1×10^{-3} and 7×10^{-3}. Black line in center assumes 4×10^{-3}

between 86% to 98%. Crossover efficiency and load resistor coupling efficiency are approximately 99%. Combined efficiency is plotted in Figure 5.33.

5.9 Wiring Layout

We use aluminum wirebond at edge of wafer to read-out bolometers. Bond pads need to have 100 μm pitch to be able to readout every bolometer in a single row of bond pads. We decided to use automatic wirebonder to make thousands of bonds. However, to be able to manually wirebond for quick test, we designed bond pads with interlocking T shape such that it effectively acts as two rows of pads with 200 μm pitch as shown in Figure 5.34. We used six fold rotational symmetric wiring pattern on wafer, such that same readout hardware can be used for all sides of wafer.

5.10 Fabrication

Fabrication of wafer was done at Marvell nano-fabrication laboratory [68]. Sinuous detector array was the first multichroic detector array to use 150 mm diameter wafer. New machine, technique and characterization method were used to successfully fabricate the detector array. Photographs from fabrication were shown in Figures 5.35, 5.36 and 5.37.

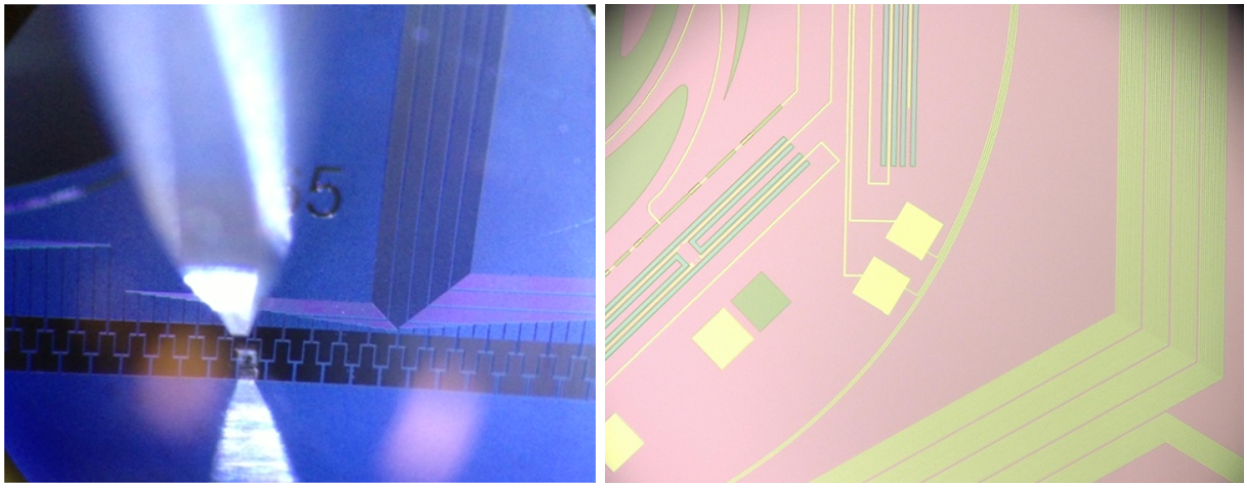

Figure 5.34: (left) Microscope photograph of bondpad. Vertical metal object is a wirebonding tip. (right) Microscope photograph of wiring layer. Wiring layer is connected to pixel wiring at two white pads in center of the photograph.

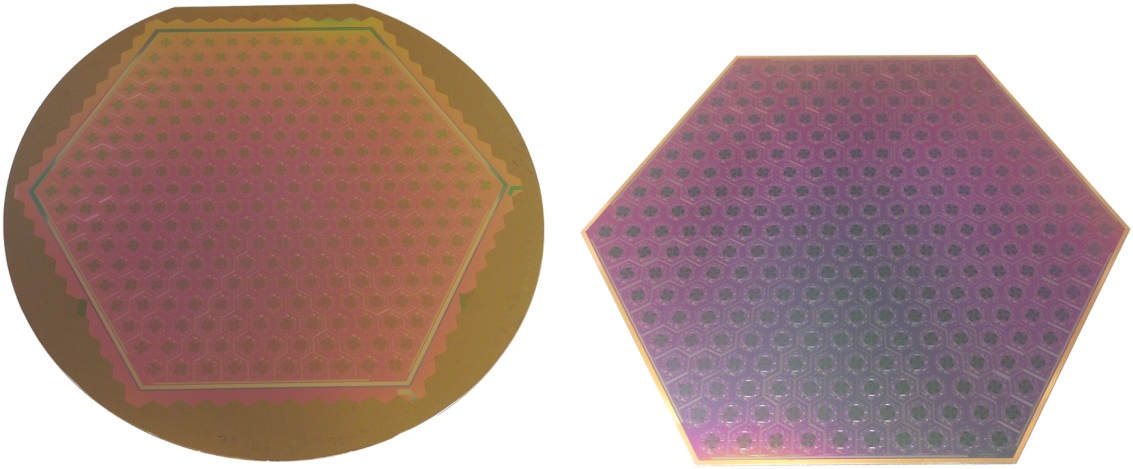

Figure 5.35: (left) Photograph of wafer in process. Detector array uses 150 mm wafer fully. (right) Photograph of detector wafer.

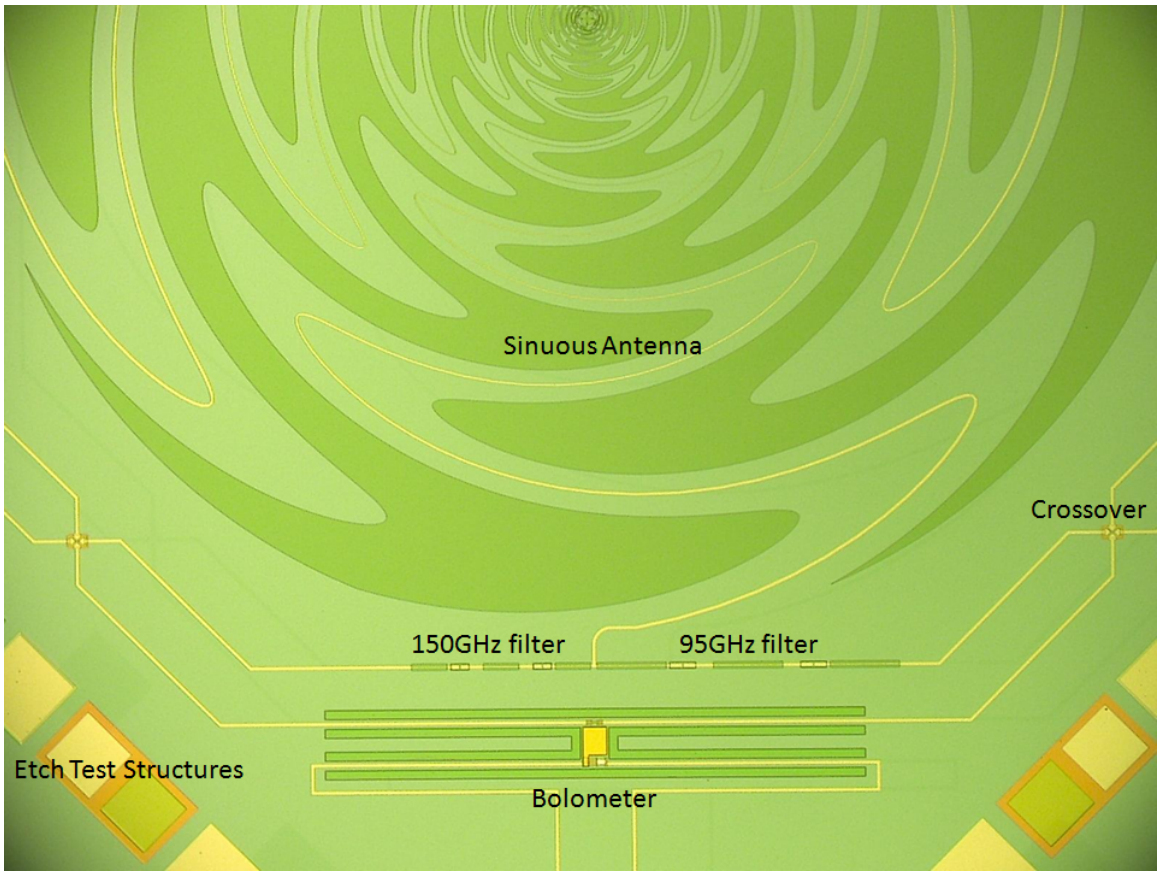

Figure 5.36: Microscope photograph of detector pixel. Sinuous antenna is on top. Transmission line snakes out of the sinuous antenna. Broadband signal is split into frequency bands at diplexing filter. Transmission lines crossover prior to detection at bolometer.

Process Flow

Process flow was summarized in Table 5.3. Fabrication process was also visualized in Figure 5.38. GCA stepper lithography machine was used to pattern wafer for every process. GCA stepper is a x5 reduction lithography machine with 0.5 μm resolution capability. GCA stepper has micro-DFAS layer-to-layer aligning capability, that achieves layer-to-layer alignment of better than 0.3 μm. Since GCA can only print maximum of 20 mm $\times$ 20 mm die at a time, large hexagonal array was put together from arrays of small hexagonal patterns. Contact mask was used once to define wirebonding traces on wafer. I-line photo-resist was used unless it was stated otherwise.

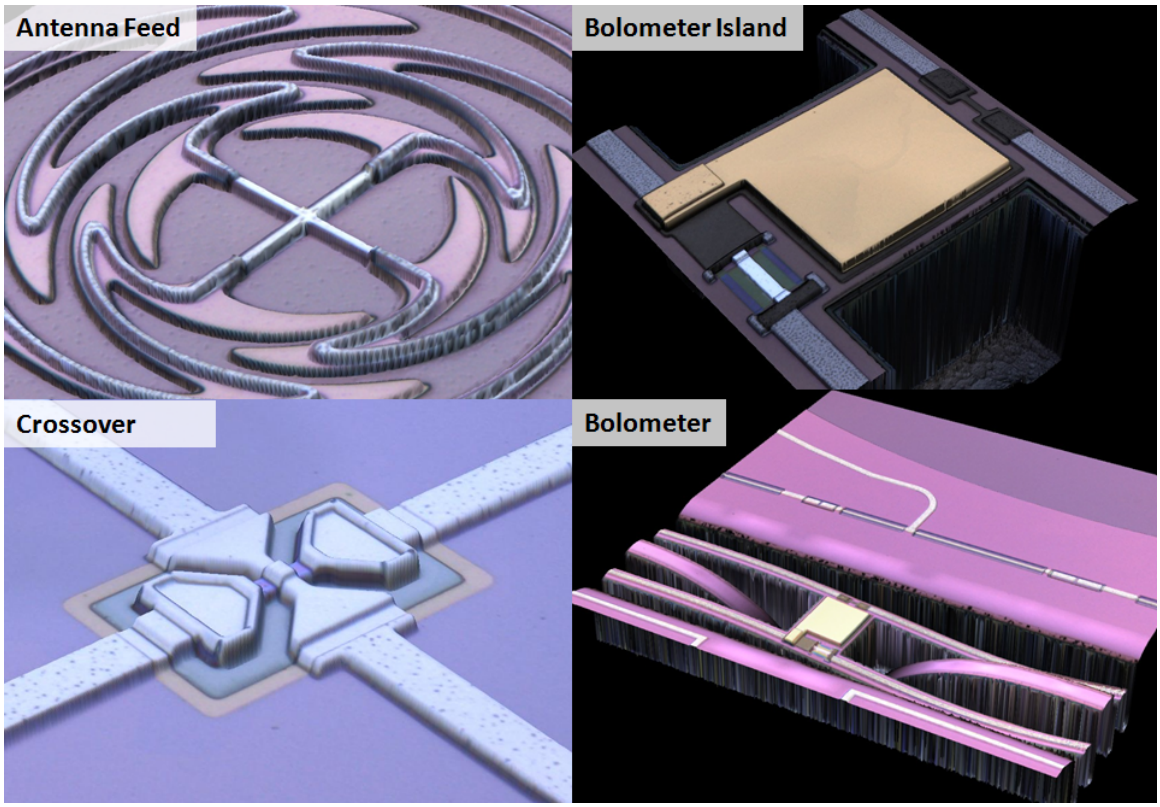

Figure 5.37: 3-D microscope photograph of various parts of detector. 3-D microscope photograph allows us to check step coverage and alignment in new way.

Low Stress Nitride

150 mm silicon wafers were cleaned in piranha bath to remove organic contaminants. Then wafers were cleaned in hydro-fluoric acid (HF) bath to remove native oxide on silicon. Wafers were first coated with 50 nm of silicon dioxide with wet-oxidation furnace. Since silicon dioxide has etch selectivity of 1:100 against XeF_2 compared to silicon, this small amount of silicon dioxide protects underside of wafer during bolometer release process. After deposition of silicon dioxide, wafer was transferred to low pressure chemical vapor deposition (LPCVD) furnace, where 1.0 μm of low stress nitride (LSN) was formed. Stress is monitored periodically to make sure the film has less than 300 MPa of stress. Low stress film allows fabrication of bolometer's weak link without breaking. The furnace provide LSN film less than 1% variability in thickness across a wafer. However, unlike 100 mm wafer process, wafer to wafer uniformity varied as much as 0.2 μm for same run depending on where in furnace wafer was located. We fabricated many small batches to obtain consistent thickness.

We etched low stress nitride in reative ion etcher (RIE) with CF_4 gas. Previously it was etched with SF_6 and small amount of O_2. We found that oxygen in plasma burned photoresist enough

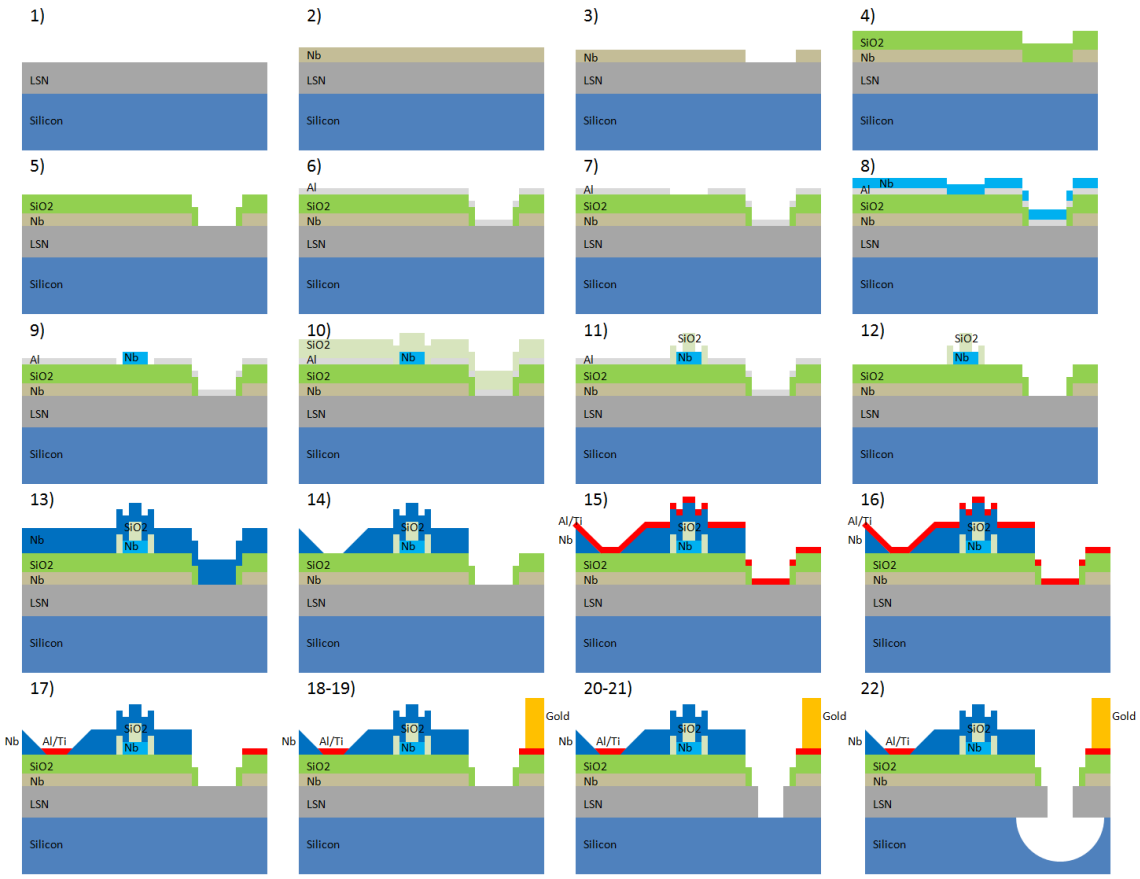

Figure 5.38: Step by step cross-section of fabrication. Step number corresponds to step ID in Table 5.3

during the process. Niobium was exposed as a result, and niobium was destroyed by XeF_2 gas in the following release process. We looked for alternative gas that etches LSN without burning photo-resist. We had successful fabrication with CF_4 plasma etch on LSN.

Niobium

Niobium was put down by DC Magnetron sputter machine. Chamber pressure during deposition was adjusted to 3 mTorr to control film stress. Machine was originally designed for 100 mm wafer. So we designed new 150 mm diameter chuck, and we tested film uniformity. The machine has a rotating magnet that modulates plasma during deposition to make deposition more uniform. Even with the rotating magnet, there was 10% difference in relative thickness radially across wafer with center being thicker.

We experimented with two different machines for niobium etch. First machine was a reactive ion etcher, RIE system 1000 TP, from the SEMI group. The machine has a 12 inch chuck that has

Step ID	Process	Machine	Thickness [μm]
1	Low stress nitride	LPCVD (furnace)	1.0
2	Deposit groundplane Nb	DC magnetron sputter	0.3
3	Etch groundplane Nb	CF_4 RIE	
4	Deposit microstrip SiO_2	350°C PECVD	0.51
5	Etch microstrip SiO_2	CHF_3/O_2 RIE	
6	Deposit mask Al	DC magnetron sputter	0.08
7	Etch mask Al	Pre mixed wet etch	
8	Deposit crossover Nb	DC magnetron sputter	0.2
9	Etch crossover Nb	CF_4 RIE	
10	Deposit crossover SiO_2	350°C PECVD	0.26
11	Etch crossover SiO_2	CHF_3/O_2 RIE	
12	Remove mask Al	Pre-mixed wet etch	
13	Deposit microstrip Nb	DC magnetron sputter	0.51
14	Etch microstrip Nb	CF_4 RIE	
15	Deposit Al/Ti bilayer	DC magnetron sputter	0.04/0.08
16	Etch Ti	SF_6/O_2 RIE	
17	Etch Al	Pre-mixed wet etch	
18	Deposit Au	Electron beam evaporation	1.5
19	Lift-off Au	Two-layers photo-resist	
20	Etch low sress nitride	CF_4 RIE	
21	Dice wafer	DISCO dicing saw	
22	Release bolometer	XeF_2	

Table 5.3: Summary of fabrication steps. Step ID corresponds to step number shown in Figure 5.38.

very uniform plasma for central 6 inch (150 mm). It also has a turbo pump to achieve high base pressure. We found experimentally that it is important to have low base pressure to successfully etch lines that are less than two micron. The machine also has end-point indicator, such that we can accurately stop the etching process. During etch process, we flow CF_4 and small amount of O_2 to create slanted edge profile for step coverage and minimize current dependant loss due to kinks in transmission line. Because of oxygen, the machine has a tendency to make a line thinner by 0.3 μm to 0.5 μm. We design lines thicker to counter this thinning effect. We checked if such thinning happened uniformly across wafer, as one of the effect we worried about was change in inductance for lumped inductor of a filter. Lines had less than 0.3 μm variation in width, which translates to 2% shift in center frequency. We have 10% tolerance from the microstrip optimization process, therefore such variation is acceptable. Second machine we looked at was inductively coupled plasma (ICP) etching machine from Lam research. Its casette-to-casette fully automated system with loadlock makes the etch process very repeatable. It has helium cooled chuck which keeps temperature of wafer low during etching. It reproduced lithographed line to 0.1 μm accuracy with

high uniformity across wafer. We fabricated wafer using both machines successfully.

Silicon Dioxide

Silicon dioxide was deposited with plasma enhanced chemical vapor deposition process. The process forms silicon oxide on 350 °C wafer with silane and nitrous oxide. Chuck that holds wafer bows from film stress. Bowed chuck heats wafer unevenly, and this causes thickness of oxide on wafer to be non-uniform. It was crucial to keep flatness of chuck to deposit even film. In the end, we were able to put down film that had uniformity of 1% across wafer. This directly affects capacitance in filter and impedance of microstrip line, but 1% change in thickness translated to negligible effect.

We etched silicon dioxide in RIE with CHF_3 and O_2. There was significant etch non-uniformity that caused edge of wafer to be etched more. This caused niobium ground plane that is underneath silicon dioxide to be etched away at edges. For antenna pixels, this is not a problem since we would removed such niobium anyways, however we wanted to keep niobium ground plane at boarder of hexagonal array such that we can make continuous ground shield. To solve this problem, we did lithography and etching of border separated from antenna pixels such that we could stop etch right at niobium groundplane for both cases.

Aluminum Titanium Bilayer

AlTi bilayer was deposited using DC magnetron sputter. Two targets coexist in same vacuum chamber. Therefore titanium could be deposited on aluminum without oxide layer formation. This was important for proximity effect to occur. Prior to the bilayer deposition, niobium oxide was removed from niobium strip line by argon RF sputter. Niobium oxide must be removed since it is a semiconductor that would act has insulator at cryogenic temperature. AlTi bilayer's transition temperature was sensitive to change in various machine parameters that we never had single recipe that gave consistent transition temperature. To solve the issue, we prepared samples with various aluminum thicknesses. We quickly measured its T_c, and deposited bilayer with the recipe that gave desireble T_c. Deposition machine retired this year, and new replacement machine was installed. We took the opportunity and installed manganese-doped aluminum target into the machine. Manganese-doped aluminum was reported to have reproducible T_c. Its T_c could be tuned by amount of manganese doping[113, 118]. In near future, aluminum manganese target should be characterized with the machine in nanolab to test its feasibility.

We etch titanium in RIE with SF_6 and O_2 plasma. We rely on aluminum under titanium to act as an etch stop. Since aluminum is very thin, we found it was important that niobium etch in previous step had smooth finish such that aluminum was able to cover entire wafer with no pinholes. Pinholes in aluminum causes niobium underneath to get attacked by SF_6 plasma during titanium etch. Aluminum is wet-tched by premixed chemical. Calibration of underetch versus etch time is important to obtain desired resistance for the load resistor. Our typical value was 1μm of undercut per 1 minute of soak.

Gold

Since gold cannot be plasma etched, we use photo-resist lift off process to pattern gold. We create overhang structure by using two different kinds of photo-resist. First we deposit 2 μm of G-line photo-resist, then we deposit 1.2 μm of I-line photo-resist. After a wafer is lithographed, we developped the wafer with developper for I-line resist. This will create accurate pattern on I-line, but it will undercut G-line resist. Thus there will be overhung structure. This allows gold that would be left behind to not be in physical contact with photo-resist. Also it creates a *window* for acetone to get underneath gold to remove photo-resist away. We deposit gold using electron beam evaporator. Power of electron gun is kept low to prevent photo-resist on wafer from burning onto wafer. Deposition thus takes few hours. For future fabrication, we would like to increase time constant of bolometer. To obtain enough heat capacitance while keeping volume of bling small, we explored palladium that is known to have higher heat capacitance than gold [103]. Evaporation of palladium requires higher temperature than gold, so deposition rate and condition of photo-resist after evaporation needs to be evaluated in future fabrication.

Crossover

Aluminum mask was used for fabrication of a crossover. Prior to making the crossover on a wafer, LSN, niobium groundplane and silicon dioxide for microstrip line is layed down on a wafer. We did not want to have etch on niobium layer for crossover to stop on the silicon dioxide as that would reduce the thickness of silicon dioxide slightly. To solve the problem, we masked most of wafer with aluminum such that niobium etch would stop on aluminum. Aluminum does not get etched with fluorine plasma used for niobium etch. We left window in aluminum that is just big enough to form crossover as shown in Figure 5.37. Aluminum wet etches away cleanly after crossover is formed in the window.

Bolometer Release

Bolometer island is released by removing silicon underneath the bolometer with XeF_2 gas. Since released bolometer will be fragile, we dice wafer into hexagonal shape prior to the release. Wafer is dried in an oven since HF forms when water molecule reacts with XeF_2 gas which would then destroy structures on wafer [11]. During etch, we monitor its progress and uniformity using release structure shown in Figreu 5.39. Test structure has identical dimension as actual bolometer island. Niobium ground plane is removed at the test structure, such that it is possible to see through silicon oxide and silicon nitride to monitor how much silicon is left under the bolometer island. Rectangular section left in middle of bolometer island as shown in Figure 5.39 is portion of silicon that is not removed yet. Using such structure, we were able to accurately tell end point and release uniformity. Uniformity across wafer is ± 5 μm. It is negligible error compared to total bolometer leg-length l.

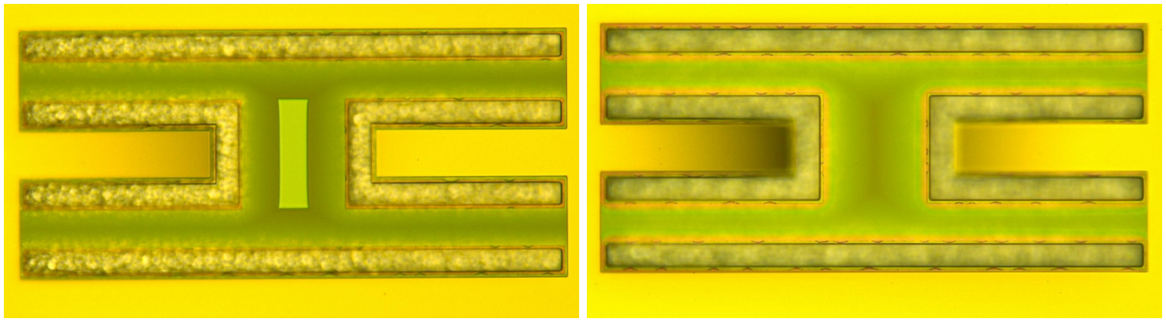

Figure 5.39: Microscope photograph of half released bolometer (left) and fully released bolometer (right). Ground plane was removed from bolometer such that silicon underneath is visible. Half-released bolometer shown unetched silicon under low stress nitride.

Cleaning

After bolometer is released, photo-resist is ashed away with oxygen plasma in RIE. We found it is very important to throughly remove photo-resist from wafer. We left wafer coated with photo-resist for few month, and we found that aluminum TES dissappeared possibly due to reacting with photo-resist or other residue chemicals. When wafer is cleaned extensively with oxygen plasma immediately after bolometer release, aluminum TES had no problem.

5.11 Lenslet Array

Development of lenslet array was based on POLARBEAR-1 design [102]. We collaborated with UCSD for the development of the POLARBEAR-2 lenslet. Bulk of work was done by UCSD team, so we just summarize the work. Major changes for lenslet array of the POLARBEAR-2 are the size of the array. 150 mm wafer was used to fabricate a *seating wafer*, a wafer with pockets for silicon lenslets. To accurately align lenslet, we etch approximately 100 μm deep pocket that has 20 μm larger diameter than lenslet. This gives 10 μm accuracy in alignment. Depth of pocket was chosen such that thickness of silicon that is left plus thickness of device wafer would equal to the extension length. To minimize loss, we use high-resistivity silicon hemisphere. AR coating was applied on the lens prior to populating the array. Then each lenslet was fixed to each pocket with small amount of stycast 2850FT. Figure 5.40 shows scanning electron microscope photohraph of seating pocket and partially populated lenslet array. Recipe for silicon trench etch was tuned to give maximally flat surface to prevent air gap between lenslette and seating wafer.

5.12 Module Design

Device wafer and lenslette array were put together in holder made from invar. We chose to use invar since its thermal contraction matches silicon's thermal contraction. We align device water and

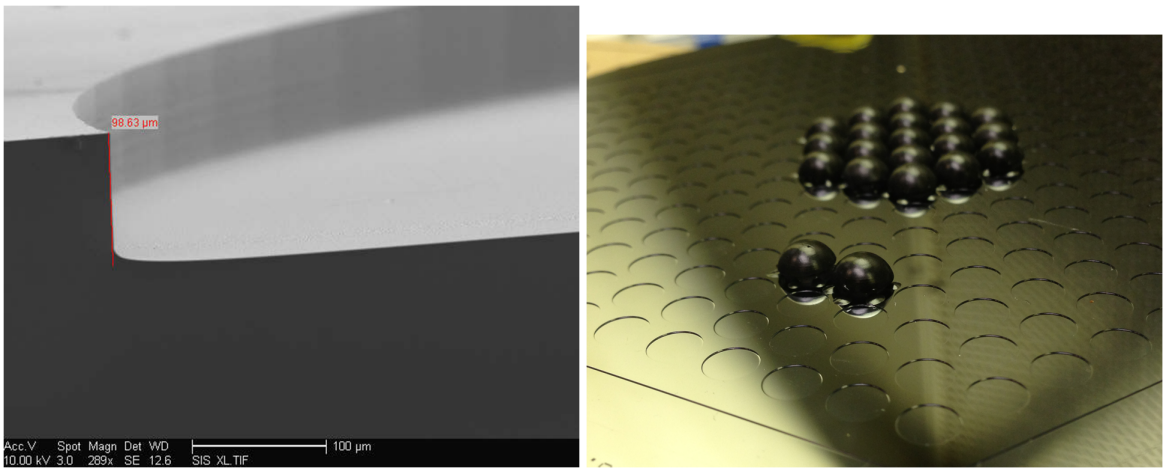

Figure 5.40: (left) SEM photograph of seating wafer cross section. (right) Photograph of partially populated lenslet array. Cortesy of Praween Siritanasak

lenslette array using infrared optical microscope as shwon in Figure 5.41. Wafer was illuminated from bottom with halogen lamp. Infrared from halogen lamp transmit through silicon, but infrared light get blocked by niobium. We etch slot in niobium to let some light through, and transmitted infrared light is captured by CCD. At the same time, optical image of seating wafer is captured from top. Thus we can overlay two images to align two wafers together. We etched 40 μm wide slot into niobium and seating wafer. As shwon in Figure 5.41, we consistently aligned device wafer to lenslette to 10 μm accuracy. We thermal cycled aligned wafer many times, and we verified that wafers stay aligned.

Invar holder

Design for POLARBEAR-2's invar holder was based on POLARBEAR-1's design [60]. We collaborated with KEK to develop invar holder for the POLARBEAR-2. Since invar holder holds wafers that are very brittle, we worried about its flatness. Invar was heat treated to remove its stress prior to machining. Machining was then done carefully to not apply stress into material. As shown in Figure 5.42 and 5.48, structure has large opening. Since the holder is twice as big in diameter as POLARBEAR-1 design, we made invar holder about twice as thick to keep its flatness. Thick holder also helps to give extra room behind antenna which turned out to be important for beam synthesis.

Backshort

Wirebond pads on device wafers are placed at the edge of wafer. Initially we considered wirebonding directly to a bondpad at a pixel from behind. To test this idea, we made printed circuit

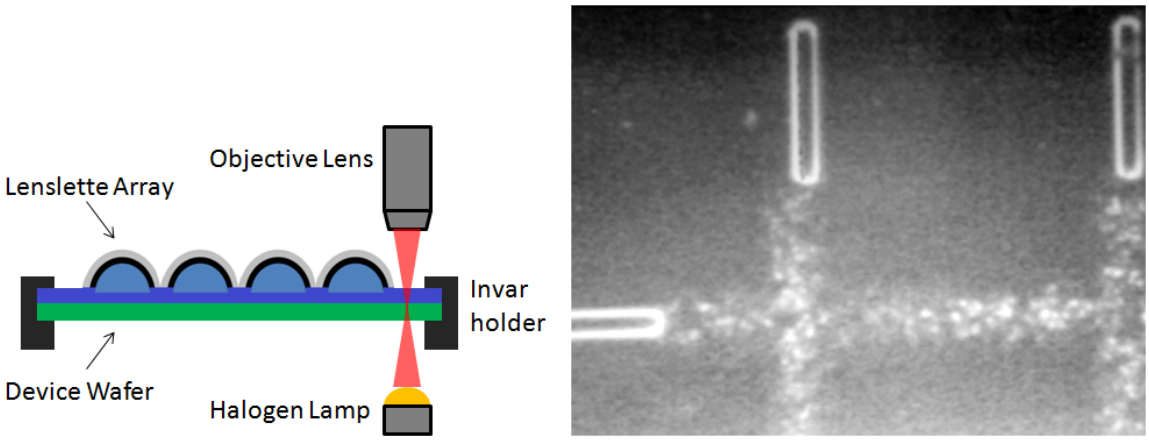

Figure 5.41: (left) Schematic drawing of alignment process. Device wafer and lenslet array wafer is mounted in an invar holder. Then alignment marks etched in both wafers were aligned with IR microscope. (right) Photograph of two alignment marks being aligned. Fuzzy cross mark is from device wafer. Sharper stub is from lenslette wafer.

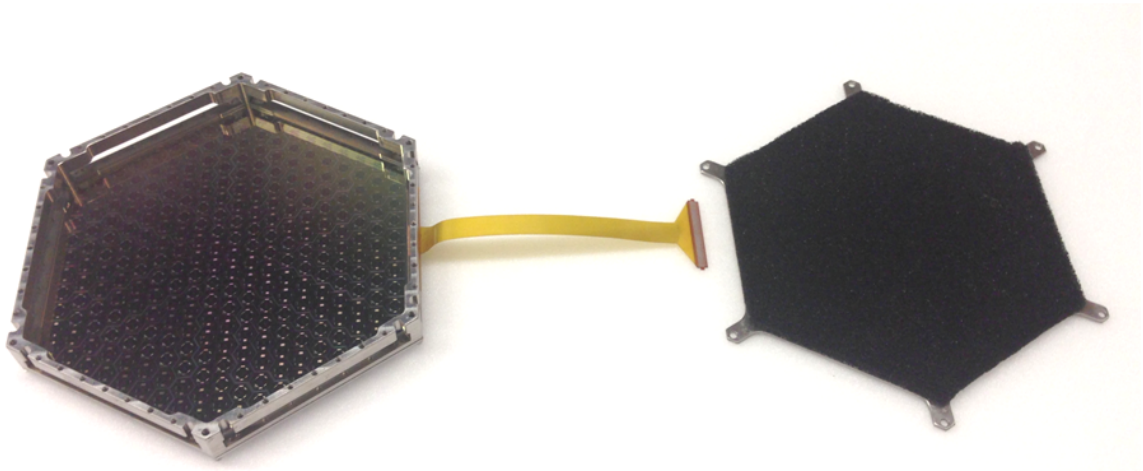

Figure 5.42: Photograph of detector wafer mounted in invar holder. Proto-type readout flexible cable is also attached. Backing plate is shown on right with ANW-72 absorber attached.

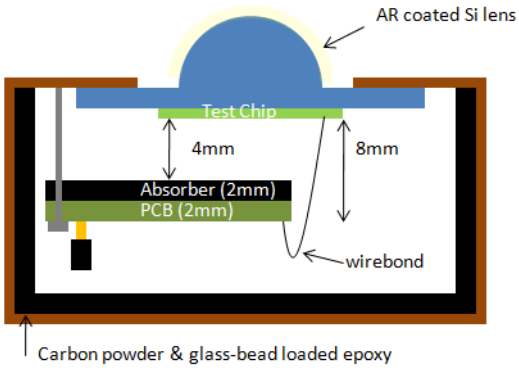

Figure 5.43: Schematic drawing of absorber test setup.

Absorber	TE reflectivity on aluminum at 150 GHz
Loaded epoxy	$\approx 20\%$
HR-10	$< 3\%$
ANW-72	$5\% - 15\%$

Table 5.4: Reflection of absorbers at 150 GHz [120].

board structure that hovered behind pixel. Then we wirebonded from the printed circuit board to a test pixel. Since printed circuit board has metal traces we thought it would be good idea to apply absorber on surface as shown in Figure 5.43. First we applied stycast 2850FT loaded with 175 μm diameter glass beads and carbon powder [18]. It gave distorted beam as shown in Figure 5.44. We then realized such loaded epoxy was excellent infrared absorber, but it is not an absorber at 150 GHz as shown in Table 5.4 [120]. According to the table, HR-10 would be the best material, but HR-10 is very fragile and porous to be used in tight space. Thus we removed loaded epoxy from the printed circuit board and re-coated it with ANW-72. We measured round beam with ANW-72 coating. We did not end up using this *3-D* readout scheme. This exercize gave us important information that we need to terminate antenna's backlobe with good absorber. The POLARBEAR-2 decided to use ANW-72 to better terminate antenna's backlobe for a better beam shape.

5.13 Readout Component Fabrication

We use frequency multiplexing to readout 36 bolometers per SQUID. Key components are inductors and capacitors that defines frequency of the readout. As we discussed in Section 4.6, we want to minimize loss in capacitor to minimize parasitic resistance in capacitor. We fabricated interdigitated capacitor on high-resistivity silicon that is reported to have loss-tangent of 2×10^{-4} at

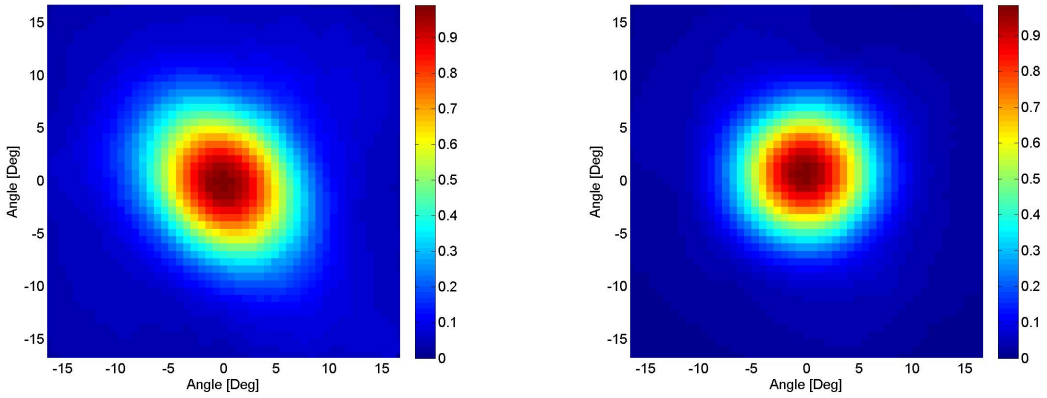

Figure 5.44: Beam from backshort testing. Beam with carbon loaded stycast as absorber material is shown in left. Beam with ANW-72 as absorber is shown in right.

4 Kelvin [65]. Fabricating interdigitated capacitor has benefit over parallel plate capacitor that it is simpler process since it only requires one metal layer. Since we use microfabrication technique to define lines for interdigitated capacitor, its relative value is tightly controlled. It is difficult to achieve high capacitance with interdigitated capacitor. We addressed the problem by fabricating interdigitated capacitor with long and thin fingers. Fingers are as wide as 5 μm and 4 mm long. Each capacitor has these narrow fingers covering approximately 4 mm times 5 mm rectangle. The POLARBEAR-2 also requires higher inductance value to increase Q of resonators to pack more channels in available bandwidth. Thus we fabricated 60 μH square spiral inductor. Inductor also required 5 μm line curled up inside of 4 mm square to get to high inductance. Inductor fabrication is also single layer process. We fabricated inductor and capacitor on same wafer.

We started by cleaning high resistivity wafer in piranha and HF to remove contaminants and native oxide from surface of wafer. After cleaning, we immediately load wafer into vacuum chamber of niobium sputter machine. After depositing 0.3 μm of niobium, wafer get patterned with GCA stepper. We etched niobium with ICP etcher since ICP etcher reproduced lithorgaphed line width better. After etching, wafer get diced into individual dies. Fabricated wafer is shown in Figure 5.45.

We tested fabricated chips in simple voltage-divider circuit shown in Figure 5.46. At resonance frequency, inductance and capacitance should get tuned out and we can make measurement of equivalent series resistance (ESR) of capacitor by measuring voltage across R_1 and R_2. Measured ESR is plotted as function of frequency in Figure 5.46. Measured values were consistent with $\tan(\delta) = 2 \times 10^{-4}$. Thus it meets the loss requirement.

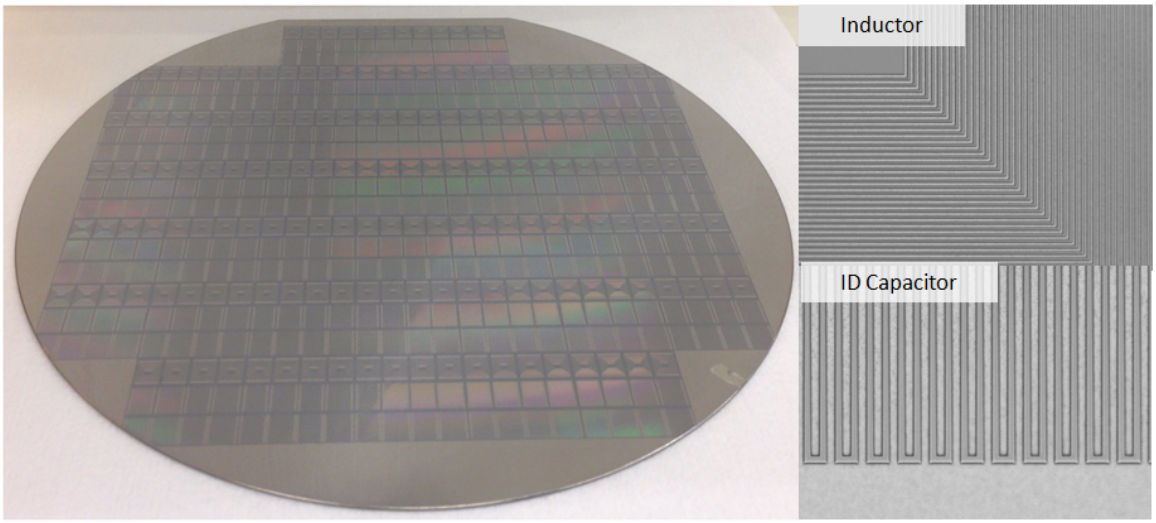

Figure 5.45: Photograph of wafer with interdigitated capacitor and inductors. Zoomed in microscope photograph is shown on right

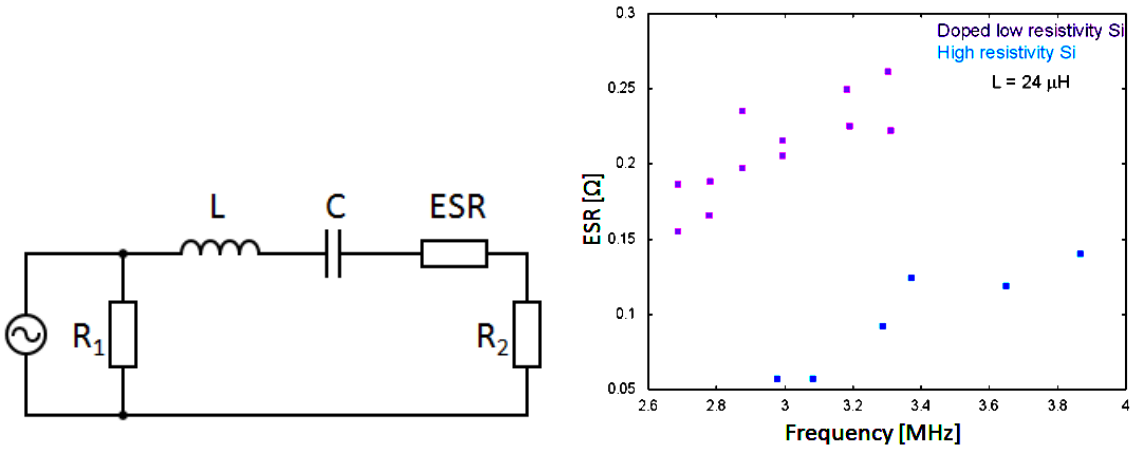

Figure 5.46: (left) Circuit diagram for ESR testing (right) Result from ESR testing is shown on right. Loss from interdigitated capacitor fabricated on high resistivity silicon is lower.

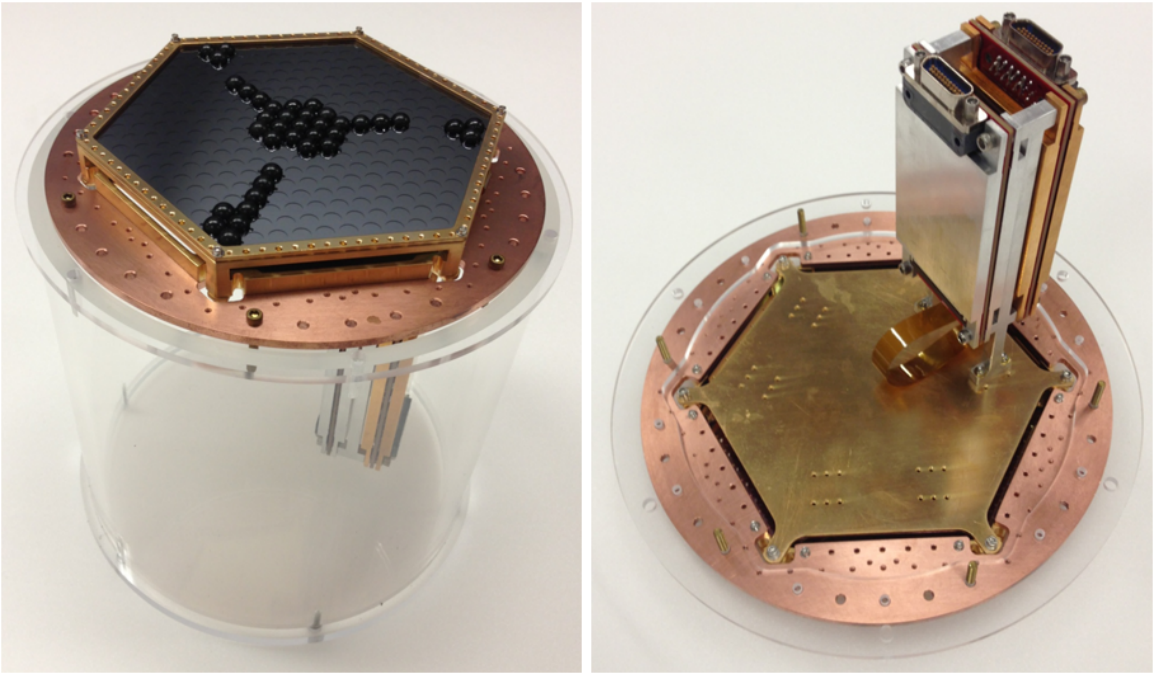

Figure 5.47: Photograph of POLARBEAR-2 detector module assembly with proto-type lenslet arrays and read-out board from the SPT-pol experiment

POLARBEAR-2 Detector Module

Figure 5.47 shows the proto-type detector module assembly. At the time when the photograph was taken, read-out printed circuit board was not ready. Thereore, we designed readout cable to be compatible with the SPT-pol read-out board. In future, we will populate the detetor array with the POLARBEAR-2 original design to fully readout all detectors.

5.14 Shipping case

POLARBEAR-2 would have many detector modules that it requires more than one institution to perform detector module testing. To make this possible, we designed shipping case that would protect detector module. We made it out of acrylic plastic such that we can see condition of the module without disassembling the case. Case has tubuler shape to make it strong. We put the case inside of foamed pelican case for futher protection as shown in Figure 5.48. To test the case, we mounted dummy silicon wafer in invar holder. We shipped to Colorado, UC San Diego, Japan, Canada and back to Berkeley. At each institution case was opened and inspected. Wafer survived shipping, and it came back to Berkeley safely.

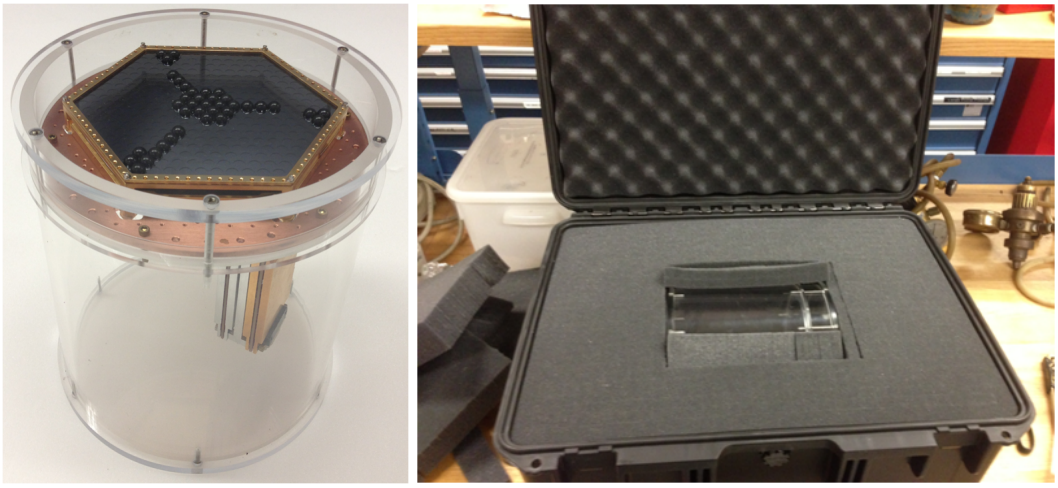

Figure 5.48: Photograph of plexiglass shipping container (left). Shipping container inside foamed case (right).

Chapter 6

Detector Characterization

6.1 Introduction

We describe detector characterization in this chapter. We will discuss how test apparatus were designed and used. We will then discuss results from measurements.

6.2 Dewar

Our detectors are designed to operate at 250 milli-Kelvin. Dewars were designed to transmit millimeter wave into dewar while meeting thermal requirement by cutting down thermal loading from infrared. In this section we will describe two dewars we used for testing.

8 inch IR-Lab Dewar

We tested the prototype pixels in an 8 inch IR Labs dewar. Dewar of this size was useful for prototype testing since it only takes eight hours to reach milli-Kelvin temperature from room temperature. We modified the dewar by adding a 4 inch diameter optical window made from Zotefoam PPA30. For infrared filters, two layers of 0.125 inch thick expanded teflon and a metal mesh low pass filter with 18 cm^{-1} cut off are anchored to a liquid nitrogen temperature [126]. Two metal mesh low pass filters with cut off at 14 cm^{-1} and 12 cm^{-1} are mounted at liquid helium buffer to further reduce the optical loading. The milli-kelvin stage is isolated from the liquid helium buffer with thin walled vespel tubes. The stage is cooled to 250 milli-Kelvin with homemade 3He adsorption fridge. Cross section of dewar is shown in Figure 6.1.

Readout Electronics

Bias voltage for bolometer was provided by simple circit shown in Figure 6.2. Small shunt resistor with 0.02 Ω that is parallel to a bolometer with typical resistance of 1 Ω provides voltage bias on a bolometer. We create voltage divider with 2K Ω room temperature resistor and 0.02 Ω bias resistor,

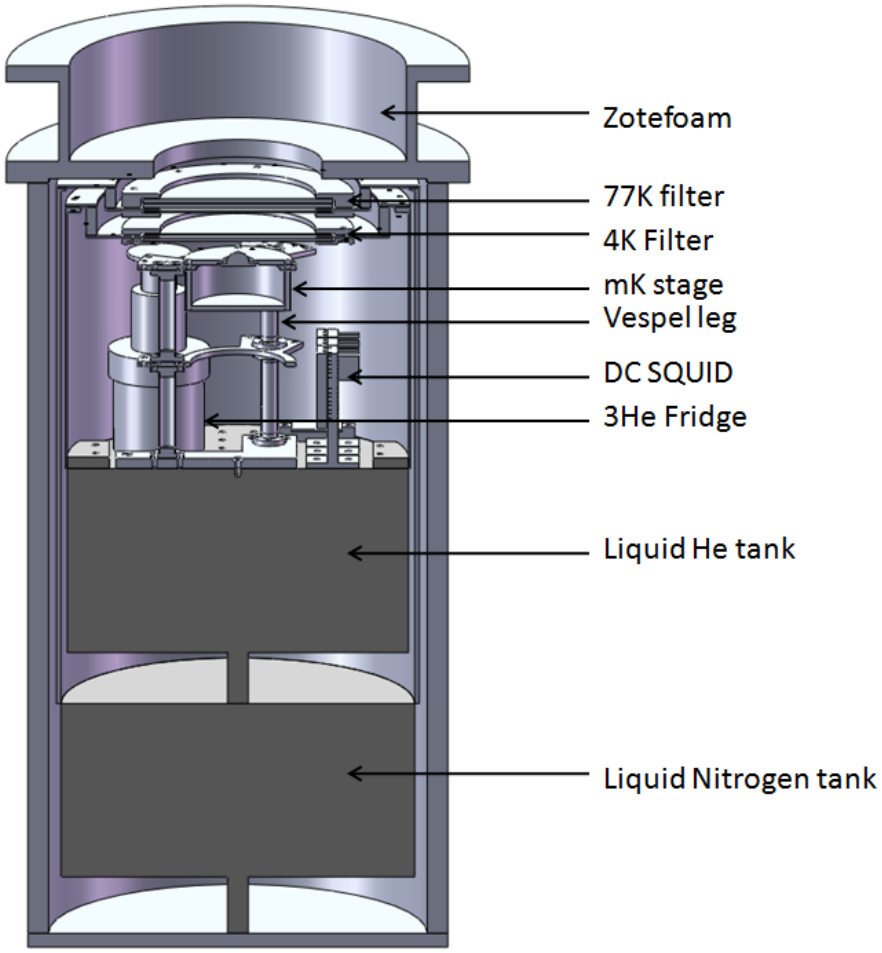

Figure 6.1: Cross section of 8 inch IR Labs dewar. Milli-Kelvin stage is buffered by liquid nitrogen and liquid helium stage. 250 milli-Kelvin base temperature is probided by 3He adsorption fridge. Dewar was modified with Zotefoam window and thermal filters to pass millimeter wave into the dewar.

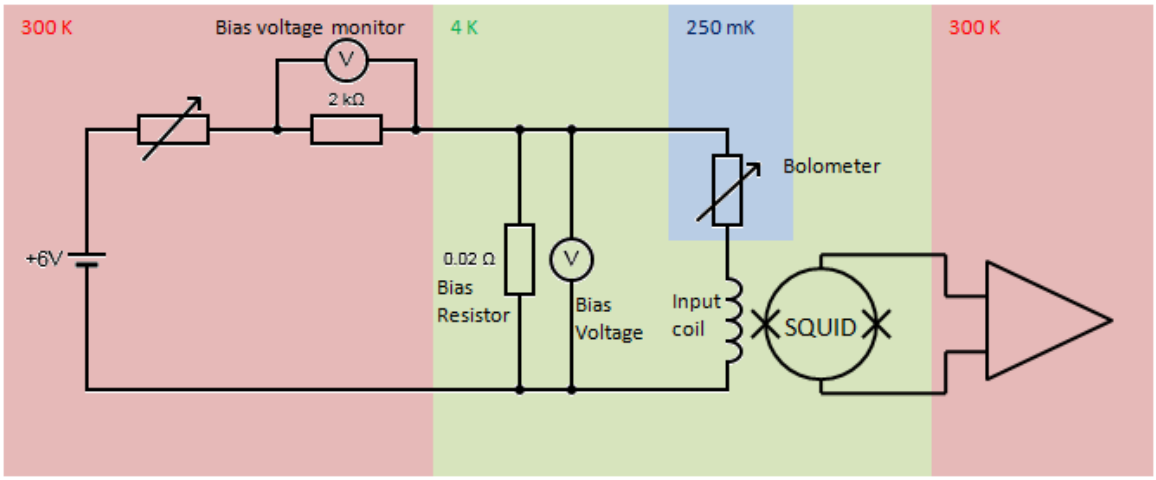

Figure 6.2: Circuit diagram for readout electronics. Colors separate circuit at different temperatures.

thus we can monitor bias voltage across bolometer by looking at voltage across 2K Ω resistor and multiply by 10^{-5}. Current through the bolometer is read out by commercially available laboratory DC SQUID from Quantum Design with its input inductor coil in series with the bolometer [101]. It is important to use superconducting line beyond bias resistor to keep voltage bias on bolometer.

Large lens test

We performed initial tests with a 14 mm diameter lens. Large lens was useful since it produced narrower beam that was easier to couple to test apparatus. For tests with a large lens, we mounted the test pixel behind the 14 mm diameter hemispherical silicon lens with 2.5 mm thick flat silicon spacer. The test pixel was fabricated on top of 0.675 mm thick silicon, thus combination of spacer and the test pixel locate the antenna at the elliptical focus. Test chip was aligned to spacer under microscope. Test chip and spacer were fixed to each other by GE varnish. We applied thermoformed quarter wavelength thick Ultem-1000 plastic on the lens for an AR coating. It gets mounted on circular copper plate on milli-Kelvin stage, and pixel is enclosed by copper can with ANW-72 absorber inside as shown in Figure 6.3.

Lenslette array test

We then tested with lens size that is similar to what we would use in the field. For detector tests with smaller lenses, we fabricated three different sizes of wafers as shown in Figure 6.4. We fabricated the POLARBEAR-2 size, the POLARBEAR-1 size and two pixel sinuous detector arrays. Pixel spacing and size of the POLARBEAR-1 size sinuous wafer was same as the POLARBEAR-1 detector array, therefore we were able to use the POLARBEAR-1 spare lenslet array and invar holder to test sinuous detector with smaller lens. Milli-Kelvin stage was modified to accomodate

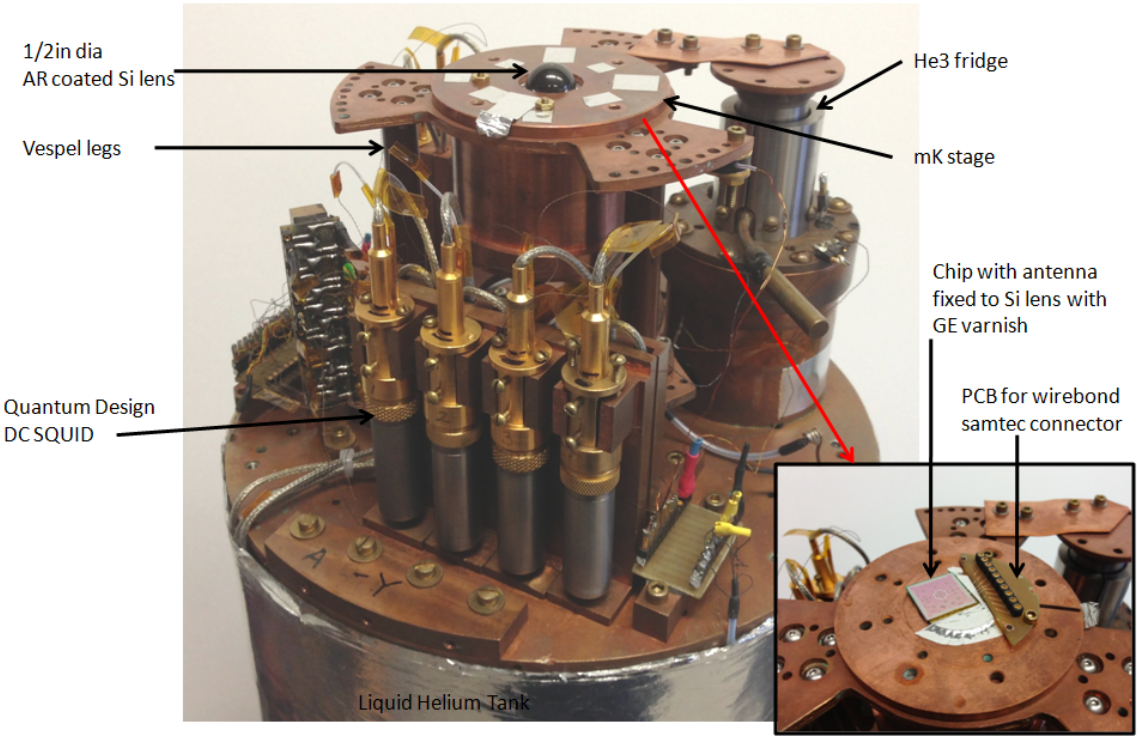

Figure 6.3: Photograph of large lens test setup. How detector pixel is mounted is shon on bottom right.

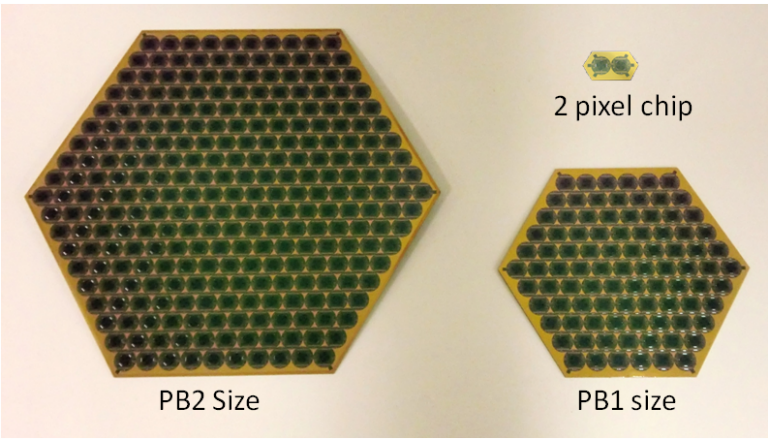

Figure 6.4: Photograph of fabricated detector wafers. We fabricated sinuous array in POLARBEAR-2 array size, POLARBEAR-1 array size and 2 pixel chip.

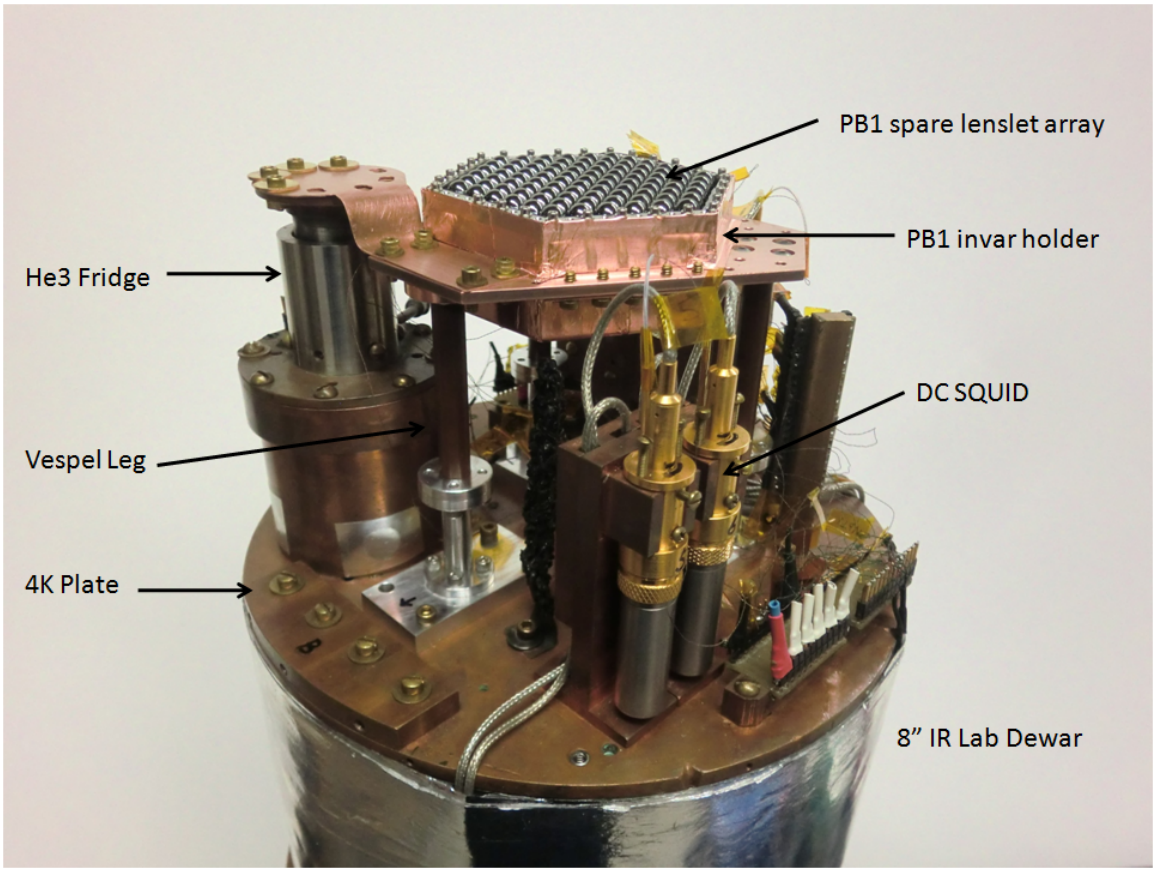

Figure 6.5: Photograph of POLARBEAR-1 size array test setup

the POLARBEAR-1 invar holder as shown in Figure 6.5. Invar holder's back plate was modified to mount wirebonding printed circuit board. We also fabricated separate backplate with ANW-72 as shown in Figure 6.6. We also fabricated small chip that has 2 pixels. Invar plate and seating chips were fabricated to align pixel to lenslette as shown in Figure 6.7.

POLARBEAR-2 Optical Test Cryostat

We tested the POLARBEAR-2 detector module in cryostat that was used for the APEX-SZ experiment [110]. Cross section of the dewar is shown in Figure 6.8. The dewar has two-stage Cryomech PTC410 pulse-tube to provide 35 watt of cooling power at 45 Kelvin and 1 watt of cooling power at 4.2 Kelvin [53].Three stage adsorption helium fridge from Simon Chase provide 350 milli-kelvin and 250 milli-Kelvin anchor point. We modified upper half of dewar from the original APEX-SZ design. We removed the lenses, and we increased aperture size such that there is enough viewing angle for every pixel to receive signal from outside of dewar. 300 Kelvin shell has 4 inch thick Zotefoam HD30 window. The window has 18 inch outer diameter and 12 inch inner opening.

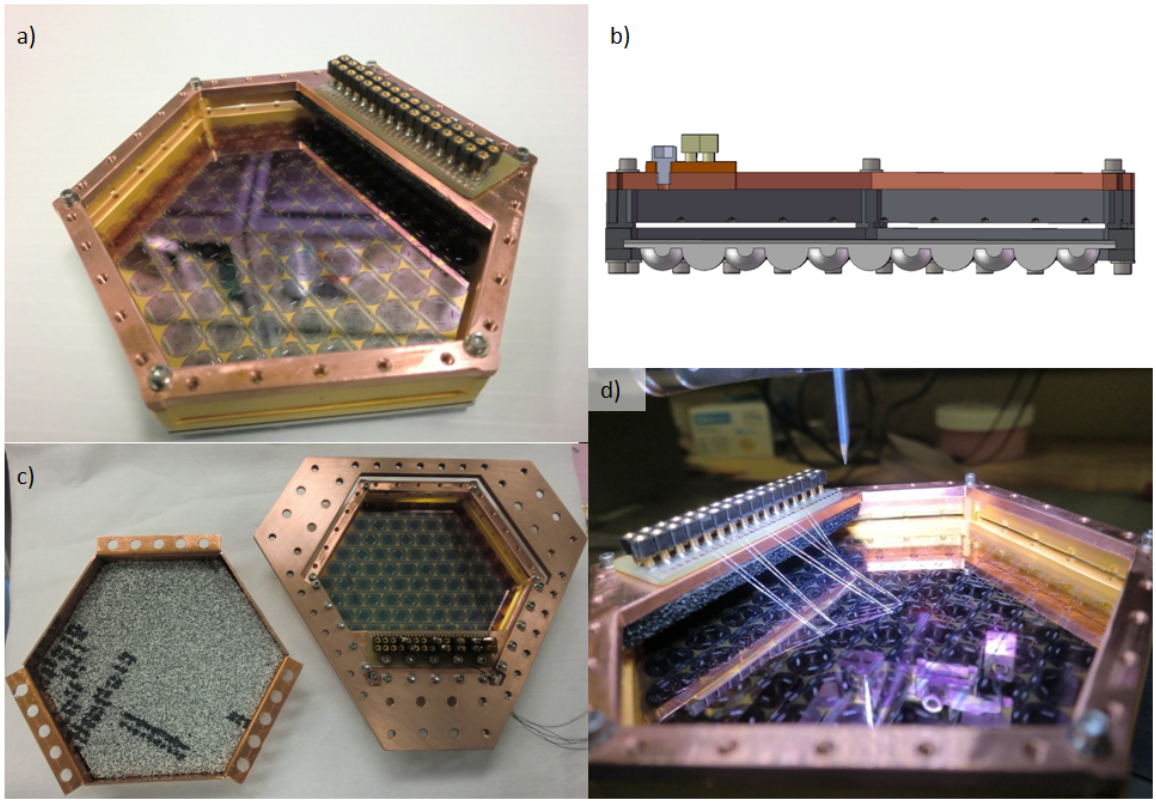

Figure 6.6: Photograph of POLARBEAR-1 size sinuous array mounted on invar holder. ANW-72 backabsorber terminates backlobe of antenna. Setup required long wirebond as shown in bottom right of the picture.

1 inch thick and 12 inch diameter teflon disk absorbs infrared radiation at 50 Kelvin stage. A metal mesh low pass filter with 10 cm^{-1} cut off are also anchored to the 50 Kelvin shell behind teflon. Four metal mesh low pass filters with cut off at 19 cm^{-1}, 15 cm^{-1}, 8.5 cm^{-1} and 5.7 cm^{-1} are anchored to 4 Kelvin shell. Finally metal mesh filter with cut off at 6.5 cm^{-1} is anchored at 0.35 Kelvin stage. Detector module is mounted on copper plate, and the copper plate is bolted onto 250 milli-Kelvin stage as shown in Figure 6.9.

Readout Electronics

Readout for detector module uses frequency multiplexing system. The circuit diagram is shown in Figure 6.10. For detector module test, we wanted to decouple readout development with detector development thus we used same readout system that was used for the POLARBEAR-1 [31].

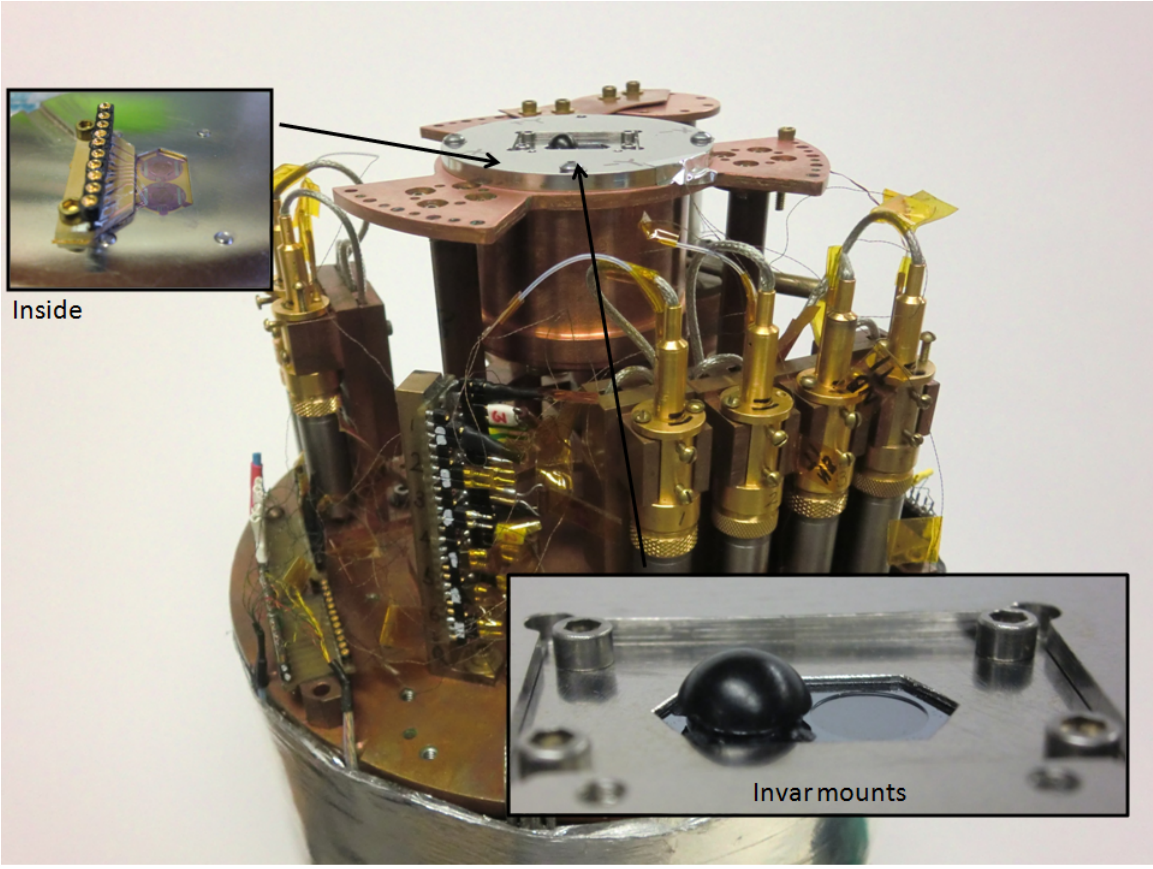

Figure 6.7: Photograph of small lens setup with 2 pixel detector array. Zoom in photo of custom invar holder is shown in bottom right.

6.3 Test Setup

Fourier Transform Spectrometer

We measured spectra of the device using the FTS. The FTS uses temperature modulated source with 800 Kelvin and 300 K eccosorb. Temperature modulated source was built with MS-1000 micro ceramic heater from Sakaguchi Dennnetsu [26]. Mirrors are 6 inch by 6 inch large in cross-section. Beam splitter was 0.010 inch thick mylar that has a beam splitter minima at 360 GHz. We focused the output of the FTS onto the pixel using spare POLARBEAR-1 collimating lens made from UHMWPE. The FTS has long enough arm to give 1 GHz resolution. The FTS setup is shown in Figure 6.11

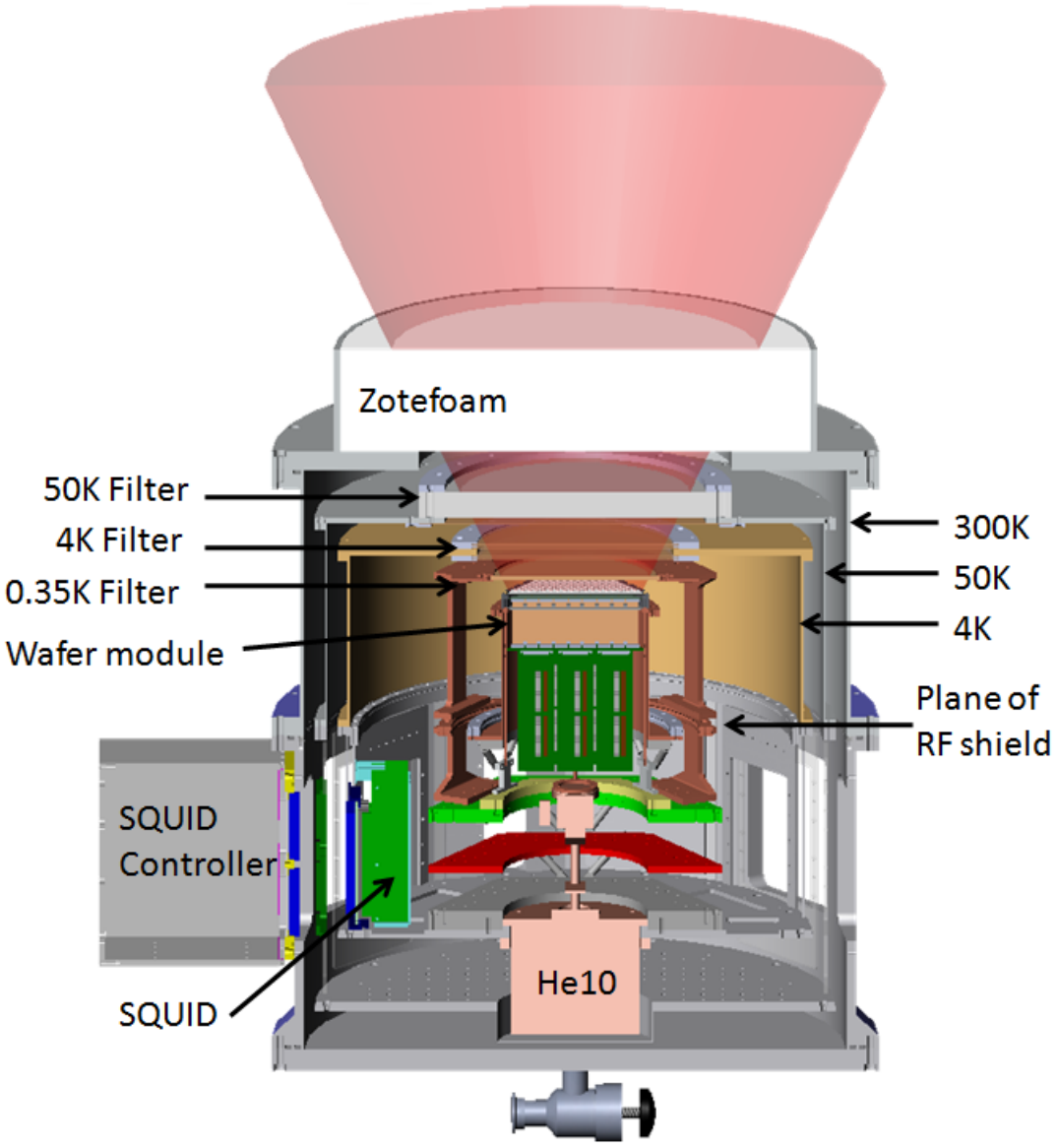

Figure 6.8: Cross section of POLARBEAR-2 optical test cryostat. Cooling power is provided by pulse-tube cooler. Milli-Kelvin temperature is provided by three-stage helium cooler. Dewar was modified from its original configuration used by APEX-SZ experiment by adding optical window and shells above plane of RF-shield.

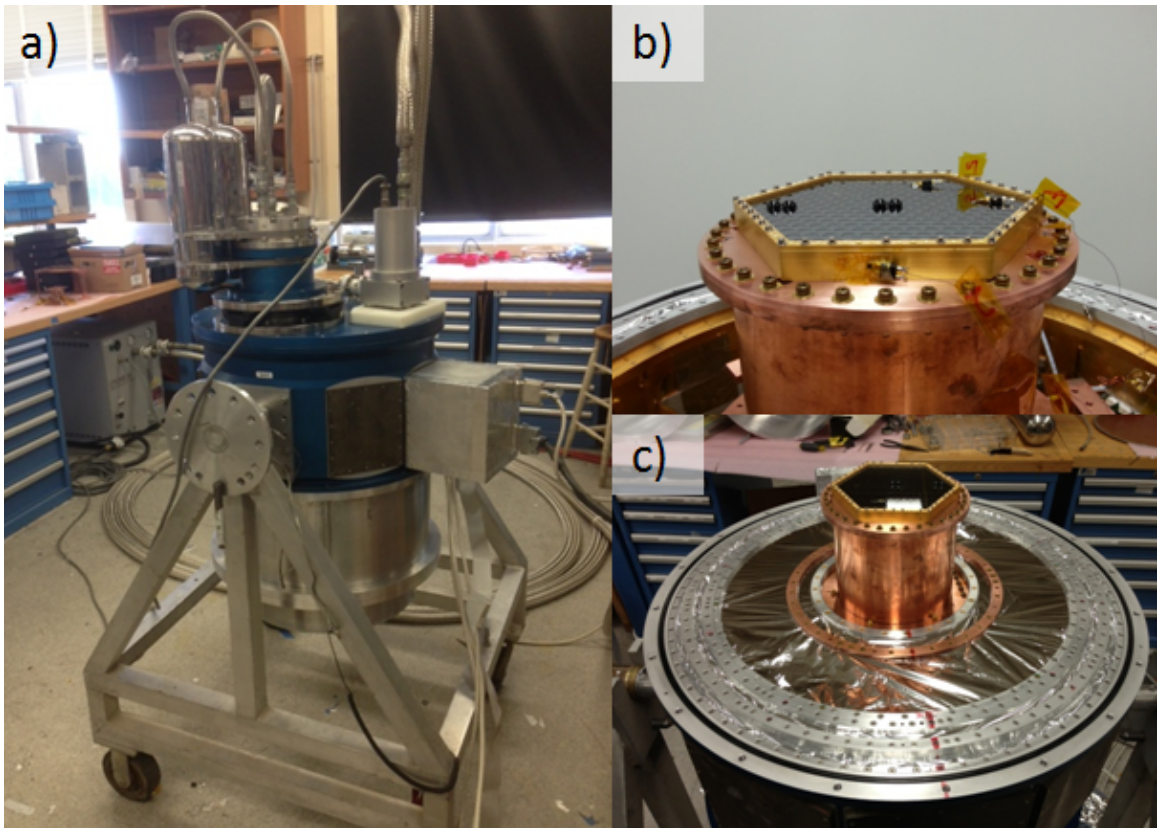

Figure 6.9: a) Photograph of POLARBEAR-2 optical test cryostat. b) Zoom in photograph of detector array mounted on milli-Kelvin stage c) Detector array mounted on milli-Kelvin stage with RF-shield installed.

Beam Map

We produced beam maps of the pixel by scanning 0.25 inch diameter temperature modulated source at 10 inches away from the antenna. The temperature modulated source is same as the one used for the FTS. We made modular source that has the ceramic source enclosed in a stainless steel box with chopper blade rotating on top. CAD for the source is shown in Figure 6.12. We scanned 3 inch $\times$ 3 inch patch with step size of 0.125 inch on motorized XY stage.

Polarization

We measured the response of the pixel to a linear polarized source by rotating wire grid polarizer between the pixel and the temperature modulated source. We made modular setup that rotates polarizer on top of beammap source as shown in Figure 6.12.

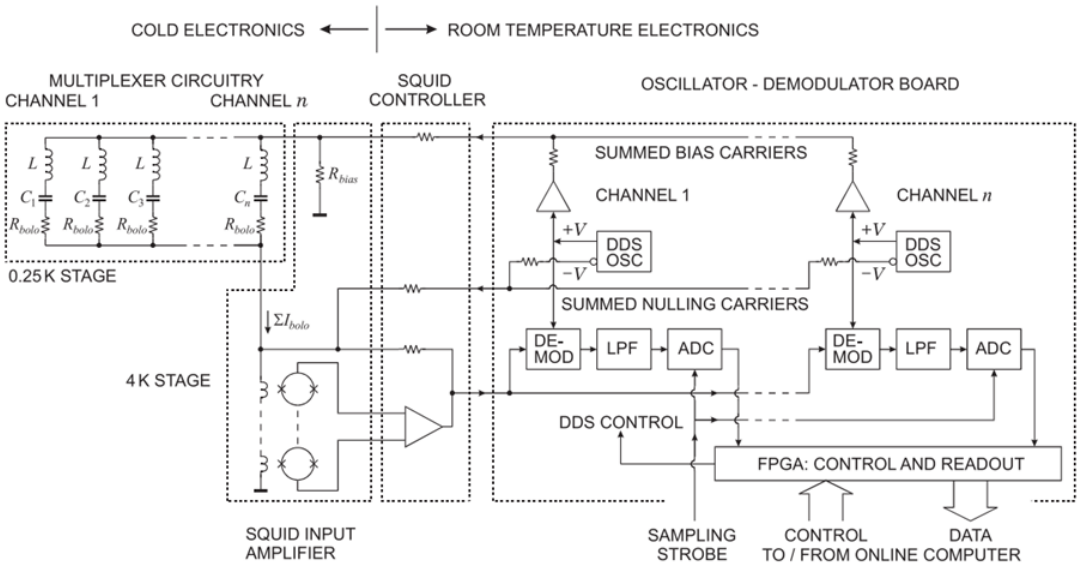

Figure 6.10: Circuit diagram of dfMUX readout system [31]

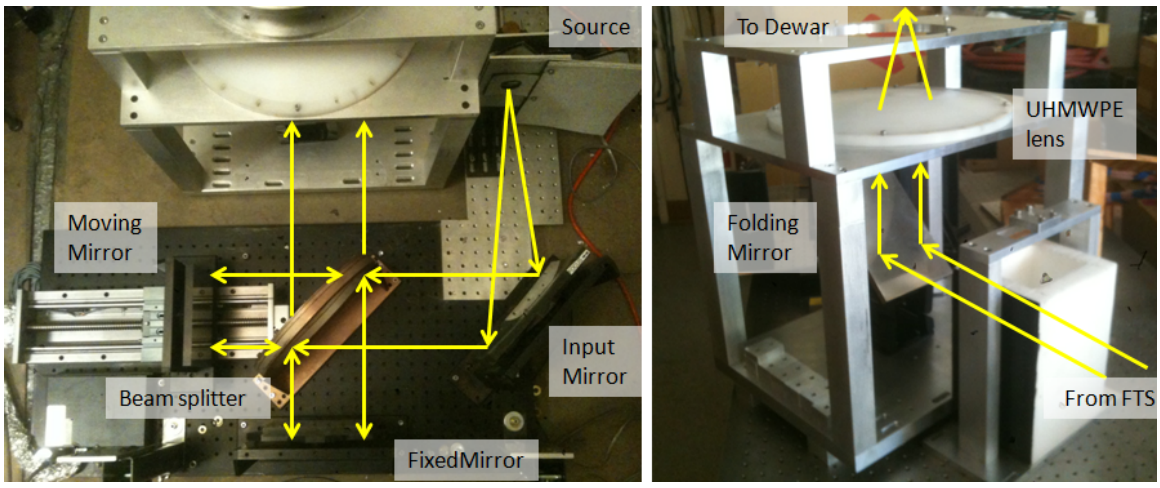

Figure 6.11: Photograph of the FTS setup. Output of FTS is reflected upwards by 45 degree mirror. Then beam was focused into dewar. When making band measurement of detector, sample holder shown on bottom right is removed.

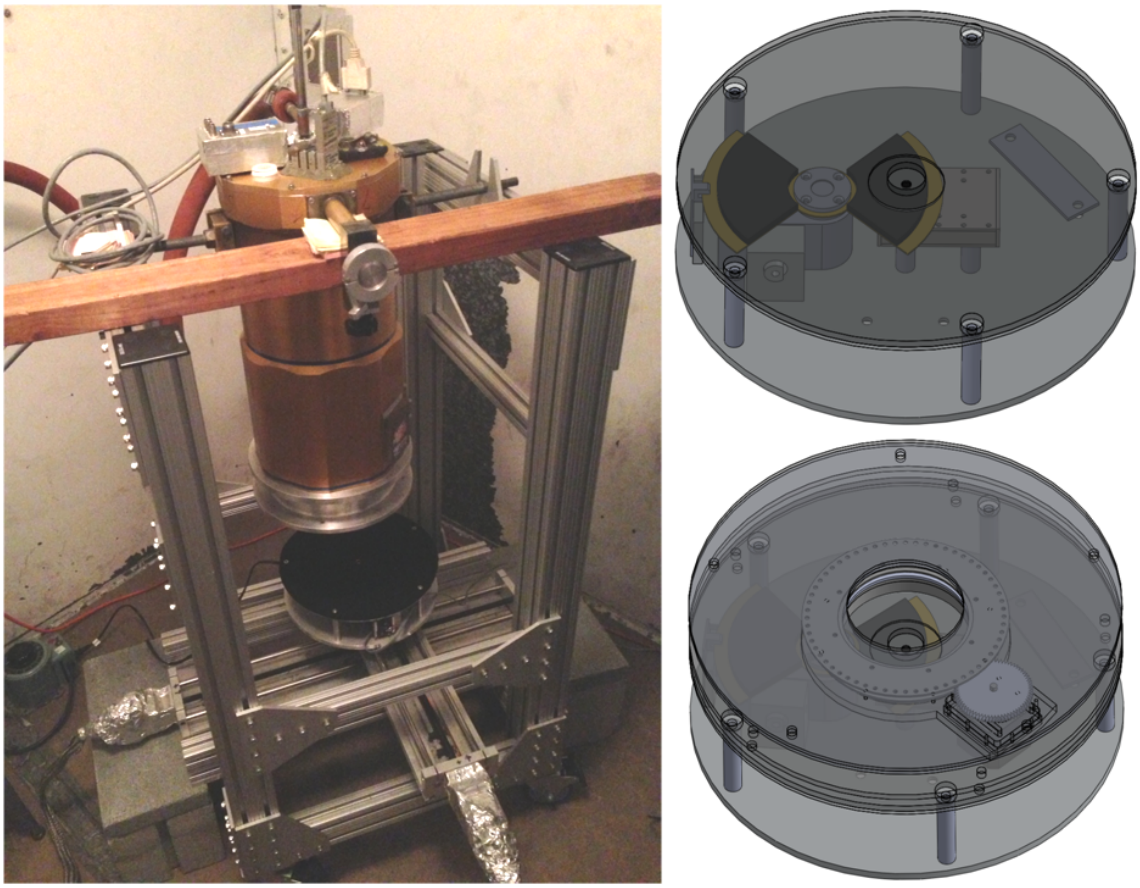

Figure 6.12: Photograph of the beam map measurement. Temperature modulated source (upper right) is mounted on X-Y stage. Polarization measurement was made at boresight by rotating wiregrid polarizer on top of temperature modulated source. CAD drawing of polarizer setup is shown on bottom right.

Efficiency

The efficiency of the device was measured with beam filling temperature modulated source. For a single moded antenna detector, the power difference between two temperature source is $k_B \Delta T \Delta \nu$ in the Rayleigh-Jean limit. Here k_B is the boltzmann constant, ΔT is the difference in temperature of modulated source. We used liquid nitrogen soaked eccosorb and room temperature eccosorb for $\Delta T = 223$ Kelvin. $\Delta \nu$ is the integrated bandwidth of the peak normalized spectrum measured with FTS. We divide power received on detector with $k_B \Delta T \Delta \nu$ to measure an end-to-end efficiency which includes dewar loss.

Filter Type	Number of Cell	Type of lenslette	Lumped Inductor
Lumped Diplexer	16	6.35 mm PB-1 spare array	Microstrip
Lumped Diplexer	16	14 mm	Microstrip
Lumped Diplexer	11	14 mm	CPW
Stub Diplexer	11	14 mm	N/A
Stub Triplexer	11	14 mm	N/A

Table 6.1: Summary of tested detectors

6.4 Result

Measurements presented here were made with the 8 inch IR-Lab Dewar. The POLARBEAR-2 optical cryostat is just coming online for testing, and it needs several calibration before we can make quantitive statement. We will present initial measurements from the dewar to demonstrate its capability of testing large detector module qualitatively. We present results from distributed diplexer with 11-cell sinuous antenna, distributed triplexer with 11-cell sinuous antenna, lumped filter diplexer with 11-cell sinuous antenna and lumped filter diplexer with 16-cell sinuous antenna with 14 mm silicon lenslette. We also present result from detector array with lumped diplexer and 16-cell sinuous coupled with the POLARBEAR-1 spare 6.35 mm silicon lenslette array. One of polarization for 16-cell sinuous detector had open at crossover due to fabrication error, thus we will present measurement from one polarization. The detector with lumped filter with 11-cell sinuous antenna had lumped inductor fabricated from CPW. The detector with lumped filter with 16-cell sinuous antenna had lumped filter fabricated from microstripline. Types of detectors tested were summarized in Table 6.1. The results from lab measurements are summarized in Table 6.2.

Spectrum

The interferogram from the FTS was apodized with triangular window function prior to the Fourier transformation. Then the spectrum was divided by analytical beam splitter function to remove the beam splitter effect [128]. The resulting spectra from distributed diplexer and distributed triplexer with 11-cell sinuous antenna are shown in Figure 6.13. The spectra from lumped filter diplexer from 11-cell sinuous antenna and 16-cell sinuous antenna are shown in Figure 6.14. Peaks of the spectra were normalized to a measured optical efficiency of each band. The results show that we successfully partitioned a broadband signal into 2 and 3 bands with matching band shape for orthogonal polarizations. Figure 6.15 shows measurement from 16-cell sinuous antenna with lumped diplexer under POLARBEAR-1 lenslette array. This shows pixels that are close to each other have matching spectra. This measurement also shows that lumped filter with microstrip line as inductor leaks higher harmonics as expected from simulation. If we calculate loss-tangent using first harmonics and third harmonics peaks from 95GHz *band* after scaling them by expected efficiencies from simulation, we obtain loss-tangent of 6×10^{-3}. However this loss-tangent would be too high for expected efficiency calculated in Figugre 5.33. Measured optical efficiency includes filter loss

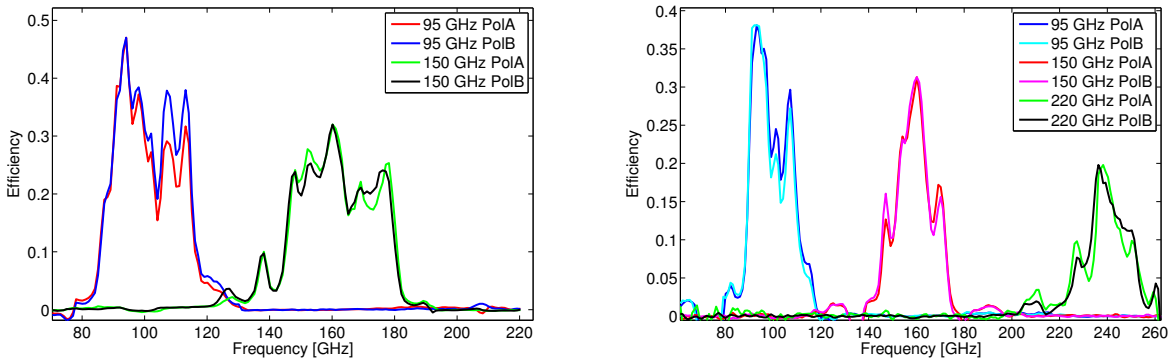

Figure 6.13: Spectrum of a distributed diplexer (left) and a distributed triplexer (right). *A* and *B* refers to two orthogonal linear polarization channels. Peaks are normalized to the measured optical efficiency. See Table 6.2 for details.

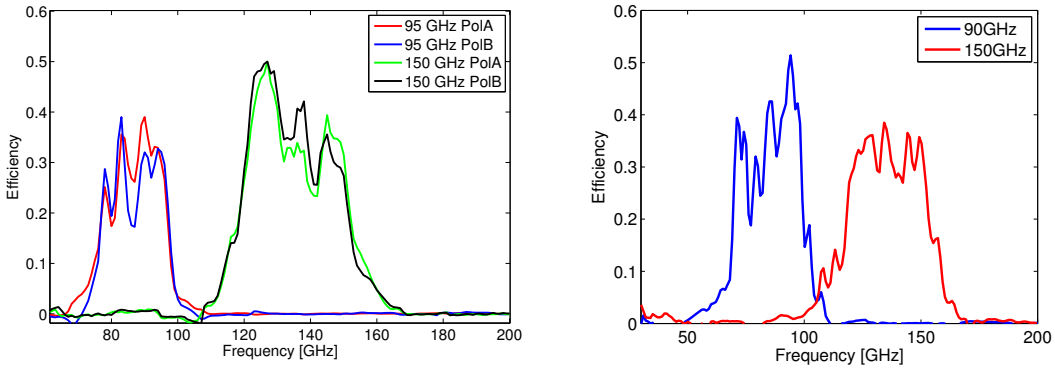

Figure 6.14: Spectrum of a lumped diplexer with 11-cell sinuous antenna (left) and spectrum of a lumped diplexer with 16-cell (right). *A* and *B* refers to two orthogonal linear polarization channels. Peaks are normalized to measured optical efficiency. See Table 6.2 for details.

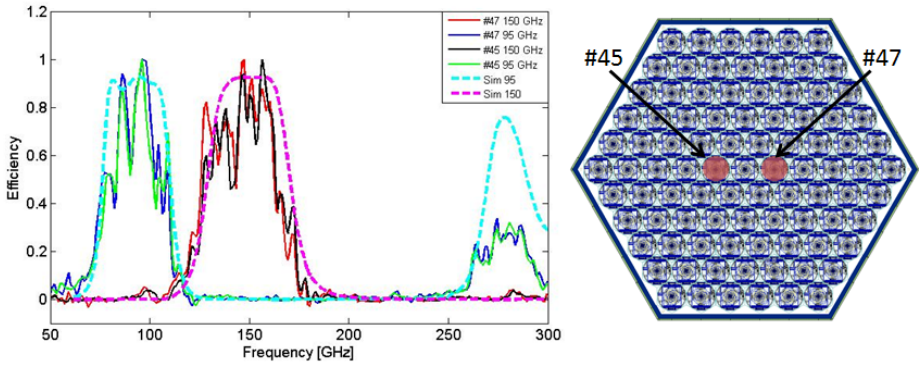

Figure 6.15: Spectrum of a lumped diplexer with 16-cell sinuous antenna under small lenslet. Data were taken from pixel #45 and #47 shown on right. Data were peak normalized and simulation result was overlayed.

in dewar. To estimate detector efficiency, we measured loss of filter stack at room temperature using the FTS. From room temperature measurement of filter stack, we estimate loss in filter stack is 75%. Calculated dewar efficiency from lumped diplexer suggests loss tangent should be approximately 4×10^{-3}. Thus on average these two measurement agrees with previously measured value of 5×10^{-3} [89].

In Figure 6.15, simulation was scaled in frequency to match center frequency of measured value. Results shows that simulation accurately predicts fractional bandwidth. For controlling the center frequency, the POLARBEAR-1 successfully tuned their band location of the filters by making correction to the filter design with feedback from lab measurements [12]. Lumped filter also has ability to be tuned with feedback as discussed in Section 5.5.

Beam map

We scanned source on a two dimensional plane. Intensity from each pixel was divided by $\cos(\theta)$ from a pixel to account for the projection effect. Ellipticity was calculated by fitting an two dimensional gaussian, and we used the definition $\varepsilon = (|\sigma_a - \sigma_b|)/(\sigma_a + \sigma_b)$, where σ_a and σ_b are spreads of gaussian curves in two orthogonal directions. Figure 6.16, Figure 6.17 and Figure 6.18 show beam maps for distributed diplexer, lumped diplexer and distributed triplexer for 11-cell antennas respectively. Characteristic feature of 11-cell beam maps are that 150 GHz beam have low ellipticity, but 95 GHz and 220 GHz have elliptic beams. We were able to fix this problem for lower frequency by increasing size of antenna by adding more cells. Figure 6.19 shows beam map for 16-cell antenna under 14 mm lenslet and 6.35 mm lenslette array. Increasing antena size fixed beam for 95 GHz band without distorting beam for 150 GHz band. Figure 6.20 shows two dimensional gaussian fit on 16-cell antenna beam with 6.35 mm lenslet. From the fit, we computed waist size of the lenslette. Waist size from two different frequencies were 2.2 mm for both frequency bands.

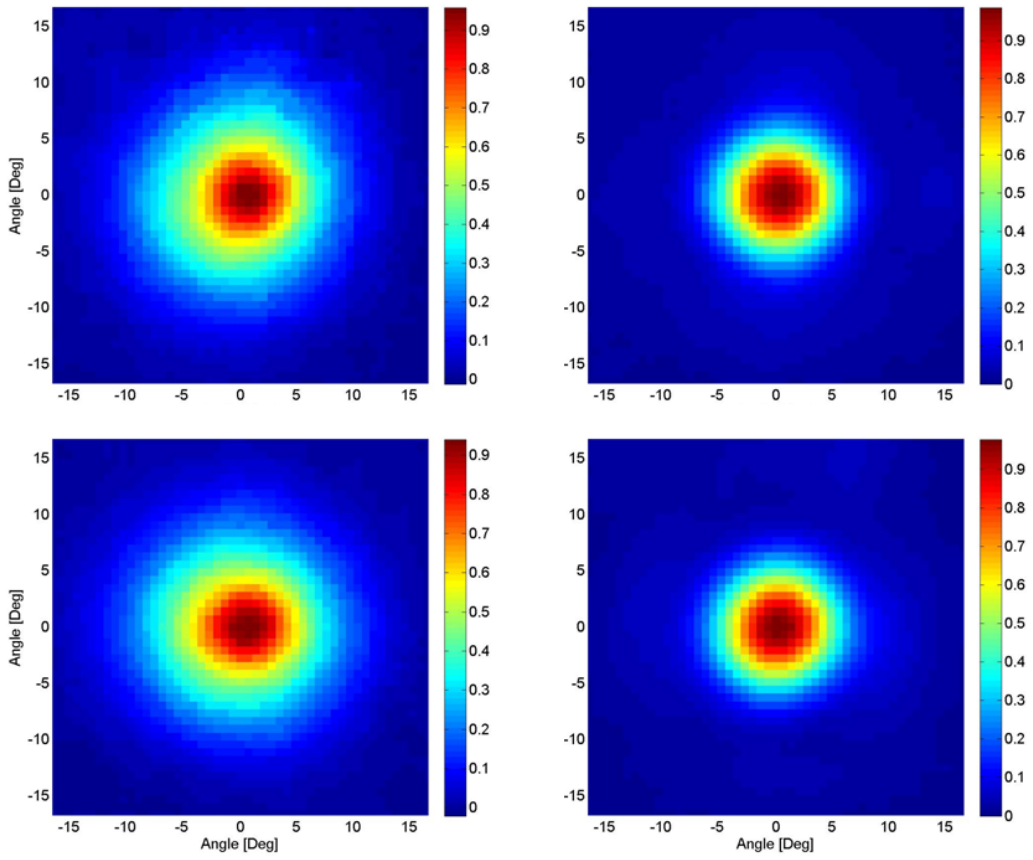

Figure 6.16: Beammap result from distributed diplexer. 95 GHz beam is shown on left and 150 GHz beam is shown on right. See Figure 6.13 for exact band location. See Table 6.2 for details.

Since the lenslette was the POLARBEAR-1 spare lenslette, it placed antenna at $L/R = 0.42$. Both lens-size and anti-reflection coating thicknesses are different between the POLARBEAR-1 and the POLARBEAR-2, so direct comparison to the simulation is difficult. Suppose we compare measured waist value to the simulated value since pixel-to-pixel spacing is same for both experiments, waist size agrees with the simulation.

Polarization

Polarization measurement results are shown in Figure 6.21 and tabulated at Table 6.2. We see a correlation between high ellipticity and high polarization leakage. Increasing antenna size for 95 GHz channel also decreased polarization leakage. We expect the wiregrid to have approximately 1% leakage, thus we are limited by systematics for low cross-pol measurement.

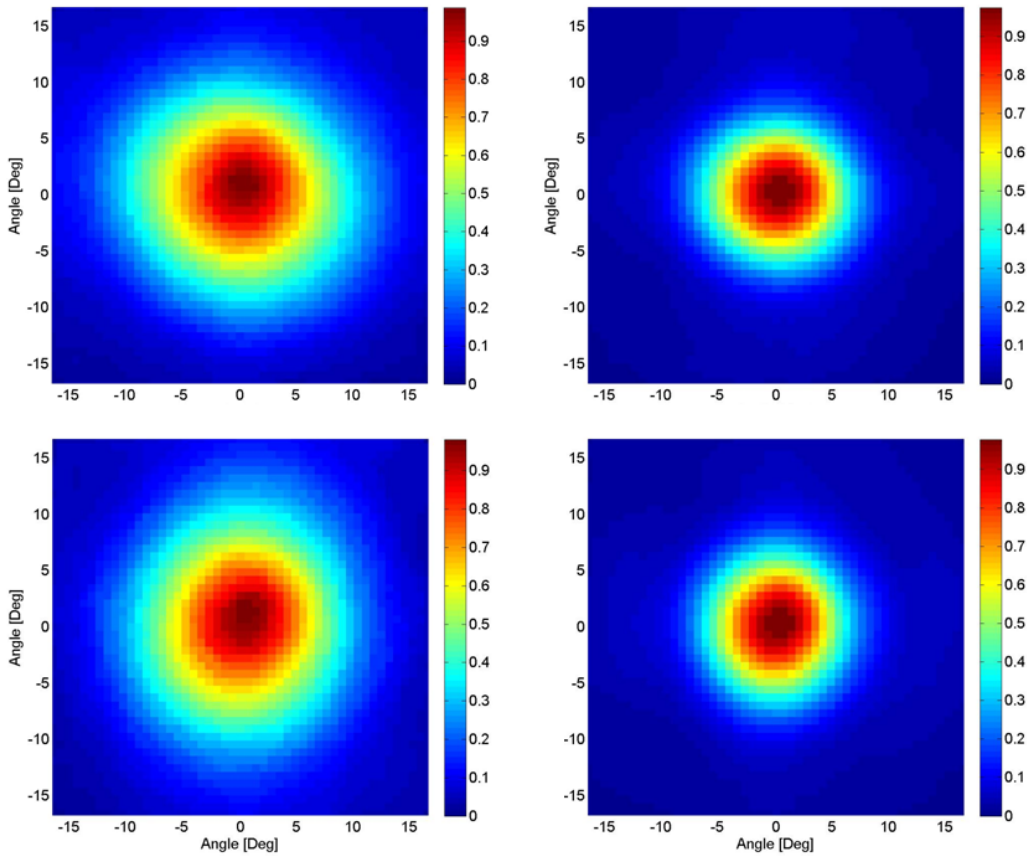

Figure 6.17: Beammap result from lumped diplexer. 95 GHz beam is shown on left and 150 GHz beam is shown on right. See Figure 6.14 for exact band location. See Table 6.2 for details.

Summary of Detector Tests

Measurements from various types of detectors were summarized in Table 6.2

Measurement from POLARBEAR-2 Optical Cryostat

Series of basic measurements were made to test if the dewar and test apparatus can be used for detector module testing. The optical test dewar's filter stack cut down thermal loading enough that the milli-Kelvin stages stayed cold over 24 hours. Also filter stack let in enough millimeter-wave that we can perform the optical test with high enough signal to noise ratio. We have not obtained accurate value on dewar efficiency since calibration of the readout chain has not been done.

We conducted some basic tests on the POLARBEAR-2 size detector array we fabricated. Since readout hardware was not ready for the POLARBEAR-2 style detector module, we created one-off

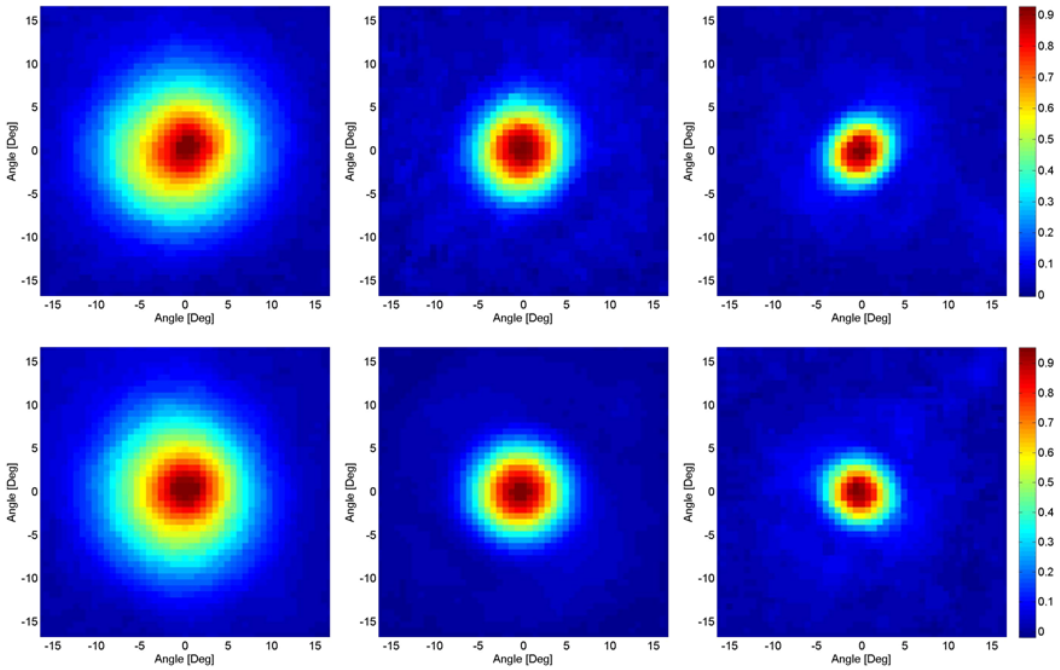

Figure 6.18: Beammap result from distributed diplexer. 95 GHz beam is shown on left and 150 GHz beam is shown on right. See Figure 6.13 for exact band location. See Table 6.2 for details.

Filter Type	N_{Cell}	ν_0 **[GHz]**	$\Delta\nu$ **[GHz]**	**Opt Eff**	**Ellipticity**	**Cross-pol**
Lump Diplexer Low Array	16	97	27.0	-	1.2%	-
Lump Diplexer Mid Array	16	148	40.3	-	1.5%	-
Lump Diplexer Low	16	86	24.0	51%	1.2%	$< 0.3\%$
Lump Diplexer Mid	16	136	37.0	39%	1.5%	$< 1.3\%$
Lump Diplexer Low	11	87	17.0	39%	3.0%	$< 2.9\%$
Lump Diplexer Mid	11	135	26.4	50%	4.5%	$< 1.7\%$
Stub Diplexer Low	11	101	20.2	47%	4.0%	$< 2.3\%$
Stub Diplexer Mid	11	162	26.2	32%	1.0%	$< 1.6\%$
Stub Triplexer Low	11	100	16.6	38%	3.0%	$< 2.5\%$
Stub Trilexer Mid	11	158	17.7	31%	1.5%	$< 2.1\%$
Stub Trilexer High	11	239	19.6	20%	4.0%	$< 4.3\%$

Table 6.2: Summary from one of the polarizations of each diplexer and triplexer. ν_0 is the center frequency of the band and $\Delta\nu$ is integrated bandwidth. Cross-pol values are upper limit value as we expect leakage from wire-grid

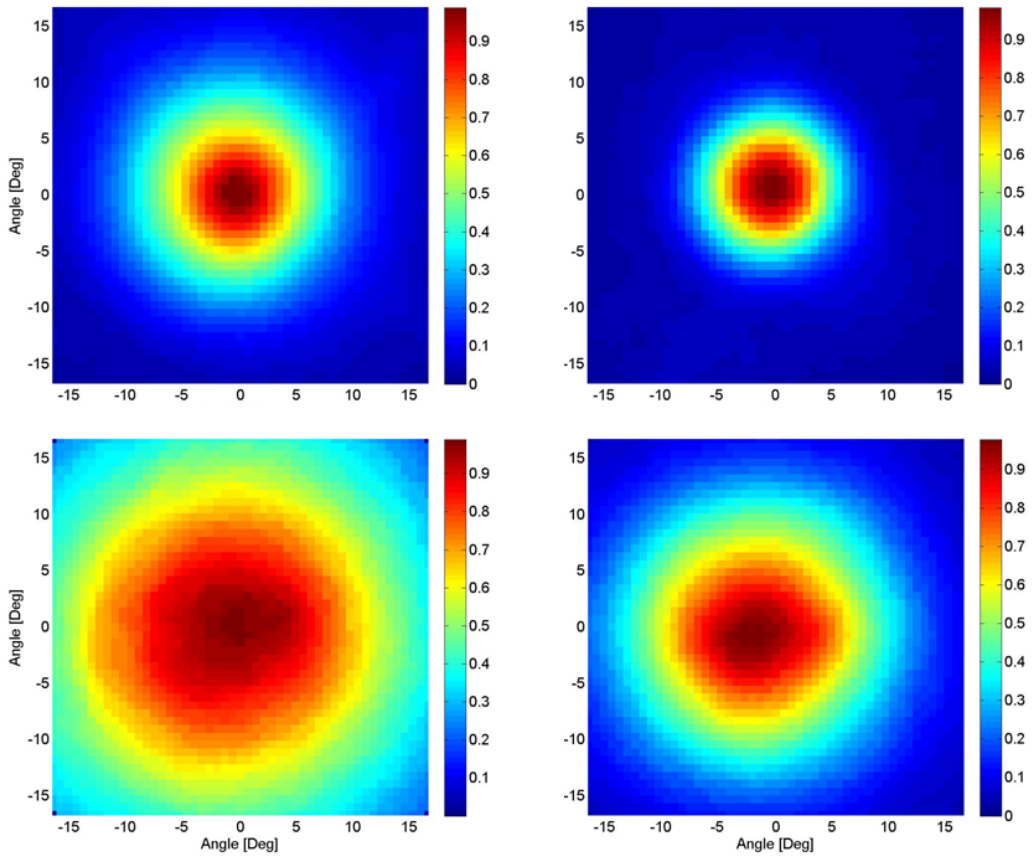

Figure 6.19: Beammap result from lumped diplexer under 14 mm lens (top) and 6.35 mm lens (bottom). 95 GHz beam is shown on left and 150 GHz beam is shown on right. See Figure 6.14 for exact band location. See Table 6.2 for details.

setup that read-out ten bolometers. We used lenslet array that was partially populated as shown in Figure 6.9. As shown in Figure 6.23, we took IV curves while looking at beam filling 77 Kelvin blackbody source and 300 Kelvin blackbody source. IV curve clearly shows that bolometer is responding to different optical power. RP curve in Figure 6.23 show dark measurement for P_{sat} measurement. Design P_{sat} for the tested bolometer was 14.6 pW, thus measured value of 15.8 pW is close given that we do not know its calibration accurately. Measurement also shows that bolometer can be tuned down to 0.65 of normal resistance. Figure 6.24 shows a spectroscopy measurement with 1 mm PWV atmosphere transmission line. We are seeing band in expected place. There is still more work needs to be done to align the FTS better, and we need to track down origin of fringes in the pass band. Figure 6.25 shows beam map and polarization measurement. Beam was measured with the proto-type POLARBEAR-2 lenslet array. We found imperfections in lenslette array such as epoxy between lens and seating wafer. These are being addressed, and we expect

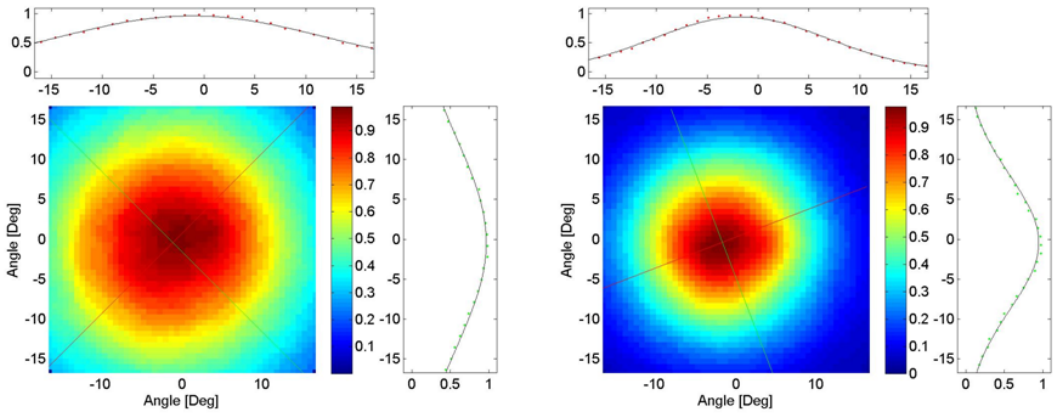

Figure 6.20: Beammap result from lumped diplexer under 6.35 mm lens. 2-D gaussian was fit. Two lines in beam represent axis of 2-D gaussian. Slice were taken along the axis, and fit on gaussain in the plane of axis is plotted. 95 GHz beam is shown on left and 150 GHz beam is shown on right. See Figure 6.14 for exact band location. See Table 6.2 for details.

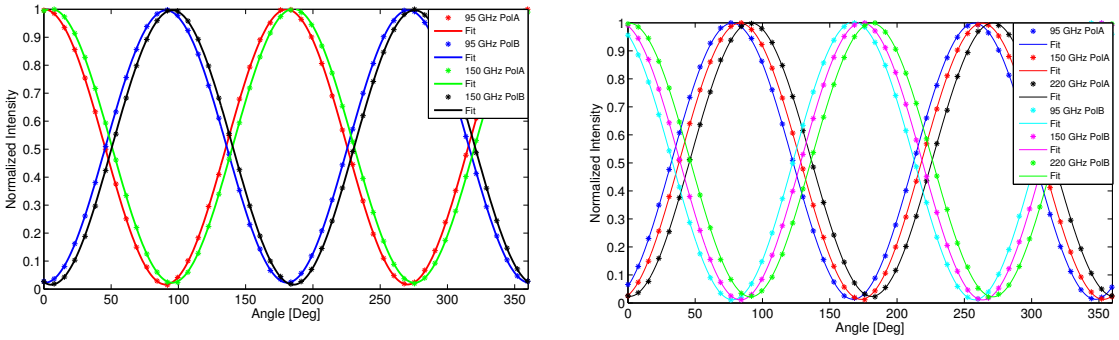

Figure 6.21: Responses of the distributed diplexer (left) and distributed triplexer (right) to a linearly polarized source as a function of relative angle between antenna and the polarizer. Plots were peak normalized prior to fitting by sum of a sine function and a constant. Cross-pol for each channels are summarized in Table 6.2.

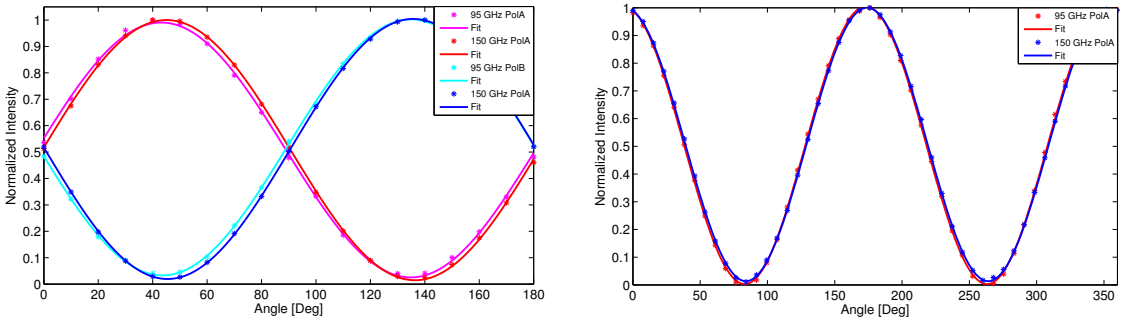

Figure 6.22: Responses of the lumped diplexer with 11-cell sinuous antenna (left) and lumped diplexer with 16-cell sinuous antenna (right) to a linearly polarized source as a function of relative angle between antenna and the polarizer. Plots were peak normalized prior to fitting by sum of a sine function and a constant. Cross-pol for each channels are summarized in Table 6.2.

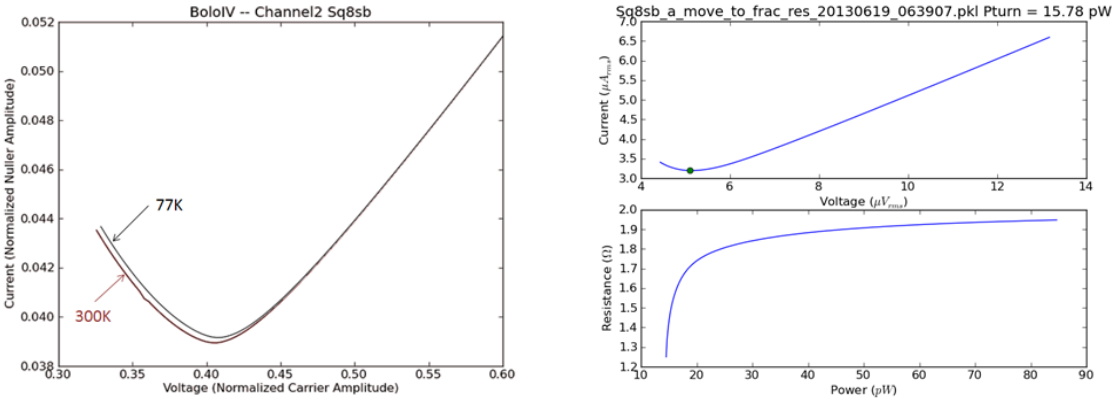

Figure 6.23: (left) I-V curve while detector is receiving optical locating from 300 Kelvin load and 77 Kelvin load. (right) I-V curve and R-P curve showing that detector biased down to $0.65R_N$.

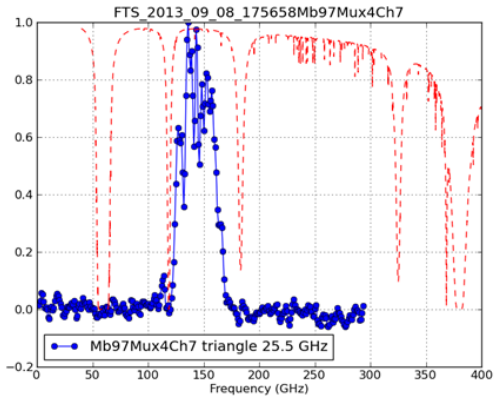

Figure 6.24: Preliminary spectrum data from POLARBEAR-2 optical cryostat. Band is placed between atmospheric windows.

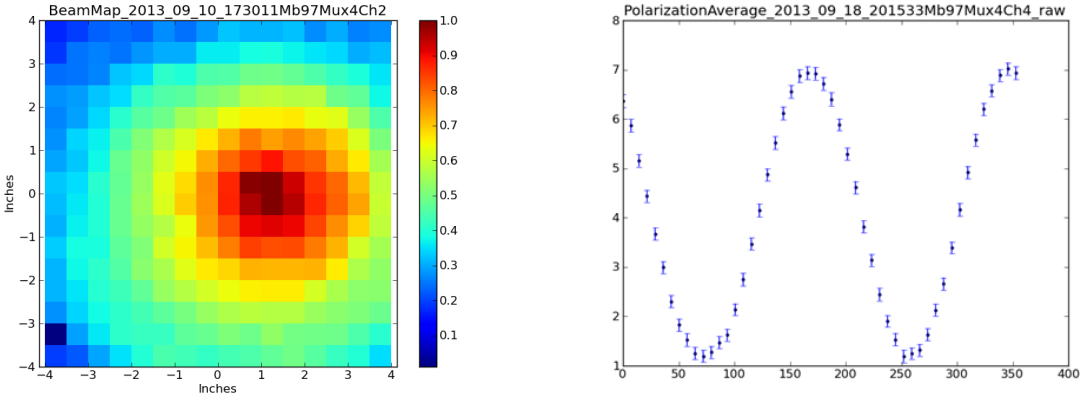

Figure 6.25: Preliminary beam map (left) and polarization data (right) from POLARBEAR-2 optical cryostat. Lenslet quality and cross-talk needs to improve to make accurate measurement on these two parametes in future.

similar or better beam performance that we obtained with POLARBEAR-1 spare lenslette array. Polarization measurement shows expected sinusoidal responce. Its cross-polarization leakage suffered from cross-talk from neighboring channel since measurement was done with aluminum TES which has higher resistance value. We can operate bolometer at lower resistance AlTi transition with cryogenically cooled attenuating filter. Lower R_{TES} would reduce the cross-talk effect. Collaborating institutions are building test dewar based on the design of this dewar such that we can compare results in similar condition.

Chapter 7

FutureDevelopment

7.1 Future Multichroic CMB Experiments

Many future CMB experiments are proposing to achieve sensitivities that require large number of bolometers. In general, there are two approaches. First approach is to make many copies of a small and simple dewar. Each dewar is for a single frequency for a simplicity. Many challenges of the multichroic designs are eliminated for this approach, but a cost of making many dewars become large. Second approach is one that the POLARBEAR-2 is taking. This approach fills a focal plane with multichroic pixels. It is more technically challenging, but once we find a solution this approach will increase the sensitivity per receiver. The second approach is desirable for experiments where the number of telescopes is limited. For example, the South Pole Telescope (SPT) was expensive to build, so it make sense to spend effort to make an efficient receiver. For the SPT's next generation CMB experiment, the SPT-3G, they are proposing to fill its focal plane with the sinuous antenna detector array. The SPT-3G will cover 95, 150 and 220 GHz simultaneously with triplexing pixels. The balloon experiment is another experiment where an efficient receiver is beneficial. The balloon experiment has a tight weight budget, and its launch opportu-

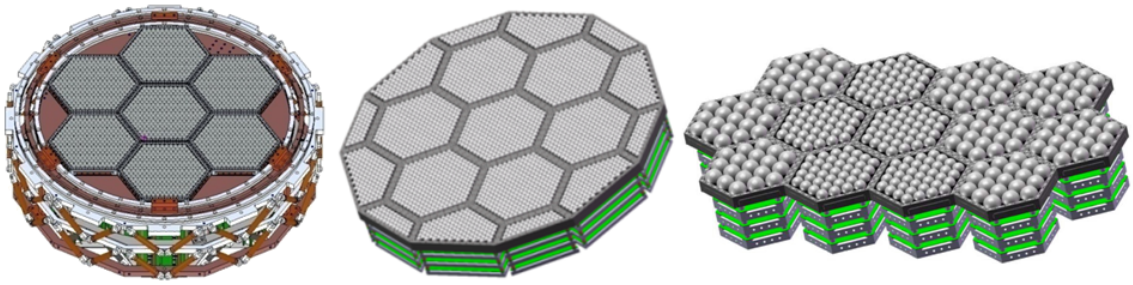

Figure 7.1: CAD drawing of proposed POLARBEAR-2's focal plane (left) SPT-3G's focal plane (center) LiteBIRD's focal plane (right)

Experiment	Location	Frequency	$N_{bolometer}$	Sensitivity
POLARBEAR-2	Atacama	95, 150 GHz	7,588	10 μK $\cdot$ arcmin
Simons Array	Atacama	95, 150, 220 GHz	22,764	6.3 μK $\cdot$ arcmin
SPT-3G	South Pole	95, 150, 220 GHz	15,234	2.0 μK $\cdot$ arcmin
EBEX6K	Balloon	95, 150, 220 GHz	6,288	5.0 μK $\cdot$ arcmin
LiteBIRD	Space	60, 78, 100	2,022	2.3 μK $\cdot$ arcmin
		140, 195, 280 GHz		

Table 7.1: Lists of proposed experiment with sinuous antenna multichroic detector array

nity is also limited. For the next generation EBEX balloon experiment, they are also proposing to use the triplexing sinuous antenna detector array. The satellite experiment has the most stringent efficiency requirement. The satellite project, LiteBIRD, is being proposed to make a full-sky and high-sensitivity measurement on B-mode. Its base plan is to use the multichroic pixel array with the sinuous triplexer technology.

We can combine the two approaches together to achieve high sensitivity in a short time, like the proposed Simons Array. The Simons Array is where we will build three copies of the POLARBEAR-2. Two receivers will observe at 95 GHz and 150 GHz. One receiver will observe at 150 GHz and 220 GHz. This approach keeps the fractional bandwidth small. Once we figure out the challenges we need to solve for two bands observation with the POLARBEAR-2, the Simons Array would achieve high sensitivity quickly. Experiments that are proposing to use the sinuous detector array are summarized in Table 7.1. CADs of the proposed focal plane design are shown in Figure 7.1 [25]. Most of these experiments have high sensitivity to constrain the tensor-to-scalar ratio at or below $r < 0.01$ at 95% confidence level. They also have sensitivity to constrain the sum of neutrino masses to 0.060 eV at 1 σ level.

7.2 Future Multichroic Detector Developments

Triplexer

SPT-3G. EBEX 6K and LiteBIRD are proposing to use the sinuous antenna detectors with triplexer filters. Even though we designed and tested the distributed triplexer, lumped triplexer is easier to design as we discussed in Section 5.5. We designed a lumped triplexer in the same way we designed the lumped diplexer. Filters for each band were optimized, and filters were simply connected to a single junction. Design and its simulated result is shown in Figure 7.2. Simulated design looks reasonable. This filter should be fabricated and tested in near future.

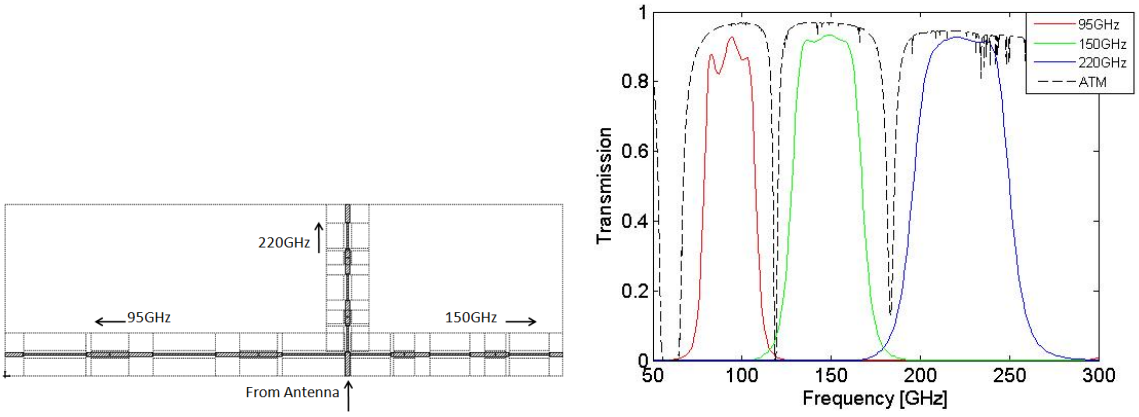

Figure 7.2: Prototype lumped triplexer design is shown on left. Simulated result is shown on right with 1 mm PWV atmospheric transmission.

Beam at Higher Frequency

As shown in Figure 6.18, beam at 220 GHz has high ellipticity. Future experiments are proposing to observe at 220 GHz to constrain dust contribution better. Sinuous antenna is scale invariant, and we also know that 150 GHz beam has low ellipticity. Thus, if we can continue decreasing feature size at center of the antenna 220 GHz beam should improve. However, as we saw in Section 5.4, center of the antenna is getting tight. It is possible to change thickness of dielectric and metal, such that smaller features are easier to fabricate. Fabrication of smaller features also require changing lithography machine to a deep-UV system.

Increasing Efficiency

For future experiments that are targeting 220 GHz, decreasing efficiency as a function of frequency is worrying. As we discussed in Section 5.8, loss as function of frequency we see efficiency measurement follows dielectric loss model. In this section, we will discuss various ways we can mitigate efficiency loss due to dielectric loss.

$\tan(\delta)$ of Dielectric

As we discussed in Section 5.8, loss in dielectric of the microstrip line is main contributor in loss of efficiency. We have not explored various PECVD parameters to study their effect to a dielectric loss. Li *et al.* reported PECVD parameters affect silicon oxide loss [74]. We should optimize our process parameters. In addition to improving a silicon oxide deposition recipe, silicon nitride is known to have lower loss. Silicon nitride has higher dielectric constant, this means impedance of microstrip line *decreases* for the same microstrip line dimension. Since antenna input impedance is

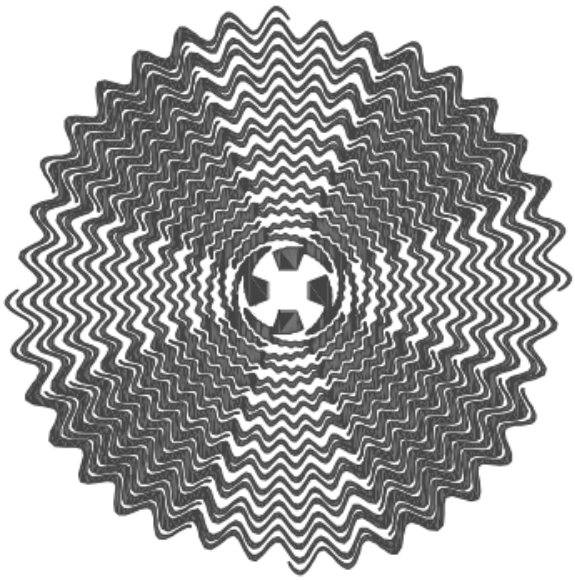

Figure 7.3: Sinuous antenna with oscillating arm. Oscillation slows wave speed on antenna. This allows smaller physical size of antenna [82].

as high as 53 Ω, we need to fabricate microstrip line with thinner line. This requires development of finer lithography technique using deep-UV lithography system.

Antenna Size

We solved the beam distortion for 95 GHz beam by increasing the antenna size. However, increasing antenna size also increased the length of the transmission line. Dielectric loss in the transmission line increases as length of the line increases. We can solve this problem by decreasing antenna size such that transmission line stays short. We tried to kill the excess current with resistive film, but it did not improve the beam shape in the simulation. It is possible to increase *effective size* of antenna by slowing down wave-speed on antenna arm. This can be done on sinuous antenna by adding wavey feature on its arm. It would look like antenna shown in Figure 7.3 [82]. Only the ground plane needs to be wavey. Thus transmission line could still be shorter.

Transmission Line Routing

Currently the microstrip line follows the sinuous equation as shown by the dark blue line in Figure 7.4. The transmission line should be re-routed to cut corners as shown by the green line. It has two benefits. First it decreases the total length of transmission line, thus it decreases the transmission line loss. Also radius of some bends are tighter than three times the width of microstripline in current design. Such tight bends add capacitance to the transmission line, and some fraction of

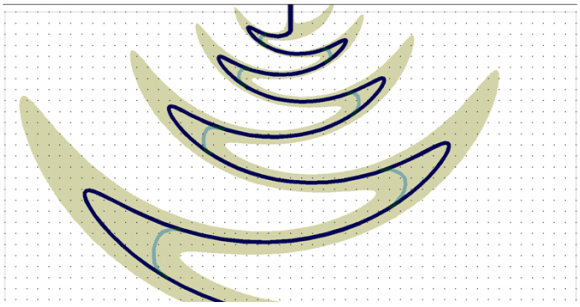

Figure 7.4: Suggestion for rerouting of transmission line on sinuous antenna. Current design follows sinuous antenna's curve (dark blue). By cutting corners as shown in light green, over all length of transmission line becomes shorter, and radius of curvature increases that would suppress reflection at corners.

power is reflected at each bends. By increasing radius of bend by cutting corners, such reflections can be suppressed.

Direct Stimulation

Evidence

We have several evidence that shows a dark bolometer, a bolometer that is not connected to antenna, is receiving optical signal. This is worrying since if a bolometer that is not connected to an antenna is receiving signal, the bolometer that is connected to the antenna is receiving power through the antenna and *direct* pickup by the bolometer. This can be cause of distorted beam, polarization leakage, and inaccurate estimate on received power. We had few dark bolometers per pixel in every proto-type pixels as shown in Figure 7.5.

We measured various responce of dark bolometer using large lens test setup explain in Section 6.2. We measured power received by dark bolometer by comparing responce to temperature modulated blackbody source between 77 Kelvin and 300 Kelvin. It received approximately 10% of neighboring optical bolometer that has 30% fractional bandwidth around 150 GHz. We tested whether such responce was due to reduction of bath temperature due to cooler ambient temperature, we modulated source at 30 Hz. We still had similar level of responce, therefore we concluded this is *optical* responce picked up by the dark bolometer.

Polarization and beam of dark bolomter were plotted in Figure 7.6. We measured that dark bolometer was approximately 20% polarized. Also its polarization axis was perpendicular to slots curved in niobium ground plane for bolometer as shown in Figure 7.5. We measured beam after centering its coordinate to optical bolometer's beam. We noticed beam was elongated parallel to the dark bolometer's slot. Also its beam was tilted *towards* bolometer.

Spectrum of optical bolometer is plotted to higher frequency in Figure 7.7. There is a rising spectrum starting around 250 GHz. We verified that such specrum could be due to direct stimu-

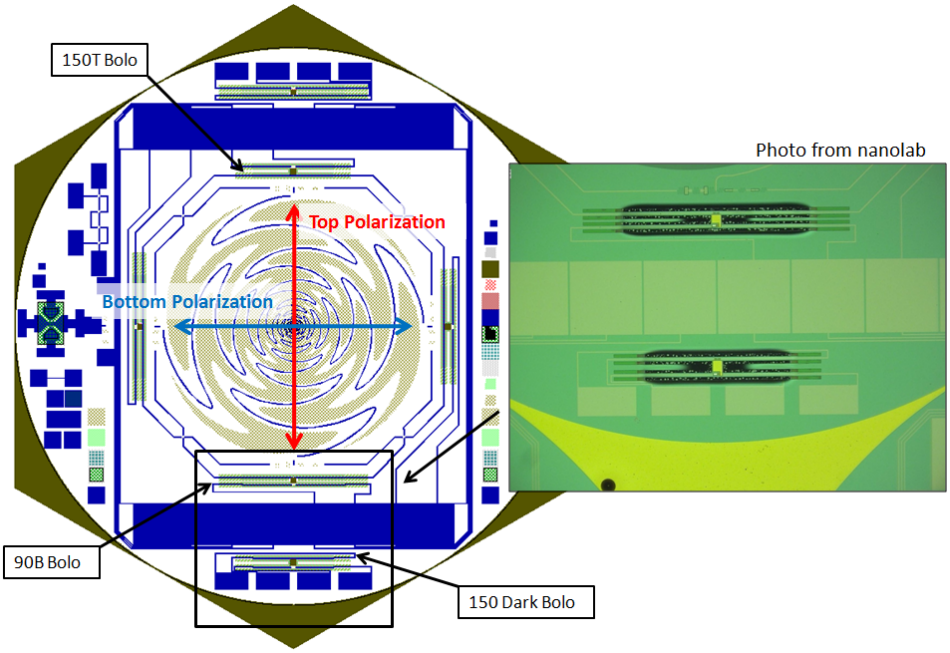

Figure 7.5: CAD drawing of detector pixel with a photograph of a dark bolometer. The dark bolometer was placed outside of wirebonding pads. Bolometer's slot was oriented parallel to one polarization of the antenna.

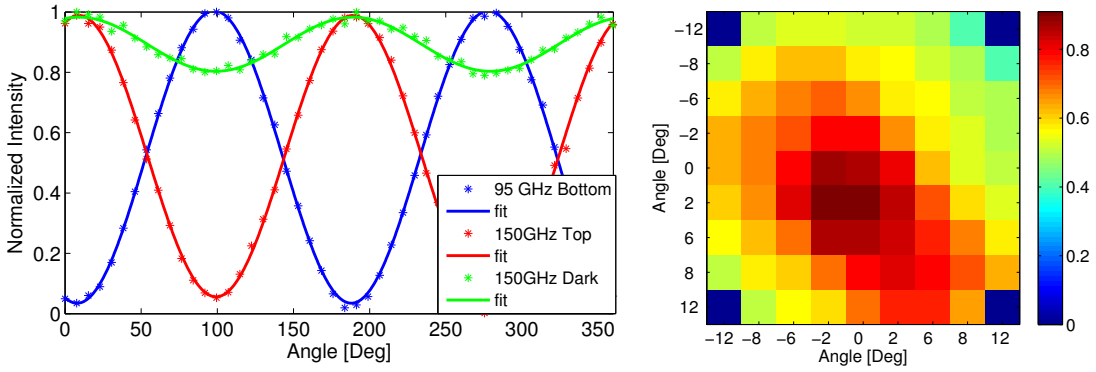

Figure 7.6: (left) Response of dark bolometer to rotating wiregrid infront of modulating thermal source. Response was normalized. Dark bolometer's beam was partially polarized, and its polarization was perpendicular to its slot. (right) beam map of dark bolometer. Beam was elongated along slot of bolometer, and beam was steered *towards* dark bolometer.

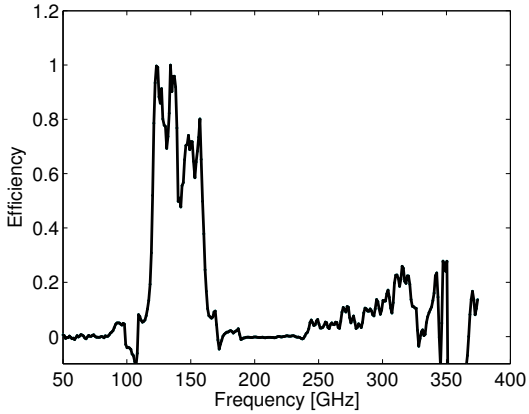

Figure 7.7: Spectrum measurement of an optical pixel to higher freqency. We suspect rising spectrum starting around 250 GHz is due to direct stimulation.

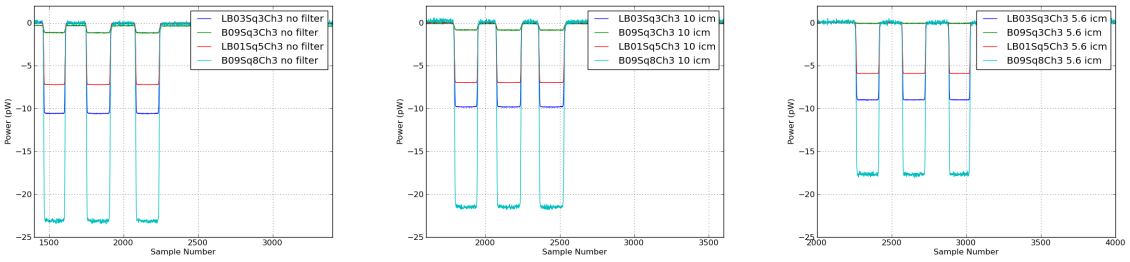

Figure 7.8: Response of optical and dark bolometer to temperature modulated source. *B09Sq3Ch3* is a dark bolometer. Other channels are optical. Dark bolometer responds to optical signal without filter (left). Dark bolometer still responds with 300 GHz low pass filter between source and detector (center). With 168 GHz low pass filter in place, the dark bolometer does not respond to a signal (right). Optical bolomters are still seeing signal. Slight decrease in optical signal with 168 GHz is because it overlaps with designed band slightly. Courtesy of Z. Kermish.

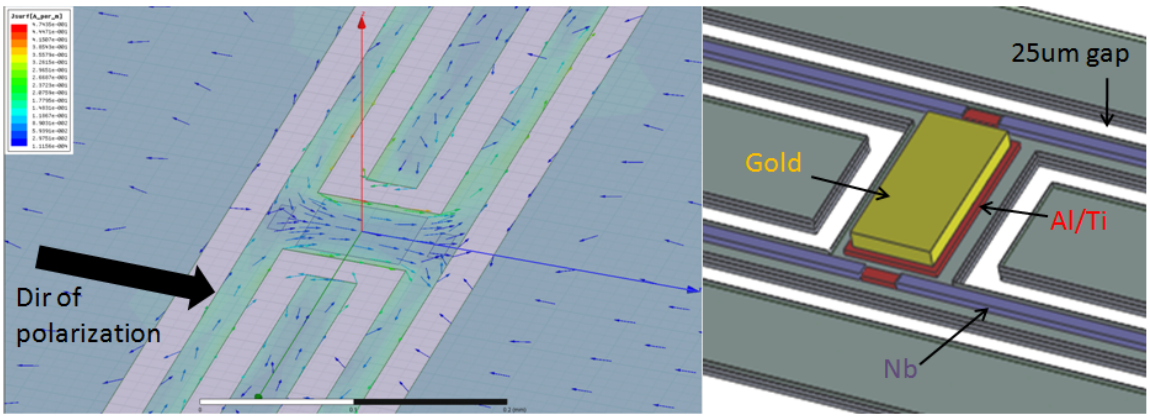

Figure 7.9: (left) EM simulation of slot curved in infinite perfect conductor in shape of bolometer. Current density is shown. High density of current flows at edge of bolometer island. Schematic drawing of bolometer island is shown on right. Lossy metals such as gold and aluminum-titanium could pick up these currents via inductive coupling.

lation on dark bolometer by comparising responce of dark bolometer with and without low-pass filter as shown in Figure 7.8. We see that responce of direct stimuation starts around 250 GHz, the POLARBEAR-1 and the POLARBEAR-2 solves this problem by inserting 180 GHz low pass filter right above focal plane. For future experiment that observes 220 GHz band, origin of direct stimulation needs to be understood and its mitigation needs to be found.

Possible Model

Given polarization direction, we thought slot in niobium ground plane was acting as slot dipole antenna. However, how power was deposited on bolometer island was not clear. We simulated polarized plane wave hitting slot curved in niobium ground plane, and we looked at how current was flowing as shown in Figure 7.9. Given how current density is high at edge of bolometer island, we thought it was depositing power onto lossy metal on bolometer island such as gold and AlTi bilayer through inductive heating. If such model was true, we can mitigate excitation through such inductive coupling by keeping lossy metal away from edge of bolometer island.

AR Coating

Broadband anti-reflection coating over large surface must be solved for the POLARBEAR-2 and future projects. We successfully made broadband anti-reflection coating on lenslet using two layer coating with Stycast 1090 and Stycast 2850FT. Collaborators at KEK investigated how demlamination happened. Alumina sample with Stycast 2805FT coated on both side did not delaminate. Same sample with Stycast 1090 coated on one side did not delaminate. However, when Stycast 1090 was applied on *both* side of alumina sample, it delaminated. We hypothesized that since sty-

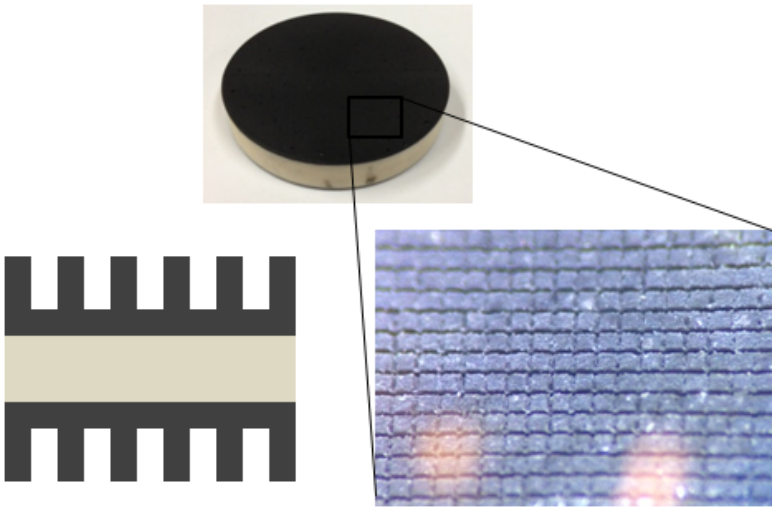

Figure 7.10: Schematic drawing of grooved AR coating (bottom left). Photograph of alumina sample coated with grooved stycast 2850FT. Groove was made with wafer dicing saw. Microscope photograph of groove is shown on bottom right.

cast 2850FT's thermal contraction was reduced by adding ceramic filler, that thermal contraction did not exert great stress on alumina. However, Stycast 1090 is a type of epoxy that has many voids imbedded into its mixture, thus when cooled such void contract by great amount and delaminates film.

Grooved AR coating

Since stycast 2850FT on both sides of alumina did not delaminate, we thought we could make two layer anti-reflection coating by machining sub-wavelength structure into stycast 2850FT as shown in Figure 7.10. This gets around the problem of stress from thermal contractuin of stycast 1090. Also since stycast 2850FT is much easier to machine than alumina, we can still make sub-wavelength structure. Initial measurement made by sample in Figure 7.10 shows that we can change its dielectric constant by making sub-wavelength structure. We are studying how accurate we can machine to meet our spec and its effect on polarization.

It is ideal if we can make sub-wavelength structure on alumina itself. It completely free us from thermal contraction issue. However, alumina is hard to machine in conventional way. Nitta *et. al* made dimples into alumina with laser pulses as shown in Figure 7.11 [119]. Time and cost of such process is high to cover 500 mm diameter lens.

Thermal Spraying

Another possible way to coat over large surface is thermal spraying. Thermal spraying sprays material at high temperature and high velocity. Its typical thickness ranges from 10 μm to millimeter,

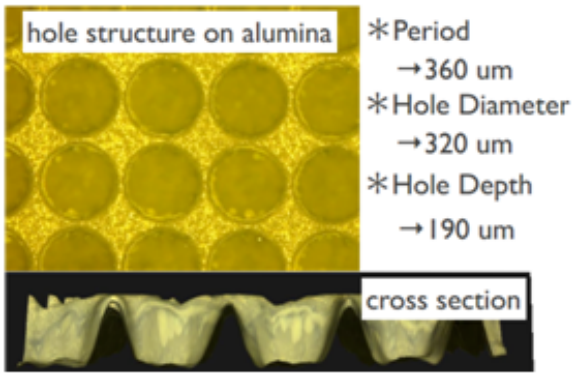

Figure 7.11: Dimples drilled in alumina with laser pulse [92]

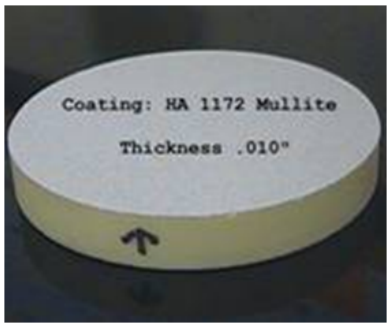

Figure 7.12: 50 mm alumina disk thermal spray coated with 250 μm thick mullite

which is perfect range for AR coating at millimeter-wave. We recently thermal spray coated alumina disk with mullite as shown in Figure 7.12. We still have a lot to study about the process such as material that can be sprayed, dielectric constants of sprayed materials, accuracy in thickness, its adhesion property and its thermal stress.

Bibliography

[1] P.A.R. Ade et al. “Planck 2013 results. XVI. Cosmological parameters”. In: (2013). arXiv: 1303.5076 [astro-ph.CO].

[2] P.A.R. Ade et al. “Planck 2013 results. XXII. Constraints on inflation”. In: (2013). arXiv: 1303.5082 [astro-ph.CO].

[3] P.A.R. Ade et al. “Planck 2013 results. XXIII. Isotropy and Statistics of the CMB”. In: (2013). arXiv: 1303.5083 [astro-ph.CO].

[4] P.A.R. Ade et al. “Planck 2013 Results. XXIV. Constraints on primordial non-Gaussianity”. In: (2013). arXiv: 1303.5084 [astro-ph.CO].

[5] N. Aghanim et al. “Planck 2013 results. XXVII. Doppler boosting of the CMB: Eppur si muove”. In: (2013). arXiv: 1303.5087 [astro-ph.CO].

[6] Karim Mohammad Pour Aghdam, Reza Faraji-Dana, and Jalil Rashed-Mohassel. “The sinuous antenna-A dual polarized feed for reflector-based searching systems”. In: {*AEU*} - *International Journal of Electronics and Communications* 59.7 (2005), pp. 392 –400. ISSN: 1434-8411. DOI: http://dx.doi.org/10.1016/j.aeue.2004.11.046. URL: http://www.sciencedirect.com/science/article/pii/S1434841104000639.

[7] Neil McN. Alford and Stuart J. Penn. “Sintered alumina with low dielectric loss”. In: *Journal of Applied Physics* 80.10 (1996).

[8] ALMA. *Atacama Large Millimeter/submillimeter Array*. 2013. URL: http://www.apex-telescope.org/weather/.

[9] R. A. Alpher, H. Bethe, and G. Gamow. “The Origin of Chemical Elements”. In: *Phys. Rev.* 73 (7 1948), pp. 803–804. DOI: 10.1103/PhysRev.73.803. URL: http://link.aps.org/doi/10.1103/PhysRev.73.803.

[10] Inc. ANSYS. *ANSYS HFSS*. 2013. URL: http://www.ansys.com/.

[11] Evan H. Appleman. “Reaction of xenon difluoride with water and with xenon trioxide”. In: *Inorg. Chem.* 6.7 (1967), pp. 1305–1310.

[12] K. Arnold. “Design and Deployment of the POLARBEAR Cosmic Microwave Background Polarization Experiment”. PhD thesis. University of California, Berkeley, 2010.

[13] K. Arnold et al. *The bolometric focal plane array of the POLARBEAR CMB experiment*. 2012. DOI: 10.1117/12.927057. URL: http://dx.doi.org/10.1117/12.927057.

[14] H.A. Leupold A.T. Hirshfeld and H.A. Boorse. "Superconducting and Normal Specific Heat of Niobium". In: *Physical Review* 127.5 (1962).

[15] F. Aubin. "Bolometer Noise Calculation Memo". In: (2009).

[16] A. Babinet. "Mémoires d'optique météorologique". In: *Comp. Rend. Acad. Sci* 4.638 (1837).

[17] C. Bischoff et al. "First Season QUIET Observations: Measurements of CMB Polarization Power Spectra at 43 GHz in the Multipole Range 25 <= ell <= 475". In: *Astrophys.J.* 741 (2011), p. 111. DOI: 10.1088/0004-637X/741/2/111. arXiv: 1012.3191 [astro-ph.CO].

[18] J. J. Bock. "Rocket-borne observation of singly ionized carbon 158 um emission from the diffuse interstellar medium". PhD thesis. University of California, Berkeley, 1994.

[19] James Bock et al. "Task force on cosmic microwave background research". In: (2006). arXiv: astro-ph/0604101 [astro-ph].

[20] H. Booker. "Slot Aerials and Their Relation to Complementary Wire Aerials". In: *J.I.E.E.* 93.620 (1946).

[21] M. Born and E. Wolf. *Principles of Optics*. 1999.

[22] W. S. BOYLE and JR. K. F. RODGERS. "Performance Characteristics of a New Low-Temperature Bolometer". In: *J. Opt. Soc. Am.* 49.1 (1959), pp. 66–69. DOI: 10.1364/JOSA.49.000066. URL: http://www.opticsinfobase.org/abstract.cfm?URI=josa-49-1-66.

[23] M.C. Buck and D.S. Filipovic. "Split-beam mode four-arm slot sinuous antenna". In: *Antennas and Wireless Propagation Letters, IEEE* 3.1 (2004), pp. 83–86. ISSN: 1536-1225. DOI: 10.1109/LAWP.2004.830004.

[24] H.C. Chiang et al. "Measurement of CMB Polarization Power Spectra from Two Years of BICEP Data". In: *Astrophys.J.* 711 (2010), pp. 1123–1140. DOI: 10.1088/0004-637X/711/2/1123. arXiv: 0906.1181 [astro-ph.CO].

[25] CMB2013. *International Conference on Cosmic Microwave Background, CMB2013, Okinawa, Japan*. 2013. URL: http://www-conf.kek.jp/cmb/2013/.

[26] Sakaguchi E.H VOC Corp. *Sakaguchi E.H VOC Corp*. 2013. URL: http://www.sakaguchi.com/gbp/.

[27] D. P. Neikirk D. B. Rutledge and D. P. Kasilingam. *Integrated circuit antennas, in Infrared and Millimeter-Waves*. Ed. by K. J. Button. 1983.

[28] Brian Keating William Krantz Adrian T. Lee Erin Quealy Paul L. Richards Praween Siritanasak Darin Rosen Aritoki Suzuki and William Walker. " Epoxy-based broadband antireflection coating for millimeter-wave optics," in: *Applied Optics* (2013 Accepted).

[29] G. Deschamps. "Impedance Properties of Complementary Multiterminal Planar Structures". In: *Antennas and Propagation, IEEE Transaction* 7.5 (1959), pp. 371–378.

[30] R. H. Dicke et al. “Cosmic Black-Body Radiation.” In: *The Astrophysical Journal* 142 (1965), pp. 414–419. DOI: 10.1086/148306.

[31] M. A. Dobbs et al. “Frequency multiplexed superconducting quantum interference device readout of large bolometer arrays for cosmic microwave background measurements”. In: *Review of Scientific Instruments* 83.7, 073113 (2012), pp. –. DOI: http://dx.doi.org/10.1063/1.4737629. URL: http://scitation.aip.org/content/aip/journal/rsi/83/7/10.1063/1.4737629.

[32] R. Duhamel. *Dual Polarized Sinuous Antennas*. United States Patent 4658262. 1987.

[33] J.M. Edwards et al. “Dual-Polarized Sinuous Antennas on Extended Hemispherical Silicon Lenses”. In: *Antennas and Propagation, IEEE Transactions on* 60.9 (2012), pp. 4082–4091. ISSN: 0018-926X. DOI: 10.1109/TAP.2012.2207048.

[34] ESA. *Planck*. 2013. URL: http://www.esa.int/Our_Activities/Space_Science/Planck.

[35] D.F. Filipovic, S.S. Gearhart, and G.M. Rebeiz. “Double-slot antennas on extended hemispherical and elliptical silicon dielectric lenses”. In: *Microwave Theory and Techniques, IEEE Transactions on* 41.10 (1993), pp. 1738–1749. ISSN: 0018-9480. DOI: 10.1109/22.247919.

[36] D.J. Fixsen. “The Temperature of the Cosmic Microwave Background”. In: *Astrophys.J.* 707 (2009), pp. 916–920. DOI: 10.1088/0004-637X/707/2/916. arXiv: 0911.1955 [astro-ph.CO].

[37] J.W. Fowler. “The Atacama Cosmology Telescope project”. In: *Proceedings of SPIE* (2004), p. 5498.

[38] E.M.T. Jones G. Matthaei and L. Young. *Microwave Filters, Impedance-Matching Networks, and Coupling Structures*. Artech House, 1980.

[39] G Gamow. “Expanding Universe and the Origin of Elements”. In: *The Physical Review* 70 (1946), p. 572.

[40] J.M. Gildemeister. “Voltage-Biased Superconducting Bolometers for Infrared and mm-Waves”. PhD thesis. University of California, Berkeley, 1995.

[41] Matthew J. Griffin, James J. Bock, and Walter K. Gear. “Relative Performance of Filled and Feedhorn-Coupled Focal-Plane Architectures”. In: *Appl. Opt.* 41.31 (2002), pp. 6543–6554. DOI: 10.1364/AO.41.006543. URL: http://ao.osa.org/abstract.cfm?URI=ao-41-31-6543.

[42] Tijmen de Haan et al. “Improved performance of TES bolometers using digital feedback”. In: (2012), 84520E–84520E–10. DOI: 10.1117/12.925658. URL: +http://dx.doi.org/10.1117/12.925658.

[43] E. E. Haller. “Physics and design of advanced IR bolometers and photoconductors.” In: *Infrared Physics* 25 (1985), pp. 257–266. DOI: 10.1016/0020-0891(85)90088-0.

[44] Nils W. Halverson. "Aperture Efficiency and Mapping Speed". In: *APEX-SZ memo* 041211a (2004).

[45] Nils W. Halverson. "NEP and Mapping Speed for 92 GHz and 150 GHz Bolometer Arrays". In: *APEX-SZ memo* 20020429a (2005).

[46] D. Hanson et al. "Detection of B-mode Polarization in the Cosmic Microwave Background with Data from the South Pole Telescope". In: (2013). arXiv: 1307.5830 [astro-ph.CO].

[47] K. Hattori et al. "Adaption of frequency-domain readout for Transition Edge Sensor bolometers for the POLARBEAR-2 Cosmic Microwave Background experiment". English. In: *Proceedings for VCI2013* (2013).

[48] E. Hecht and A. Zajac. *Optics*. 1980.

[49] H. S. Hou. "Method for Optimized Design of Dielectric Multilayer Filters". In: *Appl. Opt.* 13.8 (1974), pp. 1863–1866. DOI: 10.1364/AO.13.001863. URL: http://ao.osa.org/abstract.cfm?URI=ao-13-8-1863.

[50] W. Hu and M. White. *A CMB Polarization Primer*. 1997. URL: http://background.uchicago.edu/~whu/polar/webversion/polar.html.

[51] Wayne Hu and Takemi Okamoto. "Mass reconstruction with cmb polarization". In: *Astrophys.J.* 574 (2002), pp. 566–574. DOI: 10.1086/341110. arXiv: astro-ph/0111606 [astro-ph].

[52] E. Hubble and M. L. Humason. "The Velocity-Distance Relation among Extra-Galactic Nebulae". In: *The Astrophysical Journal* 74 (1931), p. 43. DOI: 10.1086/143323.

[53] Cryomech Inc. *Cryomech, year = 2013, url = www.cryomech.com/.*

[54] Sonnet Software Inc. *Sonnet High Frequency Electromagnetic Software*. 2013. URL: http://www.sonnetsoftware.com/.

[55] Y. Inoue. "The thermal design of the POLARBEAR-2 experiment". MA thesis. The Graduate University for Advanced Studies, 2012.

[56] K. D. Irwin. "An application of electrothermal feedback for high resolution cryogenic particle detection". In: *Applied Physics Letters* 66.15 (1995).

[57] K.D. Irwin and G.C. Hilton. "Transition-Edge Sensors". In: *Cryogenic Particle Detection*. Ed. by Christian Enss. Vol. 99. Topics in Applied Physics. Springer Berlin Heidelberg, 2005, pp. 63–150. ISBN: 978-3-540-20113-7. DOI: 10.1007/10933596_3. URL: http://dx.doi.org/10.1007/10933596_3.

[58] D. Kasilingam and D. Rutledge. "Focusing Properties of Small Lenses". In: *Int. J. Infrared Millimeter Waves* 7.10 (1986), pp. 1631–1647.

[59] M. Kerker. *The scattering of light, and other electromagnetic radiation*. 1969.

[60] Z. Kermish. "The POLARBEAR Experiment: Design and Characterization". PhD thesis. University of California, Berkeley, 2012.

[61] Zigmund D. Kermish et al. "The POLARBEAR experiment". In: *Proceedings of SPIE mm, sub-mm, and far-IR Detectors and Instr for Astro VI 2012* (2012), pp. 84521C–84521C–15. DOI: 10.1117/12.926354. URL: +http://dx.doi.org/10.1117/12.926354.

[62] A.R. Kerr. "Surface Impedance of Superconductors and Normal Conductors in EM Simulators". In: *MMA Memo No. 245* (1999).

[63] C. Kittel and H. Kroemer. *Thermal Physics*. 1980.

[64] John Kovac et al. "Detection of polarization in the cosmic microwave background using DASI". In: *Nature* 420 (2002), pp. 772–787. DOI: 10.1038/nature01269. arXiv: astro-ph/0209478 [astro-ph].

[65] J. Krupka et al. "Measurements of Permittivity, Dielectric Loss Tangent, and Resistivity of Float-Zone Silicon at Microwave Frequencies". In: *Microwave Theory and Techniques, IEEE Transactions on* 54.11 (2006), pp. 3995–4001. ISSN: 0018-9480. DOI: 10.1109/TMTT.2006.883655.

[66] S. Kumar. "Submillimeter wave camera using a novel photon detector technology". PhD thesis. California Institute of Technology, 2007.

[67] Shwetank Kumar et al. "Millimeter-Wave Lumped Element Superconducting Bandpass Filters for Multi-Color Imaging". In: *Applied Superconductivity, IEEE Transactions on* 19.3 (2009), pp. 924–929. ISSN: 1051-8223. DOI: 10.1109/TASC.2009.2017884.

[68] Marvell Nanofabrication Laboratory. *Marvell Nanofabrication Laboratory*. 2013. URL: http://nanolab.berkeley.edu/.

[69] James W. Lamb. "Miscellaneous data on materials for millimetre and submillimetre optics". English. In: *International Journal of Infrared and Millimeter Waves* 17 (12 1996), pp. 1997–2034. ISSN: 0195-9271. DOI: 10.1007/BF02069487. URL: http://dx.doi.org/10.1007/BF02069487.

[70] S. P. Langley. *BOLOMETER*. New York, The Society, 1880.

[71] Judy Lau et al. "Millimeter-wave antireflection coating for cryogenic silicon lenses". In: *Appl. Opt.* 45.16 (2006), pp. 3746–3751. DOI: 10.1364/AO.45.003746. URL: http://ao.osa.org/abstract.cfm?URI=ao-45-16-3746.

[72] S. Lee et al. "A Study on Dielectric Constants of Epoxy/$SrTiO_3$ Composite for Embedded Capacitor Films (ECFs)". In: *Advanced Packaging, IEEE Transaction* 30.3 (2007), pp. 428–433.

[73] Shih-Fu Lee et al. "Voltage-Biased Superconducting Transition-Edge Bolometer with Strong Electrothermal Feedback Operated at 370 mK". In: *Appl. Opt.* 37.16 (1998), pp. 3391–3397. DOI: 10.1364/AO.37.003391. URL: http://ao.osa.org/abstract.cfm?URI=ao-37-16-3391.

[74] D. Li et al. "Improvements in Silicon Oxide Dielectric Loss for Superconducting Microwave Detector Circuits". In: *Applied Superconductivity, IEEE Transactions on* 23.3 (2013), pp. 1501204–1501204. ISSN: 1051-8223. DOI: 10.1109/TASC.2013.2242951.

[75] Chase Research Cryogenics Ltd. *Chase Cryogenics*. 2013. URL: http://www.chasecryogenics.com/index.htm.

[76] Nihon Ceratec Co. LTD. *Nihon Ceratec*. 2013. URL: http://www.ceratech.co.jp/index_e.html.

[77] W. Holmes T. Koch J. Mulder R. Vasques L. Wild M. Yun J. Bock and A. Lange. "Microfabrication of silicon-nitride micromesh bolometric detectors for planck high frequency instrument". In: *J. Vac. Sci. Technol. B* 22.1 (2004).

[78] T. Marriage. "Detectors for the Atacama Cosmology Telescope". PhD thesis. Princeton University, 2006.

[79] P.V. Mason and R.W. Gould. "Slow-Wave Structures Utilizing Superconducting Thin-Film Transmission Lines". In: *Journal of Applied Physics* 40.5 (1969), pp. 2039–2051.

[80] J. C. Mather et al. "Measurement of the cosmic microwave background spectrum by the COBE FIRAS instrument". In: *The Astrophysical Journal* 420 (1994), pp. 439–444. DOI: 10.1086/173574.

[81] John C. Mather. "Bolometer noise: nonequilibrium theory". In: *Appl. Opt.* 21.6 (1982), pp. 1125–1129. DOI: 10.1364/AO.21.001125. URL: http://ao.osa.org/abstract.cfm?URI=ao-21-6-1125.

[82] Mohammad Matin, ed. *Ultra Wideband Communications: Novel Trends - Antennas and Propagation*. intech, 2001. DOI: 10.5772/941.

[83] T. Matsumura. "A cosmic microwave background polarimeter using a superconducting magnetic bearing". PhD thesis. University of Minnesota, 2006.

[84] Tomotake Matsumura et al. "Performance of three- and five-stack achromatic half-wave plates at millimeter wavelengths". In: *Appl. Opt.* 48.19 (2009), pp. 3614–3625. DOI: 10.1364/AO.48.003614. URL: http://ao.osa.org/abstract.cfm?URI=ao-48-19-3614.

[85] Tomotake Matsumura et al. "POLARBEAR-2 optical and polarimeter designs". In: *Proceedings of SPIE mm, sub-mm, and far-IR Detectors and Instr for Astro VI 2012* (2012), 84523E–84523E–8. DOI: 10.1117/12.926770. URL: +http://dx.doi.org/10.1117/12.926770.

[86] B. W. Maxfield and W. L. McLean. "Superconducting Penetration Depth of Niobium". In: *Phys. Rev.* 139 (5A 1965), A1515–A1522. DOI: 10.1103/PhysRev.139.A1515. URL: http://link.aps.org/doi/10.1103/PhysRev.139.A1515.

[87] J. McMahon et al. "Multi-chroic Feed-Horn Coupled TES Polarimeters". English. In: *Journal of Low Temperature Physics* 167 (5-6 2012), pp. 879–884. ISSN: 0022-2291. DOI: 10.1007/s10909-012-0612-9. URL: http://dx.doi.org/10.1007/s10909-012-0612-9.

[88] Michael J. Myers et al. "An antenna-coupled bolometer with an integrated microstrip bandpass filter". In: *Applied Physics Letters* 86.11, 114103 (2005), pp. –. DOI: http://dx.doi.org/10.1063/1.1879115. URL: http://scitation.aip.org/content/aip/journal/apl/86/11/10.1063/1.1879115.

[89] Mike Myers. *Sinuous Antenna Loss Investigation*. 2011. URL: http://bolowiki.berkeley.edu/twiki/bin/view/Main/Sinuousloss.

[90] NASA. *LAMBDA - CMB Experiments*. 2011. URL: http://lambda.gsfc.nasa.gov/links/experimental_sites.cfm.

[91] A. Neto, S. Maci, and P.J.I. de Maagt. "Reflections inside an elliptical dielectric lens antenna". In: *Microwaves, Antennas and Propagation, IEE Proceedings* 145.3 (1998), pp. 243–247. ISSN: 1350-2417. DOI: 10.1049/ip-map:19981884.

[92] T. Nitta. "Development of Optics for South Pole Sub-Millimeter Superconducting Camera - Translated from Japanese". MA thesis. Tsukuba University, 2011.

[93] R. O'Brient. "A Log-Periodic Focal-Plane Architecture for Cosmic Microwave Background Polarimetry". PhD thesis. University of California, Berkeley, 2010.

[94] Roger O'Brient et al. "A dual-polarized broadband planar antenna and channelizing filter bank for millimeter wavelengths". In: *Applied Physics Letters* 102.6, 063506 (2013), p. 063506. DOI: 10.1063/1.4791692. URL: http://link.aip.org/link/?APL/102/063506/1.

[95] Heavens O.S. *Optical Properties of Thin Solid Films*. 1955, pp. 46–96.

[96] Scott Paine. am *Atmospheric Model*. 2012. URL: https://www.cfa.harvard.edu/~spaine/am/.

[97] A. A. Penzias and R. W. Wilson. "A Measurement of Excess Antenna Temperature at 4080 Mc/s." In: *The Astrophysical Journal* 142 (1965), pp. 419–421. DOI: 10.1086/148307.

[98] N.E. Phillips. "Heat Capacity of Aluminum between 0.1K and 4.0K". In: *Physical Review* 114.3 (1959).

[99] D. M. Pozar. *Microwave Engineering*. John Wiley & Sons, Inc., 2005.

[100] C. Pryke et al. "Second and third season QUaD CMB temperature and polarization power spectra". In: *Astrophys.J.* 692 (2009), pp. 1247–1270. DOI: 10.1088/0004-637X/692/2/1247. arXiv: 0805.1944 [astro-ph].

[101] Inc. Quantum Design. *Laboratory SQUIDs*. 2013. URL: http://www.qdusa.com/products/laboratory-squids.html.

[102] E. Quealy. "The POLARBEAR cosmic microwave background polarization experiment and antireflection coatings for millimeter wave observations". PhD thesis. University of California, Berkeley, 2012.

[103] John A. Rayne. "Heat Capacity of Palladium below 4.2 K". In: *Phys. Rev.* 107 (3 1957), pp. 669–670. DOI: 10.1103/PhysRev.107.669. URL: http://link.aps.org/doi/10.1103/PhysRev.107.669.

[104] G.M. Rebeiz. “Millimeter-wave and terahertz integrated circuit antennas”. In: *Proceedings of the IEEE* 80.11 (1992), pp. 1748–1770. ISSN: 0018-9219. DOI: 10.1109/5.175253.

[105] Britt Reichborn-Kjennerud et al. *EBEX: a balloon-borne CMB polarization experiment*. 2010. DOI: 10.1117/12.857138. URL: http://dx.doi.org/10.1117/12.857138.

[106] P.L. Richards. “Bolometers for infrared and millimeter waves”. In: *Journal of Applied Physics* 76.1 (1994), pp. 1–24. ISSN: 0021-8979. DOI: 10.1063/1.357128.

[107] George B. Rybicki and Alan P. Lightman. *Radiative Processes in Astrophysics*. 2007. DOI: 10.1002/9783527618170.

[108] Ilan Sagiv et al. “The EBEX Cryostat and Supporting Electronics”. In: (2010), pp. 2166–2176. DOI: 10.1142/9789814374552_0429. arXiv: 1005.3339 [astro-ph.IM].

[109] K. Saini and R. Bradley. “The Sinuous Antenna - A dual Polarized Element for Wideband Phased Array Feed Application”. In: *Electronic Division Internal Memo No.301. National Radio Astronomy Observatory* (1996).

[110] D. Schwan et al. “APEX-SZ: The Atacama Pathfinder EXperiment Sunyaev-Zeldovich Instrument”. In: *The Messenger* 147 (Mar. 2012), pp. 7–12.

[111] Uros ˇ Seljak and Matias Zaldarriaga. “Signature of Gravity Waves in the Polarization of the Microwave Background”. In: *Phys. Rev. Lett.* 78 (11 1997), pp. 2054–2057. DOI: 10.1103/PhysRevLett.78.2054. URL: http://link.aps.org/doi/10.1103/PhysRevLett.78.2054.

[112] Inc. Silfex. *Silfex custom silicon ingots and blanks*. 2013. URL: http://www.silfex.com/products_2_0.html.

[113] Frederick W. Smith. “Effect of Manganese on the Superconductivity of Aluminum”. In: *Journal of Low Temperature Physics* 6.5/6 (1972).

[114] G. F. Smoot et al. “Structure in the COBE differential microwave radiometer first-year maps”. In: *The Astrophysical Journal* 396 (1992), pp. L1–L5. DOI: 10.1086/186504.

[115] K.T. Story et al. “A Measurement of the Cosmic Microwave Background Damping Tail from the 2500-square-degree SPT-SZ survey”. In: (2012). arXiv: 1210.7231 [astro-ph.CO].

[116] A. Suzuki et al. “Multi-chroic dual-polarization bolometric detectors for studies of the Cosmic Microwave Background”. English. In: *Journal of Low Temperature Physics* (2013 Submitted).

[117] Aritoki Suzuki et al. “Multichroic dual-polarization bolometric detectors for studies of the cosmic microwave background”. In: *Proceedings of SPIE mm, sub-mm, and far-IR Detectors and Instr for Astro VI 2012* (2012), 84523H–84523H–10. DOI: 10.1117/12.924869. URL: +http://dx.doi.org/10.1117/12.924869.

[118] G.C. Hilton K.D. Irwin W.H. Rippard J.N. Ullom S.W.Deiker W. Doriese, A. Williams L.R. Vale S.T. Ruggiero, and B.A. Young. “Superconducting transition edge sensor using dilute AlMn alloys”. In: *Applied Physics Letters* 85.11 (2004).

[119] Y. Sekimoto K. Mitsui N. Okada K. Karatsu M. Naruse M. Sekine H. Matsuo T. Noguchi T. Nitta S. Sekiguchi and M. Seta. *Anti-Reflection (AR) Coating for Cryogenic Silicon and Alumina Lenses at Millimeter-Wave Bands*. 2013.

[120] Yuki Takahashi. *Ground Shields for BICEP*. 2009. URL: http://bicep.caltech.edu/~yuki/shield/.

[121] APEX Web Team. *Atacama Pathfinder EXperiment APEX Weather monitor*. 2013. URL: http://www.apex-telescope.org/weather/.

[122] "The POLARBEAR-2 Experiment," in: *Journal of Low Temperature Physics* (2013 Submitted).

[123] "The POLARBEAR Cosmic Microwave Background Polarization Experiment," in: *Journal of Low Temperature Physics* (2013 Submitted).

[124] "Thermal conductivity and specific heat of glass ceramics". In: ().

[125] Takayuki Tomaru et al. "The POLARBEAR-2 experiment". In: *Proceedings of SPIE mm, sub-mm, and far-IR Detectors and Instr for Astro VI 2012* (2012), 84521H–84521H–10. DOI: 10.1117/12.926158. URL: +http://dx.doi.org/10.1117/12.926158.

[126] C. E. Tucker and P. A. R. Ade. *Thermal filtering for large aperture cryogenic detector arrays*. 2006.

[127] M. Pantaleev V. Belitsky C. Risacher and V. Vassilev. "Improving Accuracy of Superconducting Microstrip Line Modelling at Millimetre and Sub-Millimetre Waves". 2008. URL: https://science.nrao.edu/facilities/alma/aboutALMA/Technology/ALMA_Memo_Series/alma533/abs533.

[128] Eric W. Weisstein. *Beamsplitter*. 1999. URL: http://www.ericweisstein.com/research/thesis/node19.html.

[129] Martin J. White and Mark Srednicki. "Window functions for CMB experiments". In: *Astrophys.J.* 443 (1995), p. 6. DOI: 10.1086/175497. arXiv: astro-ph/9402037 [astro-ph].

[130] J.P. Daniel X. Begaud P. Poey and G. Dubost. *Design of Wideband Dual Polarized Slot Antenna*. 2000.

[131] G Yassin and S Withington. "Electromagnetic models for superconducting millimetre-wave and sub-millimetre-wave microstrip transmission lines". In: *Journal of Physics D: Applied Physics* 28.9 (1995), p. 1983. URL: http://stacks.iop.org/0022-3727/28/i=9/a=028.

[132] M.P. Zaitlin. "Discountinuity in the Heat Capacity of a Normal Metal-Superconductor Bilayer". In: *Solid State Communications* 41.4 (1982), pp. 317–320.

[133] J. Zhang et al. "New artificial dielectric metamaterial and its application as a terahertz antireflection coating". In: *Appl. Opt.* 48.35 (2009), pp. 6635–6642. DOI: 10.1364/AO.48.006635. URL: http://ao.osa.org/abstract.cfm?URI=ao-48-35-6635.